Universidade do Minho
Escola de Engenharia

José Luís Pina-Henriques

Masonry under Compression: Failure Analysis and Long-Term Effects

Alvenaria em Compressão: Comportamento à Rotura e Efeitos Diferidos

Outubro de 2005

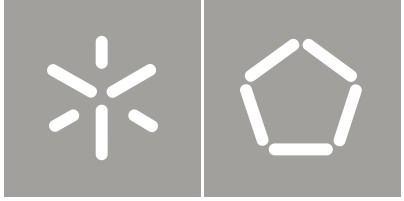

Universidade do Minho
Escola de Engenharia

José Luís Pina-Henriques

Masonry under Compression: Failure Analysis and Long-Term Effects

Alvenaria em Compressão: Comportamento à Rotura e Efeitos Diferidos

Tese de Doutoramento em Engenharia Civil

Trabalho efectuado sob a orientação de

Professor Doutor Paulo B. Lourenço
Universidade do Minho

Professora Doutora Luigia Binda
Politecnico di Milano

Outubro de 2005

Committee members

Rector of University of Minho, president

Prof. Paulo B. Lourenço, University of Minho, supervisor

Prof. Luigia Binda, Politecnico di Milano, co-supervisor

Dr. Alberto Zucchini, Italian National Agency for New Technologies, Energy and the Environment

Prof. Eduardo S. Júlio, University of Coimbra

Prof. Jorge V. Alfaiate, Instituto Superior Técnico

Prof. Paulo S. Cruz, University of Minho

ISBN 972-8692-24-2

Acknowledgements

The research reported in this thesis was carried out at the Civil Engineering Department of University of Minho, Portugal, and at the Structural Engineering Department of Politecnico di Milano, Italy. This research has been supported by the Portuguese Foundation for Science and Technology (FCT) under grant SFRH/BD/5002/2001, since November 2001.

To my supervisors, Paulo Lourenço and Luigia Binda, I owe my deepest gratitude for their inspiring guidance and huge dedication to make this work successful. I would like also to emphasize the intensity and fullness of our frequent discussions. Even if occasionally time was short, these were always a major and indispensable impulse to this work.

I wish to acknowledge all the staff of the Civil Engineering Department of University of Minho and of the Structural Engineering Department of Politecnico di Milano, especially Graça Vasconçelos, António Matos and Anna Anzani, for the insightful advice, interesting discussions and laboratory assistance. I am also indebted with Luís Neves for generously taking the time to read a draft of my thesis.

My four years stay in Guimarães could not have been more joyful thanks to my dearest friends Alberto Ribeiro, Alexandre Antunes, Artur Feio, Eduardo Pereira, Francisco Fernandes, Luís Neves, Pedro Lança, Tiago Figueira, Tiago Miranda and Vítor Cunha, who have, indeed, become part of my family. Special thanks are also due to Lorenzo Cantini and Massimiliano Barbi for making my stay in Milan so pleasant.

I would like to thank all my family for being always present and for their sincere encouragement, despite having no real interest in my research subject. I missed you. The birth of my lovely Mariana during this research period was a source of inspiration and joy. Thank you my dear wife, Carla, for your love and for your courage in ending this journey by my side.

Abstract

The work presented in this thesis has been developed at the Department of Civil Engineering of University of Minho, Portugal, and at the Department of Structural Engineering of Politecnico di Milano, Italy.

Recent sudden collapses of famous historical buildings, as the Pavia Civic Tower in 1989 or the Noto Cathedral in 1996, has drawn the attention of researchers to the compressive behaviour and time-dependent effects of heavily stressed masonry structures, with an emphasis in multiple-leaf pillars and walls, as this typology is frequently found in historical centres. The objective of this research is to contribute to the present state of knowledge in these fields.

For masonry under compression, a validation of simple analytical methods and non-linear continuum simulations based in plasticity and cracking has been performed. In fact, sophisticated non-linear models are now standard in several finite element based programs but the ability of such models to predict the compressive strength of masonry based on the properties of the constituents, units and mortar, is still an insufficiently debated issue. In the present study, the results obtained using non-linear continuum models and simple analytical methods, based on elastic considerations, have been compared with experimental results available in literature. A clear overestimation of the experimental strength by both numerical models and analytical methods was found, except by the empirical formulas provided by the European and North-American codes, which underestimated the experimental strength.

Alternative modelling approaches that account for the discrete nature of masonry components are therefore of interest, in order to provide reliable estimations of masonry compressive strength. A detailed analysis of a particle model consisting in a phenomenological discontinuum approach to represent the micro-structure of units and mortar was therefore addressed. The micro-structure attributed to masonry components is composed by linear elastic particles of polygonal shape separated by non-linear interface elements. All the inelastic phenomena occur in the interfaces and the process of fracturing consists of progressive bond-breakage. Clear advantages have been shown by the particle model, when compared to continuum models.

In the referred collapses of the Pavia Civic Tower or the Noto Cathedral, the time-dependent mechanical damage of heavily stressed walls and pillars was identified as a possible main cause of collapse. In this study, an experimental investigation has been conducted on a total of 25 ancient masonry prisms, which included standard compression tests, short-term creep tests and long-term creep tests. The results obtained and their careful interpretation are provided.

Multiple-leaf masonry walls and pillars are a typology often found in historical buildings, namely in the Noto Cathedral. Nevertheless, predicting the compressive behaviour of multiple-leaf masonry is a challenging issue, given the influence of a wide range of factors as the mechanical properties of the leaves, the leaves dimensions and the way the leaves are connected to each other. In the present study, an integrated experimental-numerical research program on the behaviour of large three-leaf masonry wallets subjected to shear and compression has been setup and novel experimental results are introduced, together with a careful numerical interpretation. A discussion on simplified calculations for practical assessment of existing walls is also addressed.

Resumo

O trabalho apresentado nesta tese foi desenvolvido no Departamento de Engenharia Civil da Universidade do Minho e no Departamento de Engenharia Estrutural do Politecnico di Milano, Itália.

O colapso súbito de algumas construções históricas famosas ocorrido recentemente, como por exemplo a Torre Cívica de Pavia em 1989 e a Catedral de Noto em 1996, despertou o interesse da comunidade científica sobre o comportamento à compressão e efeitos diferidos em estruturas de alvenaria sob estados de compressão muito elevados, nomeadamente em paredes e pilares de alvenaria composta, dada a importante presença deste tipo de elementos em centros históricos. Este trabalho tem como objectivo contribuir para o presente estado de conhecimento nestas áreas.

No caso da alvenaria submetida a esforços de compressão, procedeu-se à validação de métodos analíticos simplificados e de modelos não lineares contínuos, baseados em plasticidade e fendilhação. De facto, modelos não-lineares sofisticados são hoje correntes em diversos programas de elementos finitos. No entanto, a capacidade desses modelos em estimar correctamente a resistência à compressão da alvenaria, com base nas propriedades dos componentes, não se encontra ainda devidamente analisada. Neste trabalho, os resultados obtidos utilizando métodos numéricos do contínuo não-linear e métodos analíticos simplificados, baseados em hipóteses do domínio da elasticidade, foram comparados com resultados experimentais disponíveis na bibliografia. Constatou-se que os resultados numéricos sobrestimavam claramente os resultados experimentais, exceptuando os resultados obtidos de acordo com os regulamentos europeu e norte-americano, que os subestimavam.

Desta forma, abordagens numéricas alternativas que considerem a natureza discreta dos componentes da alvenaria revestem-se de grande importância para uma correcta previsão da resistência à compressão da alvenaria. Realizou-se, assim, uma análise detalhada de um modelo de partículas consistindo numa abordagem fenomenológica e discreta para representar a micro-estrutura das unidades e da argamassa. A micro-estrutura atribuída aos componentes da alvenaria é constituída por partículas de forma poligonal e comportamento elástico linear, separadas por interfaces com comportamento não-linear. Todos os fenómenos inelásticos ocorrem nas interfaces e o processo de fractura consiste na

progressiva rotura da ligação entre partículas. Claras vantagens foram observadas pelo modelo de partículas quando comparado com o modelo contínuo.

Nos referidos casos de colapso da Torre Cívica de Pavia e da Catedral de Noto, o comportamento diferido de paredes e pilares de alvenaria sob elevadas cargas verticais foi apontado como uma possível principal causa de colapso. Neste estudo, foi realizada uma investigação experimental em 25 provetes de alvenaria antiga, que inclui ensaios monotónicos, ensaios de fluência de curto-prazo e ensaios de fluência de longo-prazo. Os resultados obtidos e a sua interpretação cuidada são apresentados neste trabalho.

Paredes e pilares de alvenaria composta são uma tipologia frequentemente observada em construções históricas, nomeadamente na Catedral de Noto. No entanto, prever o comportamento à compressão de paredes compostas de alvenaria representa um importante desafio, dada a influência de um elevado número de factores como as propriedades mecânicas dos panos, a dimensão relativa dos panos e a forma como os panos estão ligados entre si. Neste estudo, novos resultados experimentais em provetes de três panos de grandes dimensões, ensaiados ao corte e à compressão, são apresentados em conjunto com uma interpretação numérica dos resultados. É apresentada, ainda, uma discussão sobre cálculos simplificados para avaliação expedita de paredes existentes.

Contents

1 Introduction

On 17th March 1989 the Civic Tower of Pavia suddenly collapsed without showing any apparent warning signs. Dramatically, four people were killed and severe damage was inflicted to surrounding buildings. The 60 *m* height tower was topped by a 16th century belfry while the main body had been built in successive phases during the 11th and 13th centuries. Nevertheless, the tower of Pavia is not an isolated case and several other famous examples can be referred, such as the collapse of the St. Magdalena bell-tower in Goch, Germany, in 1993, the partial collapse of the Noto Cathedral, Italy, in 1996, Binda *et al*. (2003a), and the severe damage exhibited by the bell-tower of the Monza Cathedral, Italy, see Modena *et al.* (2002). These events were a motive of great concern for the public authorities and have drawn the attention of researchers to the compressive behaviour and time-dependent effects of heavily stressed masonry structures.

Nevertheless, the compressive failure mechanism of quasi-brittle materials is rather complex, especially when compared with tensile failure. Compressive failure is characterized by the coalescence and growth of diffuse micro-cracks, accompanied by progressive localization of deformations and development of traction free macro-cracks. At ultimate stage, a distributed continuous pattern of splitting and shear cracks is formed, being responsible for failure, see Vonk (1993).

The most relevant material property when dealing with compression is clearly the compressive strength. Experimentally, this property can be obtained according to the European norm EN 1052-1, CEN (1998a), which specifies a complex testing specimen similar to the RILEM specimen, see Figure 2.1a. Mann and Betzler (1994) observed that, initially, vertical cracks appear in the units along the middle line of the specimen, *i.e.*, continuing the vertical joint. Upon increasing deformation, additional cracks appear, normally vertical cracks at the smaller side of the specimen that lead to failure by splitting of the prism. Experimental tests on representative masonry specimens are, however, relatively costly and not practical for design purposes. This fact persuaded researchers to investigate semi-empirical and analytical relations to predict masonry strength based on the components characteristics and on the type of masonry. Several semi-empirical relations can be gathered from the literature and the reader is referred to Rostampour (1973), Kirtschigg (1985), Haseltine (1987) and Vermeltfoort (1994) for details. Both European

and North-American masonry codes / specifications, CEN (2003) and ACI (2004), use empirical relations to estimate the compressive strength of masonry from the compressive strength of units and mortar. This empirical approach is obviously conservative and results from the envelope of a large set of experimental tests, meaning that the experimental strength of masonry can be severely underestimated.

Although empirical relations provide a safe basis for establishing design code provisions, little insight on the physical behaviour is obtained when compared to analytical methods. Today, it is well accepted by the research community that masonry compressive failure is mainly governed by the interaction between units and mortar. Assuming compatibility of strains between the components, the difference in stiffness leads, under uniaxial compressive loading, to a state of stress characterized by compression/biaxial tension of units and triaxial compression of mortar. This holds true, of course, when mortar is more deformable than units, which is generally the case of ancient masonry. In the pioneer work of Hilsdsdorf (1969), this phenomenon was firstly described and equilibrium based methods were derived to predict the masonry strength. Following this original work, several other theories have been developed and the reader is referred to Khoo and Hendry (1973), Francis *et al*. (1971), Atkinson *et al*. (1985) and Ohler (1986).

The new developments in computational mechanics witnessed in the last few decades have lead to the application of sophisticated numerical methods in the analysis of masonry structures. In particular, detailed modelling approaches where the masonry constituents (units and mortar) are individually represented have shown to be of great interest, see Lourenço and Rots (1997). In this way, the basic phenomena involved in masonry loading, such as load transfer mechanisms between the constituents, can be analysed.

Continuum and discontinuum (or discrete) approaches to model the masonry components can be used with the aim of reproducing the experimental behaviour of masonry. In the case of masonry under uniaxial compression, some authors indicate that continuum finite element micro-models are capable of obtaining an adequate response of the masonry composite, introducing the behaviour of masonry components, *e.g.* Brencich and Gambarotta (2005) and Roman and Gomes (2004).

Several advanced computational approaches are currently available for structural analysis developed in discontinuum frameworks, including the finite element method with

interface elements, discrete element methods and lattice models. The finite element method with interface elements widely used for structural analyses purposes and different approaches can be found in literature. For simple geometries under symmetric loading or when the crack path is known in advance from experiments, interface elements can be embedded in the finite element mesh along expected crack paths, see Rots (1988), Lourenço and Rots (1997) and Lofti and Shing (1994). If the crack pattern is not known in advance, expensive remeshing techniques, Ingraffea and Saouma (1985), or approaches where a sufficient number of interface elements are included in the mesh to account for potential crack paths, Carol *et al.* (2001), may be adopted.

Since the original work of Cundall (1971), discrete element methods have been receiving a growing interest from the scientific community due to the capabilities of such methods to deal with discrete media. As can be gathered from the literature, discrete element methods have been widely used to analyse the response of blocky assemblages, especially in the field of rock mechanics although references can also be found for blocky masonry structures, see Lemos (2001). In the field of concrete, discrete element methods were used to carry out meso- and micro-level analyses, see Lorig and Cundall (1987) and Vonk (1993).

Lattice models have been also receiving vivid attention. Its main concept is the discretization of the continuum into a framework of beam or truss elements. The simulations consist in a set of linear elastic analyses, each one corresponding to a load step. At the end of each load step, the adopted failure law is evaluated and the elements falling in its range are removed from the lattice. Lattice models have been extensively utilized in the study of tensile fracture propagation and references can be found in Schlangen (1993), Van Mier *et al*. (1995), Bazant and Planas (1998) and Van Vliet (2000). Recently, a lattice-type model has been proposed by Cusatis *et al.* (2003) aiming at a correct simulation of both tensile and compressive fracture processes.

Another important aspect in the analysis of the compressive behaviour of masonry are long-term effects. In fact, time-dependent mechanical damage under high sustained loading was identified as a main possible cause of collapse of the Pavia Civic Tower and of the Noto Cathedral.

Masonry creep depends mainly on factors such as the stress level and the temperature / humidity conditions but cyclic actions, such as wind, temperature variations

or vibrations induced by traffic or ringing bells, in the case of bell towers, have a synergetic effect, increasing material damage. For these reasons, high towers and heavily stressed pillars are the structural elements where time-dependent damage can severely occur, see Anzani *et al.* (1995) and Anzani *et al.* (2000). A comprehensive description of the phenomena involved in the time deformation of masonry can be found in Van Zijl (2000).

For low stress levels, below 40 to 50% of the compressive strength, creep deformation can be assumed proportional to the stress level. References on masonry creep within the elastic range are rather abundant in literature, see *e.g.* Ameny *et al.* (1984), Lenczner (1986) and Brooks (1990). On the contrary, creep under high stresses, even in the case of concrete, is not a sufficiently debated issue, see Bazant (1993), Papa *et al.* (1998) and Mazzotti and Savoia (2003). The fact that standard design methods for new structures are based on linear elastic material hypothesis has contributed to diminish the interest of researchers on this topic. However, ancient masonry structures are often working under low safety margins according to modern safety regulations. This can be due to inadequate knowledge of mechanics or structural modifications that occurred along centuries, resulting in overweighting of the structure and rendering importance to non-linear creep.

Multiple-leaf masonry walls and pillars are a typology often found in historical city centres worldwide, see *e.g.* Binda *et al*. (1999). Therefore, this typology is of major importance when analysing the compressive behaviour of masonry structures. The last decades have witnessed the severe damage, or even collapse, exhibited by several famous monumental buildings due to high compressive loading in multiple-leaf pillars and walls, as the referred collapse of the Noto Cathedral or the severe damage found in the churches of the Santissimo Crocefisso and Santissima Annunziata in Italy, Binda *et al.* (2001).

Most structural problems exhibited by three-leaf walls and pillars result from the poor or absent connection between the leaves, the weakness of the inner core or the deterioration of the mortar in the external joints. Several techniques such as grout injection or bed-joint reinforcement are today available for structural retrofitting, see Vintzileou and Tassios (1995), Toumbakari (2002) and Valluzzi *et al.* (2004). Nevertheless, reliable safety assessment and retrofitting with minimum intervention requires proper insight on the structural behaviour and failure mechanisms.

References in literature are rather scarce on this topic. Simple analytical models were proposed by Binda *et al.* (1991) to analyse the behaviour of multiple-leaf walls under compression. Later on, a first experimental assessment of the shear behaviour was carried by Binda *et al.* (1994) using two-leaf small scale specimens. The compressive behaviour has been also experimentally assessed by Egermann and Neuwald-Burg (1994) on three-leaf wallets. It is therefore believed that further insight on load-transfer and compressive failure mechanisms are needed.

1.1 Scope and objective of the research

This research focuses on the behaviour under compression of unreinforced masonry structures. Although mainly devoted to the study of historical structures, some of the conclusions are also relevant in the scope of new masonry. From the above text, it becomes clear that ancient structures can not be assumed to last forever and that knowledge on the phenomena involved in compressive failure is required. In particular, reliable strength estimation, long-term effects in heavily stressed structures and load transfer mechanisms in multiple-leaf walls and piers are issues where further investigation is needed. The objectives of this study are:

a) to validate analytical methods and continuum non-linear models in the collapse prediction of masonry subjected to short-term static loads;
b) to seek for alternative numerical models that can adequately estimate the compressive strength of masonry under short-term static-loads;
c) to obtain an adequate experimental characterization of creep behaviour of ancient masonry under high sustained stresses;
d) to obtain an experimental description of the compressive and shear behaviour of multiple-leaf masonry walls and, to interpret and numerically reproduce the experimental results.

1.2 Outline of the thesis

Chapter 2 addresses the ability of continuum numerical methods, based in plasticity and cracking, as well as analytical methods, to provide reliable estimations of masonry compressive strength. The analysis is carried out using a detailed modelling strategy where

units and mortar are modelled separately. A discussion on the load transfer between masonry components is presented and special attention is given to numerical failure patterns, which is an issue often disregarded. Validation of the numerical results is performed by means of a comparison with experimental results available in literature.

Chapter 3 introduces an alternative modelling approach to analyse the behaviour under compression of masonry assemblages. A meso-level approach is followed using a particle model, which consists in a phenomenological discontinuum approach to represent the micro-structure of units and mortar. This micro-structure is composed by linear elastic particles of polygonal shape separated by non-linear interface elements. All the inelastic phenomena occur in the interfaces and the process of fracturing consists of progressive bond-breakage.

Chapter 4 deals with an experimental investigation on the creep behaviour of ancient masonry under high sustained stresses. Standard compression tests, short-term creep tests and long-term creep tests were considered and a comparative discussion is given. The experimental investigation focuses on three different types of ancient masonry specimens: (a) rubble prisms from the crypt of the Monza Cathedral (16^{th} century), (b) rubble prisms recovered from the wall ruins of the Pavia Civic Tower (11^{th} to 13^{th} century) and (c) regular prisms recovered from the belfry ruins of the Pavia Civic Tower (16^{th} century).

Chapter 5 presents an integrated experimental-numerical approach to provide understanding into the load-transfer and compressive failure mechanisms of three-leaf stone masonry walls. Novel experimental results from shear and compression results in large three-leaf specimens are provided, which can contribute to the derivation of rational design rules and validation of numerical models. A careful numerical interpretation of the experimental results is given and a discussion on simplified calculations for practical assessment of existing walls is addressed.

Chapter 6 presents an extended summary and final conclusions that can be derived from this study. Moreover, suggestions for future work are presented.

2 Validation of analytical and continuum numerical methods for estimating the compressive strength of masonry

Masonry compressive behaviour is of crucial importance for design and safety assessment purposes, since masonry structures are primarily stressed in compression. However, the compressive failure mechanism of quasi-brittle materials is rather complex, especially when compared with tensile failure. Compressive failure is characterized by the coalescence and growth of diffuse micro-cracks, accompanied by progressive localization of deformations and development of traction free macro-cracks. At ultimate stage, a distributed continuous pattern of splitting and shear cracks is formed, being responsible for failure, see Vonk (1993).

The most relevant material property when dealing with compression is clearly the compressive strength. Experimentally, this property can be obtained according to the European norm EN 1052-1, CEN (1998a), which specifies a testing specimen similar to the RILEM specimen, see Figure 2.1a. Mann and Betzler (1994) observed that, initially, vertical cracks appear in the units along the middle line of the specimen, *i.e.*, continuing the vertical joint. Upon increasing deformation, additional cracks appear, normally vertical cracks at the smaller side of the specimen that lead to failure by splitting of the prism. Experimental tests on representative masonry specimens are, however, relatively costly and not practical for design purposes. This fact persuaded researchers to investigate semi-empirical and analytical relations to predict masonry strength based on the components characteristics and on the type of masonry. Several semi-empirical relations can be gathered from the literature and the reader is referred to Rostampour (1973), Kirtschigg (1985), Haseltine (1987) and Vermeltfoort (1994) for details. Both European and North-American masonry codes / specifications, CEN (2003) and ACI (2004), use empirical relations to estimate the compressive strength of masonry from the compressive strength of unit and mortar.

Although empirical relations provide a safe basis for establishing design code provisions, little insight on the physical behaviour is obtained when compared to analytical methods. Today, it is well accepted by the research community that masonry compressive

failure is mainly governed by the interaction between units and mortar. Assuming compatibility of strains between the components, the difference in stiffness leads, under uniaxial compressive loading, to a state of stress characterized by compression/biaxial tension of units and triaxial compression of mortar, see Figure 2.1b. This holds true, of course, when mortar is more deformable than units, which is generally the case of ancient masonry.

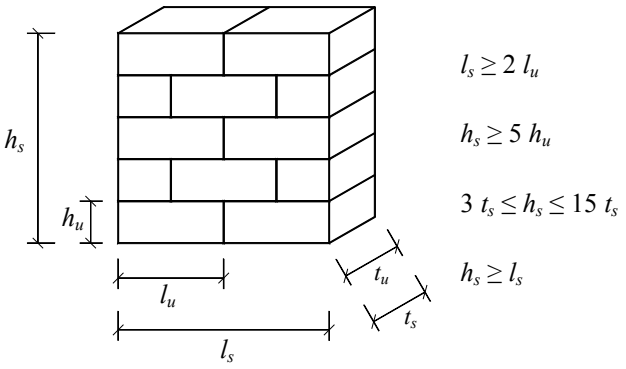

(a)

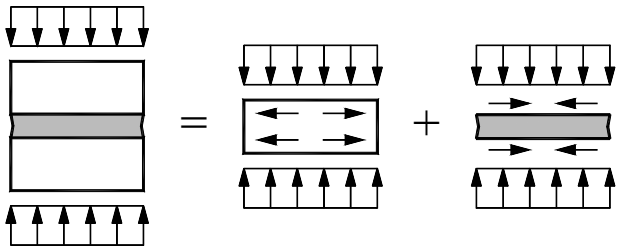

(b)

Figure 2.1 – Uniaxial behaviour of masonry: (a) test specimen according to the European standards (for units with $l_u \leq 300\ mm$ and $h_u \leq 150\ mm$), CEN (2003), and (b) schematic plane representation of stresses in masonry components. The subscript *u* refers to the unit and the subscript *s* refers to the specimen.

In the pioneer work of Hilsdsdorf (1969), this phenomenon was firstly described and an equilibrium approach was developed to predict the masonry strength. Yet, Hilsdorf (1969) assumed that failure of mortar coincides with failure of masonry, which is not necessarily true. In the theory proposed by Khoo and Hendry (1973) this problem is overcome by considering a limit strain criterion based on the lateral strain exhibited by brick units at failure. Another relevant contribution was given by Ohler (1986), who

proposed an expression that in general shows good agreement with experimental data. Failure theories that allow following stress and strain evolution upon increasing loading have been also developed. Examples can be found in Francis *et al*. (1971) and Atkinson *et al*. (1985).

The present study focuses on the ability of analytical methods and continuum non-linear finite element models, based on plasticity and cracking, to reproduce the experimental behaviour of masonry under compression. A micro-modelling strategy incorporating units and mortar is followed, which is a powerful tool in the analysis of the composite material, see Lourenço (1996a) and Brencich and Gambarotta (2005). In addition, a discussion on the load transfer between the components upon increasing loading is presented and special attention is given to the numerical failure patterns obtained, which is an issue often disregarded in literature.

2.1 Brief description of adopted experimental testing

Binda *et al*. (1988) carried out deformation controlled tests on masonry prisms with dimensions of $600 \times 500 \times 250$ mm^3, built up with nine courses of $250 \times 120 \times 55$ mm^3 solid soft mud bricks and 10 *mm* thick mortar joints. Three different types of mortar, denoted as *M1*, *M2* and *M3*, have been considered and testing aimed at the evaluation of the compressive properties of the prisms. For each type of mortar, a total of three prisms were tested.

The tests were carried out in a uniaxial testing machine MTS® 311.01.00, with non-rotating steel plates and a maximum capacity of 2500 *kN*. The applied load was measured by a load cell located between the upper plate and the testing machine, while displacements up to the peak load were measured with a removable strain gauge, see Figure 2.2. In addition, the average vertical displacement of each prism was also recorded with the machine in-built displacement transducer, permitting to capture the complete stress-strain diagram, including the softening regime. In this study, the prisms vertical strains and elastic moduli were calculated from the transducer measured displacements. Teflon sheets were placed between the prisms and the loading plates in order to minimize restraining frictional stresses.

The characteristics of the masonry components in terms of compressive strength f_c, flexural tensile strength f_f, elastic modulus E and coefficient of Poisson ν are given in Table 2.1. The results obtained for the prisms are given in Table 2.2. Prisms *P1*, *P2* and *P3* were built with mortars *M1*, *M2* and *M3* of increasing strength, respectively. The experimental failure patterns found were rather similar despite the type of mortar used, Frigerio and Frigerio (1985). Figure 2.3 depicts the typical failure pattern.

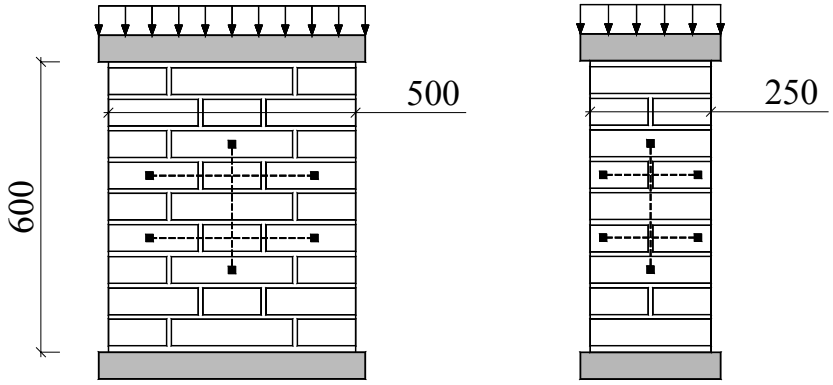

Figure 2.2 – Tested masonry wallets and location of strain gauge measurements, Binda *et al*. (1988). The dimensions are in *mm*.

Table 2.1 – Mechanical properties of the masonry components, Binda *et al*. (1988).

Component	E N/mm^2	ν -	f_c N/mm^2	f_f N/mm^2
Unit	4865	0.09	26.9	4.9
Mortar *M1*	1180	0.06	3.2	0.9
Mortar *M2*	5650	0.09	12.7	3.9
Mortar *M3*	17760	0.12	95.0	15.7

Table 2.2 – Mechanical properties of the masonry prisms, Binda *et al*. (1988).

Prism type	Mortar type	E N/mm^2	f_c N/mm^2
P1	*M1*	1110	11.0
P2	*M2*	2210	14.5
P3	*M3*	2920	17.8

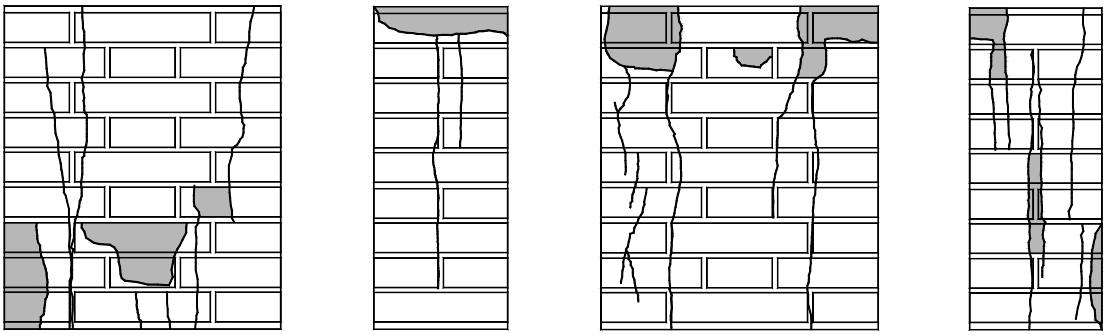

Figure 2.3 – Typical experimental failure patterns, Frigerio and Frigerio (1985). The shaded areas indicate spalling of material.

2.2 Outline of the numerical model

The simulations were carried out resorting to a *basic cell*, *i.e.*, a periodic pattern associated to a frame of reference, see Figure 2.4. For the application envisaged, units and mortar were represented by a structured continuum finite-element mesh. However, to reduce computational effort, only a quarter of the basic cell was modelled assuming adequate conditions for the in-plane boundaries, see Figure 2.5. In such way, symmetry boundary conditions were assumed for the two sides along the basic cell symmetry axes and periodicity conditions for the two sides defining the external boundary of the basic cell.

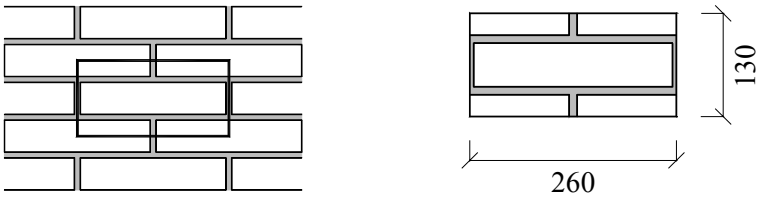

Figure 2.4 – Definition of *basic cell*: (a) running-bond masonry and (b) geometry.

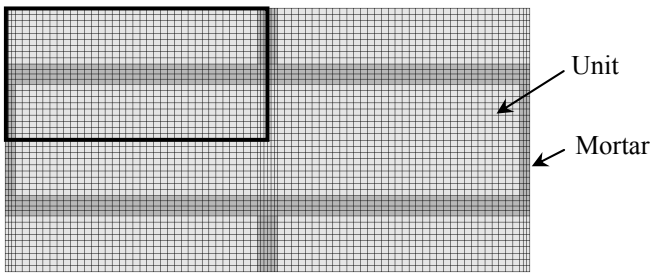

Figure 2.5 – Model used in the simulations (only the quarter indicated was simulated, assuming symmetry conditions).

It is known that the boundary conditions and the test setup affect the response of masonry under uniaxial compression. This is more significant in the post-peak regime but the peak load and pre-peak regime are also affected, see *e.g.* Mann and Betzler (1994). The choice of an appropriate test setup resulted in the CEN specimen, CEN (1998a), which leads to the usage of moderately large specimens. The author assumed that the experimental values from the actual testing program, Binda *et al*. (1988), aimed at obtaining the "true" compressive strength of masonry and, therefore, assumed the typical representative volume element (or basic cell) for such a material. Of course that this approach is only approximate of the real geometry and the obtained numerical response is phenomenological. This means that a comparison in terms of experimental and numerical failure patterns is not possible. In particular, splitting cracks usually observed in prisms tested under compression, Mann and Betzler (1994), boundary effects of the specimen and non-symmetric failure modes are not captured by the numerical analysis. Again, most of these combined effects control mainly the post-peak response, which is not the key issue in the present contribution.

Regarding the out-of-plane boundaries, three different approaches were considered: (a) plane-stress *PS*, (b) plane-strain *PE* and (c) an intermediate state, here named enhanced-plane-strain *EPE*. This last approach consists of modelling a thin out-of-plane masonry layer with 3D elements, imposing equal displacements in the two faces of the layer. Full 3D analyses with refined meshes and softening behaviour are unwieldy, and were not considered. Moreover, recent research indicates that enhanced-plane-stress analysis and 3D analysis provides very similar results, see Berto *et al*. (2005).

Each approach corresponds to a different level of out-of-plane confinement. In plane-stress, out-of-plane stresses are precluded and the specimen can freely deform in this direction. This condition holds generally true at the surface of a specimen. On the contrary, in plane-strain, out-of-plane deformations are precluded, which is the limiting condition at the centre of a thick specimen. An intermediate state between these extreme conditions is also of interest in the evaluation of the model and the enhanced-plane-strain state was considered.

For *PS* and *PE*, the masonry components were represented by approximately 1200 8-noded quadrilateral elements with 3700 nodes, totalling 7400 degrees of freedom. 3×3 Gauss integration was adopted. The material behaviour was described by a composite

plasticity model with a Drucker-Prager yield criterion in compression and a Rankine yield criterion in tension, DIANA (1999) and Feenstra (1993). The inelastic behaviour exhibits a parabolic hardening/softening diagram in compression and an exponential-type softening diagram in tension. The material behaves elastically up to one-third of the compressive strength and up to the tensile strength.

For *EPE*, modelling of the cell was carried out using approximately 900 20-noded brick elements with 6650 nodes, totalling 13300 degrees of freedom (note that the tying adopted for the out-of-plane degrees of freedom, mean that a basically 2D model is used). $3 \times 3 \times 3$ Gauss integration was adopted. The material model used in 2D simulations is not available for 3D models and a combined model with traditional smeared crack model in tension, Rots (1988), specified as a combination of tension cut-off (two orthogonal cracks), tension softening and shear retention, and Drucker-Prager plasticity in compression had to be used, DIANA (1999). The models in tension provide comparable results, Lourenço *et al.* (1995) but the plasticity based model is numerically more robust.

The loading scheme adopted in the simulations consisted in applying a vertical compressive stress at the upper and lower boundaries of the basic cell. The DIANA® finite element code, DIANA (1999), was adopted to carry out the simulations, being the non-linear equilibrium equations that arise from the finite element discretization solved using an incremental-iterative regular Newton-Raphson method, with arc-length control and line-search technique.

2.3 Definition of the model parameters

The parameters were obtained, whenever possible, from the experimental tests. However, most of the inelastic parameters were unknown and had to be estimated from other tests. Despite the effort made in the last decades, micro-simulations are often hindered by the lack of experimental data on the non-linear properties of the components.

The elastic material properties adopted were previously given in Table 2.1 and the inelastic properties are fully detailed in Table 2.3. Here, c is the cohesion, f_t is the tensile strength, ϕ is the friction angle, ψ is the dilatancy angle, Gf_t is the tensile fracture energy and Gf_c is the compressive fracture energy (cohesion related). The value adopted for the friction angle was 10º (a larger value in plane-stress would implicate an overestimation of

the biaxial strength for this specific yield criterion) and, for the dilatancy angle, a value of 5º was assumed, Vermeer and de Borst (1984). The values assumed for the fracture energy have been based in recommendations supported in experimental evidence, Lourenço (1996b) and CEB-FIP (1993), and practical requirements to ensure numerical convergence. Severe convergence problems were found due to the strongly inhomogeneous stress and strain fields that result from the analysis, especially in the case of prism *P1*, which features very large differences between the properties of units and mortar.

Table 2.3 – Inelastic properties given to masonry components.

Component	c N/mm^2	f_t N/mm^2	$\sin\phi$ -	$\sin\psi$ -	Gf_t N/mm	Gf_c N/mm
Unit	11.3	3.7	0.17	0.09	0.190	12.5
Mortar *M1*	1.3	0.7	0.17	0.09	0.350	2.7
Mortar *M2*	5.3	3.0	0.17	0.09	0.150	10.0
Mortar *M3*	39.9	12.0	0.17	0.09	0.600	23.0

2.4 Numerical results and comparison with experimental data

2.4.1 Stress-strain diagrams

The boundary conditions imposed on the model lead to equal normal displacements along each boundary but non-uniform stress fields. In this way, the average stress applied on the cell results from the integral of stresses over the upper and bottom boundaries divided by their length. The strain is the measure of an equivalent homogenised basic cell. The comparison between the numerical and experimental stress-strain diagrams is given in Figure 2.6. Here it is shown that *EPE* response is always between the extreme responses obtained with *PS* and *PE*. For this reason, enhanced-plane-strain is accepted as the reference solution for the numerical analysis in the rest of this work. It is further noted that the difference between the strength values predicted in *PS* and *PE* conditions increase with larger compressive strength ratios $f_{c,unit} / f_{c,mortar}$. This can be explained by the fact that weak mortar joints fail at a very early stage if no out-of-plane confinement is present.

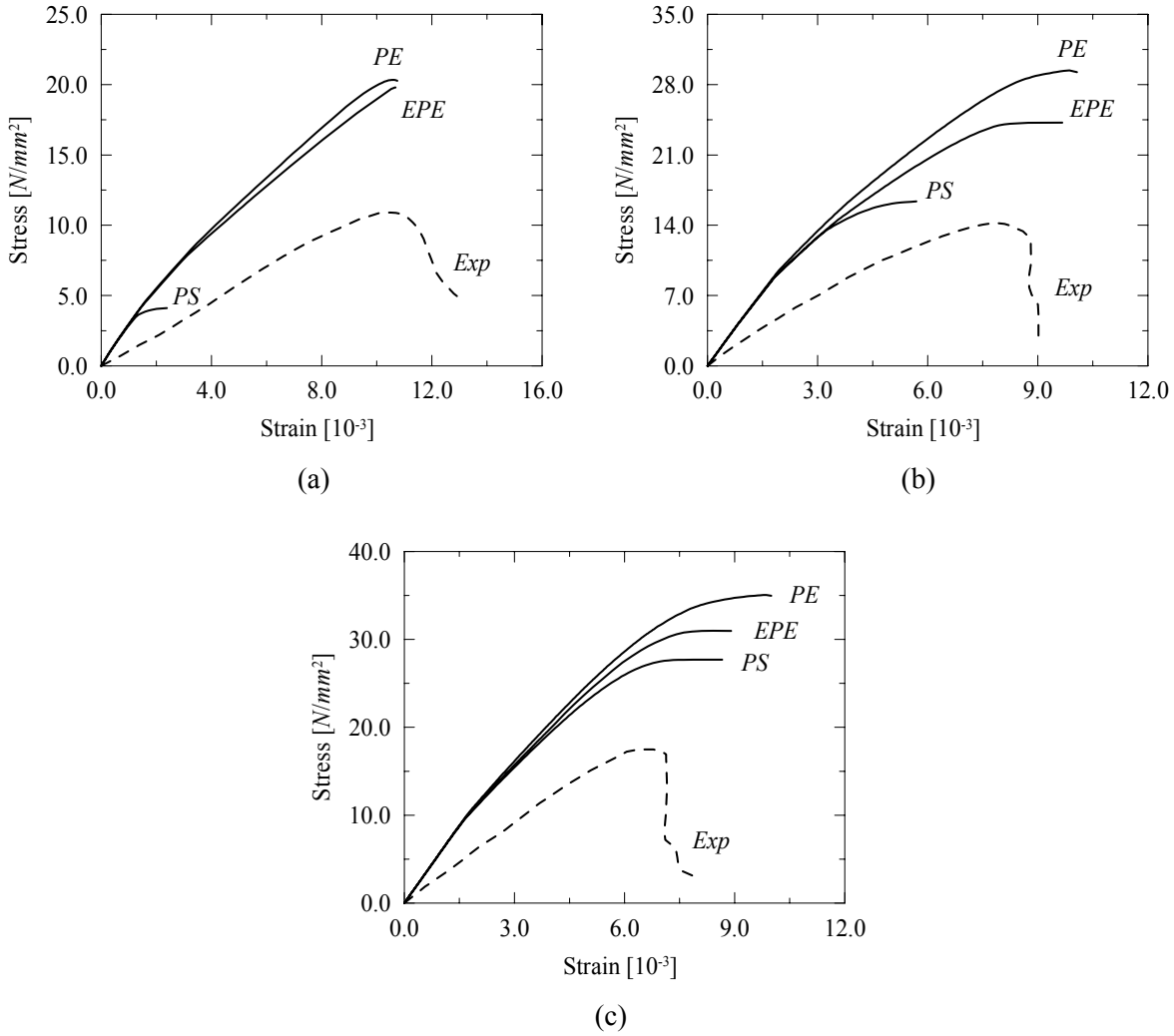

Figure 2.6 – Experimental and numerical stress-strain diagrams in *PS*, *PE* and *EPE* conditions for prisms: (a) *P1*, (b) *P2* and (c) *P3*.

Another important aspect is that the numerical strength largely overestimates the experimental strength for all the three prisms, even if the peak strain is well reproduced by the numerical analysis. Comparing the results in terms of stiffness, it is possible to observe that the numerical response is much stiffer than the experimental response. This can be explained by the fact that the stiffness of the mortar inside the composite is different from the stiffness of mortar specimens cast separately due to different laying and curing conditions, see *e.g.* Lourenço (1996a). The difficulty in evaluating the stiffness of mortar inside the composite represents a severe drawback of detailed micro-models.

To reproduce correctly the experimental elastic stiffness of the masonry prisms, the elastic modulus of the mortar had to be adjusted by inverse fitting. An estimate of the value

of the adjusted stiffness can be obtained, disregarding the interaction unit-mortar, from

$$\Delta_{y,M} = \Delta_{y,u} + \Delta_{y,m} \tag{2.1}$$

where $\Delta_{y,M}$ is the vertical displacement of a masonry prism, $\Delta_{y,u}$ is the vertical displacement contribution of the units and $\Delta_{y,m}$ is the vertical displacement contribution of the mortar joints. This equation reads, after some manipulation,

$$E_{adj} = \frac{h_m E_M E_u}{E_u (h_m + h_u) - E_M h_u} \tag{2.2}$$

here, E_{adj} is the adjusted elastic modulus of the mortar, E_u is the elastic modulus of the units, E_M is the elastic modulus of the composite given in Table 2.2, h_m is the joint thickness and h_u is the height of the units.

The adjusted elastic moduli assumed in the new simulations are given in Table 2.4. In addition, the ratios between the adjusted E_{adj} and experimental E_{exp} elastic moduli are also shown, indicating that the adjusted elastic modulus ranges between 6 and 30% of the values recorded experimentally in mortar prisms. Here, it is noted that the relation between adjusted and mortar prism elastic modulus decreases with the mortar strength. The obtained adjusted stress-strain diagrams are illustrated in Figure 2.7, together with the results obtained with the experimental stiffness for a better comparison. The strength values are similar using either the experimental mortar stiffness or the adjusted value but a dramatic difference in the peak strain was found. In fact, for the adjusted mortar stiffness, the numerical peak strain largely overestimates the experimental value and the difference increases with increasing mortar strength.

The possibility of adjusting also the mortar strength was not considered because a direct relation between strength and stiffness cannot be established in such a complex case of mortar curing, compaction and moisture exchange.

Table 2.4 – Adjusted elastic deformability parameters for mortar.

	E [N/mm^2]	E_{adj}/E_{exp}
Mortar *M1*	355	0.30
Mortar *M2*	735	0.13
Mortar *M3*	1065	0.06

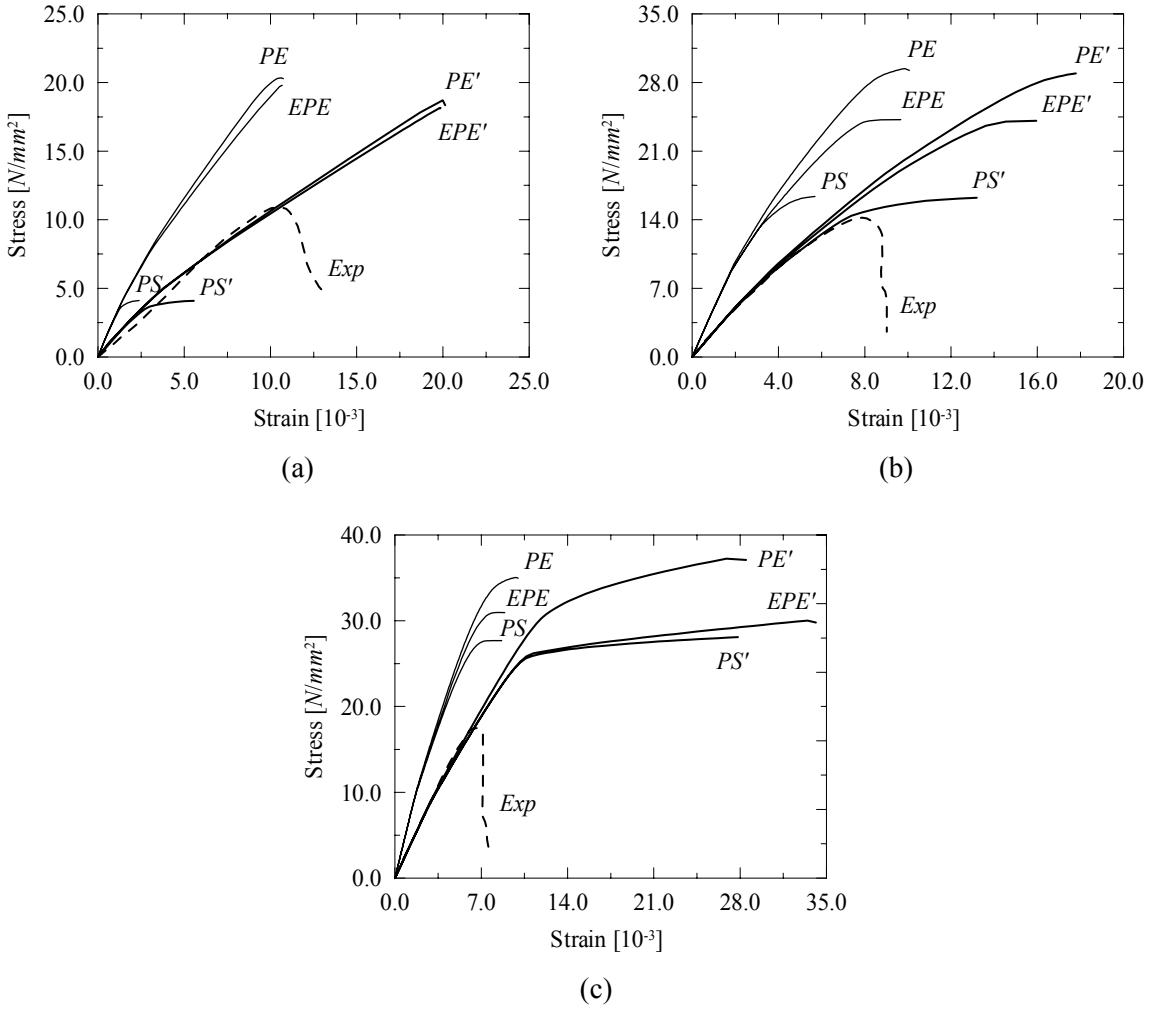

Figure 2.7 – Comparison between the stress-strain diagrams obtained with experimental (no superscript) and adjusted (′ superscript) mortar stiffness values for prisms: (a) *P1*, (b) *P2* and (c) *P3*.

2.4.2 Failure patterns

Failure patterns are an important feature when assessing numerical models. Figure 2.8 to Figure 2.13 depict the deformed meshes at failure for the three types of prism in *PS*, *PE* and *EPE* conditions. In addition, the contour of the minimum principal plastic strains is also given in the case of *EPE*.

The failure mechanisms obtained depend obviously on the modelling strategy adopted. This is numerically correct and physically non-realistic, even if it is an issue often disregarded. In *PS* conditions, prisms *P1* and *P2* fail due to crushing of the bed joints while prism *P3* fails due to vertical cracks arising in the bed-joints, together with diagonal

"crushing" that crosses the units and connects the non-aligned vertical cracks (it is noted that crushing in the centre of the units is more profound), see Figure 2.8a, Figure 2.10a and Figure 2.12a. In *PE* conditions, failure of prisms *P1* and *P2* is mainly governed by vertical cracks developing close to the centre of the units and in the head-joints. Prism *P3*, on the other hand, fails due to diffuse vertical cracking crossing both units and joints, combined with crushing of the centre of the units, see Figure 2.8b, Figure 2.10b and Figure 2.12b.

In *EPE* conditions, prism *P1* fails mainly due to the development of vertical cracks in the centre of the units and along the head-joints, being the mortar in the bed-joints severely damaged, see Figure 2.9. In the case of prism *P2*, failure occurs due to crushing of both units and mortar in a rather uniform manner, see Figure 2.11. Prism *P3* fails due to the development of several vertical cracks arising in the bed joints together with compressive damage of the units, especially at the centre, see Figure 2.13.

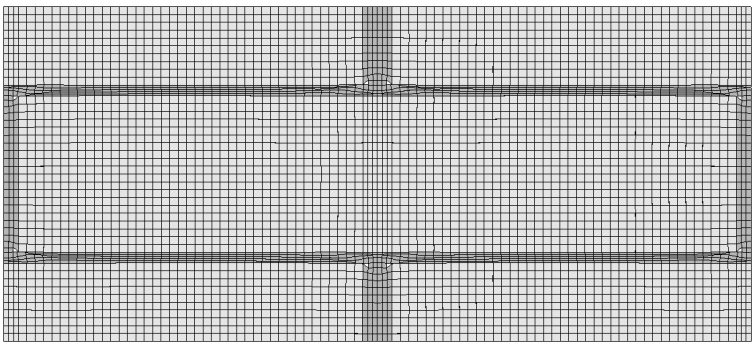

(a)

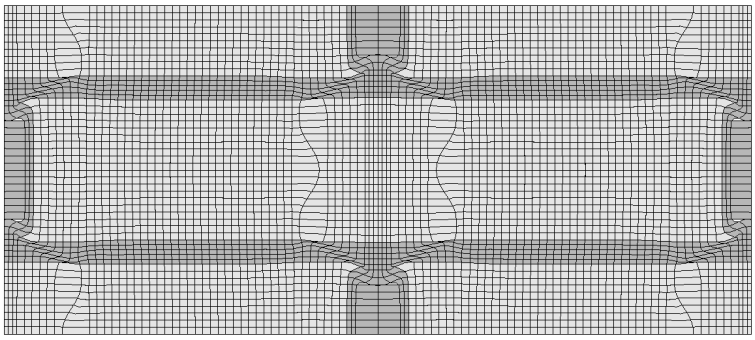

(b)

Figure 2.8 – Deformed (incremental) meshes at failure for prism *P1*: (a) *PS* and (b) *PE*.

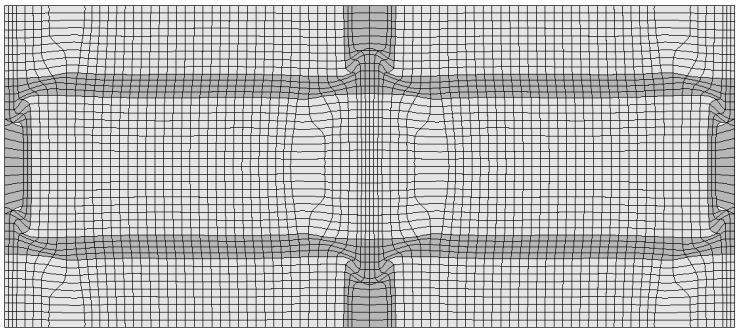

(a)

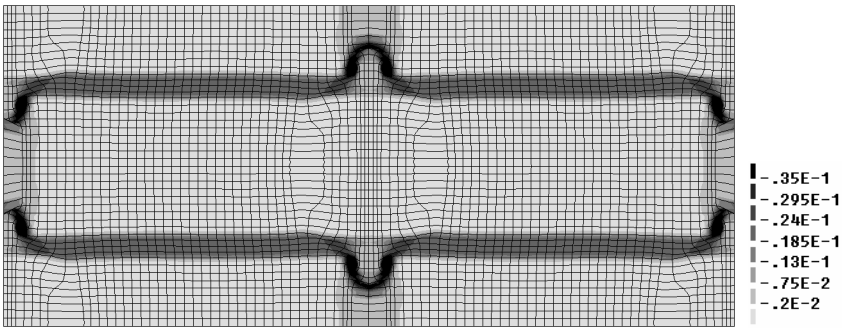

(b)

Figure 2.9 – Results obtained at failure for prism *P1* in *EPE*: (a) deformed (incremental) mesh and (b) minimum principal plastic strains.

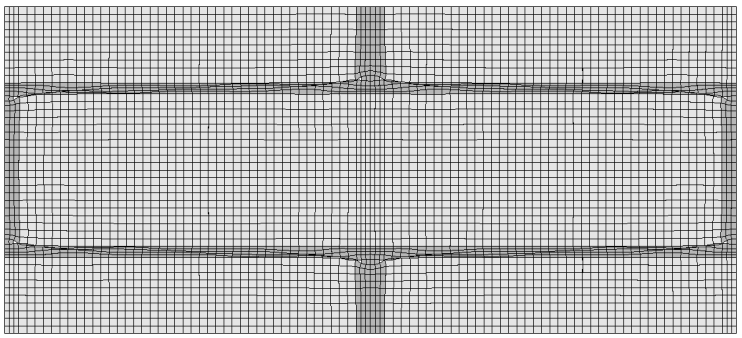

(a)

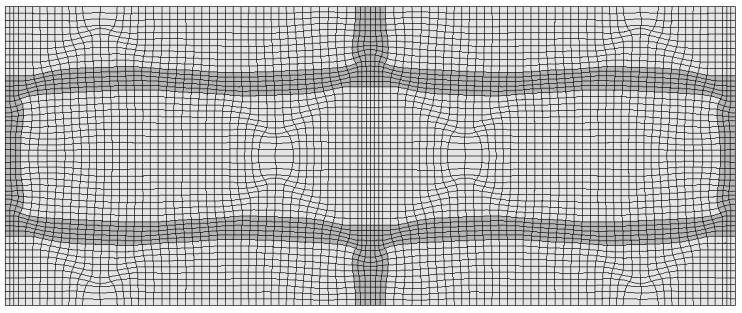

(b)

Figure 2.10 – Deformed (incremental) meshes at failure for prism *P2*: (a) *PS* and (b) *PE*.

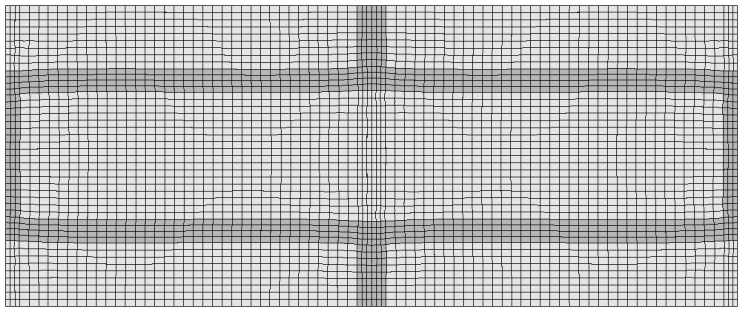

(a)

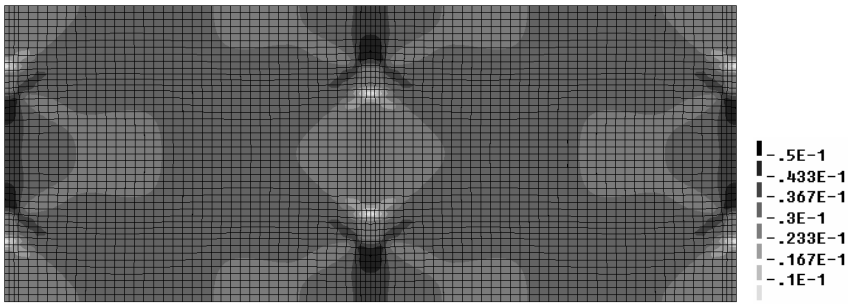

(b)

Figure 2.11 – Results obtained at failure for prism *P2* in *EPE*: (a) deformed (incremental) mesh and (b) minimum principal plastic strains.

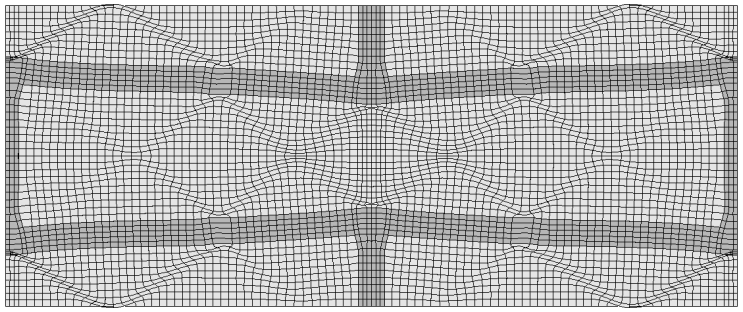

(a)

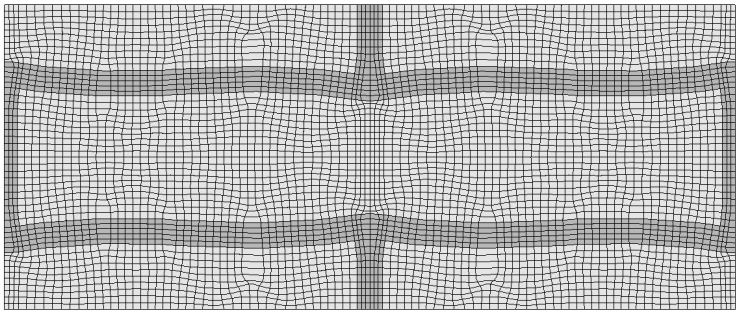

(b)

Figure 2.12 – Deformed (incremental) meshes at failure for prism *P3*: (a) *PS* and (b) *PE*.

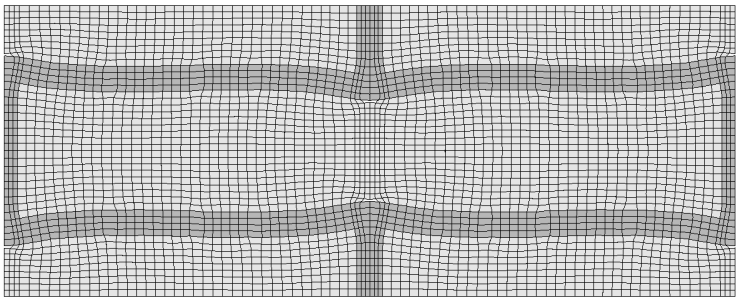

(a)

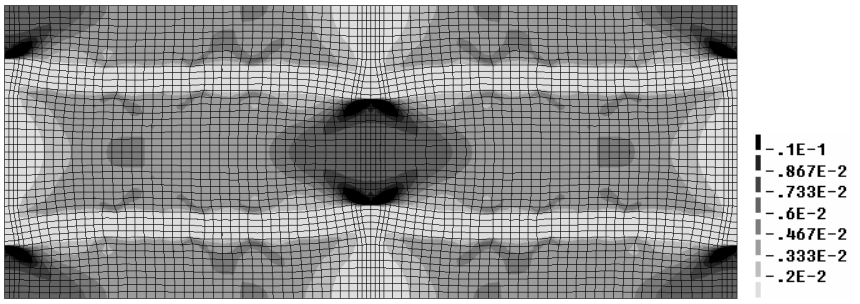

(b)

Figure 2.13 – Results obtained at failure for prism *P3* in *EPE*: (a) deformed (incremental) mesh and (b) minimum principal plastic strains.

2.4.3 Stress distribution

Insight on the stress distribution upon increasing loading can be provided by stress diagrams along different sections of the cell, see Figure 2.14. Prism *P1* was chosen as an example because it has a relatively strong unit and a rather weak mortar as often occurs in ancient masonry. Three different load levels were considered, each one corresponding to a different branch of the stress-strain diagram.

Severe non-linear behaviour and stress redistribution has been found, with failure not occurring when the maximum stress is attained at a given point of the discretization. As expected, Figure 2.14a indicates that mortar is heavily triaxially compressed and the units are under combined compression-biaxial tension. A decrease of vertical compressive stresses in the bed-joints is observed near the head-joints due to the low stiffness of the mortar, see Figure 2.14b. This unloading effect increases closer to collapse, due to inelastic behaviour of the head joints. Moreover, in Figure 2.14c, it is possible to observe that increasing stress concentration develops at the unit edges as load increases and the neighbouring head-joint fails. Also due to increasing damage in the head-joint, the centre

of the units exhibit a decrease of compressive vertical stresses as the load increases, resulting in a failure of the unit with horizontal offset with respect to the head joints.

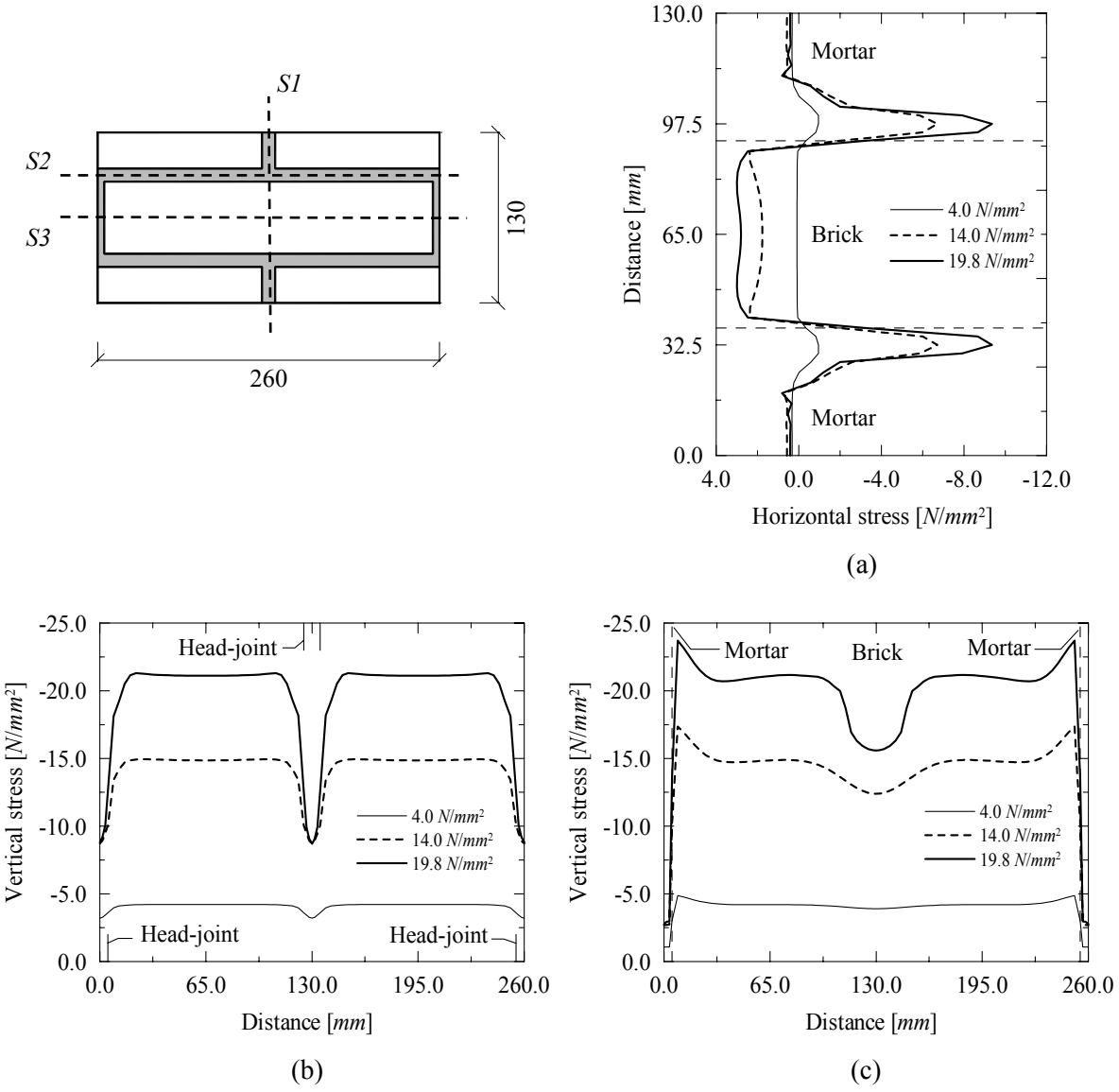

Figure 2.14 - Stress diagrams at increasing load levels for different sections of the cell (*EPE*): (a) *S1*, (b) *S2* and (c) *S3*.

2.5 Influence of masonry head-joints

In the previous Section, the ability of plasticity and cracking based models to predict the compressive strength of running-bond masonry prisms was assessed. In this Section, the influence of vertical head-joints in the compressive strength of masonry prisms is numerically addressed by comparing the results for running-bond prisms with compression

simulations on stack-bond prisms. Running-bond specimens are wider than stack-bond prisms and thus a certain confinement effect is present that could possibly lead to an increase of strength. This despite the fact that the confinement effect is mainly controlled by the ratio between the height of the specimen and the smallest in-plane dimension, as accepted by the research community and reflected in codes, see *e.g.* EC6, CEN (2003). Nevertheless, the existence of vertical joints on running-bond prisms may have an opposite effect, contributing to a reduction of the prisms strength.

Vermeltfoort (1994) carried out compression tests in RILEM running-bond prisms and in stack-bond prisms, built with different types of brick and mortar, and reported values for the ratio between running-bond and stack-bond strengths ranging between 1.0 and 1.3. Mann and Betzler (1994) have also conducted similar tests and the values presented for the same ratio ranged between 0.9 and 1.2.

The model considered is based on the same concepts, material properties and loading conditions of the model described in Section 2.2 and Section 2.3, in order to make possible a comparison between running-bond and stack-bond results. The simulations were carried out only for prisms *P1* and *P2* (in *EPE*) as they represent the most relevant cases. The stack-bond model used is depicted in Figure 2.15 and Figure 2.16.

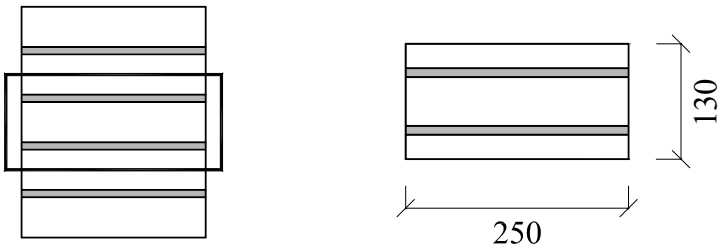

Figure 2.15 – Stack-bond basic cell: (a) stack-bond masonry prism and (b) geometry.

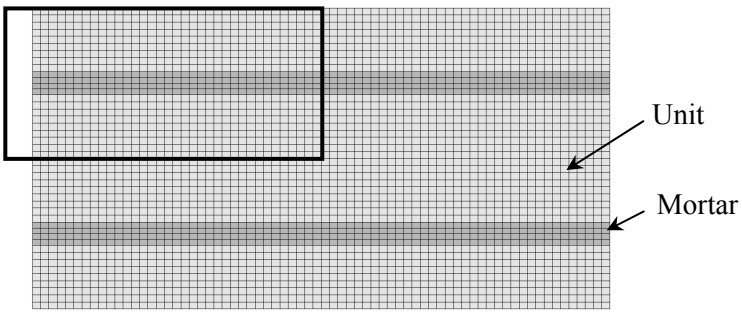

Figure 2.16 – Model used in the simulations (only the indicated quarter was simulated).

Symmetry conditions were adopted in the three continuity edges of the basic cell. With respect to the free edge, linear dependencies were established between the mesh nodes in order to obtain a deformed shape similar to the elastic shape if no restrictions were applied. To better account for non-linear effects, the imposed elastic shape was obtained for a mortar with one third of the stiffness adopted in the simulations. If such dependencies between the nodes were not applied, the numerical incremental-iterative procedure becomes unstable and, furthermore, non-realistic failure mechanisms are obtained.

Figure 2.17 illustrates the stress-strain diagrams obtained. For prisms *P1*, a strength approximately 20% higher has been predicted for stack-bond configuration when compared with running-bond. With respect to prisms *P2*, built with a stronger mortar, only a slight strength increase of 2% was observed. It is noted that the numerical results provide a prediction of the expected behaviour in ideal conditions and that the differences encountered with the experimental results reported by Vermeltfoort (1994) can be related, among other factors, with the test setup utilized.

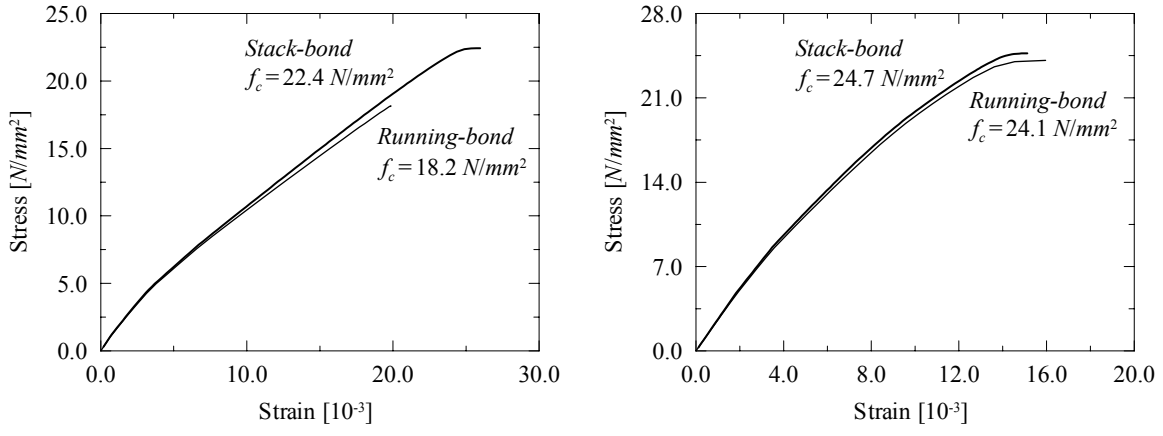

Figure 2.17 – Numerical stress-strain diagrams for stack-bond and running-bond simulations (*EPE*): (a) prisms *P1* and (b) prisms *P2*.

Figure 2.18 depicts the numerical failure patterns obtained. It can be observed that the prism *P1* fails due to vertical cracks arising in the units near the edges and by localized crushing of the mortar joints, also near the faces of the prism. For prism *P2*, failure occurs due to crushing of the units and mortar in a rather uniform manner, although localized crushing of the mortar joints near the edges is also present.

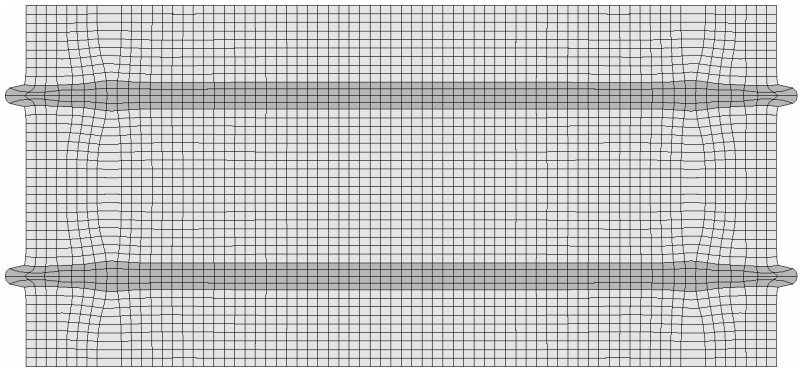

(a)

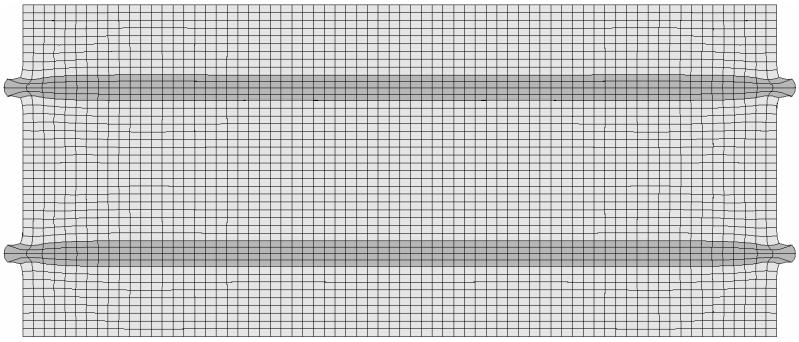

(b)

Figure 2.18 – Deformed (incremental) meshes at failure for prisms: (a) *P1* and (b) *P2.*

2.6 Calculations using simplified models

This Section contains an analytical interpretation of the experimental results, with simple calculations being used to predict the compressive strength f_c of the prisms. The following equations have been utilized:

a) equation proposed by Francis *et al*. (1971)

$$f_c = \frac{1}{1+\dfrac{\alpha\,\phi\left(\beta\,\nu_m-\nu_u\right)}{\beta\left(1-\nu_m\right)}}\cdot f_{c,u} \tag{2.3}$$

where the parameters α, β and ϕ read

$$\alpha=\frac{h_m}{h_u} \qquad \beta=\frac{E_u}{E_m} \qquad \phi=\frac{f_{c,u}}{f_{t,u}} \tag{2.4}$$

b) equation proposed by Khoo and Hendry (1973)

$$A f_c^{\,3} + B f_c^{\,2} + C f_c + D = 0 \tag{2.5}$$

where the parameters A, B, C and D are given by

$$A = -0.2487 f_{t,u} \left(\frac{1}{f_{c,u}} \right)^3 + 0.0018 \alpha \left(\frac{1}{f_{c,m}} \right)^2 \tag{2.6}$$

$$B = 1.2781 f_{t,u} \left(\frac{1}{f_{c,u}} \right)^2 - 0.0529 \alpha \left(\frac{1}{f_{c,m}} \right) \tag{2.7}$$

$$C = -2.0264 f_{t,u} \left(\frac{1}{f_{c,u}} \right) - 0.1126 \alpha \tag{2.8}$$

$$D = 0.9968 f_{t,u} + 0.1620 \alpha f_{c,m} \tag{2.9}$$

c) equation proposed by Ohler (1986)

$$f_c = f_{c,m} + \frac{s f_{c,u} - f_{c,m}}{1 + \dfrac{t h_m f_{c,u}}{m h_u f_{t,u}}} \tag{2.10}$$

where s and t are parameters defining the unit failure envelope and m is the slope of the mortar failure envelope. The values presented by Ohler (1986) for these parameters are given in Table 2.5 and Table 2.6, respectively.

d) equation provided by Eurocode 6, CEN (2003)

$$f_{c,k} = K f_{c,u}^{0.7} f_{c,m}^{0.3} \tag{2.11}$$

where $f_{c,k}$ is the masonry characteristic compressive strength and K is a parameter that depends of the type of unit and of the type of masonry.

e) equation provided by ACI Specification for Masonry Structures, ACI (2004)

$$f'_m = A\left(400 + B\, f_{c,u}\right) \ (\text{in } psi) \tag{2.12}$$

where f'_m is the specified compressive strength, in *psi*, $A = 1$ (inspected masonry) and $B = 0.2$ for Type *N* Portland cement-lime mortar or $B = 0.25$ for Type *S* or *M* Portland cement-lime mortar.

Table 2.5 – Values for the parameters *s* and *t* of Ohler (1986) equation.

	$0 < f_c/f_{c,u} < 0.33$	$0.33 < f_c/f_{c,u} < 0.67$	$0.67 < f_c/f_{c,u} < 1.0$
s	0.662	0.811	1.000
t	0.662	0.960	2.218

Table 2.6 – Values for the parameter *m* of Ohler (1986) equation.

$f_{c,m}$ [N/mm^2]	31.6	21.4	15.4	6.4
m [-]	5.3	3.6	2.4	2.1

In the equations above, $f_{c,u}$ and $f_{c,m}$ are the compressive strength of units and mortar, $f_{t,u}$ is the tensile strength of units, E_u and E_m are the elastic modulus of units and mortar, ν_u and ν_m are the coefficients of Poisson of units and mortar and h_u and h_m are the units height and mortar thickness.

The first three equations, (2.3), (2.5) and (2.10), follow from equilibrium methods under the assumption that units are uniaxially compressed - biaxially tensioned while mortar is triaxially compressed, see Hendry (1990) for a comprehensive review on these methods. For this reason, these equations are only applicable when the unit stiffness exceeds the mortar stiffness, which is the case of all the three prisms considering the mortar adjusted elastic modulus. However, in the case of prism *P3*, the very large ratio between the mortar and unit strengths precludes the application of the equations proposed by Khoo and Hendry (1973) and Ohler (1986), since their formulation only considers explicitly the mortar strength rather than the mortar elastic properties. On the contrary, the

equation proposed by Francis *et al*. (1971) only considers the mortar elastic properties and, thus, was also applied to prism *P3*.

Equation (2.11) is provided by Eurocode 6, CEN (2003), and has empirical nature. In this formula, the parameter K equals $0.8 \times 0.55 = 0.44$ for the application here envisaged. It is also noted that the mortar strength for prism *P3* was assumed equal to 20 N/mm^2, which is the maximum strength permitted by the code. The mean value of the masonry compressive strength f_c was calculated from the characteristic value $f_{c,k}$ assuming $f_c = f_{c,k} + 1.64\ \sigma$, where σ is the standard deviation. A coefficient of variation CV equal to $\sigma / f_c = 10\%$ was adopted.

Equation (2.12) is part of the unit strength method provided by ACI for masonry structures, ACI (2004), and is also of empirical nature. The parameter B was assumed to equal 0.2 in the case of mortar *M1* and 0.25 in the case of mortars *M2* and *M3*. The mean value of the masonry compressive strength f_c was calculated from the specified strength f'_m assuming $f_c = f'_m + 1.34\ \sigma$. Also here, a CV equal to 10% was considered.

The results obtained are given in Table 2.7. All the three equilibrium formulas overestimate the experimental strength, especially the equation proposed by Francis *et al*. (1971). On the contrary, EC 6 and ACI empirical formulas predict, as expected, a value lower than the experimental strength, with ACI formula providing a better estimate for the low strength mortar prisms *P1* and EC6 formula predicting a more accurate value for the high strength mortar prisms *P3*. It is further noted that Francis *et al*. (1971) equation yielded decreasing masonry strength values for prisms built with increasing strength mortar. This is not realistic and can be explained by the high sensibility of Francis *et al*. (1971) equation to the values of the coefficient of Poisson, which can be considered a drawback of this method given the difficulties in determining objectively such values. If a coefficient of Poisson equal to 0.2 is assumed for the units and the three types of mortar, the decreasing trend is no longer observed and the masonry strength values obtained are 22.1, 22.5 and 22.8 N/mm^2 for prisms *P1*, *P2* and *P3*, respectively.

It is also noted that the numerical simulations always provide over-strength, when compared to analytical solutions based in equilibrium approaches. This conflict indicates that novel approaches are required.

Table 2.7 – Experimental and analytical strength values. In brackets, the ratio between the predicted and experimental strengths is given.

Prism	Exp. Binda *et al.* (1988)	Francis *et al*. (1971) [(1)]	Khoo and Hendry (1973)	Ohler (1986)	EC 6, CEN (2003)	ACI (2004)	Numerical simulations *EPE* [(1)]
P1	11.0	25.0 (225%)	15.2 (140%)	14.8 (135%)	7.5 (70%)	9.4 (85%)	18.2 (165%)
P2	14.5	24.2 (165%)	20.2 (140%)	19.0 (130%)	11.3 (80%)	11.0 (75%)	24.1 (165%)
P3	17.8	23.4 (130%)	-	-	13.0 (75%)	11.0 (60%)	30.0 (170%)

[(1)] The given results were obtained with adjusted mortar stiffness values.

2.7 Summary

The ability of analytical methods and continuum models based on plasticity and cracking to reproduce the experimental compressive behaviour of masonry has been addressed. The comparison between obtained numerical results and experimental results available in literature from compression tests on running-bond masonry prisms allow to conclude that: (a) continuum finite element modelling largely overestimates the strength and peak strain of the prisms; (b) plane-stress, plane-strain and "enhanced-plane-strain" lead to different strengths and different failure mechanisms, which is physically non-realistic but numerically correct. The usage of 3D models or enhanced-plane-strain models is therefore recommended; (c) simplified methods to predict the strength based on elastic considerations provide results different from advanced numerical analyses and experimental values. This last conclusion has also been confirmed by Brencich and Gambarotta (2005), indicating that experimental testing or rather conservative empirical formulae are the only possible solution at the present state of knowledge.

In addition, a comparison between the numerical results obtained for running-bond prisms and simulations on stack-bond specimens was presented. A higher strength was found for the stack-bond configuration, which still requires experimental validation. Moreover, a larger difference was observed in prisms built with weaker mortars.

Suggestions for further work are: (a) to seek for alternative models that represent the micro-structure of masonry components, so that reliable estimation of the masonry strength

can be made and (b) carry out an advanced experimental program to characterize the mechanical behaviour of mortars inside a masonry composite.

3 Masonry short-term compression: a numerical investigation at the meso-level

The compressive behaviour of masonry is of crucial importance for design and safety assessment purposes, since masonry structures are primarily stressed in compression. The present approach in codes, *e.g.* CEN (2003) and ACI (2004), is to make the compressive strength of the masonry composite dependent of the compressive strength of the masonry components (unit and mortar). This empirical approach is obviously conservative and results from the envelope of a large set of experimental tests, meaning that the compressive strength of masonry can be severely underestimated. The solution today is to carry out a series of tests in expensive wallets, CEN (1998a), which is hardly feasible for all possible masonry materials. In addition, existing code formulas are clearly not applicable to irregular or rubble masonry, which is generally the case of historical masonry structures.

Continuum and discontinuum approaches to model masonry components can be used with the aim of reproducing the experimental behaviour of the composite under compression. Micro-modelling strategies are indeed powerful tools for analysing the basic phenomena occurring in masonry assemblages upon increasing loading, see Lourenço and Rots (1997). For the case of masonry under uniaxial compression, some authors indicate that continuum finite element micro-models are capable of obtaining an adequate response of the masonry composite, introducing the behaviour of masonry components, *e.g.* Brencich and Gambarotta (2005) and Roman and Gomes (2004). But the detailed analyses shown in Chapter 2, using plasticity and cracking based finite element models, demonstrated otherwise. In fact, it was shown that continuum finite element micro-models largely overestimate the experimental strength and peak strain of masonry prisms tested in compression. Values of approximately 170% were found for the ratio between the predicted and the experimental strengths. As a result, alternative discontinuum modelling approaches that consider the micro-structure of quasi-brittle materials are therefore needed to study the uniaxial compressive behaviour of masonry.

Several advanced computational approaches are currently available for structural analysis developed in discontinuum frameworks, including the finite element method with interface elements, discrete element methods and lattice models. For an exhaustive discussion on the numerical methods available the reader is referred to Jing (2003). The

finite element method with interface elements is well established and advanced solution procedures are available, see Gens *et al.* (1988) and Rots and Schellekens (1990). For simple geometries under symmetric loading or when the crack path is known in advance from experiments, interface elements can be embedded in the finite element mesh along expected crack paths, Rots (1988). If the crack pattern is not known in advance, expensive remeshing techniques, Ingraffea and Saouma (1985), or approaches where a sufficient number of interface elements are included in the mesh to account for potential crack paths, Carol *et al.* (2001), may be adopted. Typical applications of interface elements in finite element analysis of masonry structures are modelling of cracking, slipping or crushing planes, like unit-mortar interfaces or potential cracks in the units, see Lofti and Shing (1994) and Lourenço and Rots (1997).

The last decades have witnessed a growing interest of the scientific community in the development of discrete element methods due to the capabilities of such methods to deal with discrete media. Within the most popular discrete element methods, the distinct element method pioneered by Cundall (1971) and the discontinuous deformation analysis originally developed by Shi (1988) may be distinguished. As can be gathered from the literature, discrete element methods have been widely used to analyse the response of blocky assemblages, especially in the field of rock mechanics although references can also be found for blocky masonry structures, see Lemos (2001). Discrete element methods have also been used to model the micro-structure of granular and brittle disordered materials such as concrete, and examples can be found in Lorig and Cundall (1987) and Vonk (1993). The rigid-body spring network model has common features with the referred approaches, subdividing the material into a collection of rigid bodies interconnected by zero-size springs, see Bolander *et al.* (2000).

Another discontinuum approach that has been receiving vivid attention is lattice models. Its main concept is the discretization of the continuum into a framework of beam or truss elements. Generally, a regular or random triangular lattice of beam elements is adopted, being the size of the beams adjusted so that the elastic stiffness and Poisson's ratio of the complete lattice resemble the values of the continuum. The simulation consists in a set of linear elastic analyses, each one corresponding to a load step. At the end of each load step, the adopted failure law is evaluated and the elements falling in its range are removed from the lattice. Lattice models have been extensively utilized in the study of tensile fracture propagation and references can be found in Schlangen (1993), Van Mier *et*

al. (1995), Bazant and Planas (1998) and Van Vliet (2000). Recently, a lattice-type model has been proposed by Cusatis *et al.* (2003) aiming at a correct simulation of both tensile and compressive fracture processes.

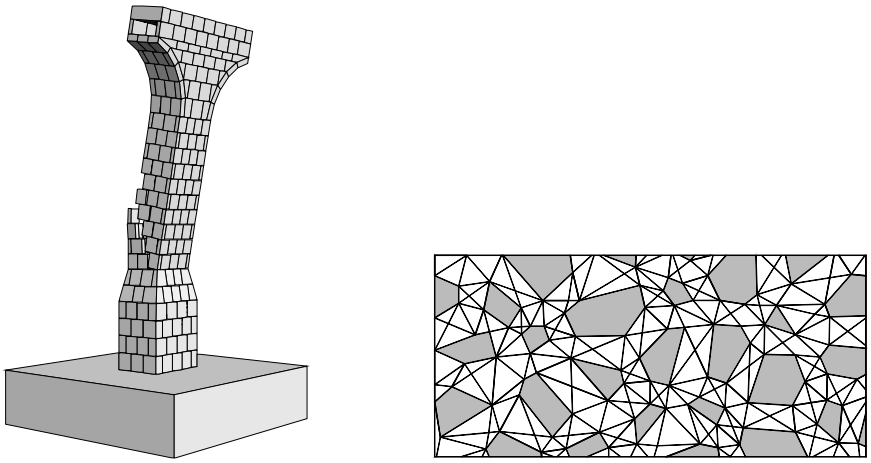

(a) (b)

Figure 3.1 – Examples of applications using discrete element method based programs: (a) simulation of an aqueduct pillar, adapted from Lemos *et al*. (1998) and (b) meso-level discretization of concrete, adapted from Vonk (1993).

In the present Chapter, a particle 2D model consisting in a phenomenological discontinuum approach based on the finite element method including interface elements is proposed to represent the micro-structure of units and mortar, attempting to reproduce adequately the compressive behaviour of masonry. Comparative analyses with experimental results and with numerical results using a continuum model are presented.

3.1 Model concept

3.1.1 Outline of the model

The proposed particle model is developed on a finite element framework. The discontinuous nature of the masonry components is considered by giving a fictitious micro-structure to units and mortar, which is composed by linear elastic continuum elements of polygonal shape (hereafter named *particles*) separated by non-linear interface elements. All the inelastic phenomena occur in the interfaces and the process of fracturing consists of

progressive bond-breakage. This is, of course, a phenomenological approach, able, nevertheless, to capture the typical failure mechanisms and global behaviour of quasi-brittle materials.

Three-noded plane stress triangular elements with one-point Gauss integration were utilized to model the particles. It is noted that the fracture process controls failure and the differences between plane stress and plane strain are, therefore, negligible. For the interfaces, four-noded line interface elements with zero thickness were adopted. A high dummy stiffness was given to the interface elements to avoid interpenetration of the particles, as it is clear that the amount of penetration is higher with decreasing interface stiffness. Stiffness values ranging from 1×10^4 to 1×10^5 N/mm^3 were chosen so that overlapping of neighbouring particles would be negligible. Rots (1988) and Schellekens (1992) reported that beyond stiffness values of 1×10^3 N/mm^3, the application of the Gauss integration scheme leads to numerical oscillations. To overcome such deficiency, a two-point Lobatto integration scheme was used.

The constitutive model used for the interface elements was formulated by Lourenço and Rots (1997) and is implemented in the finite element code adopted for the analyses, DIANA (2003). The model includes a tension cut-off for tensile failure (mode I), a Coulomb friction envelope for shear failure (mode II) and a cap mode for compressive failure. Exponential softening is present in all three modes and is preceded by hardening in the case of the cap mode. In the proposed particle model, the compressive mode was not active.

The dilatancy angle measures the uplift upon shearing. Dilatancy tends to zero with increasing plastic shear slipping or increasing normal confining pressure. These phenomena occur often combined because shear slip with dilatancy necessarily induces normal compressive stresses. The analyses here reported were performed in a non-associated plasticity context, assuming a dilatancy equal to zero. In such way, a particle can slide over the other without producing any normal displacement. Non-zero dilatancy associated with the symmetry boundary conditions adopted in the simulations could induce high normal stresses and locking of the particles, resulting in increasing strength. Also for unit-mortar interfaces, Lourenço and Rots (1997) recommend a value of zero for the dilatancy angle.

3.1.2 Mesh construction

A computer routine has been written to generate the particles, see Figure 3.2. As input data, the boundaries of the surface to mesh, the average size of the particles and a distortion factor *DF*, which controls the irregularity of the particles shape, must be given. In addition, the type and average size of the finite elements utilized must be specified. The discretization of the continuum into particles is based on the Voronoi diagram. The Voronoi diagram is a collection of regions that divide space according to a set of given points (nuclei). Each region has a polygonal convex shape and corresponds to one nucleus. All the points in one region are closer to the corresponding nucleus than to any other nucleus. To obtain the coordinates of the vertices of the Voronoi regions, the routine executes a call to an external freeware DOS program named QHULL (2001) and then processes the output data.

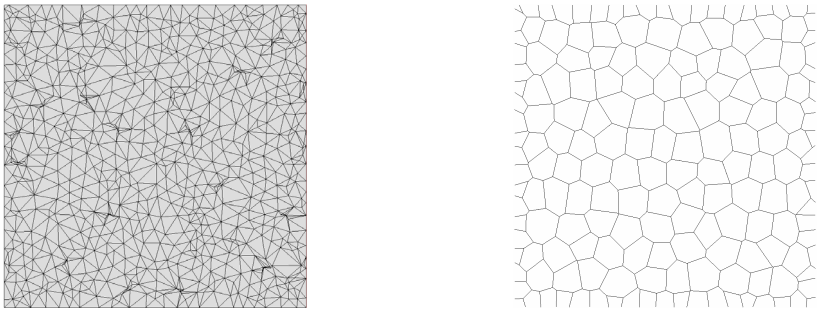

(a) (b)

Figure 3.2 – Finite element mesh: (a) particles mesh and (b) interfaces mesh.

3.1.3 Material heterogeneity

In heterogeneous materials the disorder of the material properties at the micro-level is a key issue in the fracture process. In the present model, material disorder is given by attributing to each particle and interface random material properties. For this purpose, values for the elastic modulus E of the particles and for the strength parameters of the interfaces (tensile strength f_t, cohesion c and friction coefficient $tan\phi$) were generated according to a Gaussian distribution. A lower threshold, equal to zero, and an upper threshold, equal to two times the average value have been imposed for each parameter. It is noted, as an example, that for a Gaussian distribution with a coefficient of variation of 50%, the probability to generate a value beyond the referred thresholds is 5%.

3.2 Model response. Elementary tests

3.2.1 Model utilized

Elementary tests were carried out resorting to 2D simulations of 100 × 100 mm^2 specimens in order to provide insight into the behaviour of the proposed model. Since cracks are constrained to follow particle boundaries, the influence of particle size and regularity in the mesh configuration must be investigated. For this purpose, three different values for the distortion factor *DF* were considered (0, 0.3 and 0.6) and, for each value, three different levels for the mesh refinement *MR* were assumed (denoted by *n*, 2*n* and 4*n*, and associated with an element size one-half and one-fourth of the original size *n*), see Figure 3.3. Given the random nature of the model, for each combination *DF*-*MR*, three analyses were performed using different randomly generated meshes.

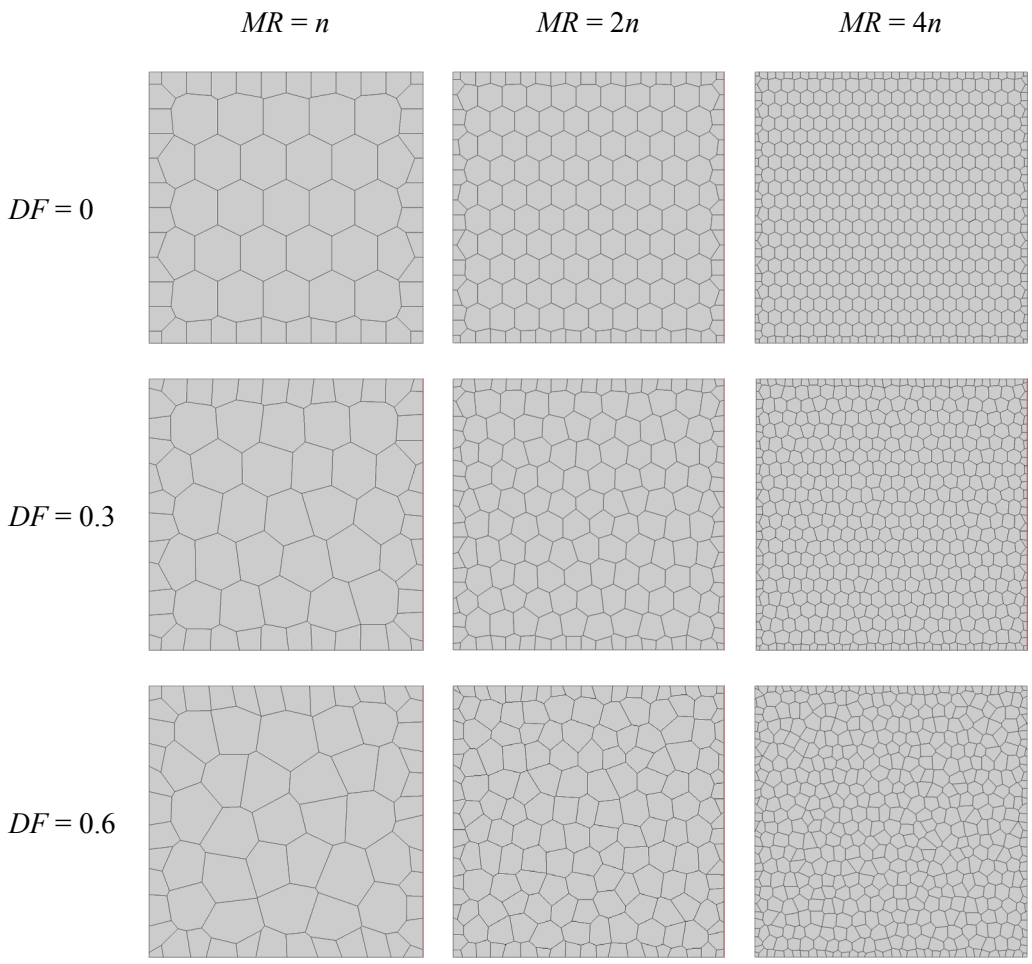

Figure 3.3 – Geometry of the 100 × 100 mm^2 specimens used in the simulations. Three distortion factors *DF* and mesh refinement levels *MR* were considered.

In-plane symmetry conditions have been adopted, carrying out the simulations as if the specimen was part of a larger portion. Hence, specimen boundaries remain straight during the analysis, aiming at reproducing macro homogeneous boundary conditions. In all simulations, the nonlinear system of equations following from the finite element discretization was solved with an incremental-iterative globally convergent Newton-Raphson method with arc-length control and line-search technique.

The same material properties were given to all specimens, so that only the influence of the micro-structure geometry would be assessed. The elastic properties attributed to the particles (elastic modulus E and coefficient of Poisson ν) and to the interfaces (normal modulus k_n and shear modulus k_s) are given in Table 3.1, in terms of the average values and corresponding coefficients of variation CV. The inelastic properties of the interfaces are shown in Table 3.2. Here, f_t is the tensile strength, G_{fI} is the mode I fracture energy, c is the cohesion, G_{fII} is the mode II fracture energy and $tan\phi$ is the friction coefficient.

Table 3.1 – Elastic properties for the particles and interfaces.

		Average values	CV [%]
Particles	E	5000 N/mm^2	30
	ν	0.15	0
Interfaces	k_n	10^4 N/mm^3	0
	k_s	10^4 N/mm^3	0

Table 3.2 – Inelastic properties for the interfaces.

	Average values	CV [%]
f_t	1.0 N/mm^2	50
G_{fI}	0.050 N/mm	50
c	1.5 N/mm^2	50
G_{fII}	0.75 N/mm	50
$tan\phi$	0.30	50

A unitary value was assumed for the tensile strength and the cohesion was obtained according to $c = 1.5\, f_t$. This relation was proposed by Lourenço (1996b) for unit-mortar interfaces. For G_{fI}, a value in agreement with the results obtained by Van der Pluijm (1999) was adopted and for G_{fII} a value about five times higher the value proposed by Lourenço (1996b) for unit-mortar interfaces (0.1 c) was used. The friction coefficient was

chosen so that the ratio between the specimen compressive and tensile strengths was about ten, which is a ratio often found for masonry units, see Schubert (1988). Given that the approach followed is phenomenological and not physical, the values adopted for the coefficient of variation of the different material parameters are not related with their experimental variability but were chosen so that the overall response of the model resembles the experimental response.

3.2.2 Tensile uniaxial behaviour

The specimens described in the previous Section were numerically simulated in uniaxial tension. Figure 3.4 illustrates typical stress-strain diagrams obtained. Three types of tensile response can be clearly distinguished regardless of the particle size and mesh distortion. Each type of response is associated with a different failure pattern and, for each one, the specimen mode I fracture energy can range from a value similar to the mode I fracture energy given to the interface elements up to a very large value due to a residual plateau. Such residual plateau develops when diagonal cracks appear, originating friction between the particles due to the imposed boundary (symmetry) conditions. This is clearly a problem of the boundary conditions and not of the model approach.

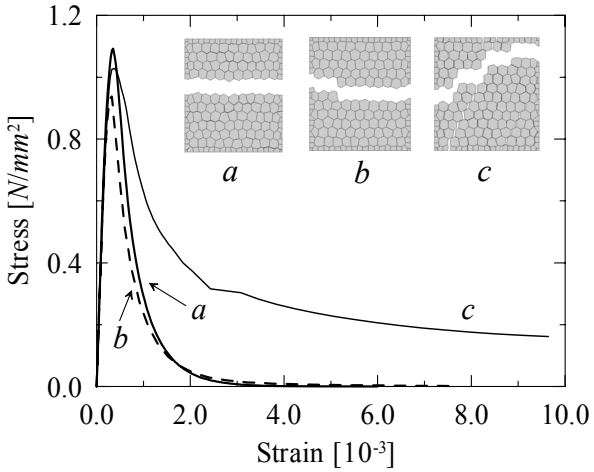

Figure 3.4 – Tensile stress-strain diagrams and failure patterns obtained for specimens with $MR = 2n$ and $DF = 0.3$.

The values obtained for the specimens tensile strength, according to the level of mesh refinement and the distortion factor, are given in Table 3.3. Slightly decreasing values for the tensile strength were found for increasing values of the distortion factor. However, the average values can be considered as mesh size and mesh distortion independent for practical purposes. Moreover, it is noted that increasing mesh refinement is accompanied by decreasing variability of the strength values and rather low values for the coefficient of variation are obtained for $MR = 4n$.

Table 3.3 – Average values from three analyses obtained for the tensile strength f_t [N/mm^2] according to different levels of mesh refinement MR and distortion factors DF (values in brackets give the coefficient of variation).

	$MR = n$	$MR = 2n$	$MR = 4n$
$DF = 0$	1.1 (11.8%)	1.1 (9.8%)	1.1 (4.1%)
$DF = 0.3$	0.9 (9.8%)	1.0 (7.6%)	1.1 (4.1%)
$DF = 0.6$	0.9 (13.3%)	1.0 (1.1%)	1.0 (1.4%)

Figure 3.5 illustrates typical tensile crack propagation under increasing load. Three loading stages have been considered: 80% of the peak load, peak load and ultimate load. Initially, several cracks start developing but at some point localization of deformation occur in one crack while, in the others, unloading occurs. Figure 3.6 depicts typical failure patterns obtained for different refinement and distortion levels. Rather irregular failure patterns were obtained despite the particle size and mesh distortion, influencing the model response as shown above in Figure 3.4.

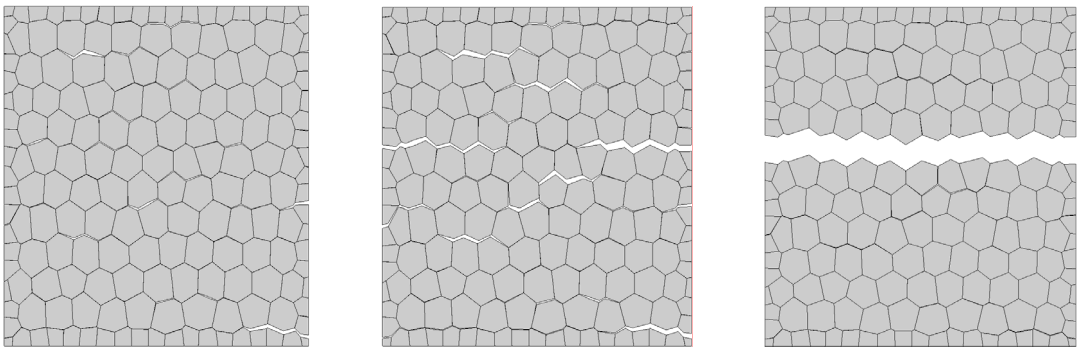

(a) (b) (c)

Figure 3.5 – Typical progressive tensile failure of a specimen. Deformed meshes at: (a) 80% of the peak load, (b) peak load and (c) ultimate load.

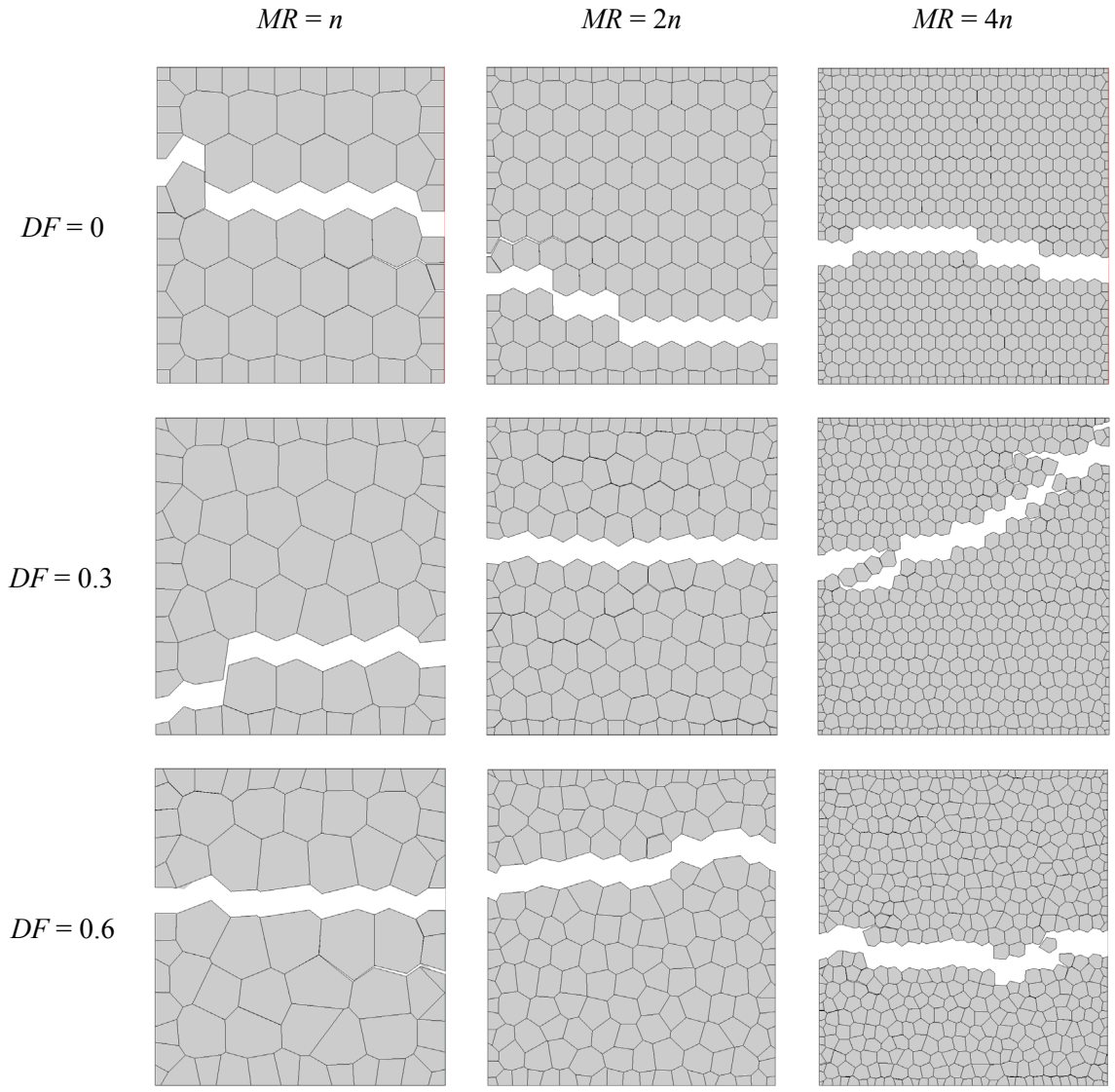

Figure 3.6 – Typical deformed meshes obtained from the tension simulations. Three distortion factors *DF* and mesh refinement levels *MR* were considered.

3.2.3 Compressive uniaxial behaviour

Typical stress-strain diagrams obtained for each type of geometry are given in Figure 3.7. The behaviour observed shows that increasing distortion of the particles leads to decreasing brittleness. Moreover, a relation between brittleness and mesh refinement seems to be also present. In fact, specimens with a refinement level n show a more brittle behaviour, characterized by sudden load drops, than specimens with refinement levels $2n$ and $4n$. However, it is noted that there is not much difference in the response beyond a level of refinement of $2n$.

Table 3.4 illustrates the values for the compressive strength of the specimens f_c, according to the mesh distortion and level of refinement. It is noted that there is increasing variability of the strength values with increasing distortion and size of the particles. The variation obtained (it is stressed that a different mesh was generated for each analysis) fairly reproduces experimental variability of results. It is further noted that the strength values show a slight decreasing trend with increasing distortion, especially for lower levels of mesh refinement. Nevertheless, the average values for 2*n* and 4*n* can be considered as mesh size and mesh distortion independent for practical purposes. For this reason, relations between structural and particle sizes lower than seven to ten should be avoided.

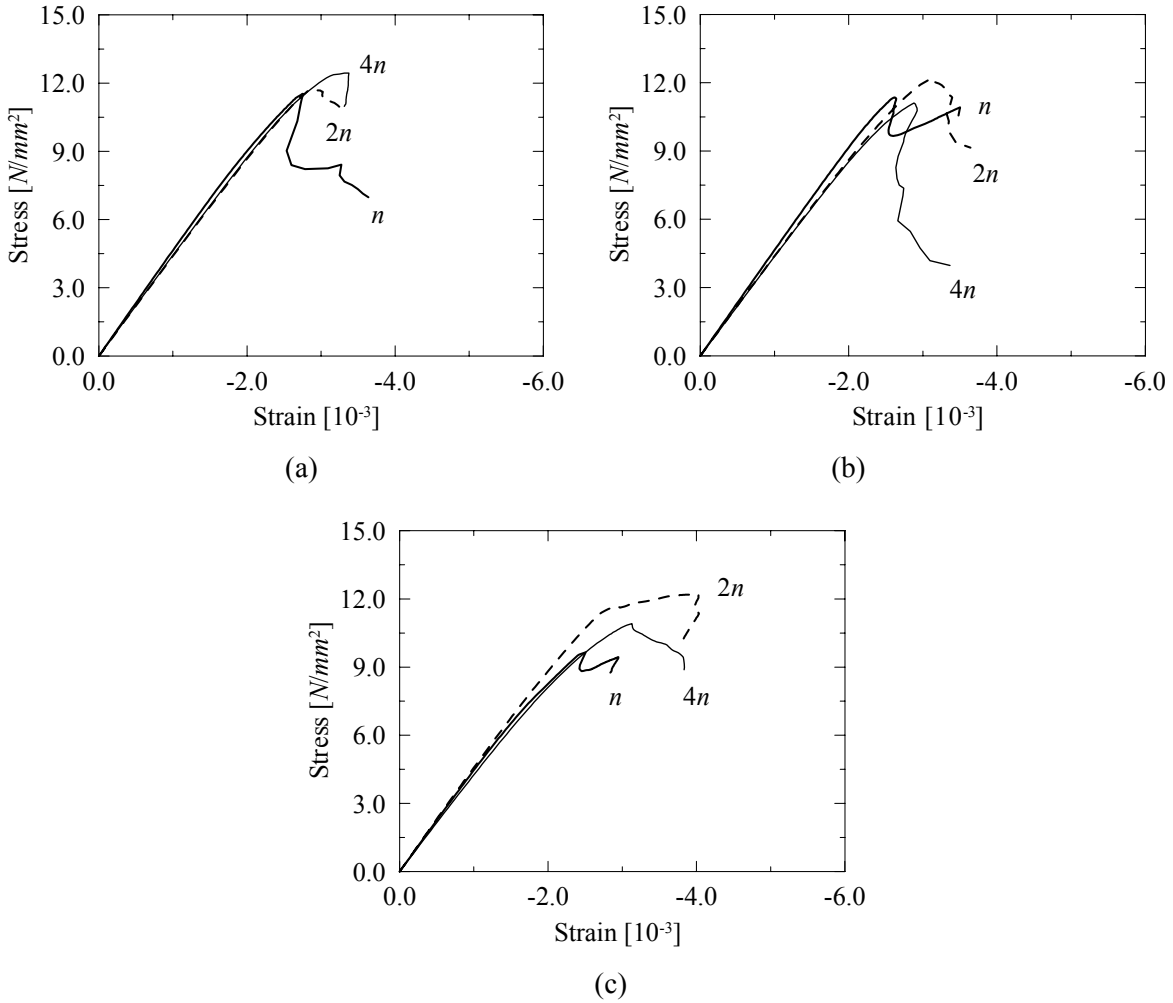

Figure 3.7 – Typical compressive stress-strain diagrams obtained for three different levels of mesh refinement (*n*, 2*n* and 4*n*) and three different distortion factors: (a) *DF* = 0, (b) *DF* = 0.3 and (c) *DF* = 0.6.

Table 3.4 – Average values from three analyses obtained for the compressive strength f_c [N/mm^2] according to different values of mesh refinement *MR* and distortion factor *DF* (values in brackets give the coefficient of variation).

	MR = *n*	*MR* = 2*n*	*MR* = 4*n*
DF = 0	12.0 (10.4%)	11.6 (0.6%)	12.0 (6.7%)
DF = 0.3	10.9 (15.4%)	11.1 (10.4%)	11.6 (3.3%)
DF = 0.6	9.9 (15.3%)	11.0 (13.8%)	11.4 (8.4%)

Figure 3.8 illustrates typical compressive crack propagation under increasing load. Again, three loading stages have been considered: 80% of the peak load, peak load and ultimate load. Well-known phenomena such as crack bridging and branching can be observed. Typical failure patterns obtained for the different specimens are depicted in Figure 3.9. It is clear that under certain combinations of particle distortion and mesh refinement, the failure pattern becomes biased by the mesh configuration. For instance, for *DF* = 0 and *MR* = 4*n*, the crack pattern denotes a clear diagonal tendency while, for example, for *DF* = 0.6 and *MR* = 4*n*, the crack pattern resembles experienced compression crack patterns with predominant vertical cracks. Thus, mesh configuration has a larger influence in the crack pattern of meshes with low distortion factors and high refinement levels. Nevertheless, the value of the failure load is not affected by the mesh preferential orientation.

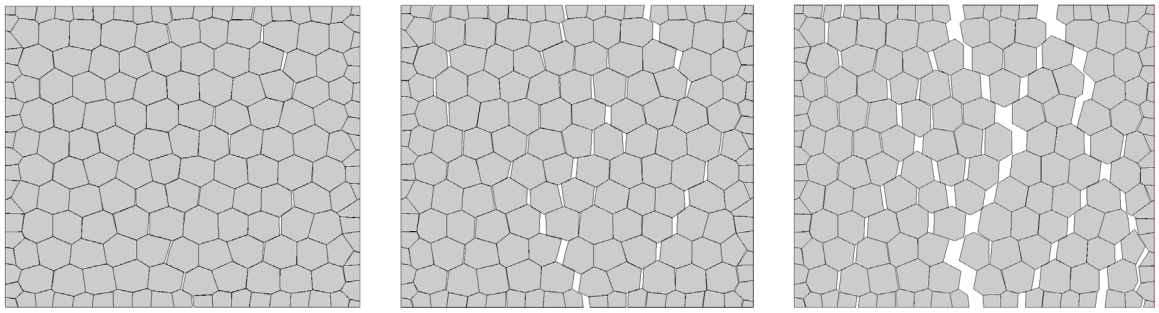

(a) (b) (c)

Figure 3.8 – Typical progressive compressive failure of a specimen. Deformed meshes at: (a) 80% of the peak load, (b) peak load and (c) ultimate load.

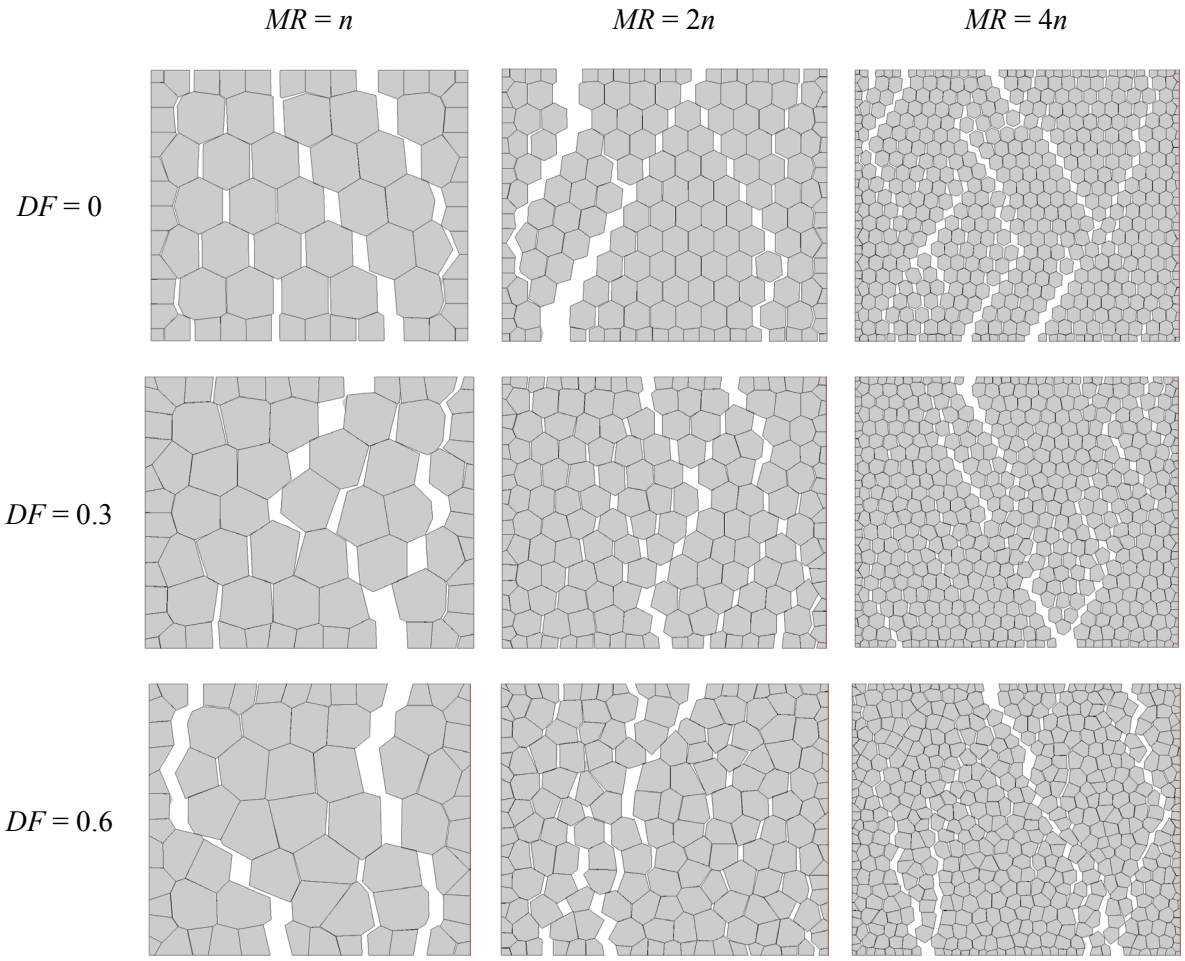

Figure 3.9 – Typical deformed meshes obtained from the compression simulations, using three distortion factors *DF* and mesh refinement levels *MR*.

An assessment of the contribution of the interfaces tensile and shear parameters to the compressive strength of the specimens was also performed. To achieve this purpose, compression simulations assuming different values for the tensile parameters (strength and fracture energy) were considered firstly while the model shear parameters were kept constant, see Table 3.5. The same approach was repeated for the shear parameters and the results obtained are given in Table 3.6. As expected, a decreasing trend of the compressive strength with decreasing values of the tensile and shear parameters was found, even if the simulation reduces the variation in the input significantly. However, the influence of the tensile parameters is smaller than the influence of the shear parameters. Such results seem to indicate that the compressive failure of the model in discussion is mainly governed by the parameters describing the shear behaviour.

Table 3.5 – Average compressive strength f_c from three analyses assuming different values for the interfaces tensile strength f_t. In brackets, the ratio against the reference bold value is given.

	$c = 1.5\ N/mm^2$		
$f_t\ [N/mm^2]$	**1.0**	0.5 (-50%)	0.25 (-75%)
$f_c\ [N/mm^2]$	**11.1**	9.9 (-11%)	9.2 (-17%)

Table 3.6 – Average compressive strength f_c from three analyses assuming different values for the interfaces cohesion c. In brackets, the ratio against the reference bold value is given.

	$f_t = 1.0\ N/mm^2$		
$c\ [N/mm^2]$	**1.5**	0.75 (-50%)	0.37 (-75%)
$f_c\ [N/mm^2]$	**11.1**	8.1 (-27%)	6.5 (-41%)

3.2.4 Size effect

The effect of size is an important issue when estimating the strength or stress-strain relationship of quasibrittle materials. In the early 1980's, it became clear that size effect of such materials is mainly related with the release of the structure stored energy into the front of the propagating fracture or cracking zone and can not be explained solely by Weibull-type statistics of random micro-defects, see Bazant and Planas (1998) and Kim and Yi (2002) for comprehensive reviews. In fact, the larger the structure, the greater is the volume from which the energy is released and since the fracture front dissipates the same amount of energy, regardless of the structure size, in a larger structure the failure load must be lower. Although size effect has been widely studied for tensile failure, cracking localization is also present under compressive loading and, thus, also compressed elements show size effect, *e.g.* Van Mier (1997). It is now well known that compressive strength and post-peak ductility tend to increase with decreasing size of the structural element.

In the field of concrete, models where the material structure is represented have proved to be of great interest in understanding size effect phenomenon. In such simulations, the model parameters are set to a level below the level of observation (macro-level) and do not depend on size. Insight on this type of approach can be found in Vonk (1993) and Van Vliet (2000).

The ability of the proposed model to describe the influence of the specimen size has been assessed by simulations on square specimens with 100×100, 50×50 and

$10 \times 10\ mm^2$. In addition, the influence of the shape of the specimen has been investigated by considering rectangular specimens with different height over width ratios ($10 \times 30\ mm^2$ and $30 \times 10\ mm^2$). A distortion factor $DF = 0.3$ and a mesh refinement $MR = 2n$ have been considered. In the case of square specimens, the mesh configuration and the material properties were kept constant, being the specimens only scaled. In this way, the results can be directly compared without the effect of randomness. In the case of the rectangular specimens, the same procedure could not be applied and three simulations were carried out for each shape considering the same average parameters adopted in the square specimens simulations.

From the stress-strain diagrams illustrated in Figure 3.10a it can be observed that the size of the specimens has a remarkable influence in the response of the model. In fact, size dependency is one of the advantages of particle-type models when compared to softening continuum models, see *e.g.* Cusatis *et al.* (2003). Moreover, it is noted that the shape of the elements has a minor influence on the strength but an increase of brittleness was found for higher height over width ratios, see Figure 3.10b.

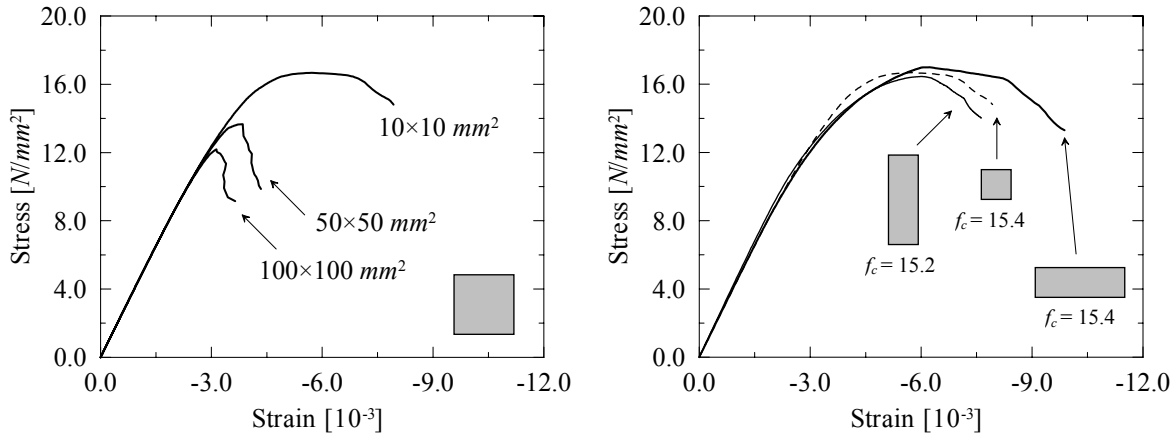

Figure 3.10 – Stress-strain diagrams obtained for specimens with: (a) different size and (b) different shape. In this last figure, typical diagrams and the average compressive strength values f_c [N/mm^2] obtained from three different simulations are given for each shape (10×30, 10×10 and $30 \times 10\ mm^2$).

The size dependent responses exhibited by the model can be explained based on the following energy balance

$$\int_V E\,dv = \int_S G_f\,ds \tag{3.1}$$

where the first term is the volume integral of the maximum specific energy E (by volume) stored in the specimen and the second term is the integral of the total energy released in the interfaces during the fracture process. G_f is, then, the fracture energy given to the interface elements in the model. Moreover, specimens with equal strengths must store the same specific energy E. Considering equal shape 2D elements only differing by a scale factor, it is reasonable to assume that the crack patterns would resemble and that the number of cracks would be similar. In this way, the dissipation zone is increasing proportionally to the height of the specimen and, by energy balance, also is the stored energy. However, for the specimens to have the same strength, the maximum stored energy should be increasing proportionally to the area of the element. If the fracture energy given to the interface elements is modified to account for these aspects, see Equation (3.2), size independent responses are obtained.

$$G_{f,1} = G_{f,2}\,\frac{b_1}{b_2} \tag{3.2}$$

In the above, b is the width of the specimens and the subscript stands for the different size specimens under consideration. Figure 3.11 illustrates the stress-strain diagrams obtained regarding the $100 \times 100\ mm^2$ specimen as reference and by adapting the fracture energy (mode I and mode II) of the $50 \times 50\ mm^2$ and $10 \times 10\ mm^2$ specimens according to Equation (3.2). It can be observed that the response becomes totally independent from the specimen size. When there is only an increase in the height or width of the specimen, it was shown that the strength value predicted by the particle model is almost not affected, see Figure 3.10b. This can be explained by the fact that the increase of the stored energy is proportional to the increase of the dissipation zone. In fact, in the case of an increase in height, the cracks length can be assumed to increases roughly as much as the specimen height while in the case of an increase in width, the number of cracks can be considered to increase proportionally.

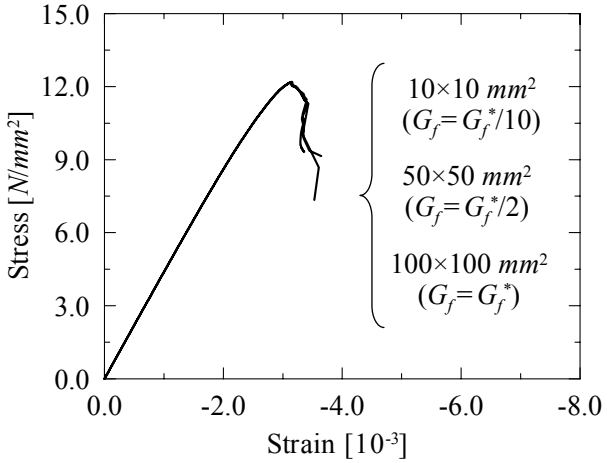

Figure 3.11 – Stress-strain diagrams obtained by modifying the fracture energy G_f given to interfaces as a function of the initial value G_f^*.

3.3 Modelling masonry

In the previous Sections, the proposed particle model has been introduced and insight on the model behaviour has been provided. In this Section, the ability of the model to reproduce the behaviour of running-bond masonry prisms under uniaxial compression is assessed by means of a comparison with the experimental results reported in Section 2.1 and with the numerical results using a non-linear continuum finite element model as described in Section 2.4.

3.3.1 Model utilized

The numerical simulations were carried out employing the basic cell introduced in Section 2.2, see Figure 3.12. Again, it is emphasised that the followed approach is only approximate of the real geometry and that the obtained numerical response is phenomenological, which means that a comparison in terms of experimental and numerical failure patterns is not possible. In particular, splitting cracks usually observed in prisms tested under compression, Mann and Betzler (1994), boundary effects of the specimen and non-symmetric failure modes are not captured by the numerical analysis. Nevertheless, most of these effects control mainly the post-peak response, which is not the key issue in the present contribution.

The particle model is composed by approximately 13000 linear triangular continuum elements, 6000 linear line interface elements and 15000 nodes. Macro homogeneous symmetry conditions and a distortion factor equal to 0.3 have been assumed.

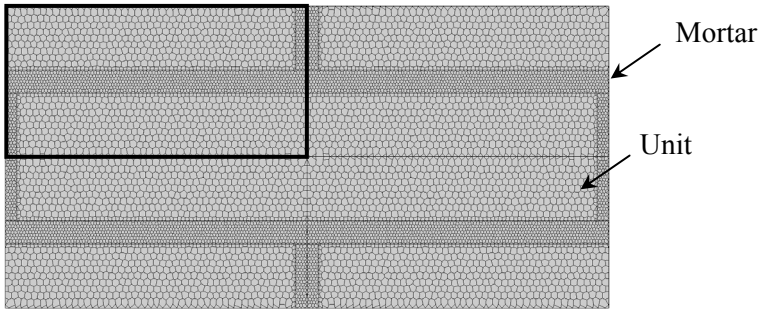

Figure 3.12 – Particle model of the masonry cell (only the quarter indicated was simulated, assuming symmetry conditions).

The material parameters were defined by comparing the experimental and numerical responses of units and mortar considered separately. Each material was modelled resorting to specimens with the same average particle size, mesh distortion and dimensions of the masonry components used in the composite model (basic cell).

Given the stochastic nature of the model, five simulations were performed for each masonry component assuming equal average values for the model material parameters. The parameters were obtained, whenever possible, from the described experimental tests but most of the inelastic parameters were unknown and had to be estimated. It is noted that the particles average elastic modulus E is larger than the experimental value due to the contribution of the interfaces deformability, characterized by k_n and k_s, to the overall deformability of the specimen. This correction is necessary despite the high dummy stiffnesses assumed.

On the contrary, the values adopted for the interfaces tensile strength f_t are slightly lower than the specimens experimental tensile strength, given the contribution of the interfaces shear strength due to the irregular fracture plane. Again, the cohesion c was taken, in general, equal to $1.5\,f_t$ Lourenço (1996b). However, quite low experimental ratios between the compressive and tensile strengths were reported for the units and mortars

considered here, with values ranging between four and eight. Due to this reason, cohesion values lower than 1.5 f_t had to be adopted for mortars *M1* and *M2*.

The values for the friction coefficient $tan\phi$ were adopted so that the numerical compressive strength showed a good agreement with the experimental strength. The values assumed for mode I fracture energy G_{fI} have been based in recommendations supported in experimental evidence, see CEB-FIP (1993) and Van der Pluijm (1999). For mode II fracture energy G_{fII}, a value equal to 0.5 c was assumed, with the exception of the very high strength mortar *M3*, for which a lower value equal to 0.3 c was adopted.

The complete material parameters adopted are given in Table 3.7 and, for such input, the response obtained is given in Table 3.8. In addition, typical numerical stress-strain diagrams for both units and mortar specimens are illustrated in Figure 3.13.

Table 3.7 – Values assumed for the material parameters (in brackets, the adopted coefficient of variation is given).

		Unit	*M1*	*M2*	*M3*
Particles	E [N/mm^2]	6000 (30%)	1500 (30%)	7000 (30%)	22000 (30%)
	ν [-]	0.09 (0%)	0.06 (0%)	0.09 (0%)	0.12 (0%)
Interfaces	k_n [N/mm^3]	1×10^4 (0%)	1×10^4 (0%)	3×10^4 (0%)	8×10^4 (0%)
	k_s [N/mm^3]	1×10^4 (0%)	1×10^4 (0%)	3×10^4 (0%)	8×10^4 (0%)
	f_t [N/mm^2]	3.40 (45%)	0.75 (45%)	3.50 (45%)	10.50 (45%)
	G_{fI} [N/mm]	0.170 (45%)	0.038 (45%)	0.175 (45%)	0.525 (45%)
	c [N/mm^2]	5.10 (45%)	0.30 (45%)	0.70 (45%)	15.75 (45%)
	G_{fII} [N/mm]	2.55 (45%)	0.15 (45%)	0.35 (45%)	3.15 (45%)
	$tan\phi$ [-]	0.10 (45%)	0.00 (0%)	0.00 (0%)	0.10 (45%)

Table 3.8 – Numerical response obtained for the masonry components (in brackets, the coefficient of variation is given).

	Unit	*M1*	*M2*	*M3*
f_c [N/mm^2]	27.2 (2.7%)	3.2 (5.0%)	12.7 (5.4%)	95.8 (4.4%)
f_t [N/mm^2]	3.61 (1.4%)	0.64 (4.7%)	2.70 (4.2%)	11.62 (6.6%)
E [N/mm^2]	4786 (1.9%)	1309 (1.4%)	5632 (3.0%)	17176 (3.1%)

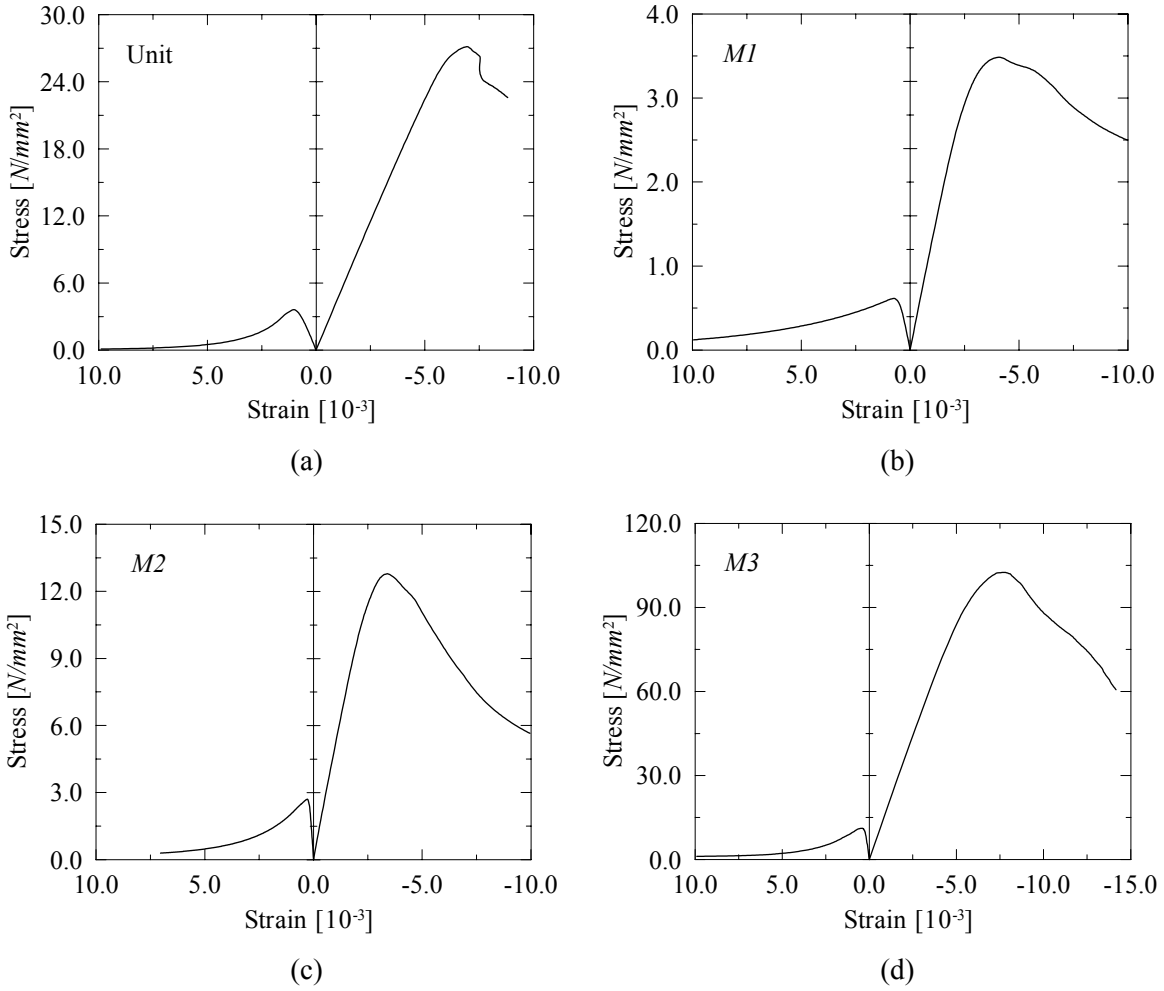

Figure 3.13 – Typical numerical stress-strain diagrams obtained for the masonry components: (a) unit, (b) mortar *M1*, (c) mortar *M2* and (d) mortar *M3*.

3.3.2 Numerical results and comparison with experimental data

In order to reproduce correctly the elastic stiffness of the masonry prisms, *P1*, *P2* and *P3*, the experimental elastic modulus of the mortar E had to be adjusted by inverse fitting. In fact, the mortar experimental stiffness leads to a clear overstiff response of the numerical specimens. This can be explained by the fact that the mechanical properties of mortar inside the composite are different from mortar specimens cast separately. This is due to mortar laying and curing and represents a severe drawback of detailed micro-models. Table 3.9 gives the adjusted mortar stiffness values E^* used in the simulations.

Table 3.9 – Adjusted stiffness values E^* for the mortar.

Mortar type	Particles	Interfaces	
	E [N/mm^2]	k_n [N/mm^3]	k_s [N/mm^3]
M1	355	10^4	10^4
M2	750	10^4	10^4
M3	1200	10^4	10^4

The numerical results obtained for the masonry prisms considering the mortar experimental *Num_E* and adjusted *Num_E** stiffnesses are given in Table 3.10 for both particle and continuum models, where f_c is the compressive strength and ε_p is the peak strain. In addition, the prisms experimental results are shown for a better comparison. It is noted, however, that the reference solution for the numerical simulations is the solution provided by *Num_E**. Figure 3.14 depicts the experimental and numerical stress-strain diagrams.

Table 3.10 – Experimental results *Exp* and numerical results using experimental *Num_E* and adjusted *Num_E** mortar stiffness values.

		Continuum model			Particle model		
		P1	*P2*	*P3*	*P1*	*P2*	*P3*
f_c [N/mm^2]	***Exp***	**11.0**	**14.5**	**17.8**	**11.0**	**14.5**	**17.8**
	Num_E	19.8	24.2	31.0	15.5	19.3	30.8
	Num_E*	18.2	24.1	30.0	15.4	17.3	24.6
ε_p [10^{-3}]	***Exp***	**10.5**	**7.9**	**6.6**	**10.5**	**7.9**	**6.6**
	Num_E	10.6	9.7	8.4	5.4	4.6	6.2
	Num_E*	19.9	16.0	33.5	11.8	8.1	8.9

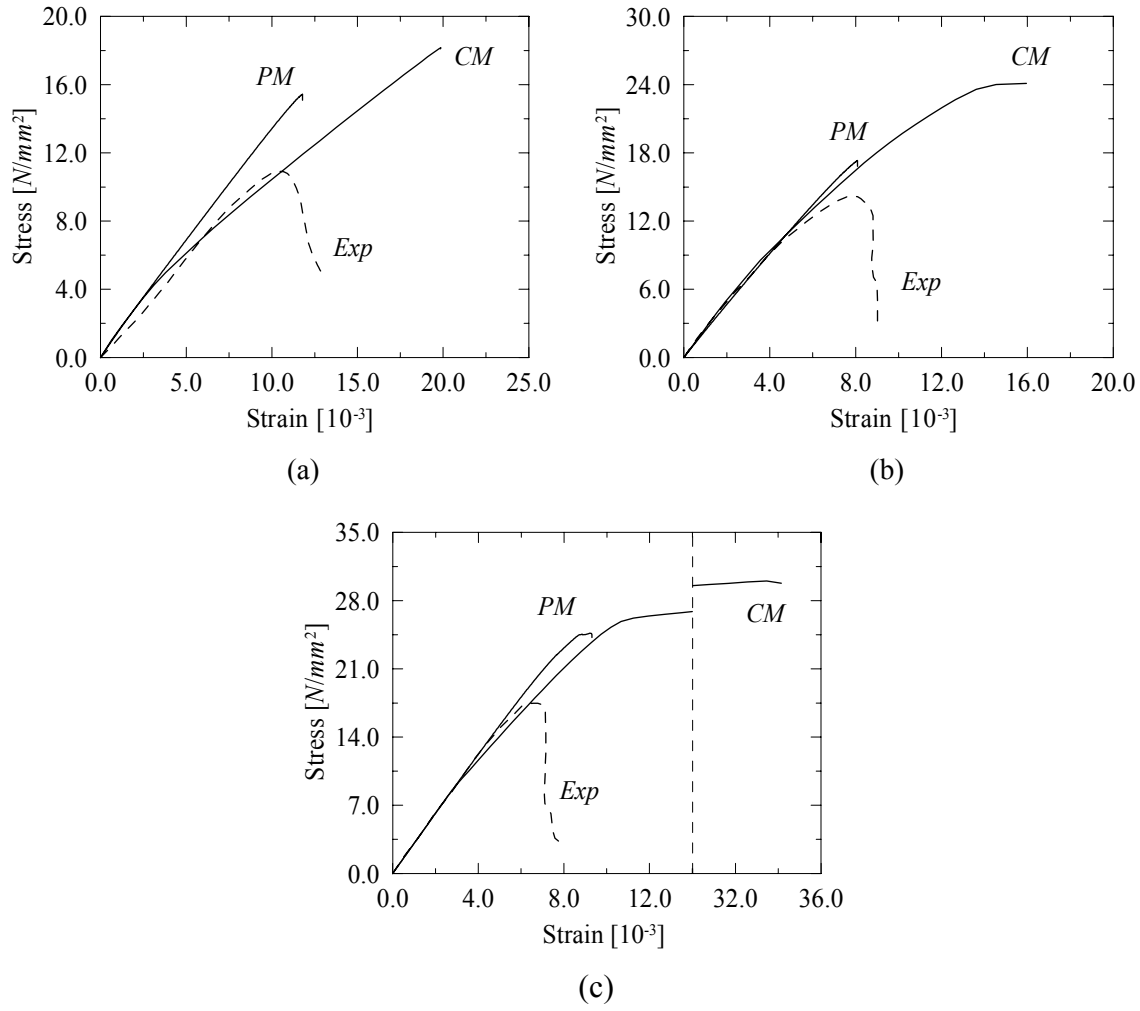

Figure 3.14 – Numerical and experimental stress-strain diagrams, using adjusted mortar stiffness values for prisms: (a) *P1*, (b) *P2* and (c) *P3*. In the diagrams, *PM* stands for particle model, *CM* for continuum model, see Section 2.4, and *Exp* for experimental data, see Section 2.1.

From the given results, it is clear that the experimental collapse load is overestimated by both particle and continuum models, and that the predicted strength is affected by the mortar stiffness, especially in the case of the particle model. However, a much better agreement with the experimental strength and peak strain has been achieved with the particle model. In fact, the numerical over experimental strength ratios ranged between 165 to 170% in the case of the continuum model while in the case of the particle model, strength ratios ranging between 120 and 140% were found. The results obtained also show that the peak strain values are well reproduced by the particle model but large overestimations are obtained with the continuum model. In fact, for this last model, experimental over numerical peak strain ratios ranging between 190 and 510% were found.

Failure patterns are an important feature when assessing numerical models. The (incremental) deformed meshes near failure are depicted in Figure 3.15. It is noted that despite the fact that only a quarter of the basic cell has been modelled, the results are shown in the entire basic cell to obtain more legible figures.

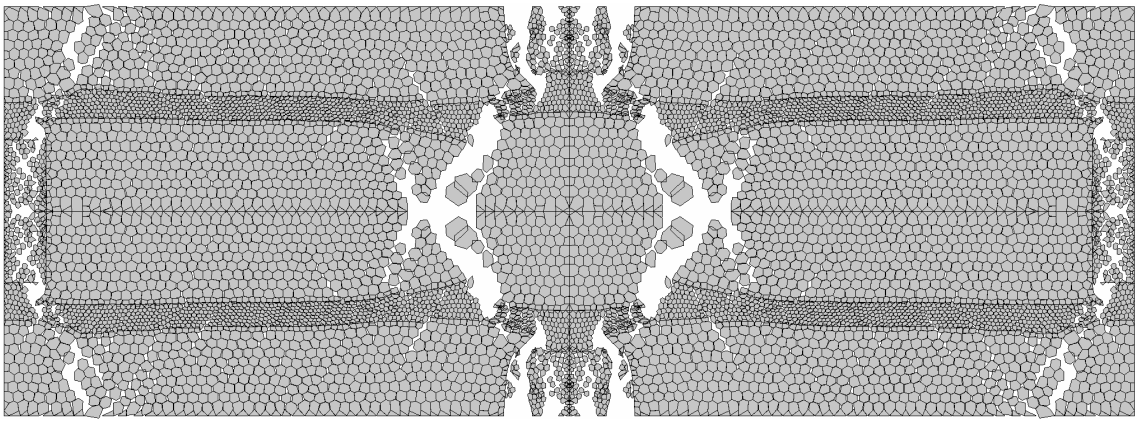

(a)

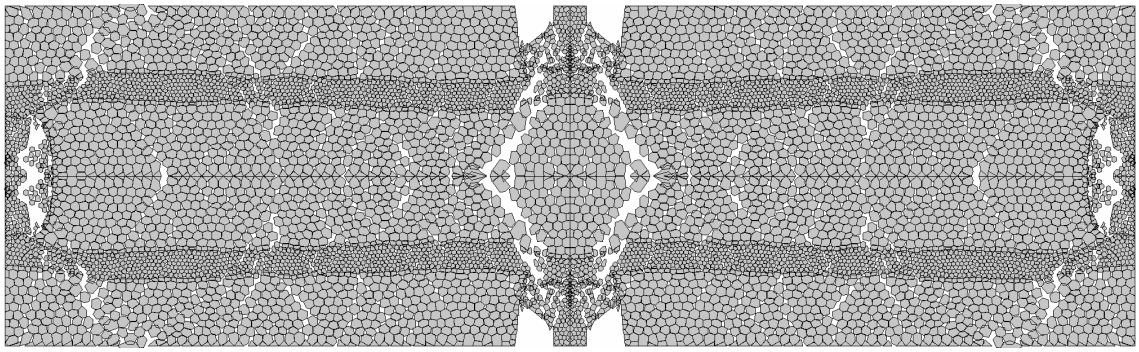

(b)

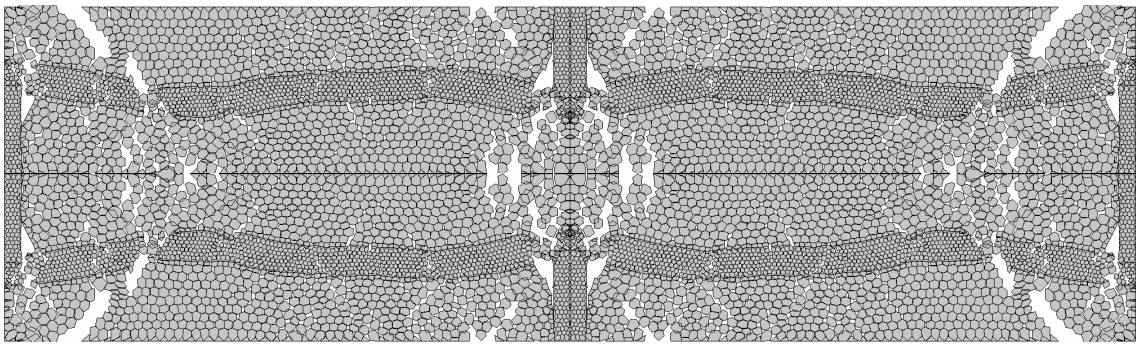

(c)

Figure 3.15 – Deformed (incremental) meshes near failure for prisms: (a) *P1*, (b) *P2* and (c) *P3*.

The numerical failure patterns obtained are similar for both continuum, see Section 2.4.2, and particle models. In the case of prism *P1*, failure occurs mainly due to the development of vertical cracks in the centre of the units and along the head-joints, being the mortar in the bed-joints severely damaged. Prism *P2* fails due to diffuse damage developing in units and mortar in a rather uniform manner. In the case of prism *P3*, diffuse damage is also present but localized crushing of the units can be clearly observed at one-half and one-sixth of the units length.

3.3.3 Influence of masonry head-joints

A discussion on the influence of vertical head-joints in the response of masonry prisms subjected to compressive loading was introduced in Section 2.5, where a comparison between simulations on running-bond and stack-bond masonry specimens using a continuum-type model was presented. It has been observed that, for the same constituents, stack-bond prisms show a higher strength than running-bond prisms. In this Section, the simulations for the stack-bond configuration are repeated using the proposed particle model, see Figure 3.16, and a comparison with the results obtained in the previous Section is provided. As for continuum simulations, only prisms *P1* and *P2* were analysed, as they represent the most relevant cases. The boundary conditions adopted were identical to the ones used in continuum simulations and the reader is referred to Section 2.5. The material properties given to the masonry constituents have been already described in Section 3.3.1.

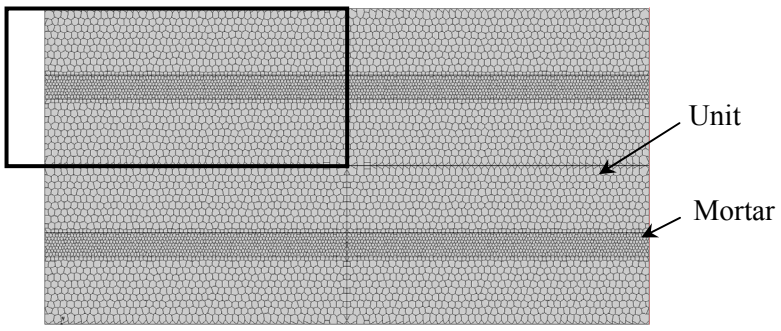

Figure 3.16 – Model used in the simulations (only the indicated quarter was simulated).

Figure 3.17 illustrates the results obtained. A higher strength was shown by stack-bond prisms when compared to running-bond specimens, in agreement with continuum

results. In fact, a higher strength of approximately 15% was found for prisms *P1* and of approximately 10% for prisms *P2*. Again, a smaller difference in the strength values was observed in the case of prisms *P2*, which were built with a stronger mortar, although the difference observed with the particle model is not as large as the one provided by the continuum model. The numerical failure patterns are shown in Figure 3.18 and Figure 3.19 for prisms *P1* and *P2*, respectively. Crushing of the bed-joints, especially in the case of prism *P1*, and cracks arising in the units near the specimen edges can be observed. As in running-bond simulations, a more diffuse failure pattern was observed for the higher strength mortar prism *P2*.

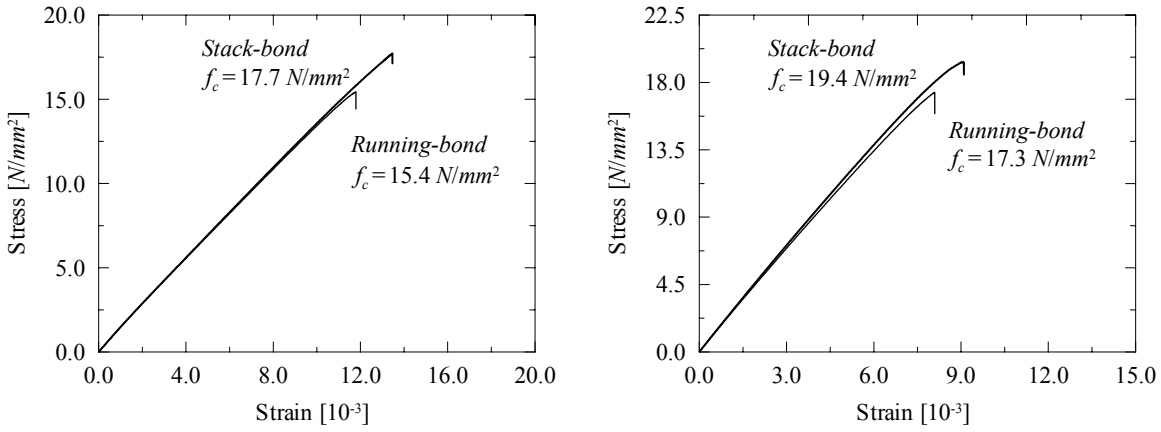

Figure 3.17 – Numerical stress-strain diagrams for stack-bond and running-bond simulations: (a) prisms *P1* and (b) prisms *P2*.

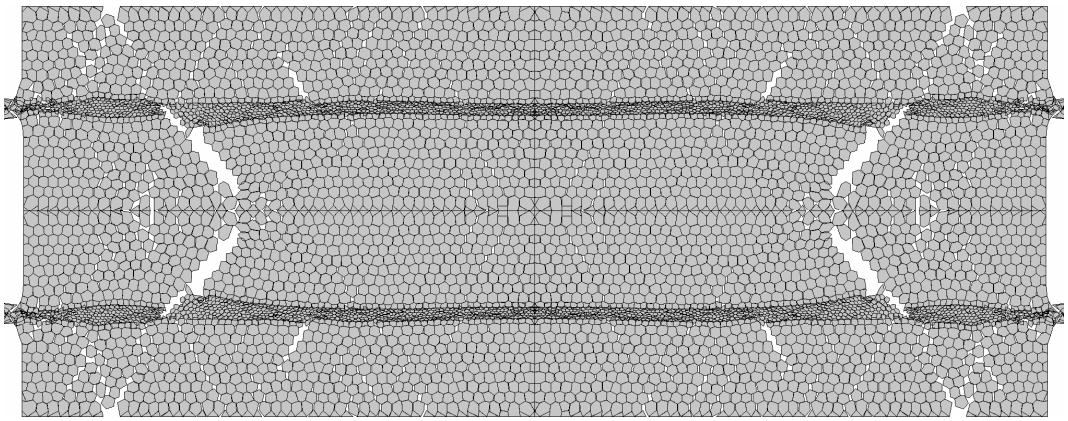

Figure 3.18 – Deformed (incremental) mesh at failure for prism *P1*.

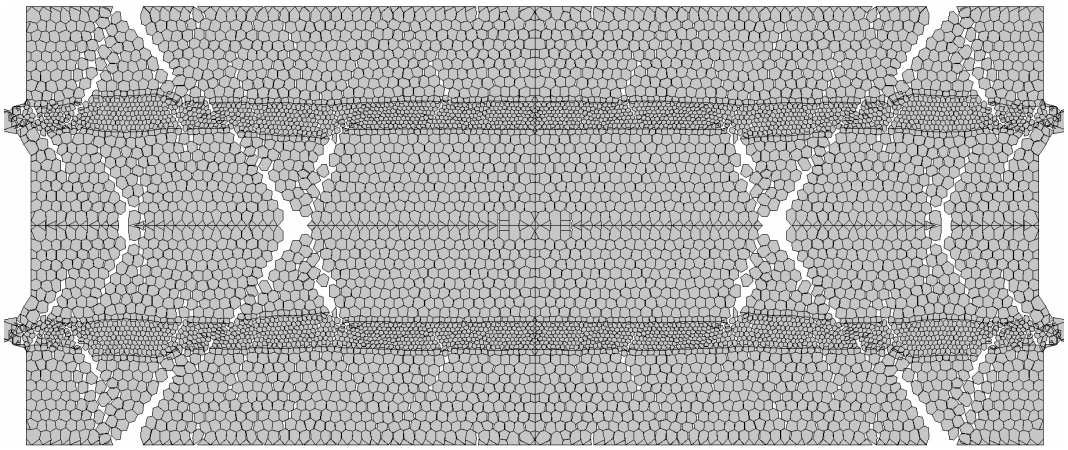

Figure 3.19 – Deformed (incremental) mesh at failure for prism *P2*.

3.4 Summary

The analysis of masonry assemblages using detailed modelling strategies is a challenging task. A particle model consisting in a phenomenological discontinuum approach has been proposed to represent the microstructure of masonry components, attempting to adequately reproduce the experimental behaviour of masonry under compression. The model is discussed in detail, including proposals for selection of numerical data, sensitivity studies, fracture processes and failure mechanisms, and size effect studies. Finally, the particle model is compared with experimental results on masonry wallets under uniaxial compression and with numerical simulations using a continuum finite element model.

It is possible to conclude that: (a) discontinuum models show clear advantages when compared to continuum models, based in plasticity and cracking, in predicting the compressive strength and peak strain of masonry prisms from the properties of the constituents; (b) compressive and tensile strength values provided by the particle model can be considered as particle size and particle distortion independent for practical purposes; (c) relations between structural and particle sizes lower than seven to ten should be avoided in simulations; (d) size dependent responses have been obtained with the proposed model; and (e) shear parameters rather than tensile parameters play a major role at the micro-level and greatly influence the overall response of compressed masonry, as also confirmed by Vonk (1993).

Suggestions for further work are extending the particle model to 3D configurations and seek for other models developed in discontinuum frameworks in order to provide reliable estimations of masonry compressive strength.

4 Masonry behaviour under high sustained stresses

On 17th March 1989 the Civic Tower of Pavia suddenly collapsed without showing any apparent warning signs, see Figure 4.1. Dramatically, four people were killed and severe damage was inflicted to surrounding buildings. The 60 *m* height tower was topped by a 16th century belfry while the main body had been built in successive phases during the 11th and 13th centuries. The tower walls were 2.8 *m* thick, made of irregular courses of brick fragments and small stones in a mortar matrix, and exhibited a thin external brick cladding with an average thickness of 0.150 *m*. On the contrary, the belfry was made of regular brick masonry.

(a) (b)

Figure 4.1 – Pavia Civic Tower: (a) before collapse and (b) remaining ruins.

The collapse of the tower was a motive of great concern for the public authorities and for the technical community. Thus, the collapse rapidly became a focus of interest among masonry researchers and several masonry blocks were recovered from the ruins for mechanical and physical/chemical laboratory testing, see Binda *et al.* (1992). Such tests permitted to identify the time-dependent mechanical damage of the tower walls due to high sustained loading as a possible main cause of collapse.

The tower of Pavia is not an isolated case and several other famous examples can be referred, such as the collapse of the St. Magdalena bell-tower in Goch, Germany, in 1993,

the partial collapse of the Noto Cathedral, Italy, in 1996, see Binda *et al*. (2003a), and the severe damage exhibited by the bell-tower of the Monza Cathedral, Italy, see Modena *et al.* (2002).

(a) (b)

Figure 4.2 – Famous examples of collapse or damage due to high sustained loading: (a) Noto Cathedral after partial collapse and (b) bell-tower of the Monza Cathedral exhibiting severe damage.

Masonry creep depends mainly on factors such as the stress level and the temperature / humidity conditions but cyclic actions, such as wind, temperature variations or vibrations induced by traffic or ringing bells, in the case of bell towers, have a synergetic effect, increasing material damage. For these reasons, high towers and heavily stressed pillars are the structural elements where time-dependent damage can severely occur, see Anzani *et al.* (1995) and Anzani *et al.* (2000).

Traditionally, three creep stages can be recognised. A *primary* stage were the creep rate decreases gradually, a *secondary* stage where the creep rate remains approximately constant and a *tertiary* stage where the creep rate increases rapidly towards failure. A sufficiently high stress level must be applied so that the two last stages are initiated. In the secondary stage, diffuse and thin vertical cracking propagates and coalesces into macro-cracks that may lead, possibly, to creep failure of the material. Creep of cementitious materials is generally attributed to cracking growth and interpartical bond breakage due to moisture seepage. In fact, under sustained loading, forced moisture redistribution can occur

in the pore structure of the material causing debonding and rebonding of the micro-structure particles, Bazant (1988). In the case of concrete or new masonry, if drying shrinkage is occurring simultaneously to creep, the time-dependent deformation is increased due to a coupled effect known as the *Pickett effect*, Pickett (1942). Time-dependent deformation in a constant hygral and thermal environment, and in the absence of cracking, is denominated by *basic creep*, see *e.g.* Neville (1997). A comprehensive discussion on the viscous behaviour of masonry can be found in Van Zijl (2000).

For low stress levels, below 40 to 50% of the compressive strength, only primary creep is present and creep deformation can be assumed proportional to the stress level. References on masonry creep within the elastic range are rather abundant in literature, see *e.g.* Ameny *et al.* (1984), Lenczner (1986) and Brooks (1990). On the contrary, creep under high stresses, even in the case of concrete, is not a sufficiently debated issue, Bazant (1993), Papa *et al.* (1998) and Mazzotti and Savoia (2003). The fact that standard design methods for new structures are based on linear elastic material hypothesis has contributed to diminish the interest of researchers on this topic. However, ancient masonry structures are often working under low safety margins according to modern safety regulations. This can be due to inadequate knowledge of mechanics or structural modifications that occurred along centuries, resulting in overweighting of the structure and rendering importance to non-linear creep.

The present Chapter provides a contribution towards a description of the time-dependent behaviour of masonry under high compressive stresses. Standard uniaxial compression tests, short-term creep tests and long-term creep tests were considered with the aim of presenting a comparative discussion. The experimental investigation focuses on three types of ancient masonry specimens: (a) rubble masonry prisms from the crypt of the Monza Cathedral (16^{th} century), (b) rubble masonry prisms recovered from the wall ruins of the Pavia Civic Tower (11^{th} to 13^{th} century) and (c) regular masonry prisms recovered from the belfry ruins of the Pavia Civic Tower (16^{th} century). The present study is part of an ongoing experimental research jointly carried out by University of Minho, Portugal, and by Politecnico di Milano, Italy.

4.1 Tested specimens

The experimental investigation was carried out on ancient masonry prisms due to the difficulty of producing laboratory specimens that correctly represent the material typically found in historical masonry structures. A major obstacle to fabricate specimens is mortar maturation, which has a significant influence on the viscous behaviour of masonry and can not be adequately reproduced in new specimens. On the other hand, the high cost and very limited number of ancient masonry specimens available for destructive testing are obvious. Because the previous experience with similar materials in the scientific community is rather poor, the current testing program was fundamental but represents a learning process. In particular, recommendations for testing such specimens could only be given in the end of the testing program.

When the purpose is the characterization of the creep behaviour of ancient masonry, it should be stressed that considerable differences exist within the general denomination of *masonry*. In fact, several types of masonry can be found, influenced by the age of construction and by the geographical, cultural and technical backgrounds. Even so, common characteristics exist as the arrangement and size of the units that can help researchers to group the diversity of masonry types. In this study, three types of masonry were addressed: (a) rubble masonry collected from a wall in the crypt of the Monza Cathedral, which is made of bricks and stones laid in irregular courses; (b) rubble masonry recovered from the ruins of the walls of the Pavia Civic Tower, made of pieces of brick and stone randomly distributed in the mortar matrix; and (c) regular coursed brick masonry recovered from the ruins of the belfry of the Pavia Civic Tower. Figure 4.3 and Figure 4.4 illustrate the typical aspect of the specimens and the typical preparation of the specimens, respectively. Hereafter, the specimens coming from the Monza Cathedral are denoted by *MRu*, the rubble specimens from the walls of the Pavia Civic Tower are named by *PRu* and the regular specimens from the belfry of the Pavia Civic Tower are denominated by *PRe*.

The dimensions of the *MRu* specimens were $(200\pm5) \times (200\pm5) \times (320\pm10)$ mm^3 while the rubble and regular Pavia specimens were $(200\pm5) \times (200\pm5) \times (330\pm20)$ mm^3. Before subsequent testing under compression, the loaded faces of the prisms were regularized with a cement based mortar layer approximately 10 mm thick. In all tests, Teflon sheets were introduced between the prisms and the loading plates to minimize restraining frictional stresses. A summary of the tests performed is given in Table 4.1.

(a) (b) (c)

Figure 4.3 – Tested prisms: (a) *MRu* specimens, (b) *PRu* specimens and (c) *PRe* specimens.

(a) (b)

Figure 4.4 – Preparation of the specimens recovered from the ruins of the Pavia Civic Tower: (a) *PRu* and (b) *PRe*.

Table 4.1 – Quantity of specimens for each type of test.

Type of prism	Compression tests	Short-term creep tests	Long-term creep tests
MRu	-	6	-
PRu	1	4	-
PRe	4	4	6

4.2 Standard compression tests

Compression tests were conducted in one *PRu* specimen and four *PRe* specimens. The tests were partly carried out in University of Minho (specimens *PRe_1* and *PRe_2*) and in Politecnico di Milano (specimens *PRu_1*, *PRe_3* and *PRe_4*). The specimens had to be

tested with different test setups according to the conditions locally available at each laboratory. In this way, the tests performed in University of Minho were carried out in a uniaxial hydraulic testing machine with non-rotating steel plates and a maximum capacity of 2000 *kN*. The load was monotonically increased under displacement control at a rate of 4 $\mu m/s$. The applied load was measured by a load cell located between the upper plate and the testing machine, and displacements in the specimens were recorded by two vertical inductive displacement transducers HBM (10 *mm* range), positioned at two different faces of the prisms and by two horizontal transducers positioned at the other two faces.

The tests performed in Politecnico di Milano were carried out using a uniaxial servo-controlled MTS® 311.01.00 testing machine, with non-rotating steel plates and a maximum capacity of 2500 *kN*. Loading was applied under displacement control at a rate of 1 $\mu m/s$. The applied load was recorded by a load cell and displacements were measured resorting to a vertical and a horizontal displacement transducers GEFRAN PY2-10 (10 *mm* range) positioned at each face of the prisms. For all tested specimens, longitudinal displacements were measured over approximately 200 *mm* span and transversal displacements over about 150 *mm* span.

The results obtained are illustrated in Figure 4.5. Here, the negative sign is adopted for contraction (longitudinal or vertical strains ε_v) and the positive sign is adopted for elongation (transversal or horizontal strains ε_h). It is noted that the fact that only two horizontal transducers per specimen were considered in the case of specimen *PRe_1* explains the null horizontal deformations exhibited up to the peak load. Table 4.2 and

Table 4.3 gives a summary of the test results in terms of the elastic modulus E, compressive strength f_c and peak strain ε_p. The elastic modulus was calculated as the average slope of the stress-strain diagram between 30 and 50% of f_c. It is noted that the elastic modulus is the parameter showing the largest variability, approximately the double of the values found for the strength and peak strain. Even if only one specimen is available for the rubble masonry, the difference in strength is striking, as the strength of the rubble masonry seems to be around one third of the regular masonry value. No significant differences are found in terms of elastic modulus and peak strength.

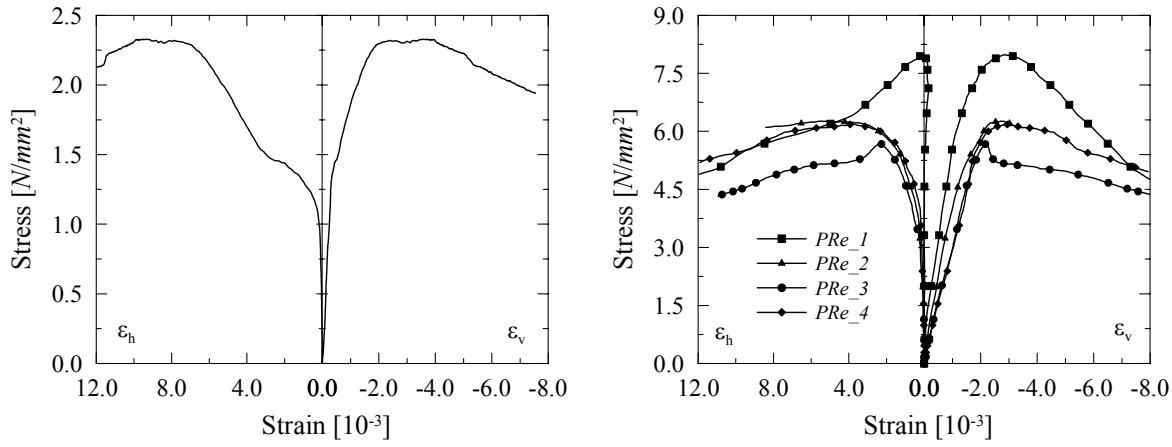

Figure 4.5 – Stress-strain diagrams obtained from compression tests on: (a) *PRu* specimens and (b) *PRe* specimens.

Table 4.2 – Results obtained from compression tests on *PRu* specimens.

Specimen	E N/mm^2	f_c N/mm^2	ε_p 10^{-3}
PRu_1	3430	2.3	2.9

Table 4.3 – Results obtained from compression tests on *PRe* specimens. In brackets, the coefficient of variation is given.

Specimen	E N/mm^2	f_c N/mm^2	ε_p 10^{-3}
PRe_1	4980	8.0	2.7
PRe_2	4515	6.3	2.9
PRe_3	2510	5.7	2.2
PRe_4	2720	6.2	3.0
Average	**3680 (34%)**	**6.6 (15%)**	**2.7 (13%)**

4.3 Short-term creep tests

4.3.1 Experimental setup

Short-term creep tests were carried out at Politecnico di Milano using, again, the uniaxial servo-controlled MTS® 311.01.00 testing machine, with non-rotating steel plates and a maximum capacity of 2500 *kN*, see Figure 4.6a. The displacements in the specimens were recorded by a vertical and a horizontal displacement transducer GEFRAN PY2-10 (10 *mm*

range) positioned in each face of the prisms, in a total of eight transducers per specimen, see Figure 4.6b. Vertical transducers measured the average longitudinal deformation over approximately 200 *mm* span and horizontal transducers measured the average transversal deformation over approximately 150 *mm* span.

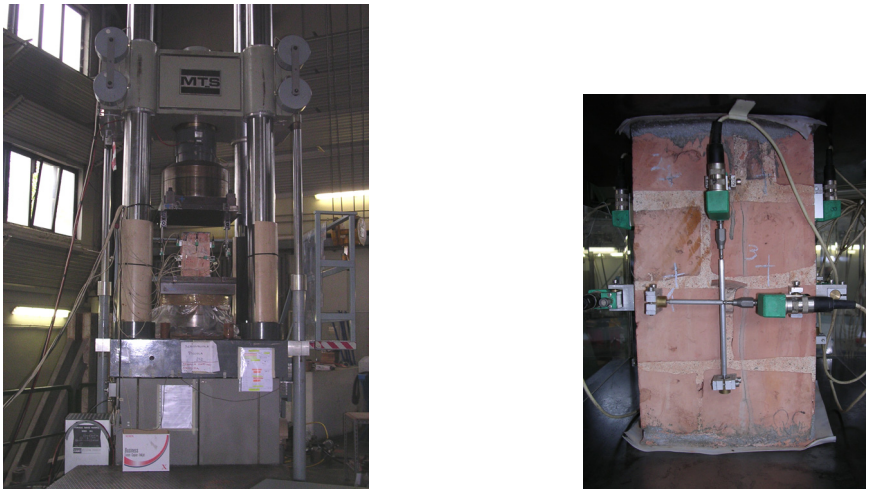

(a) (b)

Figure 4.6 – Test setup: (a) MTS® testing machine and (b) instrumented (*PRe*) specimen.

4.3.2 Testing program

A total of six *MRu* specimens, four *PRu* and four *PRe* specimens were tested for short-term creep. In standard creep tests, a specimen is subjected to a constant load and strain is recorded at subsequent times. Reproduction of the test with a series of different loads gives a family of creep curves, which characterize the creep behaviour of the material. However, in the case of ancient masonry, this procedure has severe drawbacks due to the high scatter of the material strength and the limited number of specimens available. To overcome these problems and to obtain as much information as possible from each specimen, a stepped load-time diagram has been applied to the specimens.

The *MRu* specimens were tested by applying successive load steps of 0.25 N/mm^2 at intervals of three hours. In this way, failure could occur either during the loading phase (short-term failure) or during sustained loading (tertiary creep). An attempt to obtain creep failure of the specimens was pursued by increasing the duration of the last steps whenever the strain rate was similar to the values observed in previously tested specimens. This issue will be further addressed in Section 4.5.

PRu and *PRe* specimens were tested with a slightly improved procedure where the load was kept constant for periods of eight hours. In this case, load steps of 0.30 N/mm^2 were applied. The period under sustained load was extended as an attempt to obtain a more accurate description of the viscous behaviour.

4.3.3 Test results

Figure 4.8 depicts the average vertical (longitudinal) and horizontal (transversal) strains obtained for *MRu* specimens, respectively ε_v and ε_h. In addition, for the same specimens, Table 4.4 gives a summary of the experimental results in terms of the elastic modulus E, peak stress f_c' and time to failure T, which corresponds to the duration of the creep test. The values for the elastic modulus E were calculated as an average from the second to forth load steps (0.25 to 1.0 N/mm^2). Annex A.1 illustrates the time-stress-strain diagrams for each specimen, providing a detailed description of the test results. Accordingly, the experimental results obtained for *PRu* specimens are given in Figure 4.8a, Table 4.5 and Annex A.2 while the results for *PRe* specimens are illustrated in Figure 4.8b, Table 4.6 and Annex A.3.

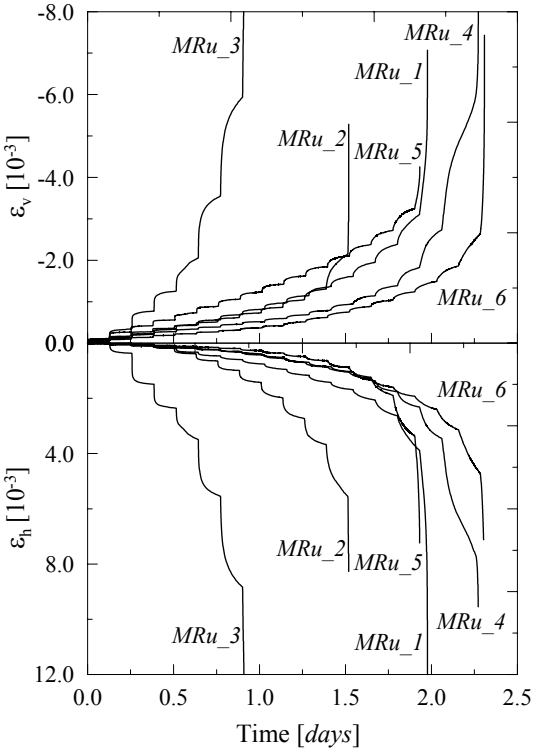

Figure 4.7 – Strain-time diagrams obtained from short-term creep tests on *MRu* specimens.

Table 4.4 – Results obtained from short-term creep tests on *MRu* specimens. In brackets, the coefficient of variation is given.

Specimen	E N/mm^2	f_c' N/mm^2	T *days*
MRu_1	3730	4.00	2.0
MRu_2	3455	3.25	1.5
MRu_3	1505	2.00	0.9
MRu_4	5870	4.25	2.3
MRu_5	2485	4.00	1.9
MRu_6	6395	4.75	2.3
Average	**3905 (49%)**	**3.7 (26%)**	**1.8**

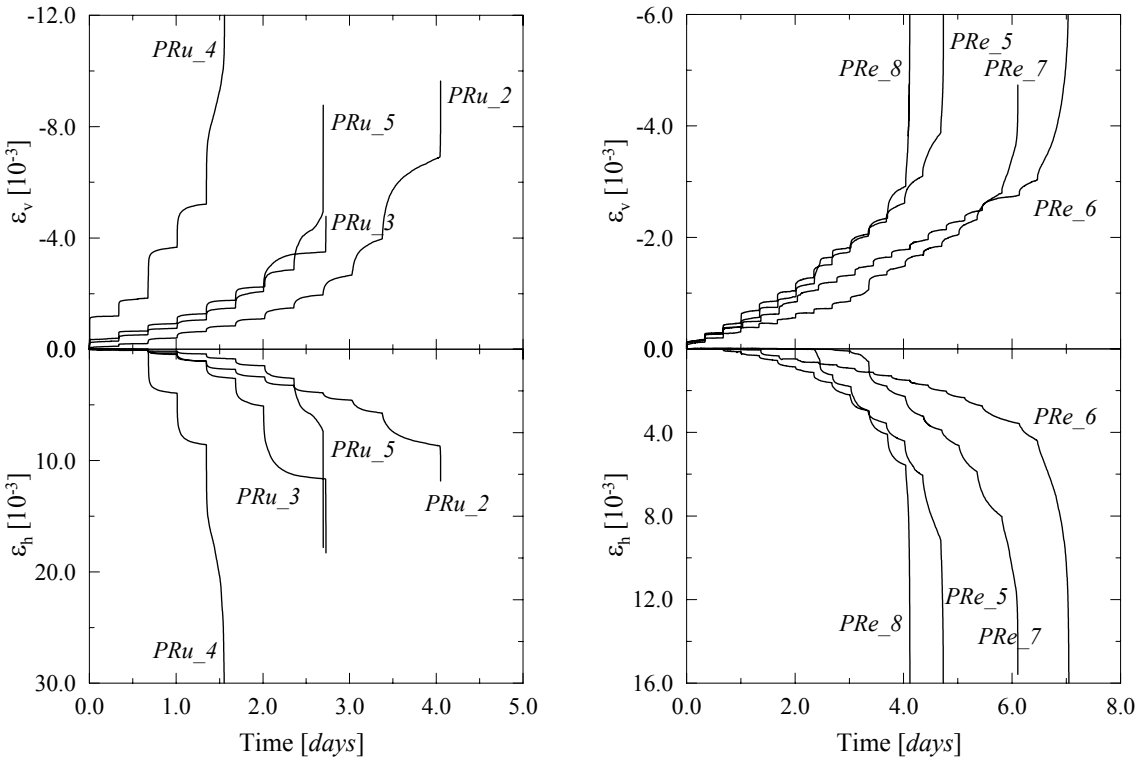

(a) (b)

Figure 4.8 – Strain-time diagrams obtained from short-term creep tests on specimens: (a) *PRu* and (b) *PRe*.

Table 4.5 – Results obtained from short-term creep tests on *PRu* specimens. In brackets, the coefficient of variation is given.

Specimen	E N/mm^2	f_c' N/mm^2	T *days*
PRu_2	4480	3.60	4.0
PRu_3	2005	2.40	2.7
PRu_4	740	1.50	1.6
PRu_5	1395	2.60	2.7
Average	**2155 (76%)**	**2.5 (34%)**	**2.8**

Table 4.6 – Results obtained from short-term creep tests on *PRe* specimens. In brackets, the coefficient of variation is given.

Specimen	E N/mm^2	f_c' N/mm^2	T *days*
PRe_5	2700	4.50	4.7
PRe_6	3185	5.70	7.0
PRe_7	4075	5.40	6.1
PRe_8	3815	3.90	4.1
Average	**3445 (18%)**	**4.9 (17%)**	**5.5**

The sample is too small to extract any conclusion and, in the case of *PRe* specimens, the difference in strength from the uniaxial standard compression tests ($f_c = 6.6\ N/mm^2$) and the short-term tests ($f_c' = 4.9\ N/mm^2$) has no strong relevance. In terms of average elastic modulus, the difference is marginal. As expected, larger coefficients of variation were found for rubble specimens than for regular specimens.

With respect to crack patterns, thin and diffuse vertical cracks developed in the specimens during testing but large cracks and spalling were only observed at failure. This failure mode is particularly dangerous as it can lead to erroneous conclusions about the safety level of existing structures. It is further noted that, in the case of rubble specimens, cracks mainly develop in the mortar matrix and, at failure, expulsion of the brick and stone fragments was observed. On the contrary, in the case of regular specimens, cracks propagated across both units and mortar. Figure 4.9 and Figure 4.10 illustrate, as examples, the crack pattern evolution of the rubble specimen *PRu_3* and of the regular specimen *PRe_7*, respectively.

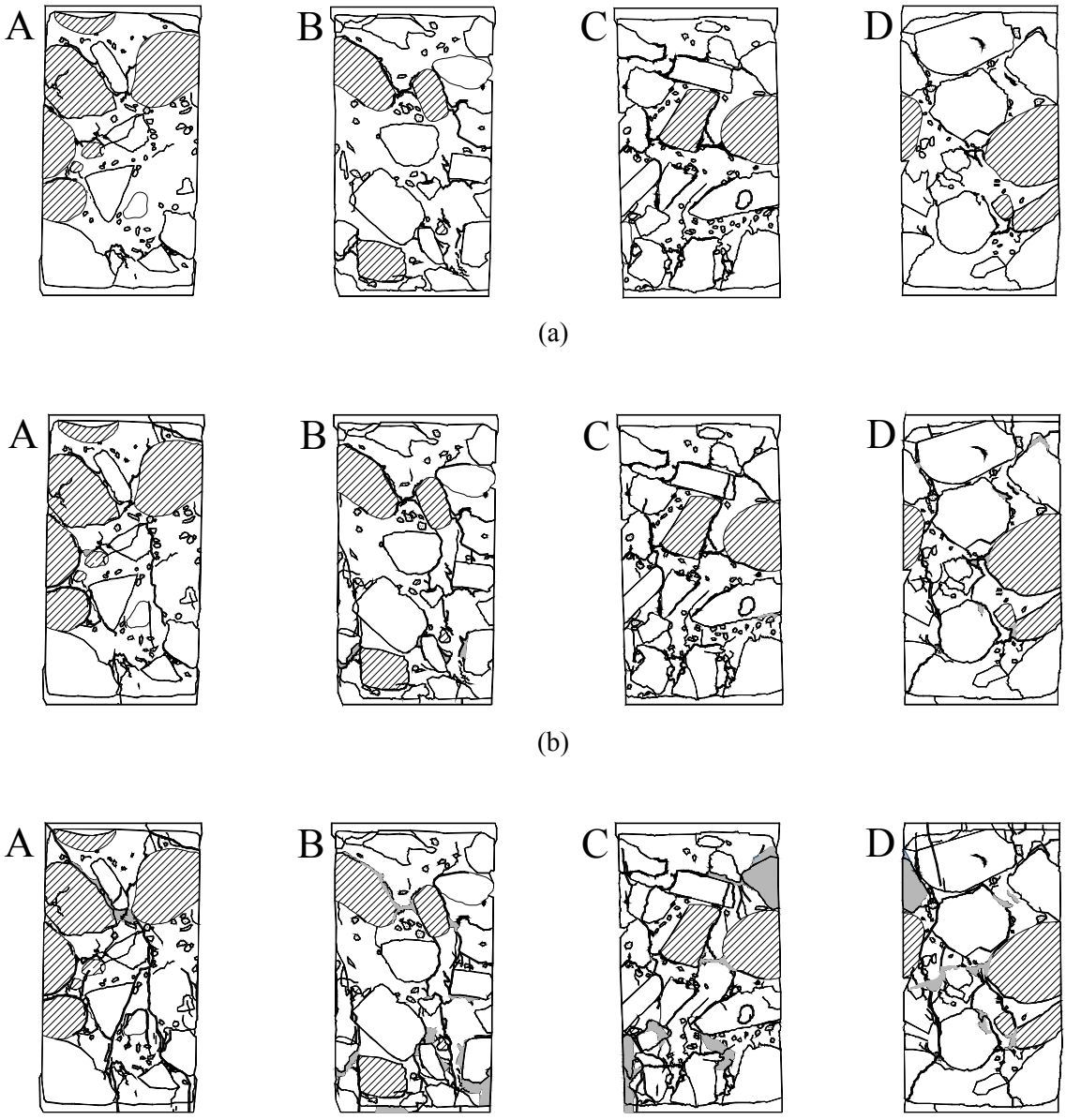

Figure 4.9 – Crack pattern evolution for specimen *PRu_3*: (a) prior to testing, (b) at approximately 80% of f_c' (corresponds to a test duration of 2.0 days) and (c) at failure. The oblique pattern indicates stone and the shaded areas indicate spalling/loss of material.

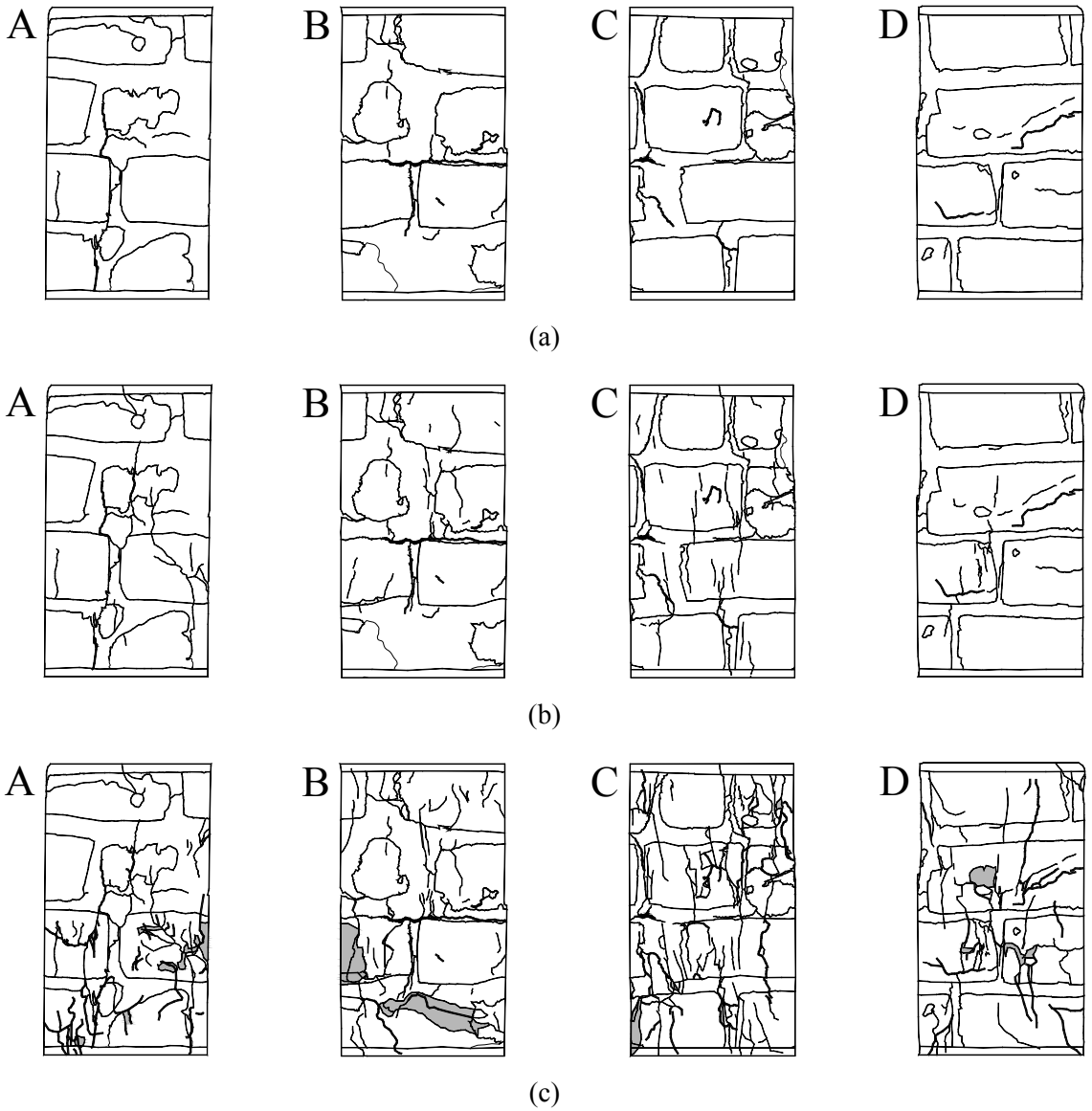

Figure 4.10 – Crack pattern evolution for specimen *PRe_7*: (a) prior to testing, (b) at approximately 80% of f_c' (corresponds to a test duration of 5.0 days) and (c) at failure. Shaded areas indicate spalling/loss of material.

4.4 Long-term creep tests

4.4.1 Experimental setup

Long-term creep tests require specific testing machines able to keep the load constant for long periods. In this study, three steel frames were specially designed and built to perform the tests conducted at University of Minho, see Figure 4.11a,b. Each frame includes two loading steel plates, a hydraulic jack, a pressure gauge and a gas reservoir to stabilize the applied load. The lower steel plate was fixed while the upper plate was hinged. The

equipment was designed to test two prisms simultaneously, separated by a steel plate. Upon failure of one of the specimens, the equipment is unloaded to remove the failed specimen and re-loaded with the remaining specimen.

(a) (b) (c)

Figure 4.11 – Testing apparatus: (a) hydraulic frame, (b) specimens under testing and (c) removable strain gauge and contact seats glued to the specimen.

Longitudinal and transversal deformations were measured on each face of the prisms with a removable strain-gauge LASER ELECTRONIQUE TP, see Figure 4.11c. Longitudinal deformations were measured over three mortar bed-joints with an approximate span of 250 *mm* while transversal deformations were measured over one head-joint with an approximate span of 145 *mm*. In addition, one inductive transducer HBM (10 *mm* range) per specimen was employed in the longitudinal direction to act as control of the strain-gauge measurements. It is noted that in the face of the specimen where the transducer was placed, the transversal displacement was not measured. In this way, the average longitudinal displacement of each specimen results from four strain-gauge measurements, while the transversal displacement results from three strain-gauge measurements. The tests were carried out under controlled conditions of temperature (22 ± 2ºC) and humidity (55 ± 10%), which were recorded by a data logger TESTOSTOR 175-2.

4.4.2 Testing program

The tests were conducted on six *PRe* specimens. As in short-term creep tests, the load was applied by successive steps and kept constant for a given period. Two different load histories have been considered in order to better define future testing programs in similar specimens. A total of two prisms were tested by applying an initial stress of 1.50 N/mm^2 and successive steps of 0.65 N/mm^2. The initial load step corresponds, approximately, to 25% of the compressive strength f_c obtained from the standard compression tests described in Section 4.2, while further load steps correspond, approximately, to 10% of f_c. The duration of each period under constant load was of three months.

The other four specimens were initially loaded at 4.10 N/mm^2 (approximately 60% of f_c) with subsequent load increases of 0.65 N/mm^2 (about 10% of f_c), applied at intervals of six months. Both load histories adopted have been defined in order that the estimated duration of the tests would be of about two years.

4.4.3 Test results

Figure 4.12 illustrates the average vertical (longitudinal) and horizontal (transversal) strains obtained for *PRe* prisms tested with constant load periods of three months. Table 4.7 gives a summary of the experimental results obtained and Annex A.4 shows detailed time-stress-strain diagrams for each tested specimen.

For specimens tested with constant load periods of six months, Figure 4.13 shows, as an example, the strain evolution at each face of specimen *PRe_12* and, also, the average strain-time diagrams obtained for all tested prisms. In addition, Table 4.8 gives a summary of the results and Annex A.5 illustrates the time-stress-strain diagrams obtained. From Figure 4.13a it is possible to observe that the strain evolution is different in each face of the prisms. This behaviour is typical of compression tests in quasi-brittle materials but, in the present experiments, such feature is more salient due to the hinged upper loading plate. Another important aspect is that in some specimens cracks suddenly arise during constant load steps, resulting in a strain jump in the strain-time diagram, see *e.g.* the diagrams of specimen *PRe_10* at 325 days or *PRe_11* at 450 days shown in Figure 4.12 and Figure 4.13, respectively.

The values obtained for the compressive strength are within the range obtained for the standard compressive strength and short-term creep tests. Displacements recorded with the transducers employed (one per specimen) were found to be in agreement with the strain-gauge measurements.

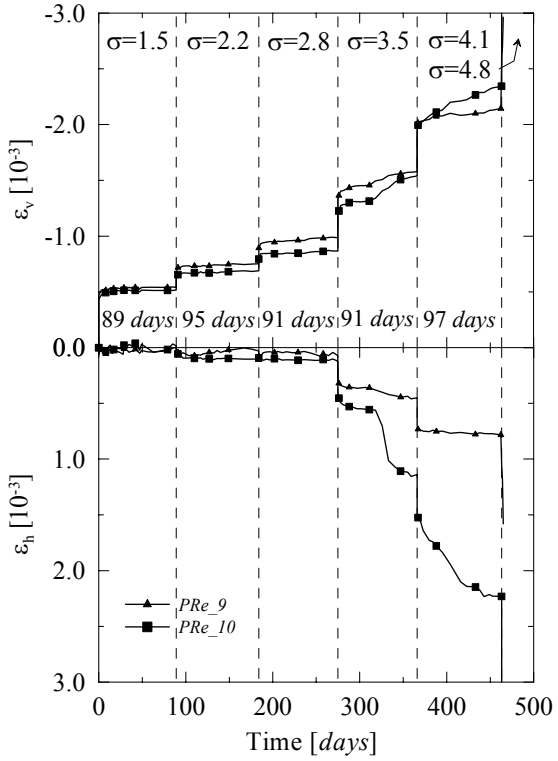

Figure 4.12 – Strain-time diagrams obtained from long-term creep tests (constant load periods of three months) for *PRe* specimens. σ stands for applied stress in N/mm^2.

Table 4.7 – Results obtained from long-term creep tests on *PRe* specimens (constant load periods of three months).

Specimen	E N/mm^2	f_c' N/mm^2	T *days*
PRe_9	5055	4.75	465
PRe_10	4380	4.75	464
Average	**4718**	**4.8**	**465**

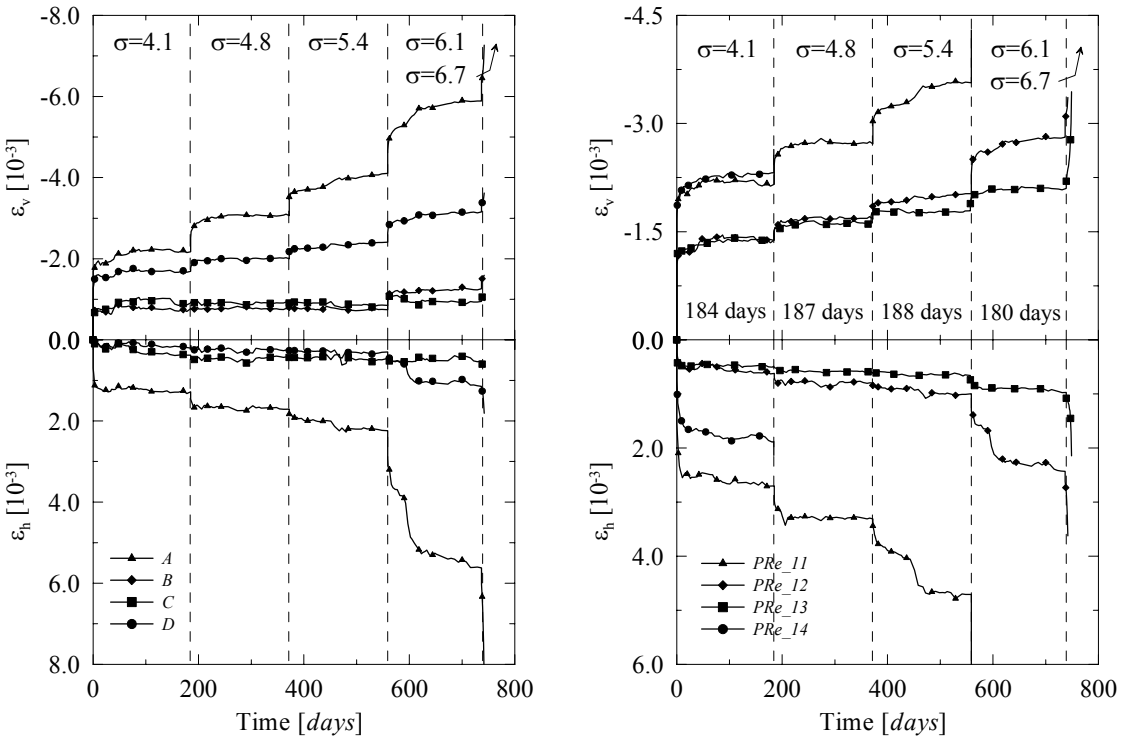

Figure 4.13 – Strain-time diagrams obtained from long-term creep tests (constant load periods of six months) for *PRe* specimens: (a) strain evolution on each face of prism *PRe_12* and (b) (average) strain evolution for all tested prisms. σ stands for applied stress in N/mm^2.

Table 4.8 – Results obtained from long-term creep tests on *PRe* specimens (constant load periods of six months). In brackets, the coefficient of variation is given.

Specimen	E N/mm^2	f_c' N/mm^2	T *days*
PRe_11	3720	6.05	559
PRe_12	5055	6.70	742
PRe_13	4345	6.70	749
PRe_14	3270	4.75	184
Average	**4100 (19%)**	**6.1 (15%)**	**559**

Figure 4.14 depicts the crack pattern evolution for specimen *PRe_13* as an example. Again, diffuse vertical cracks developing during testing have been observed, with large cracks and spalling occurring near failure. It is noted that the specimens with lower values of f_c' presented the most diffused crack patterns. Severe non-uniform distribution of damage can be observed along the four faces of the specimens, confirming the results shown in Figure 4.13a.

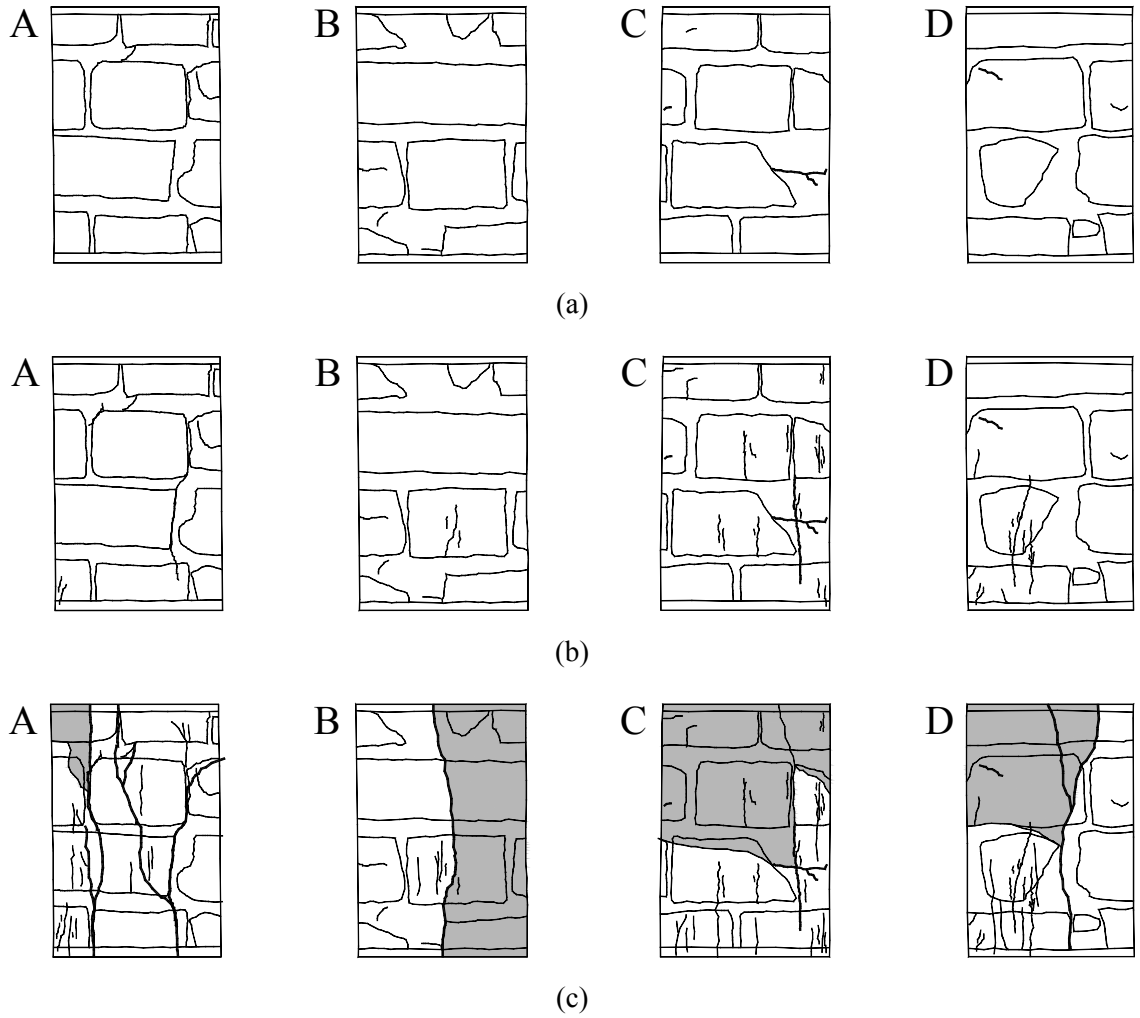

Figure 4.14 – Crack pattern evolution for specimen *PRe_13*: (a) prior to testing, (b) at 80% of f_c' (corresponds to a test duration of 550 days) and (c) at failure. Shaded areas indicate spalling/loss of material.

4.5 Discussion of the results

In this Section, attention is mainly given to the results obtained with *PRe* specimens because, in this case, both short-term and long-term creep tests were carried out. A more careful interpretation of the results obtained from the rubble specimens can only be made when further experimental data is available from the ongoing testing program. It is noted that the short-term compressive strength f_c of each prism tested in creep is unknown and can only be estimated. In this Section, the peak stress values f_c' obtained from the creep tests are considered as a close estimate of the compressive strength f_c. Even if, in reality, the compressive strength f_c does not correspond to f_c', such values remain the closest estimate in a material as heterogeneous as the one addressed in this study.

Figure 4.15 illustrates the evolution of the creep coefficient, defined as the ratio between the creep strain and the elastic strain, calculated from the short-term and long-term creep tests results. For each specimen, the creep coefficient was calculated considering all creep diagrams at low stress levels (below 45% of f_c'). It is further noted that the creep coefficient obtained from short-term creep tests was calculated from the average of the four tested specimens while the values obtained from long-term creep tests result from the average of the two specimens tested with constant load periods of three months. In the remaining four specimens tested in long-term creep, a first load step of approximately 60% of f_c was applied and, thus, such tests can not be used to calculate creep coefficients.

Creep coefficients of approximately 0.10 and 0.15 were found at the end of 8 hours and 90 days of sustained loading, respectively, confirming that most creep strain occurs in an early stage. Another important aspect is that the creep coefficient found at the end of 90 days is significantly lower than the values recommended by EC6, CEN (2003), for masonry made with clay units, which range from 0.5 to 1.0. This can be explained by the fact that EC6 values refer to new masonry, where maturation of mortar is in an initial stage and, also, because the specimens tested had already been under service loads for approximately five centuries prior to testing.

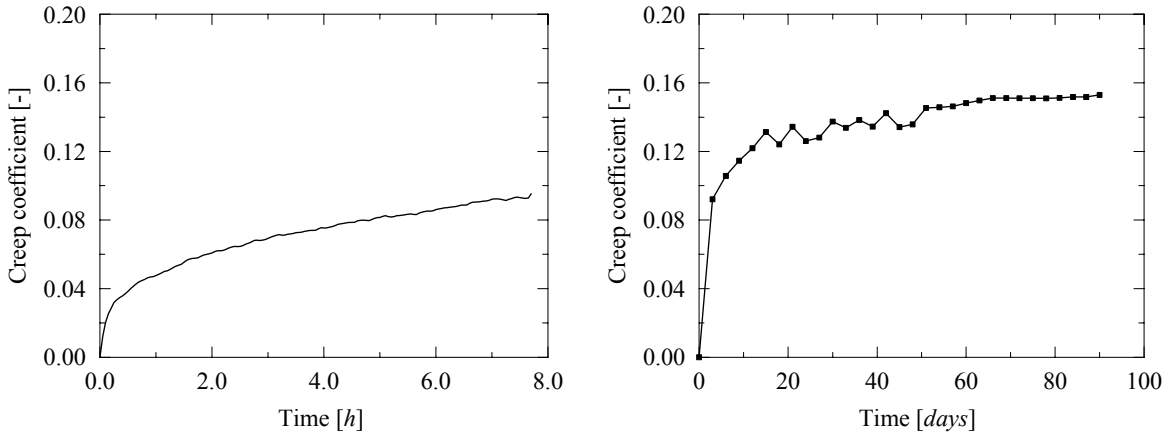

Figure 4.15 – Variation of the creep coefficient with time obtained for *PRe* specimens: (a) short-term creep results and (b) long-term creep results (constant load periods of three months).

Figure 4.16 shows the strain rate evolution, vertical $\dot{\varepsilon}_v$ and horizontal $\dot{\varepsilon}_h$, versus the applied stress over strength ratio σ / f_c' for *PRe* specimens under short-term creep tests. Strain-rate values were calculated between the sixth and eighth hours of each constant load step. It is expected that vertical strain rate values would be negative and horizontal strain rate values positive but some exceptions were found. This can be explained by minor variations in the applied load or changes in the environmental conditions. Such values have been considered equal to zero in the strain-rate diagrams shown in the rest of this Section.

In Figure 4.16a three phases can be distinguished: for low stress levels (up to 50% of f_c'), the vertical strain rate is approximately constant and rather low; for medium stress levels (between 50% and 80% of f_c'), the vertical strain rate increases at a moderate pace; and, for high stress levels (over 80% of f_c'), a remarkable growth of the strain rate stress can be observed. The existence of three distinct phases had also been reported by Mazzotti and Savoia (2002) on short-term creep tests performed on concrete specimens. Figure 4.16b shows that beyond 50% of f_c', crack growth initiates, influencing the creep behaviour of the material.

The results obtained for *PRu* specimens under short-term creep are illustrated in Figure 4.17. In this case, the scattered nature of the material is more evident and the three phases identified above cannot be so clearly observed. Even so, the results show that significant growth of the strain rate, either vertical or horizontal, occurs at an earlier stage than in the case of *PRe* specimens, approximately beyond 70% of f_c'.

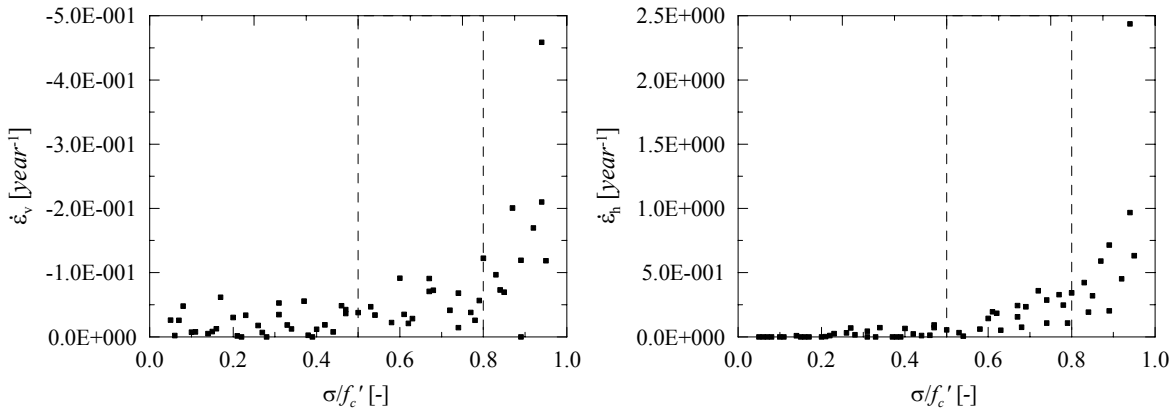

(a) (b)

Figure 4.16 – Strain rate evolution versus applied stress over strength ratio for short-term creep tests on *PRe* prisms: (a) vertical strain rate and (b) horizontal strain rate.

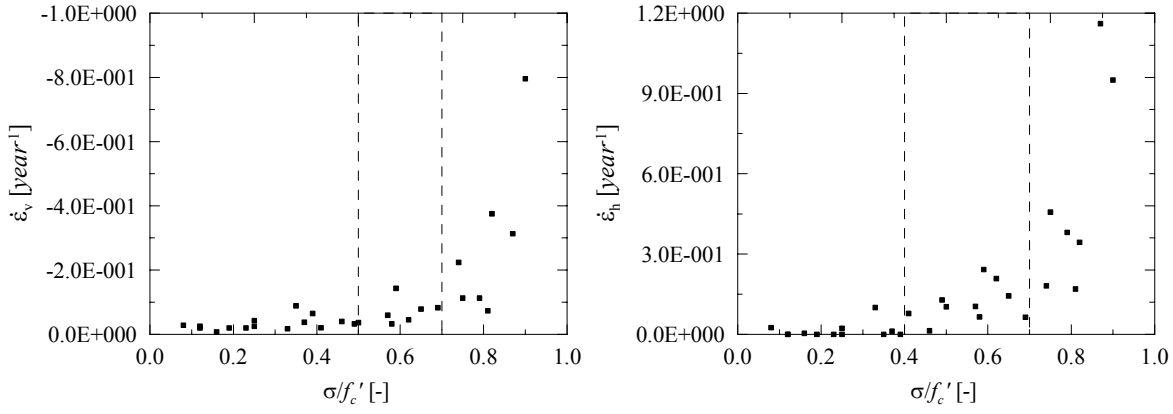

Figure 4.17 – Strain rate evolution versus applied stress over strength ratio for short-term creep tests on *PRu* prisms: (a) vertical strain rate and (b) horizontal strain rate.

Figure 4.18 and Figure 4.19 illustrate the strain rate evolution versus stress over strength ratio for long-term creep tests with constant load periods of three months and six months, respectively, carried out on *PRe* specimens. Strain rates were calculated from the average results over the last 30 days in the case of the tests with constant load periods of three months and over the last 90 days in the case of the tests with constant load periods of six months.

It is noted that the number of results is rather short and further testing is needed to better fundament the observations made. Nevertheless, the difference between the strain rate values obtained from short-term creep tests and long-term creep tests is striking. In fact, strain rates ranging from zero to -5.0×10^{-1} $year^{-1}$ were observed in short-term creep tests while in long-term creep tests, values ranging from zero to -1.0×10^{-3} $year^{-1}$ were found. Such difference precludes any possibility of extrapolation between the results obtained from the two types of test. Furthermore, this indicates that primary creep is not extinguished at the end of 8 *h* under sustained loading and, thus, secondary creep can not be measured from short-term creep tests. Such results must, therefore, be interpreted carefully.

Another important aspect is that secondary creep was observed to initiate between 60 and 70% of f_c. It is further noted that larger strain rate values were obtained for the prisms tested with constant load periods of three months, stressing the scattered nature of the masonry tested.

An hyperbolic least squares fit of the experimental data obtained from the long-term creep tests with constant load periods of six months was computed, which can be quite useful in calibrating non-linear creep models. The hyperbolic curve adopted is in the following form

$$\dot{\varepsilon} = \frac{0.4\,a}{1-\sigma/f_c} + a \tag{4.1}$$

which yields zero for $\sigma/f_c = 0.6$ and has a vertical asymptote for $\sigma/f_c = 1.0$. From the least squares method, a = -6.76 × 10^{-5} for the vertical strain rate and a = 1.19 × 10^{-4} for the horizontal strain rate.

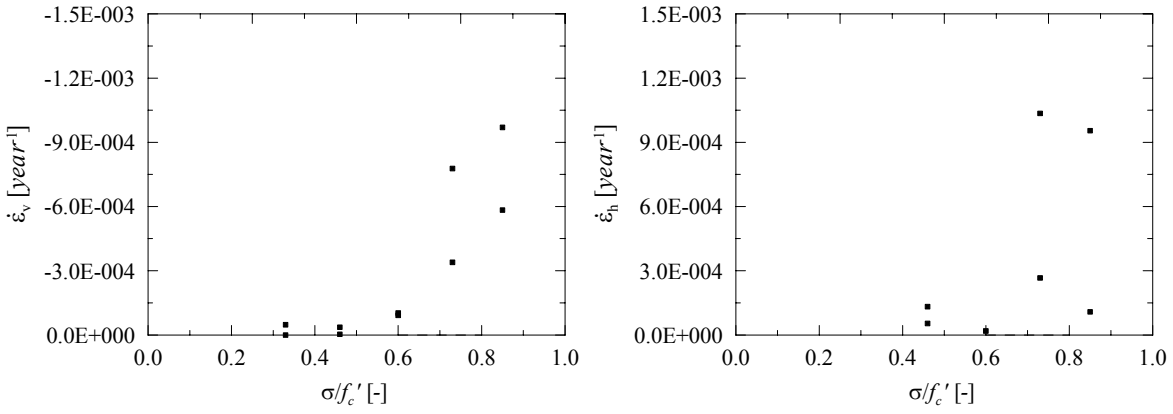

(a) (b)

Figure 4.18 – Average strain rate in the last 30 days versus applied stress over strength ratio for long-term creep tests (three months steps): (a) vertical strain rate and (b) horizontal strain rate.

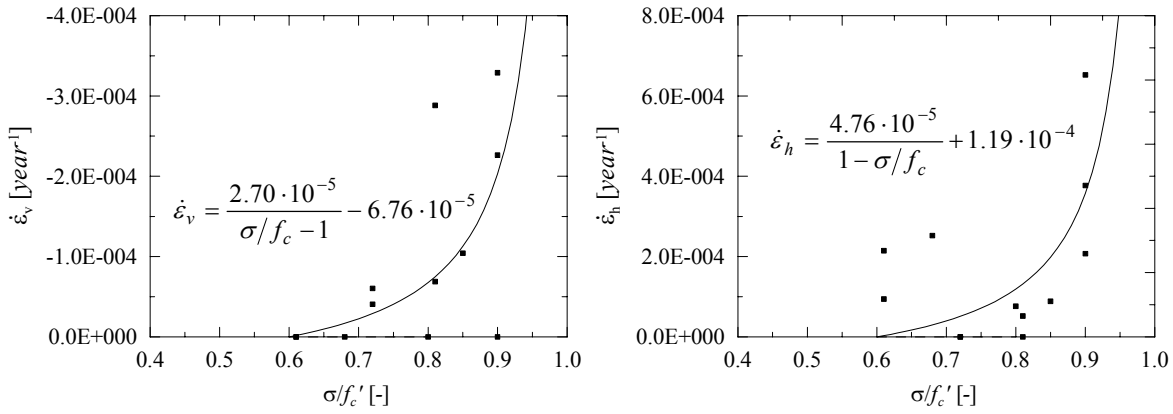

(a) (b)

Figure 4.19 – Average strain rate in the last 90 days versus applied stress over strength ratio for long-term creep tests (six months steps): (a) vertical strain rate and (b) horizontal strain rate.

The striking difference between strain rate values in short-term and long-term creep tests draws attention over what should be the minimum duration of constant load periods when conducting creep tests at high stress levels. A reasonable criterion is believed to be keeping the load constant until only secondary creep is present, *i.e.* until a fairly constant strain rate is attained. For this purpose, the vertical and horizontal strain rates where calculated for each 15 days period of the total 180 days constant load steps, as illustrated in Figure 4.20. It is noted that only results corresponding to load levels larger than 60% of f_c' were considered. The results obtained indicate that the strain rate gets approximately constant after 70-80 days in the case of longitudinal strains and after 30-40 days in the case of transversal strains.

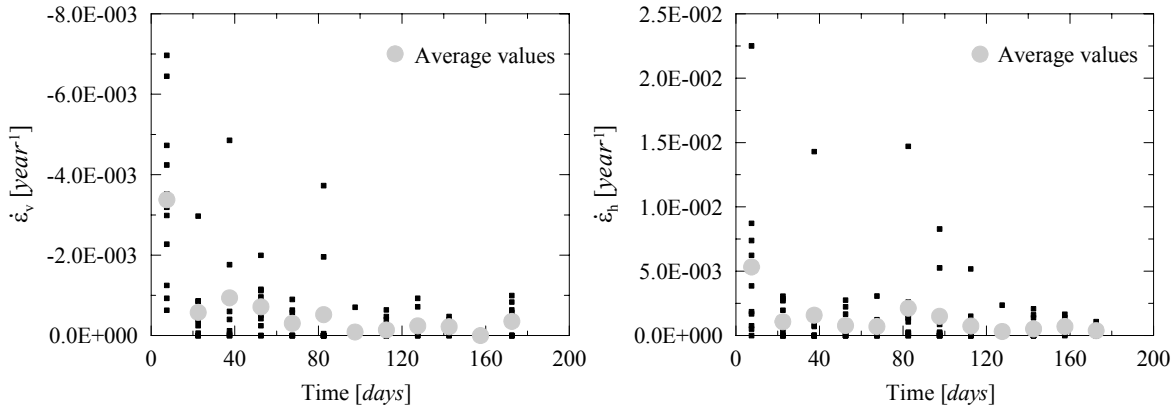

Figure 4.20 – Strain-rate evolution in time for applied stresses larger than 60% f_c': (a) vertical strain rate and (b) horizontal strain rate.

4.6 Summary

The creep behaviour under high stresses of three different types of ancient masonry specimens has been analysed. Short-term creep tests have been conducted on regular and rubble masonry prisms recovered from the ruins of the collapsed Pavia Civic Tower and, also, on rubble prisms collected in the crypt of the Monza Cathedral. In addition, long-term creep tests were also carried out on regular prisms coming from the Pavia Civic Tower.

From experimental practice, it is possible to conclude that creep tests on ancient masonry prisms should be carried out by applying the load in successive steps, at a given time interval, starting from a low stress level. In this way, a throughout description of the

viscous behaviour of the material can be obtained. Creep tests in which the load is applied in a single step are unwieldy in the case of ancient masonry due to the high scatter in the mechanical properties and to the small number of specimens usually available.

The time period between successive load steps should be sufficiently long to extinguish primary creep. In fact, the evolution for different stress levels of the strain rate associated to secondary creep can only in such way be evaluated. From the results obtained on the regular masonry prisms tested, a minimum time period under sustained loading of 70 to 80 days should be adopted. For this reason, remarkable differences were observed between secondary creep rates calculated from short-term or long-term creep tests. Short-term creep results should, therefore, be interpreted carefully.

Finally, it should be stressed that secondary creep was found to initiate at 60 to 70% of the compressive strength. A hyperbolic fit to describe the evolution of secondary creep rate with the applied stress-level has been suggested in the present study.

5 Multiple-leaf masonry walls: load transfer and compressive failure

Multiple-leaf masonry walls are a typology often found in historical city centres worldwide and usually consist of two or three leaves made up of different materials such as stone, brick or rubble masonry, see *e.g.* Binda *et al*. (1999). In the case of three-leaf walls, two outer shells and a thick inner core of rubble material are generally present. The last decades have witnessed the severe damage, or even collapse, exhibited by several famous monumental buildings due to high compressive loading in multiple-leaf pillars and walls. Recent examples are the collapse of the Cathedral of Noto, Italy, in 1996, see Binda *et al*. (2003a), and the severe damage found in the churches of the Santissimo Crocefisso and Santissima Annunziata, see Binda *et al.* (2001), also in Italy.

Most structural problems exhibited by three-leaf walls and pillars result from the poor or absent connection between the leaves, the weakness of the inner core or the deterioration of the mortar in the external joints. Several techniques such as grout injection or bed-joint reinforcement are today available for structural retrofitting, see Vintzileou and Tassios (1995), Toumbakari (2002) and Valluzzi *et al.* (2004). Nevertheless, reliable safety assessment and retrofitting with minimum intervention requires proper insight on the structural behaviour and failure mechanisms, which is an especially complex issue in the case of three-leaf walls. In fact, the stress distribution is largely dependent of the mechanical properties of the leaves, of the leaves dimensions and of the way the leaves are connected to each other.

References in literature are rather scarce on this topic. Binda *et al.* (1991) proposed some simple analytical models regarding two extreme situations: presence of stiff horizontal elements capable of distributing the load to the leaves proportionally to their axial stiffness and absence of such elements, making the load transfer dependent on the bond properties of the collar joints. Later on, a first experimental assessment of the shear behaviour of two-leaf walls was reported by Binda *et al.* (1994) using small scale specimens.

Egermann and Neuwald-Burg (1994) carried out an extensive compression testing program on three-leaf wallets. The experimental results showed that the outer-leaves exhibit a lower strength inside the composite system than when individually loaded and

that the inner-leaves have the opposite behaviour. The different responses were attributed to the fact that the outer shells are not only compressed but are also under bending moments, and that the infill is confined.

Recently, Drei and Fontana (2001) carried out a numerical study to assess the influence of different material properties and geometries in the response of multiple-leaf walls subjected to transversal loads. The results obtained indicate that large shear stress concentrations are likely to occur in keyed collar joints, which have a decisive effect on the global safety of the structure. Such stress concentrations are dependent on the leaves relative thicknesses and on the geometry of the shear keys.

The present work illustrates an integrated experimental-numerical approach to provide understanding into the behaviour and failure mechanisms of three-leaf stone masonry walls. Experimental data on shear and compression tests on large scale specimens is provided, which can contribute to the derivation of rational design rules and validation of numerical models. Firstly, the testing program and obtained experimental data are addressed and, afterwards, the experimental results are analysed making use of simplified calculations and, also, to sophisticated numerical tools.

5.1 Experimental work

A set of twelve three-leaf stone wallets with dimensions of $310 \times 510 \times 790\ mm^3$, composed by two outer-leaves of ashlar masonry and an inner core of rubble masonry were built and tested at the Politecnico di Milano, see Figure 5.1. Two types of collar joints (with and without shear keys) and two types of stones (a limestone named *Noto*, frequently used locally, and a sandstone named *Serena*, frequently used in central and southern Italy) have been considered. It is noted that the same type of stone was used for both outer and inner-leaves. The construction process is illustrated in Figure 5.2 and the wallets are shown in Figure 5.3 and Figure 5.4. The loading faces of the specimens were regularized with a cement based mortar approximately $15\ mm$ thick. The wallets were denoted by their geometrical and material properties according to Table 5.1.

The wallets were tested according to three different procedures:

a) Shear tests. A monotonic load was applied to the inner-leaf while the outer-leaves were supported (triplet test). This test is similar to the EN 1052-3, CEN (2002).

b) Compression tests on single leaves. Outer and inner-leaves were tested individually under uniaxial compression.

c) Compression tests on full wallets. A monotonic load was applied to the complete transversal section of the wallets.

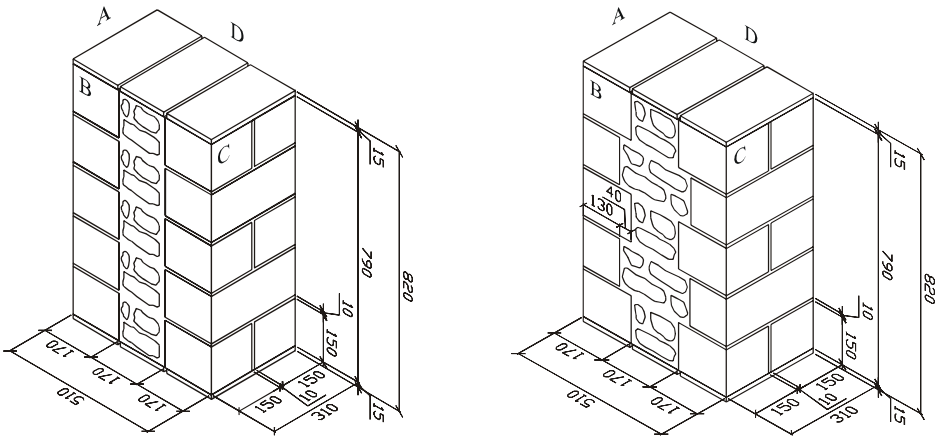

Figure 5.1 – Wallets dimensions in *mm*: (a) straight collar joints and (b) keyed collar joints.

Figure 5.2 – Construction of the wallets.

(a) (b) (c)

Figure 5.3 – *Noto* wallets: (a) front view of a specimen with straight collar joints, (b) front view of a specimen with keyed collar joints and (c) lateral view.

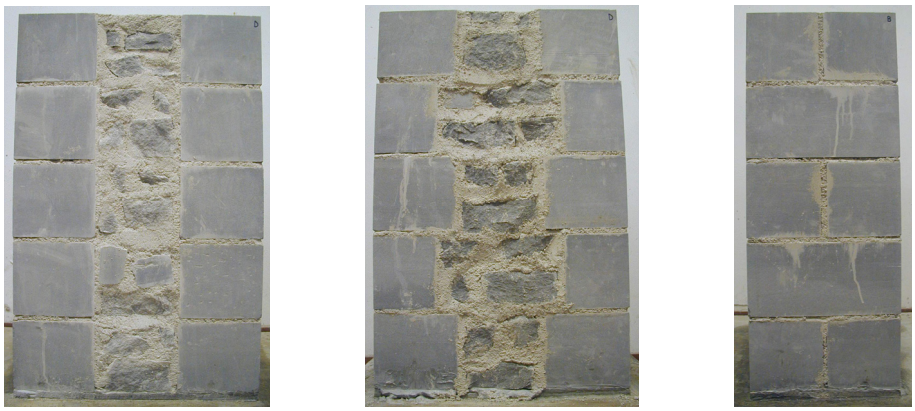

(a) (b) (c)

Figure 5.4 – *Serena* wallets: (a) front view of a specimen with straight collar joints, (b) front view of a specimen with keyed collar joints and (c) lateral view.

Table 5.1 – Denomination of the tested wallets. The first letter corresponds to the type of stone (*N* for *Noto* and *S* for *Serena*) while the second letter stands for the type of connection (*S* for straight and *K* for keyed).

	Straight collar joints	Keyed collar joints
Noto limestone	*NS1*, *NS2*, *NS3*	*NK1*, *NK2*, *NK3*
Serena sandstone	*SS1*, *SS2*, *SS3*	*SK1*, *SK2*, *SK3*

5.1.1 Description of masonry components

Units

Physical and mechanical tests were carried out on cylindrical samples cored from the stone units used to build the wallets. The units were cored considering two different orientations: along the loading direction *A* and along the bedding direction *B* of the units in the wallets, so that the anisotropy of the material could be characterized.

The physical tests consisted on the determination of the bulk density and open porosity, according to EN 772-4, CEN (1998b), see Figure 5.5. Six cylindrical specimens with a diameter of 80 *mm* and a height of 145 *mm* were considered for each type of stone. The average results obtained in terms of the bulk density $\rho_{b,s}$ and of the open porosity P_o are given in Table 5.2. The values found illustrate the significantly different physical properties of the two stones. The *Noto* limestone exhibits high open porosity and low weight while the *Serena* sandstone exhibits a 1.5 times larger weight and seven times less porosity.

(a)

(b)

(c)

Figure 5.5 – Bulk density and open porosity tests: (a) drying of the specimens to constant mass, (b) weighting of the specimens and (c) saturating with deionised water.

Table 5.2 – Average results for the bulk density and open porosity of the stones. The coefficient of variation *CV* is also given.

Type of stone	$\rho_{b,s}$ kg/m^3	*CV* %	P_o %	*CV* %
Noto	1760	1.5	15.4	4.5
Serena	2570	0.3	2.1	5.7

Uniaxial compressive tests were carried out after the physical tests, on the same cylindrical samples, according to EN 772-1, CEN (2000). Conditioning of the specimens was performed according to the air-dry conditions stated in the normative. The height of the specimens was limited to the 150 *mm* height of the stone units from which the specimens were extracted and, for this reason, a height over diameter ratio less than 2.0 was utilized. The ASTM standard C39, ASTM (2004), accounts for the effect of ratios less than 2.0 in concrete specimens by introducing a correction factor. For the ratio adopted in the experiments, 1.75, the reduction factor equals 0.98, which is quite small when compared with the data variability and, thus, was not considered. Three specimens for each combination type of stone/orientation were tested.

The test setup adopted is illustrated in Figure 5.6. For the *Noto* specimens, a non-standard uniaxial testing machine with a hydraulic actuator with a maximum capacity of 300 *kN* was used. The lateral deformations were measured with a clip gauge TML UB-A while the vertical deformations were measured using three strain transducers HBM DD1. In addition, two displacement transducers HBM W5TK measured the displacement between the loading plates. The post-peak behaviour of the specimens can only be followed resorting to the displacement transducers, as the strain transducers fixed to the samples are normally perturbed by developing cracks. The tests were carried out under displacement control at a displacement rate of 10 $\mu m/s$, permitting to trace the softening path. The loading capacity of the actuator was insufficient to reach failure of the *Serena* specimens and, thus, the specimens were loaded only up to 250 *kN* (about 50 to 60% of the strength) using the above test setup in order to determine the elastic parameters. Afterwards, the specimens strength was determined under loading control in a ALFRED J. AMSLER 4122 press with a maximum capacity of 2000 *kN*. Yet, in this testing machine, only the peak load could be recorded.

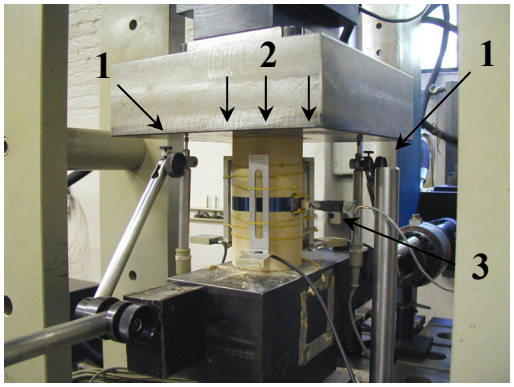

1 - Displacement transducer

2 - Strain transducers

3 - Clip gauge

(a) (b)

Figure 5.6 – Compression tests: (a) test setup used to determine the mechanical properties of the *Noto* specimens and the elastic properties of the *Serena* specimens and (b) test setup used to determine the strength of the *Serena* specimens.

The average values for the compressive strength f_c, peak strain ε_p, modulus of elasticity E and coefficient of Poisson ν are given in Table 5.3. The complete results obtained as well as the stress-strain diagrams are given in Annex B.1. It is noted that E and ν were calculated, in general, between 30 and 60% of f_c. According to the results obtained, the *Serena* stone exhibits, in the loading direction, a strength about five times larger than the *Noto* stone and about the double of the stiffness. It is further noted that both stones exhibit a larger strength and a smaller coefficient of variation in the loading direction than in the bedding direction. Such behaviour is due to the fact that the units bedding plane coincides with the natural bedding plane of the stone (rift). Failure patterns are illustrated in Figure 5.7.

Table 5.3 – Average results obtained from the compression tests on stone specimens (values in brackets give the *CV*).

Type of stone	Orientation [1]	f_c N/mm^2	ε_p 10^{-3}	E N/mm^2	ν -
Noto	*A*	20.6 (7%)	2.4	9475	0.10
Noto	*B*	17.6 (22%)	2.3	8525	0.09
Serena	*A*	104.2 (1%)	[2]	18218	0.19
Serena	*B*	89.0 (15%)	[2]	23293	0.21

[1] *A* stands for coring of the specimens along the *loading direction* of the units in the wallets and *B* for the *bedding direction*.

[2] The *Serena* specimens had to be tested in a machine with a higher capacity, which did not allow recording displacement values.

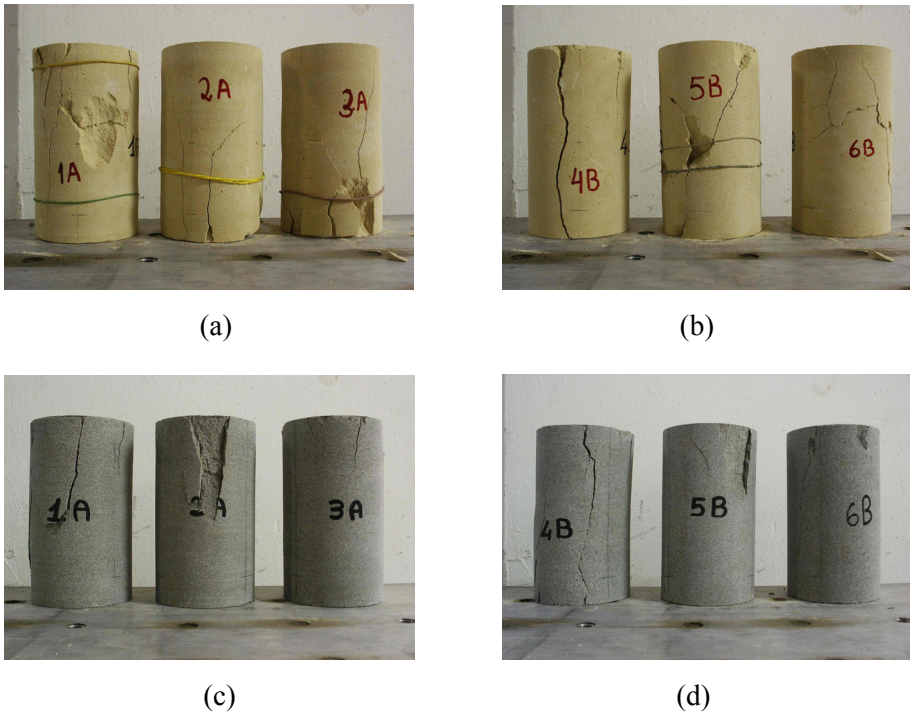

(a) (b)

(c) (d)

Figure 5.7 – Failure patterns for the compression tests: (a) *Noto* specimens oriented along direction *A* and (b) along direction *B*, (c) *Serena* specimens oriented along direction *A* and (d) along direction *B*.

The tensile strength was obtained by the splitting test, also known as Brazilian test. This test is not yet specified by any European standard and the RILEM recommendation for concrete CPC6, RILEM (1994), was adopted. According to the recommendation, the splitting tensile strength $f_{t,s}$ is determined by

$$f_{t,s} = \frac{2\,P}{\pi\,A} \tag{5.1}$$

In the above, P is the maximum load and A is the area of the theoretic failure surface. The tests were carried out on six cylindrical specimens for each type of stone with a diameter and height of 80 *mm*. The specimens were obtained by sawing in half three cylinders cored along the bedding direction *B* of the units. This direction is the most relevant with respect to the tensile strength as it is the direction where principal tensile stresses occur when units are vertically loaded. A non-standard uniaxial testing machine with a maximum capacity of 250 *kN* was used, see Figure 5.8a. Two packing strips in cardboard were placed between the loading plates and the specimens, so that punctual loading could be avoided, see Figure 5.8b.

(a) (b)

Figure 5.8 – Splitting tests: (a) test apparatus and (b) detail of the setup.

The average results obtained are given in Table 5.4 while the complete set of results is given in Annex B.1. In the case of concrete, the splitting tensile strength $f_{t,s}$ is about 5 to 12% higher than the direct tensile strength f_t, see Neville (1997). Here, f_t has been considered equal to $0.9\,f_{t,s}$. According to the results obtained, the *Noto* stone exhibits an average tensile strength three times smaller than the *Serena* stone. Concerning the ratio between the compressive and tensile strengths, a value of ten times was found for the *Noto* stone and a value of seventeen times was found for the *Serena* stone. Figure 5.9 illustrates the failure patterns.

Table 5.4 – Average results obtained from the tension tests on the stone specimens (values in brackets give the *CV*).

Type of stone	Orientation	$f_{t,s}$ N/mm^2	f_t N/mm^2
Noto	*B*	2.05 (13%)	1.8
Serena	*B*	6.00 (12%)	5.4

(a) (b)

Figure 5.9 – Failure patterns for the tension tests: (a) *Noto* specimens and (b) *Serena* specimens.

Mortar

A commercial premixed hydraulic lime mortar denominated *Albaria Allettamento*, Italy, was adopted to build the wallets. Flexural and compressive tests were carried out according to EN 1015-11, CEN (1999). The flexural tests were carried out on $40 \times 40 \times 160\ mm^3$ prisms casted in steel molds, see Figure 5.10. Noteworthy, with this procedure the water absorption effect of the units is ignored and thus these specimens are not fully representative of the mortar inside the masonry composite, see *e.g.* Lourenço (1996a).

The specimens were cured and stored at constant temperature and relative humidity conditions of $20℃$ and 90%, respectively. Compressive tests were carried out after the flexural tests on the two resulting halves of the prisms. The tests were performed at four ages: 28 days, 75 days (corresponding to the beginning of the tests on the wallets), 90 days and 172 days (corresponding to the end of the testing program). For each curing stage a total of six prisms were tested, each three coming from two different batches.

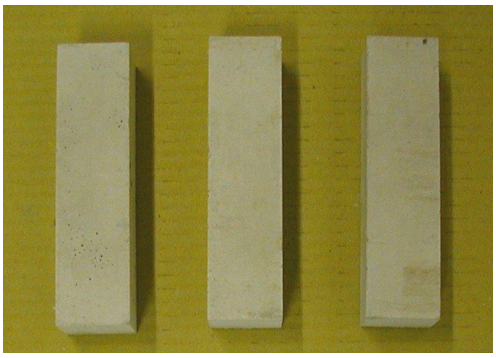

Figure 5.10 – Mortar prisms.

The flexural tensile strength f_f (in N/mm^2) was determined from standard three point bending tests using the following expression, CEN (1999)

$$f_f = 1.5 \cdot \frac{F\,l}{b\,d^2} \tag{5.2}$$

Here, F is the maximum load applied (in N), l is the distance between the axes of the support rollers (in mm) and b and d are the width and depth of the specimen (in mm). The flexural tensile strength is obtained assuming a linear stress distribution at failure, as yielded by the linear elastic beam theory. However, such distribution is clearly non-linear and is significantly influenced by the fracture energy of the material. If the fracture energy

is zero, failure occurs once the extreme fibre reaches the tensile strength and the ultimate moment is the moment obtained assuming a linear stress distribution. But for very high fracture energy values, the ultimate moment can be magnified by a factor of three due to stress redistribution, see Lourenço (1997) for a numerical assessment. An experimental comparison between the tensile and flexural strengths of masonry prisms was carried out by Van der Pluijm (1999). Values of 1.5 and 1.2 were found for the ratio between the flexural strength and the tensile strength for clay units with a general purpose mortar and for calcium silicate blocks with thin mortar joints, respectively. In general, a factor of 1.5 can be assumed. Another important aspect is the height of the specimen. In fact, the influence of the post-peak behaviour of the material in the flexural response of the specimen diminishes with increasing height.

A testing machine METRO COM PFI 0.25 with a maximum capacity of 25 *kN* was used for the flexural tests and a testing machine METRO COM PMP 25 with a maximum capacity of 250 *kN* was used for the compression tests, see Figure 5.11. Table 5.5 gives the average results obtained for the flexural strength f_f and for the compressive strength f_c. In addition, the number of specimens tested n and the coefficient of variation CV are also indicated. The complete results are given in Annex B.2. The results found yield average values for the flexural and compressive strengths during the testing period (75 to 172 days) of 2.2 N/mm^2 and 10.3 N/mm^2, respectively. An increase of 15% for the flexural strength and of 20% for the compressive strength was found since the beginning of the tests until its completion.

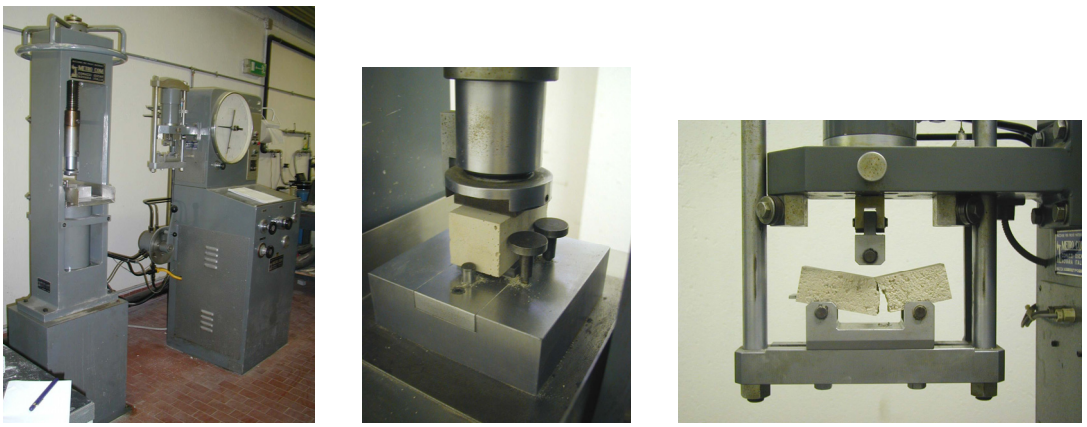

(a) (b) (c)

Figure 5.11 – Test setup for the compressive and flexural tests on mortar specimens: (a) testing machine, (b) detail of the compressive test setup and (c) detail of the flexural test setup.

Table 5.5 – Average results obtained from the flexural and compression tests on mortar specimens (values in brackets give the *CV*).

Curing time	*n*		f_f	f_c
days	flexion	compression	N/mm^2	N/mm^2
28	6	12	1.5 (6%)	7.4 (3%)
75	6	12	1.9 (13%)	9.2 (6%)
90	6	12	2.3 (10%)	9.7 (7%)
172	6	12	2.2 (9%)	11.2 (5%)

5.1.2 Sonic characterization of the wallets

Sonic tests have been carried out on the wallets aiming at an overall characterization of the composite material. Sonic tests refer to the transmission and reflection of mechanical stress waves through a medium at sonic frequencies. The method is based on the generation of an elastic wave resorting to a force hammer and on its reception with an accelerometer. In the present tests, the direct transmission procedure was adopted, which consists in placing the transmitter and the receiver in directly opposite positions. From the resulting wave velocity, an evaluation in terms of material uniformity, presence of voids and cracks, and compressive strength can be made. In general, a higher velocity corresponds to a better quality and homogeneous material. Further insight on this subject can be found in Binda *et al.* (2003b) and McCann and Forde (2001).

The equipment used to carry out the tests was a transmitter (hammer) DYTRAN 5801A5, a receiver (accelerometer) BRUEL & KJAER 4370 and an oscilloscope PANASONIC VP7510A. The average sonic velocity V_s and coefficient of variation *CV* are given in Table 5.6 for wallets with straight collar joints and in Table 5.7 for wallets with keyed collar joints. The results are grouped according to the testing locations, see Figure 5.12.

Table 5.6 – Average sonic velocities for wallets with straight collar joints.

Direction	Propagation medium	Testing locations	*Noto* wallets		*Serena* wallets	
			V_s [*m/s*]	*CV* [%]	V_s [*m/s*]	*CV* [%]
A – C	outer-inner-outer-leaves	1 to 8	2305.7	8.9	2269.3	22.7
B – D	outer-leaf	9,11,15,17	2271.0	14.4	2730.7	8.7
B – D	outer-leaf	12,14,18,20	2301.0	14.0	2307.5	12.3
B – D	inner-leaf	10,13,16,19	2248.6	15.8	1835.0	14.7

Table 5.7 – Average sonic velocities for wallets with keyed collar joints.

Direction	Propagation medium	Testing locations	*Noto* wallets		*Serena* wallets	
			Vs [*m/s*]	*CV* [%]	*Vs* [*m/s*]	*CV* [%]
A – C	outer-inner-outer-leaves	1,2,5,6	2219.0	11.6	2235.2	9.9
A – C	outer-inner-outer-leaves	3,4,7,8	2168.4	8.7	2390.2	5.6
B – D	outer-leaf	9,11,15,17	2302.1	12.8	3082.1	8.3
B – D	outer-leaf	12,14,18,20	2078.9	13.0	2527.0	14.6
B – D	inner-leaf	10,13,16,19	2415.9	25.0	1968.5	21.4

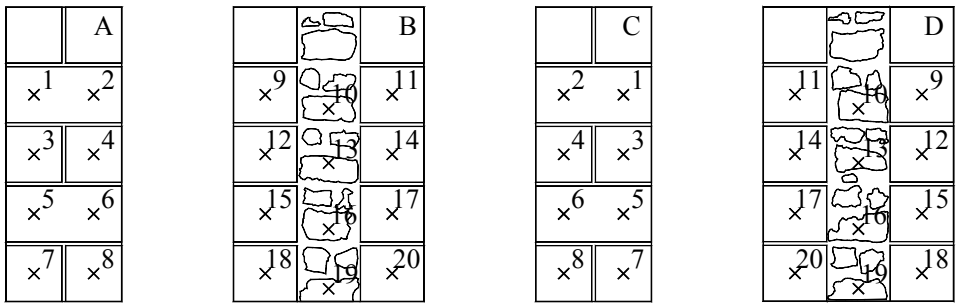

(a)

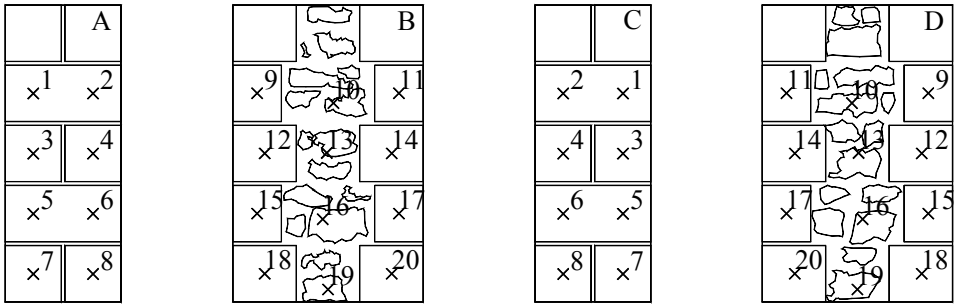

(b)

Figure 5.12 – Testing locations for the wallets: (a) with straight collar joints and (b) with keyed collar joints.

Some relevant remarks are as follows:

a) The sonic velocities between the outer and inner *Noto* leaves are very similar.

b) The sonic velocities in the outer-leaves of the *Serena* wallets are much larger than in the inner-leaves. The sonic velocity across the three leaves is in between the velocity in the outer and inner-leaves.

c) In the *Noto* wallets with keyed collar joints, the velocities in the courses with indentations are similar to the ones without.

d) In the case of the *Serena* wallets with keyed collar joints the velocities in the courses with indentations are slightly larger than in the ones without.
e) Confronting the velocities across the external leaves between courses with and without the vertical joints, it is possible to verify that the *Serena* wallets exhibit a much larger difference than the *Noto* wallets, meaning that the adhesion stone-mortar is much weaker. Here, it is noted that the high porosity of the *Noto* stone increases the penetration of the mortar in the stone.

5.1.3 Experimental setup

The tests on the wallets have been performed in a uniaxial testing machine MTS® 311.01.00 with non-rotating loading plates and a maximum capacity of 2500 *kN*. All the tests have been carried out under displacement control so that the softening behaviour of the wallets could be followed. A displacement rate of 1 $\mu m/s$ was adopted. Teflon sheets have been placed between the wallets and the loading plates to minimize restraining frictional stresses. For a discussion on the influence of different loading plates in compression tests the reader is referred to Vonk (1993).

A different test-setup was adopted according to the type of test: shear, compression of single leaves and compression of full wallets. The shear tests were performed using the setup illustrated in Figure 5.13. The adopted configuration is similar to the one described in EN 1052-3 (CEN, 2002). The tests were carried out in the absence of normal confining load.

After the shear tests, the resulting separated leaves from the wallets with straight collar joints remained practically undamaged and were tested in compression. The outer-leaves from the *Noto* wallets were tested simultaneously and the upper loading plates had simply to be displaced from the centre of the wallet to the edges. Afterwards, the outer-leaves were removed and the inner-leaf was tested individually, see Figure 5.14a. On the contrary, the outer-leaves of the *Serena* wallets had to be tested individually due to the much higher strength. In this case, after the shear tests, the leaves had to be removed from the testing machine and then, individually, placed again on the machine, see Figure 5.14b. The test setup for the compression tests on full wallets is shown in Figure 5.15.

Deformations in the wallets were recorded with up to 14 displacement transducers GEFRAN PY2-10 (10 *mm* range). The bases of the transducers were fixed in the

specimens by metallic bolts. In addition, displacements were also measured with the internal displacement transducer of the actuator.

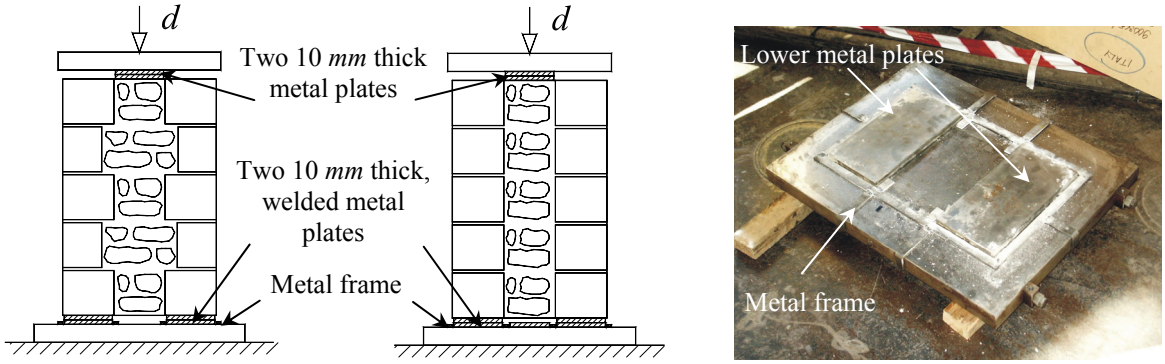

Figure 5.13 – Test setup for the shear tests: (a) wallets with straight collar joints, (b) wallets with keyed collar joints and (c) metal frame used to fix the lower metal plates.

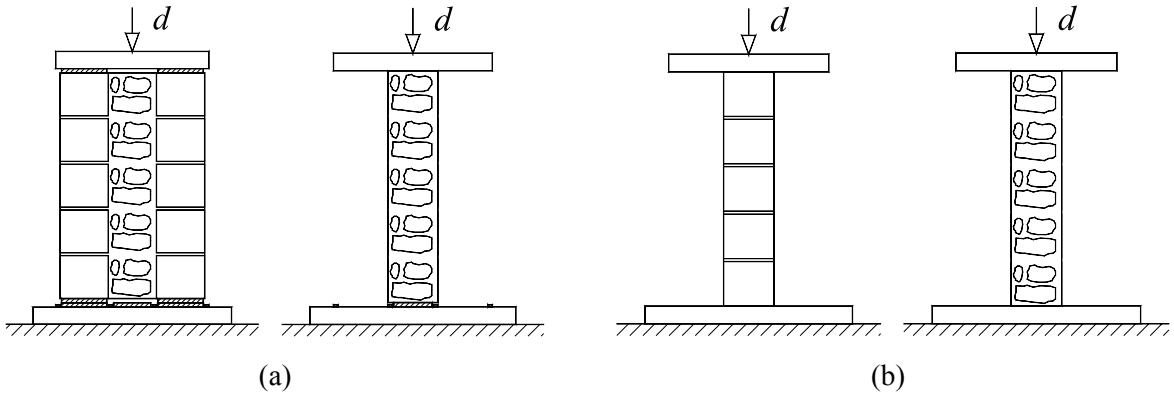

Figure 5.14 – Test setup for the compression tests on single leaves: (a) *Noto* wallets and (b) *Serena* wallets.

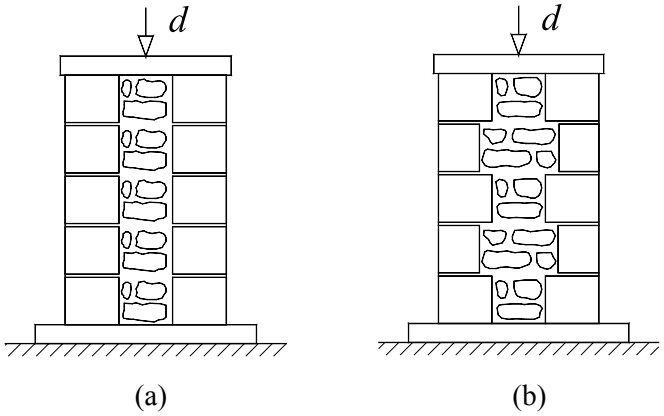

Figure 5.15 – Test setup for the compression tests on full wallets: (a) straight collar joints and (b) keyed collar joints.

For transport purposes and placement on the testing plate, the wallets were previously confined using two wooden plates and a metal frame, see Figure 5.16a. The wooden plates were covered by a layer of a rubber-type material and a sheet of sandpaper. Once on top of the testing plate, the wallets were grasped and moved to the testing machine using a laboratory crane, see Figure 5.16b,c.

(a)

(b)

(c)

Figure 5.16 – Transportation of the wallets: (a) positioning on top of the testing plate, (b) transportation and (c) placement on the testing machine.

5.1.4 Results of shear tests

Two wallets for each combination type of stone - type of connection were tested in a total of eight specimens. The load-displacement diagrams obtained with the internal actuator transducer are illustrated in Figure 5.17. In the case of the wallets with straight collar joints, a non-symmetric response of the connections was found, with failure occurring non-simultaneously. Such behaviour had also been found by Binda *et al.* (1993), Mirabella

Roberti *et al.* (1998) and Lourenço *et al.* (2004), and must be considered characteristic of the triplet test.

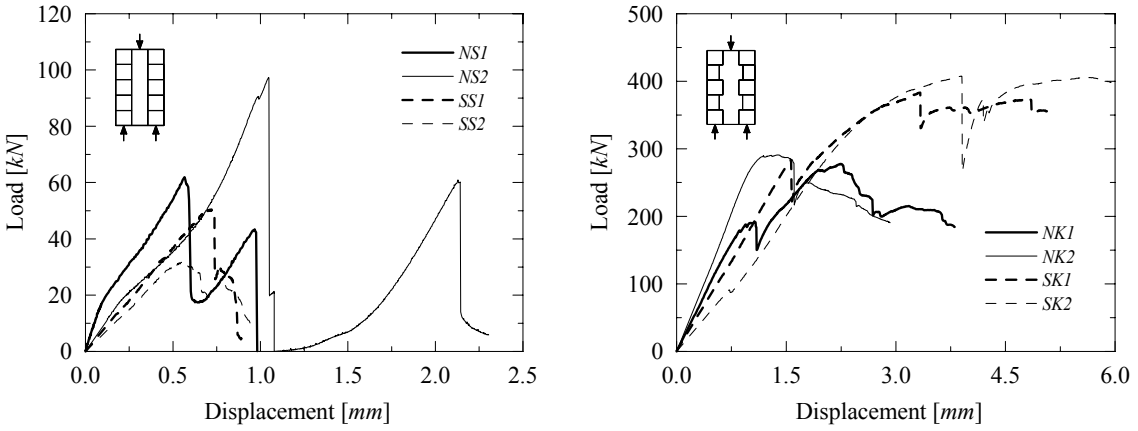

Figure 5.17 – Load-displacement diagrams obtained for the shear tests with the internal actuator transducer: (a) straight collar joints and (b) keyed collar joints.

The first peak in the diagrams of Figure 5.17a corresponds to the failure of the weakest connection and provides the shear strength τ_r for a shear area of $2 \times 310 \times 790\ mm^2$. After failure of the first connection a minor rotation of the two leaves still connected was observed due to the eccentricity of the applied load. From that point on the test cannot be intended as a triplet test due to the change in the loading scheme and, therefore, the values related to the second connection to fail should be considered carefully. Namely, the second peak represents the combination of a higher shear strength for the second joint and some minor friction in the first joint due to bending. If the effect of bending is neglected, the second peak provides the shear strength of the strongest joint τ_r', for a shear area of $310 \times 790\ mm^2$. This holds true only because no confining pressure is present.

For the wallets with keyed collar joints, the shear strength was calculated assuming straight connections and, thus, the value represents an "equivalent" shear strength. Table 5.8, Table 5.9 and Table 5.10 give the results obtained. In the case of straight collar joints wallets, the average shear strengths (τ_r and τ_r') and displacements (δ and δ') corresponding to the first and second load peaks are presented. For keyed collar joints wallets, the average values of the shear strength and the corresponding displacements are given.

Table 5.8 – Results of the shear tests for wallets with straight collar joints.

Wallet	Type of stone	First load peak	τ_r	δ	Second load peak	τ_r'	δ'
		kN	*N/mm²*	*mm*	*kN*	*N/mm²*	*mm*
NS1	*Noto*	61.9	0.13	0.57	43.4	0.18	0.97
NS2	*Noto*	97.4	0.20	1.05	61.0	0.25	2.13
SS1	*Serena*	50.4	0.10	0.72	29.4	0.12	0.77
SS2	*Serena*	31.7	0.07	0.55	24.7	0.10	0.79

Table 5.9 – Results of the shear tests for wallets with keyed collar joints.

Wallet	Type of stone	Peak load	τ_r	δ
		kN	*N/mm²*	*mm*
NK1	*Noto*	277.7	0.57	2.24
NK2	*Noto*	291.1	0.59	1.40
SK1	*Serena*	383.3	0.78	3.33
SK2	*Serena*	407.6	0.83	3.91

Table 5.10 – Average results obtained from the shear tests.

Wallet	Type of stone	Type of connection	τ_r	δ	τ_r'	δ'
			N/mm²	*mm*	*N/mm²*	*mm*
NS1, *NS2*	*Noto*	Straight	0.17	0.81	0.22	1.55
SS1, *SS2*	*Serena*	Straight	0.09	0.64	0.11	0.78
NK1, *NK2*	*Noto*	Keyed	0.58	1.82	-	-
SK1, *SK2*	*Serena*	Keyed	0.81	3.62	-	-

From the results obtained it is possible to observe that while the shear strength of straight collar joints wallets is mainly influenced by the physical properties of the stone, as the porosity that is closely related to the stone-mortar adhesion, in the case of keyed collar joints wallets, the strength of the stone is of major significance.

In terms of ductility, the specimens with straight collar joints show a similar behaviour for both types of stones. The failure is quite brittle and without showing any residual strength, given that the test setup allows the wallets to move freely outwards. Regarding the wallets with keyed collar joints, the *Serena* specimens exhibit a less brittle behaviour than the *Noto* specimens.

Further insight on the wallets behaviour can be obtained from the diagrams of the transducers fixed in the faces of the specimens. An appreciation of only the most salient features is given in here but the complete load-displacement diagrams are illustrated in

Annex B.3. Transducers lengths are given in Annex B.8. It is noted that given the novel nature of the tests conducted, improvements in the transducers position were made during the tests and, thus, the position of the transducers is not the same for all wallets. Relative shear displacements at the connections have been evaluated by positioning "short" transducers (*T3*, *T5*, *T10* and *T11*) and "long" transducers (*T4* and *T12*) as illustrated in Figure 5.18. Failure of the connections in the *Noto* wallets occurred in a quite brittle manner as can be verified by the behaviour of the "short" transducers, which show zero values until near the peak load, see *T10* and *T11* in Figure 5.19a. However, it can still be observed that the connection does not fail all at once but that the crack rapidly develops from the top (*T11*) to the bottom (*T10*).

The "long" transducers behave in a quite different manner, showing increasing shortening until initiation of the shear cracks, with subsequent inversion of the trend and sudden elongation, see *T4* in Figure 5.19a. Such behaviour can be explained by the fact that "long" transducers are not only measuring shear slippage at the connection but are also influenced by the deformation of the leaves.

On the contrary, *Serena* wallets with straight collar joints show a progressive development of the shear cracks since an early stage, yielding a less brittle failure than the *Noto* wallets. This behaviour is confirmed by the diagrams of the "short" transducers *T3* and *T5* shown in Figure 5.19b. This different behaviour can be explained by the weak adhesion between the *Serena* stone and the mortar.

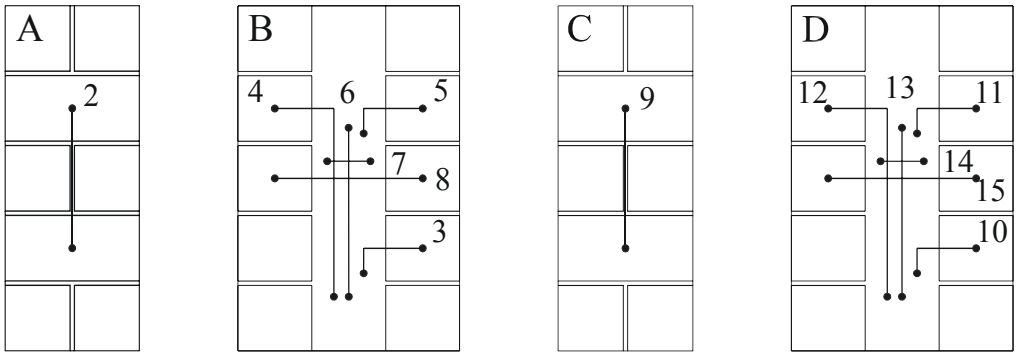

Figure 5.18 – Position of the transducers for wallets *NS2* and *SS2*.

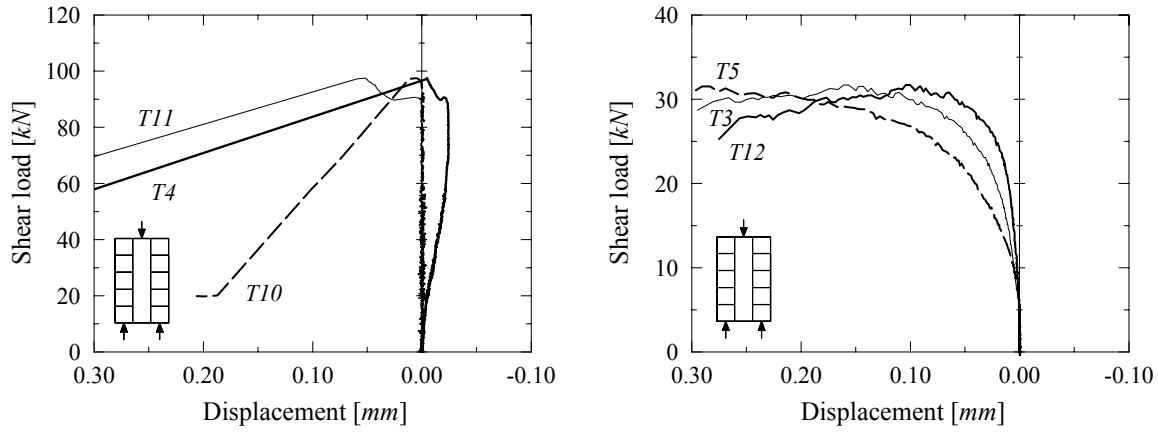

Figure 5.19 – Load-displacement diagrams for wallets with straight collar joints: (a) *Noto* specimen (*NS2*) and (b) *Serena* specimen (*SS2*). Positive sign is adopted for elongation and negative for contraction.

Regarding the wallets with keyed collar joints it can be observed that the transducers positioned in the outer-leaves above the central indentation (*T10* and *T12* in Figure 5.20) exhibit, initially, an increasing shortening as expected. However, after a determined load level the transducers start to show an elongation, see Figure 5.21. Such behaviour can be attributed to the fact that the two upper courses of the wallets are being pushed outwards by the applied load. It can also be observed that the transducers positioned in the inner-leaf above the central indentation (*T11*) show larger deformations than the correspondent transducers below them (*T14*). This can be observed in a rather clear manner up to a certain load level, before transducers become disturbed by the appearance of cracks. Such behaviour results from the load transfer between inner and outer-leaves. This process cannot be observed so clearly in the outer-leaves, partly due to the complex behaviour of transducers *T10* and *T12*, as explained above.

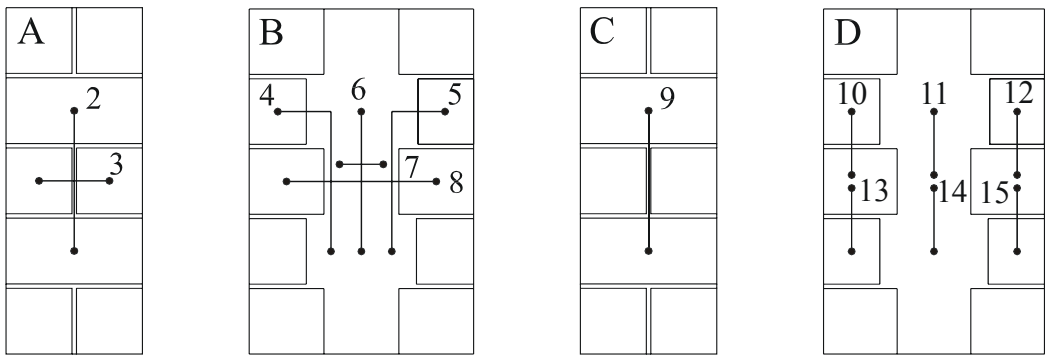

Figure 5.20 – Position of the transducers for wallets *NK1*, *NK2*, *SK1* and *SK2*.

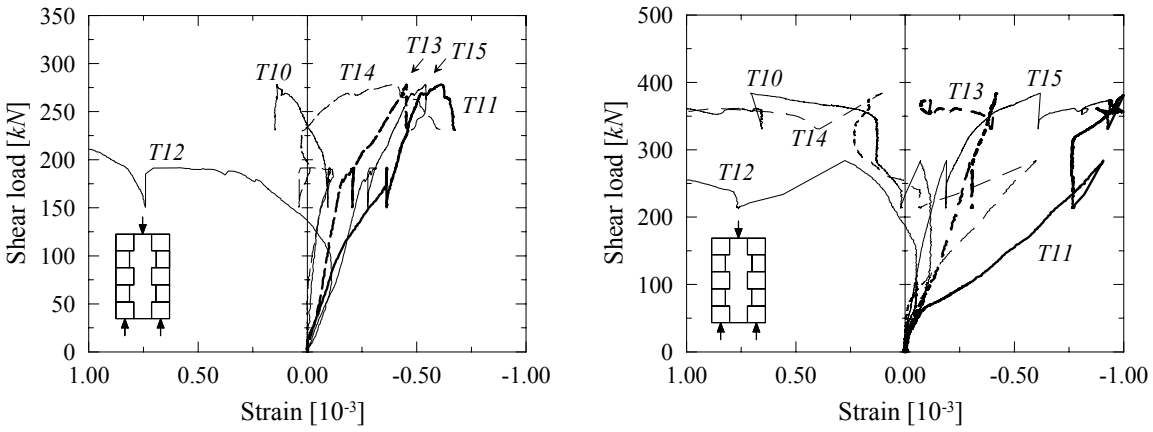

Figure 5.21 – Load-displacement diagrams for wallets with keyed collar joints: (a) *Noto* specimen (*NK1*) and (b) *Serena* specimen (*SK1*). Positive sign is adopted for elongation and negative for contraction.

Typical ultimate crack patterns are illustrated in Figure 5.22. The crack patterns for all the specimens and along three different stages: first appeared cracks, at peak load and the final crack pattern are shown in Annex B.4. Wallets *NK1* and *NK2* were showing some thin cracks prior to testing and, in these two cases, also the crack patterns at the beginning of the test are shown in Annex B.4.

Straight collar joints wallets failed due to the development of two vertical shear cracks along the connections. No other visible damage was observed at the end of the test. In the case of the specimens with keyed collar joints, the cracking pattern was different according to the type of stone. For the *Noto* specimens, damage was observed in both outer and inner-leaves. In the inner-leaves, more severely damaged, diagonal cracks were observed, developing from the shear keys and passing through the inner-leaf stones. Concerning the outer-leaves, diagonal cracks near the base appeared. At ultimate stage, full separation in three irregular leaves could be observed.

In the *Serena* specimens, the cracks developed only in the inner-leaf. However, in this case, cracks usually went around the stones instead of breaking them, due to the larger strength and smaller stone-mortar adhesion. At ultimate stage, it is clearer to observe that only the inner-leaf collapsed.

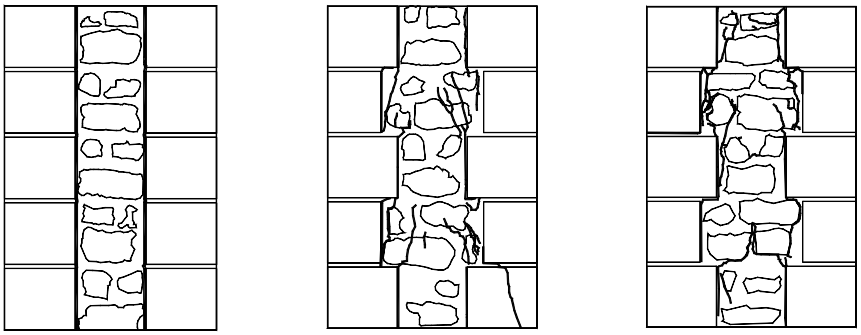

(a) (b) (c)

Figure 5.22 – Typical ultimate crack patterns for (a) straight collar joints wallets (*NS1*) and keyed collar joints wallets: (b) *Noto* (*NK1*) and (c) *Serena* (*SK2*).

5.1.5 Results of compression tests on single leaves

Compression tests were performed on the single leaves of the wallets with straight collar joints, previously tested in shear, see Section 5.1.4. In the case of the *Noto* specimens, both outer-leaves were tested simultaneously, trying to reproduce what may happen in real composite walls: shear failure of the connections followed by transfer of almost all the load to the external stiffer elements. This can explain the type of damage found in massive pillars, see Binda *et al.* (2003a). In the case of the *Serena* leaves, which were much more resistant, the same procedure could not be adopted due to the limited capacity of the testing machine and, thus, the leaves had to be tested separately. The specimens were unloaded after reaching approximately 70% of f_c in the post-peak regime.

A comparison between the stress-strain diagrams obtained for the outer and inner-leaves is shown in Figure 5.23. The results obtained, including the strength f_c, the peak strain ε_p, the elastic modulus E and the Poisson coefficient ν are given in Table 5.11 and Table 5.12. From the given results it is observed that the *Noto* outer-leaves exhibit a strength of about 45% the stone strength and the inner-leaf about 20%. In the case of the *Serena* leaves, the same ratios are about 40% for the outer-leaves and only 4% for the inner-leaf, which stresses the major influence of the mortar in the inner-leaf failure. Another interesting aspect is that the ratio between the strength of the *Serena* and *Noto* stones, which is approximately equal to five, is similar to the ratio between the strength of the outer-leaves but the same is not true for the inner-leaves, which exhibit practically equal strengths. It is further noted that the *Serena* inner-leaves exhibit a less brittle behaviour than the *Noto* specimens, again due to the higher strength of the stones, forcing cracks to go around them instead of passing through.

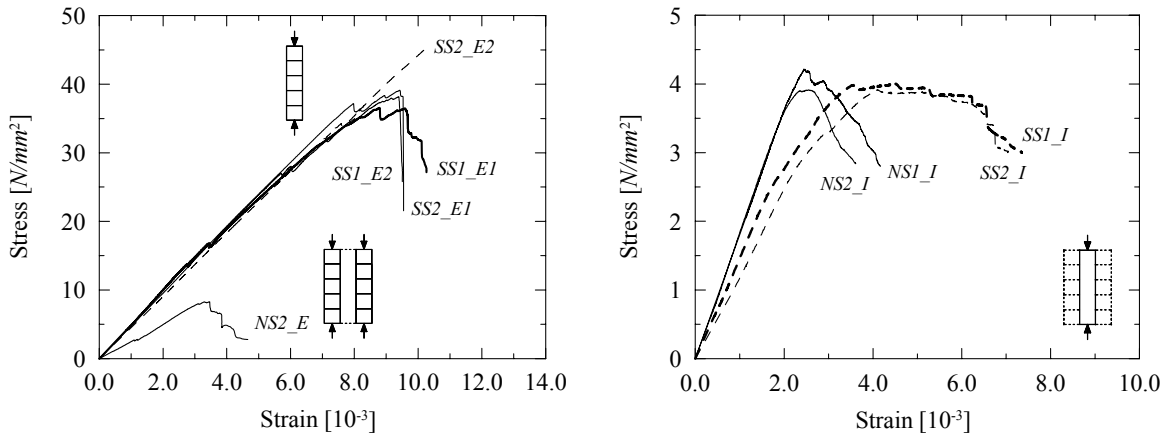

Figure 5.23 – Stress-strain diagrams obtained from compression tests on single leaves using the internal actuator transducer: (a) outer-leaves and (b) inner-leaves. A problem in the acquisition system prevented fully capturing the *NS1_E* diagram and, thus, it is not shown. It is also noted that failure of specimen *SS2_E2* could not be attained within the capacity of the testing machine.

Table 5.11 – Results obtained from the compression tests on single leaves.

Specimen	Peak load	f_c	Peak disp.	ε_p	E	ν
	kN	*N/mm²*	*mm*	10^{-3}	*N/mm²*	-
NS1_E (both)	950.6	9.0	-	-	3680	-
NS2_E (both)	874.1	8.3	2.71	3.3	2615	-
SS1_E1	1925.7	36.5	7.22	8.8	5145	-
SS1_E2	2011.1	38.2	7.71	9.4	4965	-
SS2_E1	2061.4	39.1	7.71	9.4	4825	-
SS2_E2	> 2380.0	> 45.2	> 8.53	> 10.4	4540	-
NS1_I	222.1	4.2	2.01	2.5	1805	0.10
NS2_I	206.3	3.9	2.13	2.6	1850	0.20
SS1_I	211.0	4.0	3.69	4.5	1515	0.17
SS2_I	206.5	3.9	3.36	4.1	1295	0.18

Table 5.12 – Average results.

Specimen	Type of stone	Type of leaf	Peak load	f_c	ε_p	E	ν
			kN	*N/mm²*	10^{-3}	*N/mm²*	-
NS_E	*Noto*	outer (both)	912	8.7	3.3 (1)	3150	-
SS_E	*Serena*	outer (each)	2095	39.8	9.5	4870	-
NS_I	*Noto*	inner	214	4.1	2.6	1830	0.15
SS_I	*Serena*	inner	209	4.0	4.3	1405	0.18

(1) Results from a single value.

Figure 5.25 to Figure 5.27 illustrate selected stress-strain diagrams obtained from the displacement transducers fixed to the specimens as well as their position. The complete set of stress-strain diagrams is given in Annex B.5. Transducers lengths are given in Annex B.8. As can be observed, the diagrams of the outer-leaves are much more disturbed by the development of cracks than the diagrams of the inner-leaves and a conclusion can be hardly drawn from the collected data.

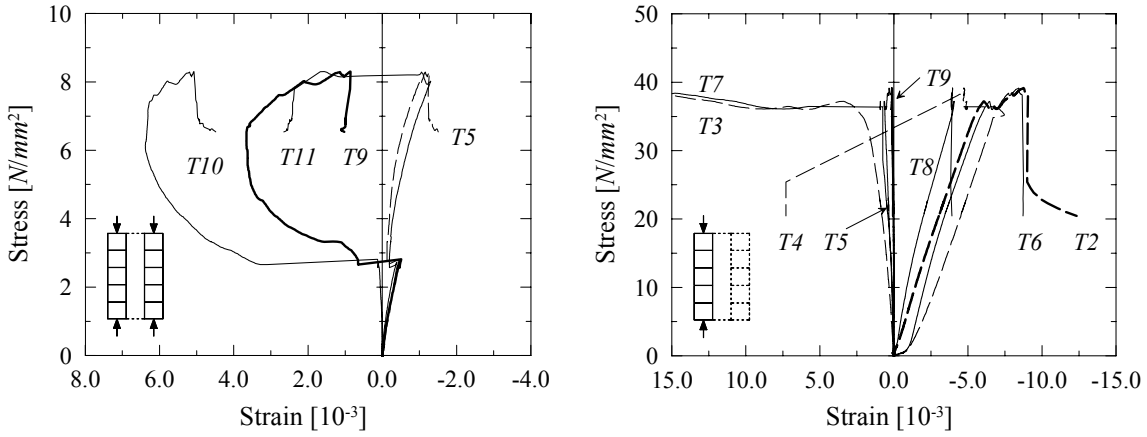

(a) (b)

Figure 5.24 – Stress-strain diagrams obtained from compression tests on outer-leaves using the displacement transducers attached to the specimens: (a) *NS2_E* and (b) *SS2_E1*. Positive sign is adopted for elongation and negative for contraction.

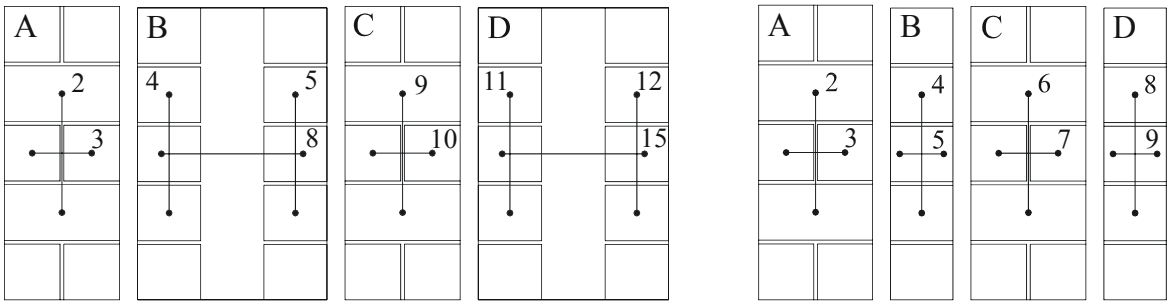

(a) (b)

Figure 5.25 – Position of the transducers for (a) *NS2_E* and (b) *SS2_E1*.

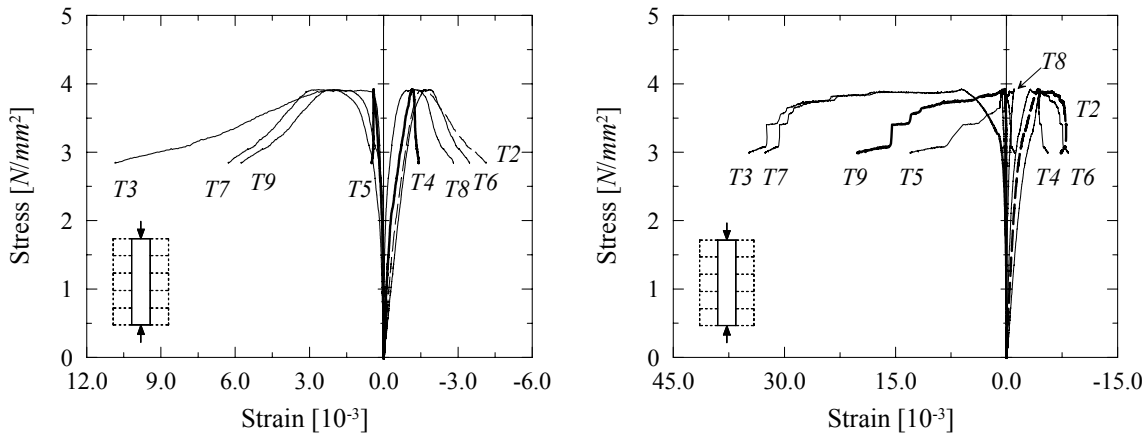

Figure 5.26 – Stress-strain diagrams obtained from compression tests on inner-leaves using the displacement transducers attached to the specimens: (a) *NS2_I* and (b) *SS2_I*. Positive sign is adopted for elongation and negative for contraction.

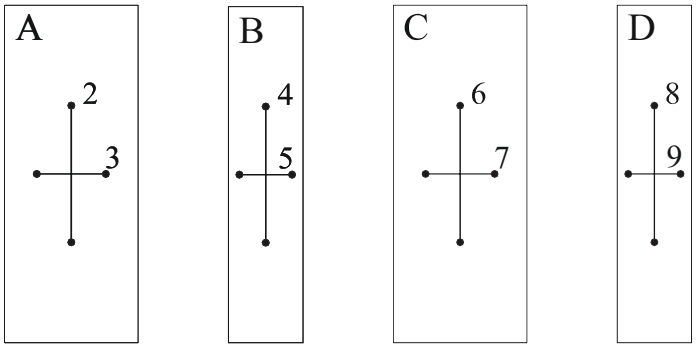

Figure 5.27 – Position of the transducers for (a) *NS2_I* and (b) *SS2_I*.

The volume change of a specimen under increasing compressive loading is usually measured in terms of its volumetric strain ε_{vol}, defined as $\varepsilon_{vol} = \varepsilon_1 + \varepsilon_2 + \varepsilon_3$. Here, ε_1 is the longitudinal strain and ε_2 and ε_3 are the transversal strains. At low load levels, the volume of quasi-brittle specimens decreases and, at high stresses, the volume starts to increase due to progressive crack growth. The volumetric strain is illustrated in Figure 5.28 for the inner-leaf specimens *NS2_I* and *SS2_I*. The minimum volume was found for values of approximately 70 to 80% of the peak load with a fast volume increase (dilatancy) after the peak. A similar behaviour is exhibited by concrete and the reader is referred *e.g.* to Van Mier (1997).

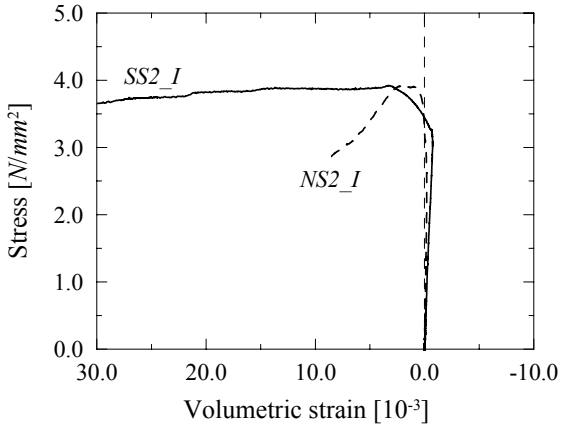

Figure 5.28 – Stress-volumetric strain diagrams for inner-leaf specimens *NS2_I* and *SS2_I*.

Typical failure patterns are depicted in Figure 5.29 and Figure 5.30 for the outer and for the inner-leaves, respectively. The shaded areas indicate spalling of the stone. The crack patterns for all specimens along three different stages: first cracks to appear, at peak load and the final crack pattern are shown in Annex B.6. It can be observed that the outer-leaves fail due to the development of several vertical cracks and spalling mainly near the base and top of the specimens. In the faces without vertical joints, the cracks start to occur randomly, whereas in the faces with vertical joints cracks start to appear following the vertical joints. Concerning the inner-leaves, it is noted that failure is due to the development of vertical cracks that, in the case of the *Noto* specimens, cross through the stones while, in the case of the *Serena* specimens, mainly go around the stones due to the higher strength and lower adhesion stone-mortar.

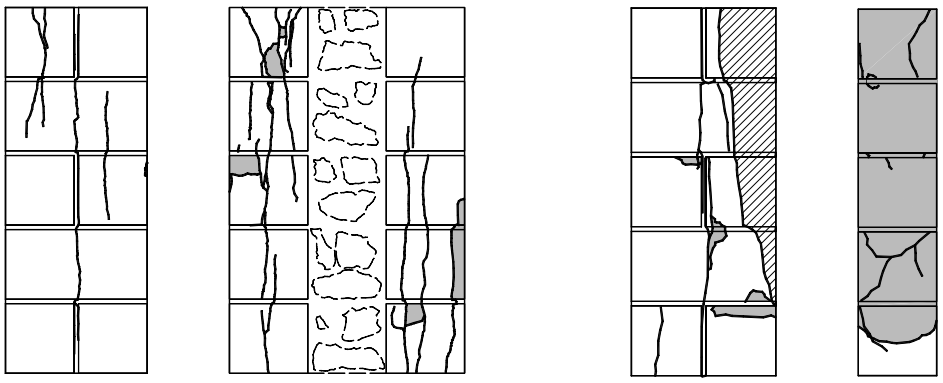

(a) (b)

Figure 5.29 – Typical ultimate failure patterns for the outer-leaves: (a) *Noto* stone and (b) *Serena* stone.

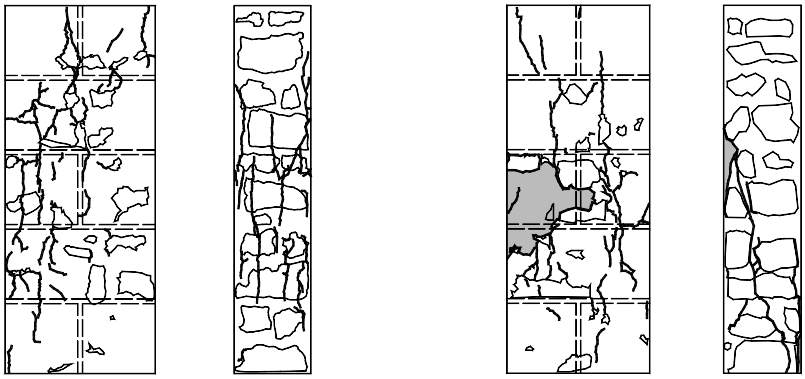

(a) (b)

Figure 5.30 – Typical ultimate failure patterns for the inner-leaves: (a) *Noto* stone and (b) *Serena* stone.

5.1.6 Results of compression tests on full wallets

One wallet of each type (stone/connection combination) was tested in compression, in a total of four specimens. However, the peak load for the *Serena* wallets was beyond the capacity of the testing machine and a maximum load of 2380 *kN* was applied. The *Noto* wallets have been unloaded after achieving approximately 60% of f_c in the post-peak regime. The stress-strain diagrams obtained with the internal actuator transducer are shown in Figure 5.31. Table 5.13 gives the results found.

The following observations can be made from the results, even if the limited number of tests precludes any conclusive statement:

a) The strength of the *Noto* wallet with keyed collar joints is about 10% higher than the wallet with straight collar joints.
b) The *Noto* wallet with keyed collar joints exhibits a less brittle behaviour than the wallet with straight collar joints.
c) The peak load of any of the two *Noto* wallets tested is not much higher than the peak load of the single outer-leaves (912.3 *kN*), although the cross-sectional areas are different and, hence, the strength.

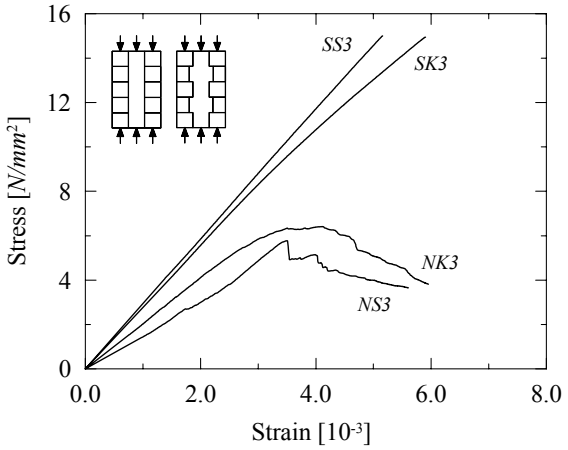

Figure 5.31 – Stress-strain diagrams obtained from compression tests on full wallets, using the internal actuator transducer.

Table 5.13 – Results obtained from the compression tests on full wallets.

Wallet	Type of stone	Type of connection	Peak load *kN*	f_c N/mm^2	ε_p 10^{-3}	E N/mm^2
NS3	*Noto*	straight	913	5.8	3.5	1770
SS3	*Serena*	straight	> 2380	> 15.1	> 5.2	2940
NK3	*Noto*	keyed	1013	6.4	4.1	2085
SK3	*Serena*	keyed	> 2380	> 15.1	> 5.9	2725

The stress-strain diagrams obtained with the transducers fixed to the specimens as well as the transducers position are shown in Figure 5.32 and Figure 5.33 for wallets with straight collar joints, and in Figure 5.34 and Figure 5.35 for wallets with keyed collar joints. Transducers lengths are given in Annex B.8. Larger vertical strains were found in the outer-leaves than in the inner-leaves for wallets with straight collar joints, see Figure 5.32. Such behaviour is not completely clear but can be attributed to bedding of the inner-leaf prior to testing, which prevented mobilization of the inner-leaf bearing capacity. On the contrary, in the case of wallets with keyed collar joints, vertical strains in the different leaves are rather similar, emphasising the role of shear keys in obtaining a uniform distribution of strains, see Figure 5.33.

Such behaviour can also be confirmed by comparing the horizontal deformation of the wallets (given by *T8* and *T15*) with the horizontal strain of the inner-leaves (*T5* and *T12* for straight collar joints wallets and *T9* and *T14* for keyed collar joints wallets), which shows that only in the case of keyed wallets the inner-leaf is deforming since the beginning of the test. Finally, it should be referred that transducers *T8* and *T15* on Figure 5.32b

exhibit an unexpected behaviour. This is probably due to a minor inclination of the outer-leaves prior to testing.

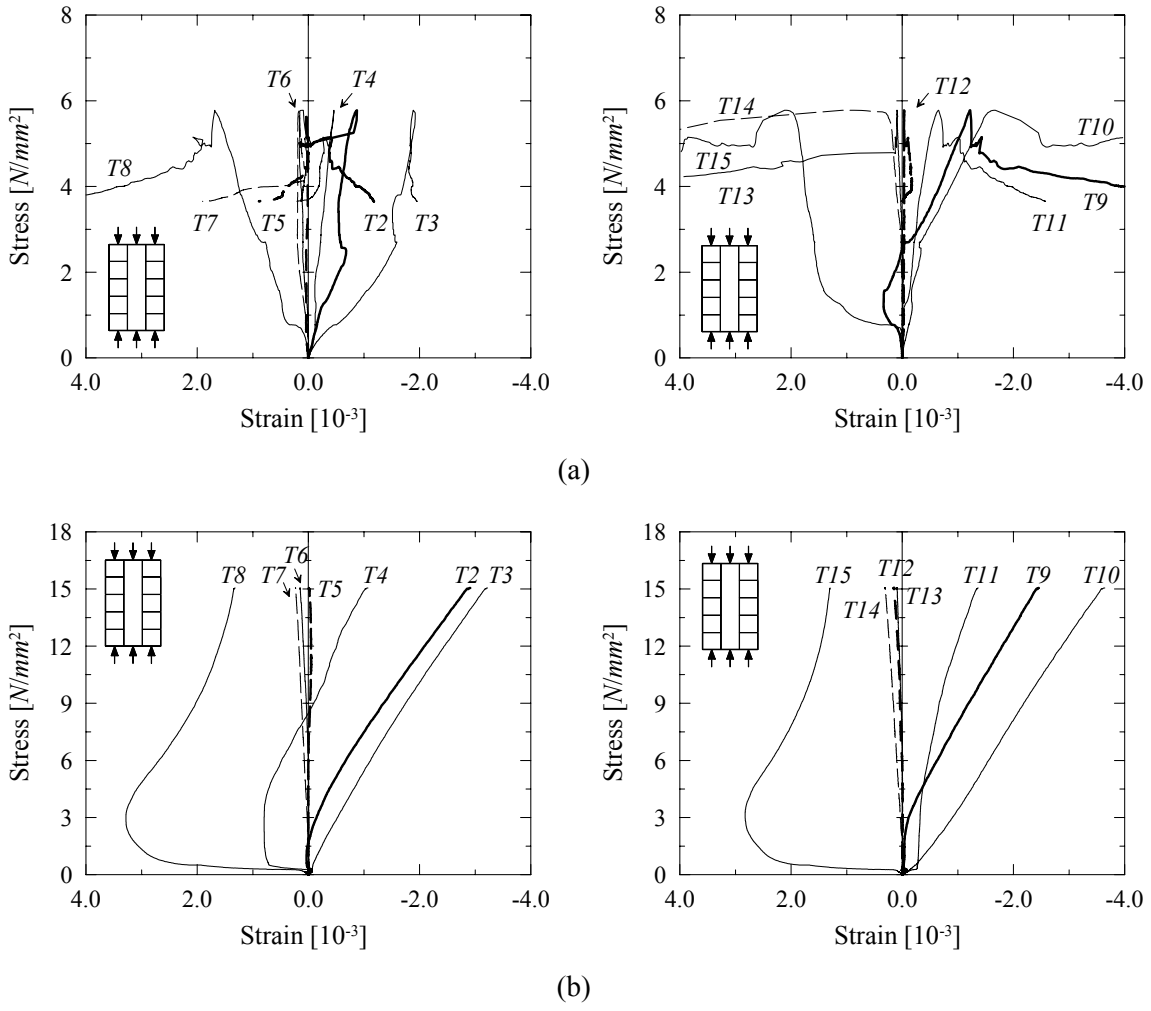

Figure 5.32 – Stress-strain diagrams for wallets with straight collar joints: (a) *Noto* (*NS3*) and (b) *Serena* (*SS3*). Positive sign is adopted for elongation and negative for contraction.

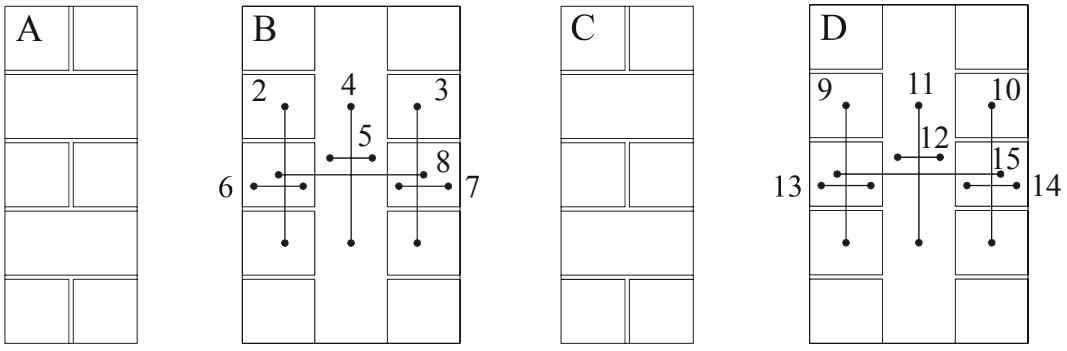

Figure 5.33 – Position of the transducers for wallets *NS3* and *SS3*.

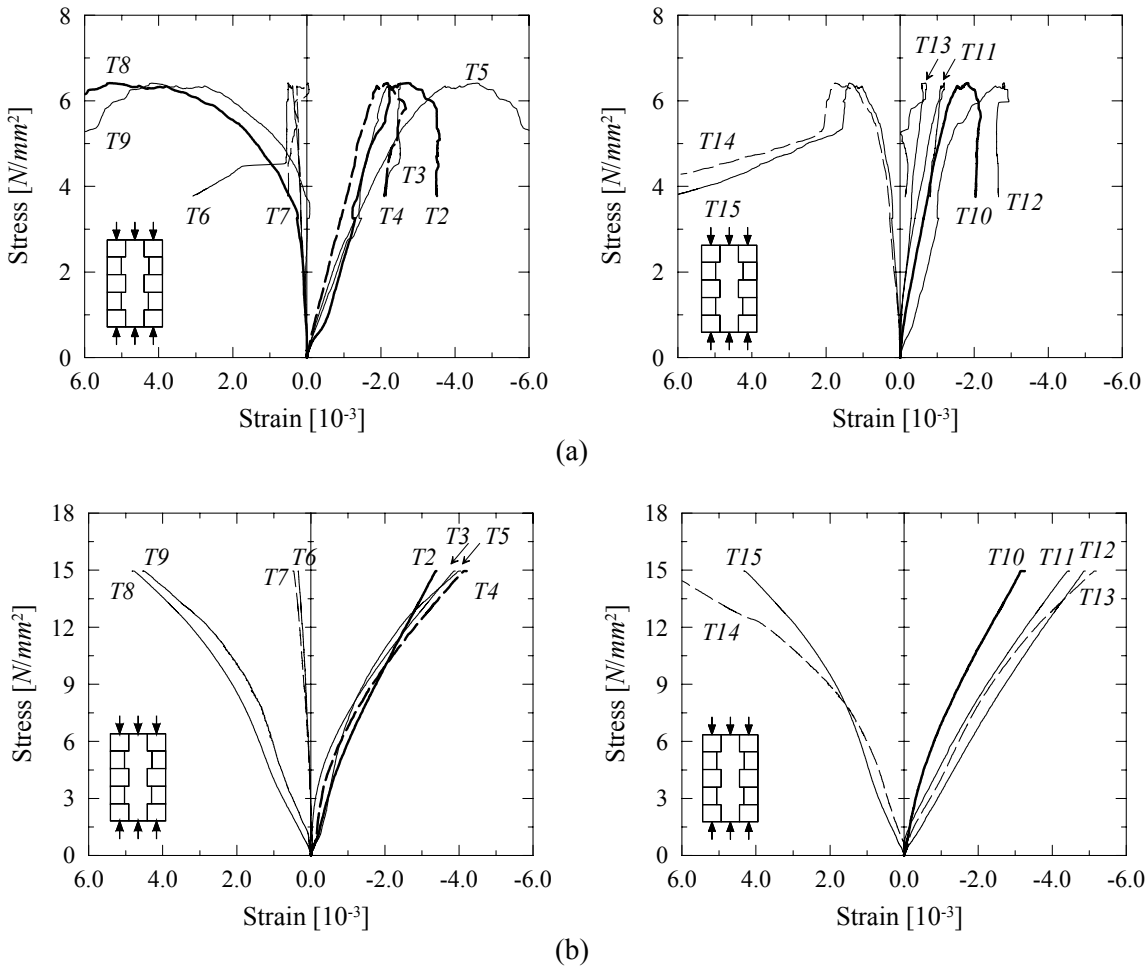

Figure 5.34 – Stress-strain diagrams for wallets with keyed collar joints: (a) *Noto* (*NK3*) and (b) *Serena* (*SK3*). Positive sign is adopted for elongation and negative for contraction.

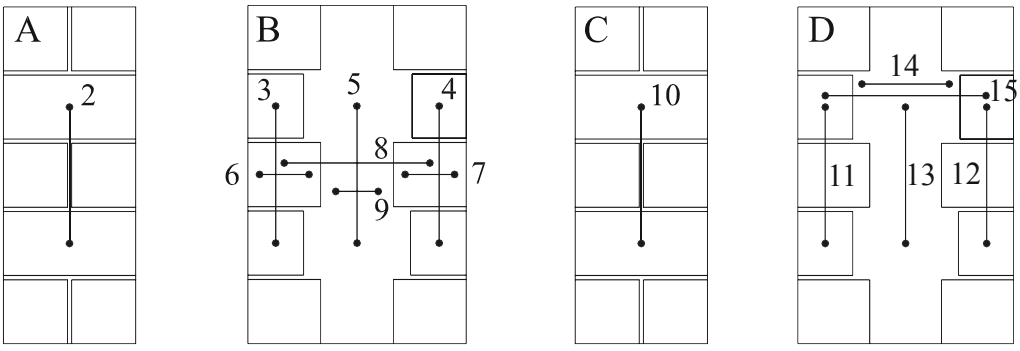

Figure 5.35 – Position of the transducers for wallets *NK3* and *SK3*.

Typical failure patterns are illustrated in Figure 5.36. The complete crack patterns for three different stages: first cracks to appear, at peak load and the final crack pattern are shown in Annex B.7. Shaded areas indicate spalling of the stone. The *Noto* wallet with straight connections failed due to the development of several vertical cracks in the outer-

leaves while the inner-leaf was practically undamaged. In the case of the *Noto* wallet with keyed connections, the outer-leaves exhibited a more severe and diffuse cracking pattern with several vertical cracks developing in the inner-leaf near the peak load. Regarding the *Serena* wallet with keyed connections and despite the fact that the peak load was not attained, the development of some cracks in the inner-leaf could be observed. Moreover, it is noted that cracks usually star to develop in the lateral faces of the wallets, in courses with single stones (no vertical joints).

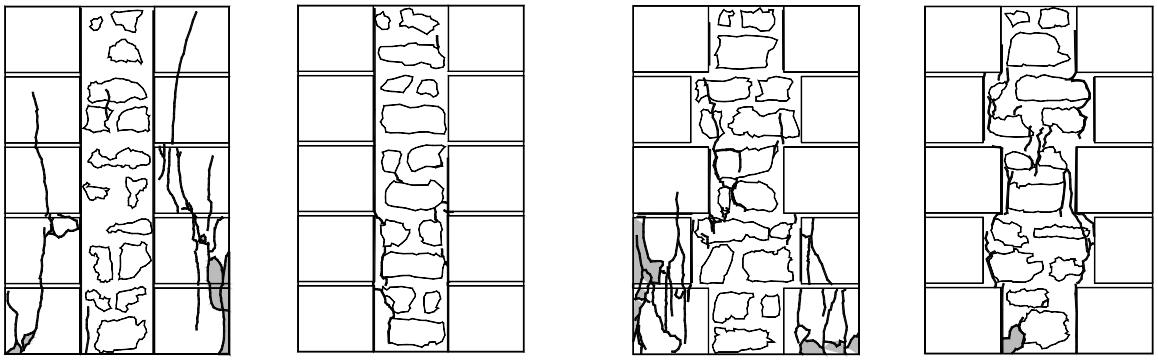

(a) (b) (c) (d)

Figure 5.36 – Failure patterns for wallets with straight collar joints: (a) *Noto* (*NS3*) and (b) *Serena* (*SS3*); and for wallets with keyed collar joints: (c) *Noto* (*NK3*) and (b) *Serena* (*SK3*).

5.2 Simplified calculations

This Section contains a first analytical interpretation of the experimental results, with simple calculations being used to predict the compressive strength of the wallets. It is noted that the experimental results found should be considered as indicative and conclusions should be taken carefully due to the small number of specimens.

The compressive strength of composite sections f_c can be estimated making use of the following equations, each one assuming different hypotheses:

a) the external load is completely supported by the stiffer elements, *i.e.*, the outer-leaves:

$$f_c = \frac{2\,t_e}{2\,t_e + t_i} \cdot f_e \tag{5.3}$$

b) the external load is supported by each leaf according to its cross-sectional area ratio:

$$f_c = \frac{2\,t_e}{2\,t_e + t_i} \cdot f_e + \frac{t_i}{2\,t_e + t_i} \cdot f_i \tag{5.4}$$

c) the external load is supported by each leaf according to its area ratio and adjusted by a correction factor, see Egermann and Neuwald-Burg (1994):

$$f_c = \frac{2\,t_e}{2\,t_e + t_i} \cdot \theta_e \cdot f_e + \frac{t_i}{2\,t_e + t_i} \cdot \theta_i \cdot f_i \tag{5.5}$$

In the above, t_e and t_i are the thicknesses of the outer and inner-leaves and f_e and f_i are the uniaxial compressive strengths of the outer and inner-leaves. The parameters θ_e and θ_i are correction factors for the outer and inner-leaves, assuming that the outer-leaves are under biaxial compressive stresses and bending moments and, thus, their uniaxial strength should be reduced and that the inner-leaf is under a multi-axial compressive state of stress and, therefore, its uniaxial strength should be increased.

The results obtained for the wallets with and without shear keys are given in Table 5.14. In the case of the wallets with keyed collar joints, the thickness assumed for the inner-leaf includes the length of the shear keys. With respect to the application of Eq. (5.5), the values adopted for the correction parameters were $\theta_e = 0.7$ and $\theta_i = 1.3$, Egermann and Neuwald-Burg (1994). It is further noted that Eq. (5.3) was not used to estimate the strength of the wallets with keyed joints because, in this case, it is clear that the inner-leaf is collaborating in the composite response.

Table 5.14 – Predicted compressive strength values for the tested wallets.

Wallet	Type of stone	Type of connection	Experimental f_c N/mm^2	Predicted f_c $[N/mm^2]$		
				Eq. (5.3)	Eq. (5.4)	Eq. (5.5)
NS3	*Noto*	straight	5.8	5.8	7.2	5.8
SS3	*Serena*	straight	> 15.1	25.3	26.6	19.4
NK3	*Noto*	keyed	6.4	-	6.4	5.7
SK3	*Serena*	keyed	> 15.1	-	21.3	16.1

The value predicted for the compressive strength of the wallets with straight collar joints using Eq. (5.3) and Eq. (5.5) show an excellent agreement with the experimental results. Note that, however, the fact that the experimental and the predicted values are exactly the same should be considered as just a coincidence. The stress-strain diagrams illustrated in Figure 5.37a show that the inner-leaf vertical deformations do not accompany the vertical deformations of the outer-leaves and that, at failure, the inner-leaf strain is significantly smaller than its peak strain when individually tested, see also Figure 5.38a. As a consequence, the bearing capacity of the inner-leaf is only partially mobilized and the hypothesis of Eq. (5.3) holds fairly true. The causes for the different deformations in the leaves are not completely clear but a possible reason may be attributed to settling of the inner-leaf prior to testing. It is noted that the stress values shown in Figure 5.37 represent average values obtained from the external load. Moreover, the deformation values were obtained from the transducers shown in Figure 5.33 for straight collar joints wallets (outer-leaf 1: *T2* and *T10*; outer-leaf 2: *T3* and *T9*; inner-leaf: *T4* and *T11*) and in Figure 5.35 for keyed collar joints wallets (outer-leaf 1: *T2*, *T3* and *T12*; outer-leaf 2: *T4*, *T10* and *T11*; inner-leaf: *T5* and *T13*). Concerning Figure 5.38, deformations were obtained from the compression tests on the single leaves and on the full wallets using the actuator in-built displacement transducer.

In the case of the wallets with keyed collar joints, Eq. (5.4) yielded the best result while the strength predicted by Eq. (5.5) is less than the experimental value for the *Noto* wallets. This indicates that the inner-leaf is collaborating in the wallets response, as confirmed by Figure 5.37b and Figure 5.38b, but the assumptions of a strength reduction of the outer-leaves due to bending and a strength increase of the inner-leaf due to confinement do not apply. This can be explained by the test boundary conditions, which allow horizontal displacements to occur at the top and bottom of the wallets. In such way, the effects of outer-leaves bending and inner-leaf confinement are diminished.

Finally, it should be noted that each equation considered independently predicts a larger strength for the wallets with straight collar joints than for the wallets with keyed collar joints. This is due to the reduction of the cross-sectional area of the outer-leaves in the case of the specimens with shear keys. However, the opposite behaviour was found in experiments. The reason of such behaviour can be attributed to the fact, as already mentioned, that the inner-leaf was almost not collaborating in the experimental response in the case of wallets with straight collar joints.

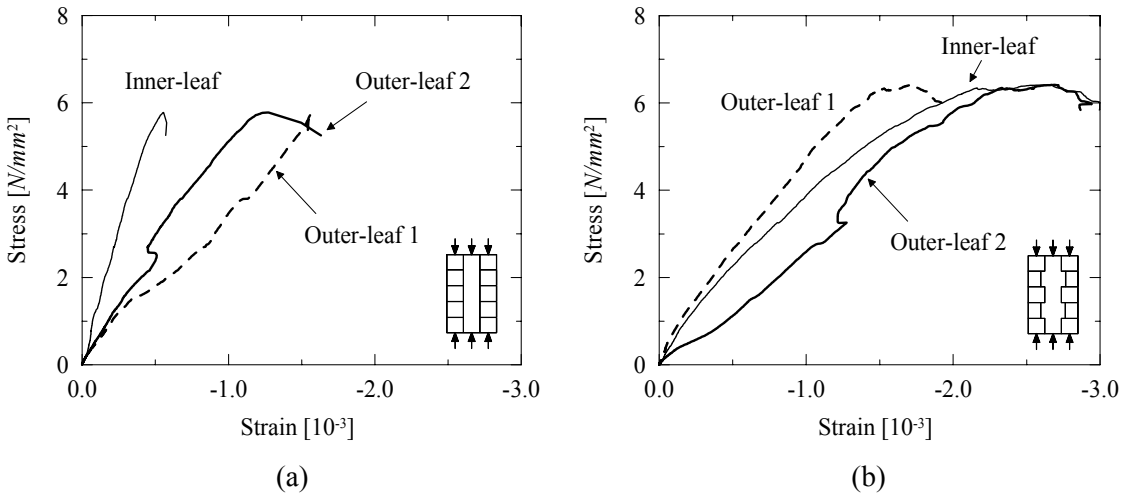

Figure 5.37 – Compression stress-strain diagrams of the leaves inside the composite *Noto* wallets: (a) straight collar joints (*NS3*) and (b) keyed collar joints (*NK3*).

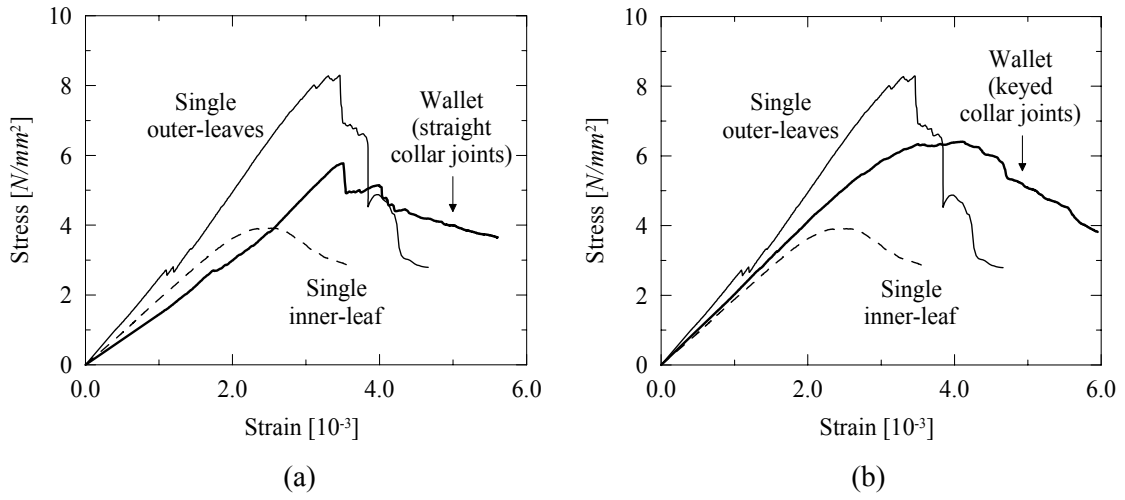

Figure 5.38 – Comparison between the compression stress-strain diagrams obtained from the single inner and outer-leaves and from the full wallets, built with the *Noto* stone: (a) straight collar joints (*NS3*) and (b) keyed collar joints (*NK3*).

5.3 Numerical simulations

This Section deals with the numerical simulation of the experimental tests, contributing to the results interpretation. The leaves of the wallets were represented using plane stress continuum elements (8-noded) with 2×2 Gauss integration while line interface elements (6-noded) with 3×3 Lobatto integration have been adopted for the collar joints. The analyses were carried out with indirect displacement control with line search. It is further noted that the self-weight of the wallets was not considered.

For the material behaviour, a composite plasticity model with a Drucker-Prager yield criterion in compression and a Rankine yield criterion in tension was adopted. The inelastic behaviour exhibits a parabolic hardening/softening diagram in compression and an exponential-type diagram in tension. The material behaves elastically up to one-third of the compressive strength and up to the tensile strength. For the interface elements a combined cracking-shearing-crushing model developed by Lourenço and Rots (1997) was adopted. The compressive mode was, however, not active and interface failure could only occur by shear or/and tensile yielding. Both shear and tensile modes exhibit exponential-type softening.

The elastic material properties adopted for the wallets leaves are given in Table 5.15 and the inelastic properties in Table 5.16. Here, E is the elastic modulus, ν is the Poisson coefficient, c is the cohesion, f_t is the tensile strength, ϕ is the friction angle, ψ is the dilatancy angle, Gf_c is the (cohesion related) compressive fracture energy and Gf_I is the tensile fracture energy.

Table 5.15 – Elastic properties for the wallets leaves.

Material	E N/mm^2	ν -
Outer-leaves	3150	0.10
Inner-leaf	2100	0.15

Table 5.16 – Inelastic properties for the wallets leaves.

Material	c N/mm^2	f_t N/mm^2	$\sin\phi$ -	$\sin\psi$ -	Gf_c[(a)] N/mm	Gf_I[(b)] N/mm
Outer-leaves	3.7	1.8	0.17	0.09	5.0	0.070
Inner-leaf	1.7	0.3	0.17	0.09	5.0	0.035

(a) The values given for the compressive fracture energy are cohesion related.

(b) For the shear simulations of the keyed wallets, the values adopted for Gf_I were 0.150 (outer-leaves) and 0.070 N/mm (inner-leaf), so that numerical convergence could be achieved.

The cohesion was obtained from Eq. (5.6), which derives from the Drucker-Prager yield function applied to uniaxial compression. Here, f_c is the compressive strength. The tensile strength of the outer-leaves was considered equal to the tensile strength of the stone, assuming, thus, vertical cracking. The tensile strength of the inner-leaf was obtained

according to $f_t = f_c/15$, which is a relation often found in masonry specimens. The value adopted for the friction angle ϕ was 10º (a larger value in plane-stress would implicate an overestimation of the biaxial strength for this specific yield criterion) and, for the dilatancy angle ψ, a value of 5º was assumed. For the tensile fracture energy, a value in agreement with the experimental results reported by Van der Pluijm (1999) for brick specimens was adopted. The values of the elastic modulus and of the compressive fracture energy were adopted so that the numerical response of the specimens best fitted the experimental response, see Figure 5.39.

$$c = \frac{1 - \sin\phi}{2\cos\phi} f_c \tag{5.6}$$

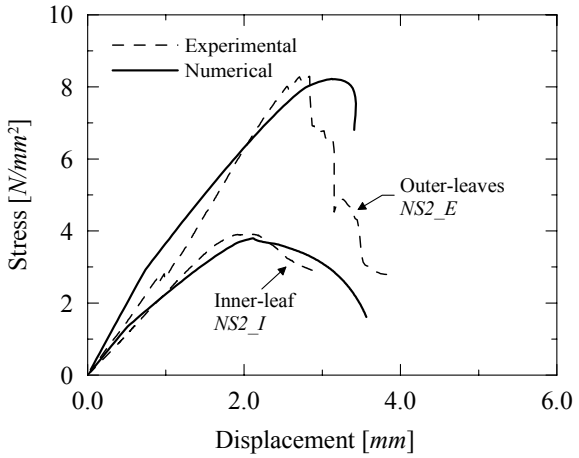

Figure 5.39 – Compression stress-displacement diagrams for the leaves of the *Noto* wallets.

The elastic material properties assumed for the collar joints are given in Table 5.17 and the inelastic properties are given in Table 5.18. The parameters were obtained, whenever possible, from the shear test on wallet *NS1* but most of the inelastic parameters were unknown and had to be estimated. The interfaces shear stiffness k_s was adopted so that the numerical and experimental elastic responses showed a good agreement. Based on elastic assumptions, the normal stiffness k_n can be obtained according to $k_n = k_s \times 2\ (1 + \nu) = 1.0\ N/mm^3$, where $\nu = 0.2$ is the coefficient of Poisson. However, higher values had to be adopted in order to avoid interpenetration of the two continuums separated by the interfaces.

The cohesion c for the first connection to fail was given experimentally but for the second connection a value was adopted so that the numerical response resembled the

experimental response. The values of the remaining inelastic parameters (tensile strength f_t, friction coefficient $tan\phi$, dilatancy coefficient $tan\psi$, mode I fracture energy Gf_I and mode II fracture energy Gf_{II}) were adopted in agreement with the values experimentally found by Van der Pluijm (1999) and recommended by Lourenço (1996b) for unit-mortar interfaces.

Table 5.17 – Elastic properties for the collar joints.

Collar joint	k_n N/mm^3	k_s N/mm^3
1 (left)	150	0.4
2 (right)	150	0.4

Table 5.18 – Inelastic properties for the collar joints.

Collar joint	c N/mm^2	f_t N/mm^2	$tan\ \phi$ -	$tan\ \psi$ -	Gf_I N/mm	Gf_{II} N/mm
1 (left)	0.13	0.09	0.70	0.00	0.015	0.050
2 (right)	0.21	0.14	0.70	0.00	0.015	0.060

5.3.1 Shear simulations

The shear tests for both types of wallets, either with or without shear keys, were numerically reproduced. As it will become clear later in the text, the testing boundary conditions are a key issue for the correct interpretation of the results. The experimental test setup was composed by two steel plates at the bottom, supporting the outer-leaves, and a third plate over the inner-leaf, through which a vertical load was applied. Additionally, sheets of Teflon were placed between the steel plates and the wallets. Therefore, the shear interaction between the plates and the wallets is not a clear issue and must be further investigated.

For the wallets with straight collar joints, this aspect has been assessed by considering four different shear stiffnesses k_s at the supports:

a) $k_s = 0$, the specimen is free to slide over the steel plates.
b) $k_s = \infty$, shear slip is precluded between the specimen and the plates.
c) Constant $k_s = 0.01\ N/mm^3$, an intermediate constant shear stiffness is applied and, thus, shear slip can occur but the horizontal reactions at the boundaries increase with increasing displacement.

d) Non-linear k_s. At the level of the upper plate, shear slip is free to occur up to a certain relative displacement, beyond which, shear slip is completely restrained. A transition phase for k_s was also considered. At the level of the bottom supports, shear slip is precluded.

Regarding the normal stiffness k_n given to the boundaries, the same behaviour was adopted for all cases. Zero stiffness in tension and infinite stiffness in compression were considered. Figure 5.40 illustrates the experimental load-displacement diagram obtained for the wallet *NS1* and the numerical diagrams obtained according to the different boundary conditions. It is noted that the two experimental load peaks correspond to the failure of each connection.

Regarding the numerical diagrams, for boundaries with $k_s = 0$, after failure of the first connection the specimen starts sliding until complete degradation of strength and, thus, only one of the two connections fails. Another interesting point is that the collapse load is underestimated. Such difference is due to the absence of horizontal constraints at the bottom, which leads to a failure that is not exclusively governed by shear but is accompanied also by flexural tensile stresses.

For supports with $k_s = \infty$, a smooth load drop due to material softening follows the failure of the first connection. However, it is not as sudden or as deep as the experimental load drop. In terms of collapse loads, the first load peak shows a good agreement with the experimental results but the second load peak, corresponding to the failure of the second connection, is largely overestimated. This is, again, due to the softening behaviour of the first connection to fail, which is still contributing to the specimen strength when the second connection fails.

For a constant shear stiffness $k_s = 0.01\ N/mm^3$, the value of the first load peak equals the value for $k_s = 0$ and, thus, is also underestimated. After the failure of the first connection, the specimen starts sliding over the boundaries with the load suddenly dropping. However, in this case, after some amount of shear slip, the horizontal reactions at the supports become mobilized and a load increase is observed until failure of the second connection occurs. The comparison with the experimental response shows, nevertheless, that an understiff response was obtained for the second increasing branch.

These results demonstrate that to capture correctly the experimental behaviour, the boundary conditions adopted must allow some amount of shear slip at the supports after

the failure of the first connection and, afterwards, restrain it completely. Therefore, a non-linear k_s was adopted for the upper boundary together with complete shear slip restriction at the bottom boundaries. Good agreement with the experimental response was found, see Figure 5.40b. Even so, the slope of the second increasing branch is slightly underestimated. This shows that the hypothesis assumed of equal shear stiffness for the two connections is, probably, not true for this specimen, with the second connection showing a stiffer behaviour than the first connection. Figure 5.41 depicts the progressive shear failure of the wallet.

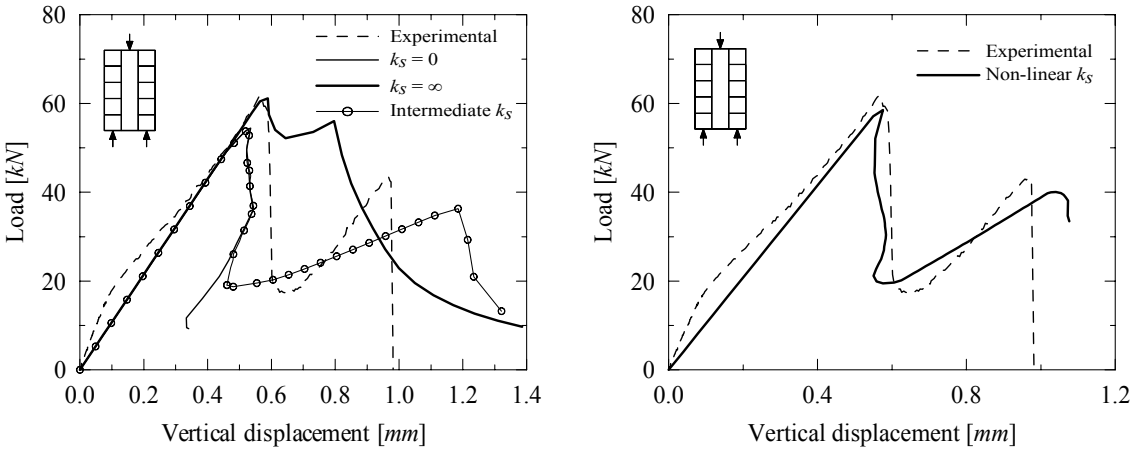

Figure 5.40 – Numerical and experimental (*NSI*) shear load-displacement diagrams for straight collar joints wallets. Different shear stiffnesses were considered at boundaries: (a) constant and (b) non-linear.

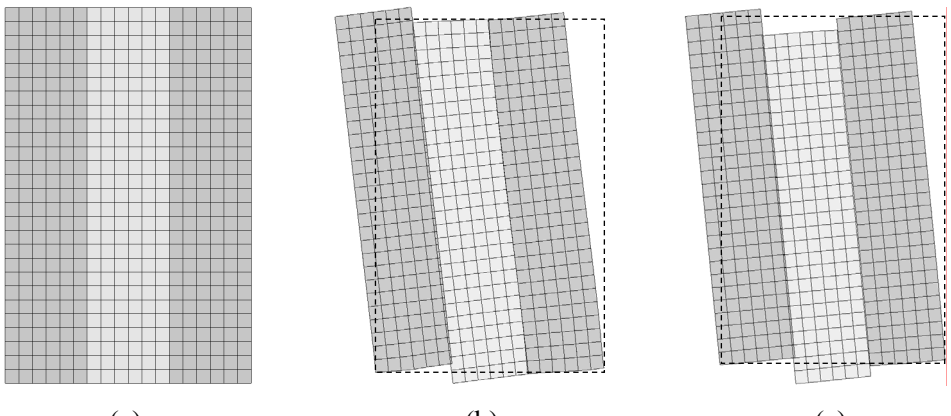

Figure 5.41 – Progressive shear failure for non-linear k_s boundary conditions: (a) mesh adopted, (b) deformed (incremental) mesh after failure of the first connection and (c) deformed (total) mesh after failure of the second connection.

In the case of keyed collar joints wallets, the influence of the boundary conditions in the response was assessed by a similar procedure. Here, three different shear stiffnesses at the boundaries were considered: (a) $k_s = 0$, (b) $k_s = \infty$ and (c) an intermediate constant $k_s = 2.0\ N/mm^3$.

The comparison between the numerical and the experimental load-displacement diagrams is given in Figure 5.42. The deformed meshes at failure for each numerical diagram are depicted in Figure 5.43. The collapse load obtained for zero shear stiffness at the boundaries is significantly lower than the experimental collapse load. In this situation, the specimen fails due to a vertical crack that arises in the weaker connection (left), developing along the shear keys. For infinite shear stiffness at the boundaries, a much better agreement with the experimental collapse load is found. Here, failure is governed by crushing of the inner-leaf near the top.

In the experimental failure mechanism, both described modes seem to be present and, thus, an intermediate k_s was considered in order to reproduce more accurately the behaviour found. The collapse load obtained was almost the same as for $k_s = \infty$ and is about 80% of the experimental collapse load. In this case, failure occurs due to combined shearing-crushing of the inner-leaf near the top and due to the development of vertical cracks along the shear keys, see Figure 5.43c.

For the intermediate k_s at the supports, Figure 5.44 illustrates the contour of minimum principal stresses for the elastic regime and the principal plastic strains at failure. In Figure 5.44a, it is visible the transfer of compressive stresses from the inner-leaf to the outer-leaves, through the shear keys. In Figure 5.44b,c, the shearing-crushing of the inner-leaf near the top and the tensile damage in the inner-leaf, along the shear keys, is confirmed as failure mechanism.

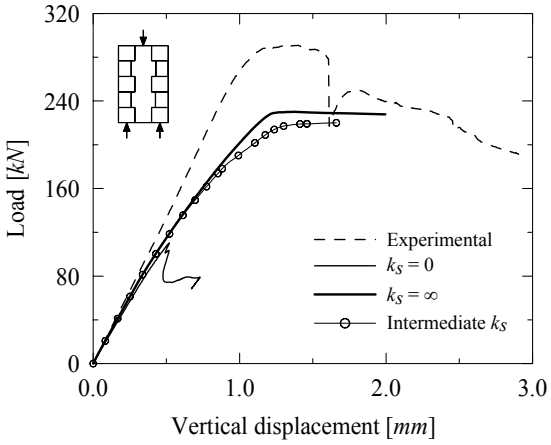

Figure 5.42 – Numerical and experimental (*NK2*) shear load-displacement diagrams for keyed collar joints wallets. Different shear stiffnesses k_s were considered at the boundaries.

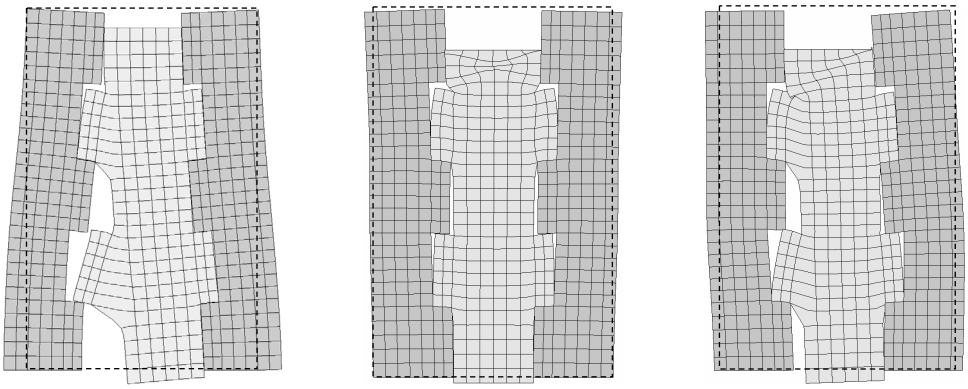

(a) (b) (c)

Figure 5.43 – Deformed meshes at failure for different shear stiffnesses k_s at the supports: (a) $k_s = 0$, (b) $k_s = \infty$ and (c) intermediate k_s.

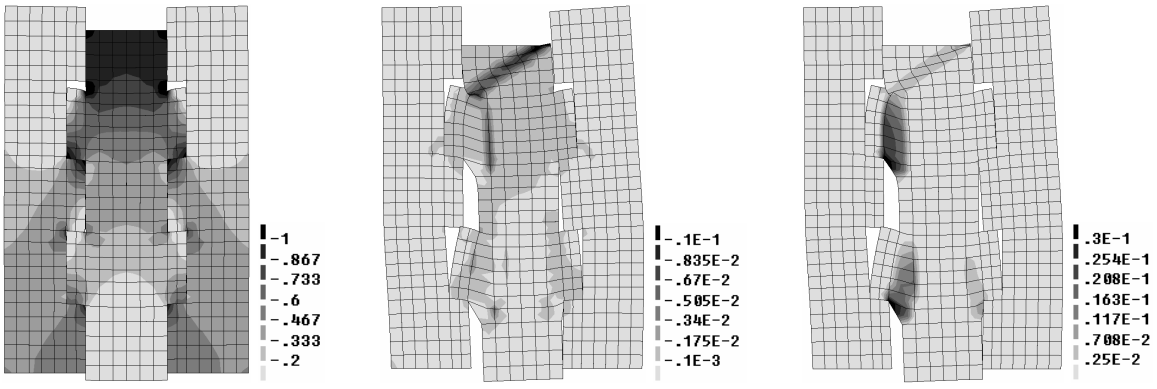

(a) (b) (c)

Figure 5.44 – Results obtained for the shear simulations on keyed wallets, adopting the intermediate k_s: (a) principal minimum stresses for an applied load of 50 *kN* (elastic regime) and principal plastic strains at failure: (b) minimum and (c) maximum.

5.3.2 Compression simulations on full wallets

The compression tests on wallets with and without shear keys have also been analysed. Friction between wallets and boundaries has been neglected in the simulations. In the case of the wallet with straight connections, a row of mesh elements at middle height was made slightly imperfect and a 10% lower compressive strength was given. The objective is to trigger the strain localization.

A comparison between numerical and experimental stress-strain diagrams is given in Figure 5.45. Good agreement is found in the case of the wallet with keyed collar joints. In the case of the wallet with straight collar joints, the predicted strength is about 20% higher than the experimental strength. As discussed in Section 5.2, the inner-leaf is almost not collaborating in the experimental response, which can partially explain the difference found between the experimental and numerical strength values.

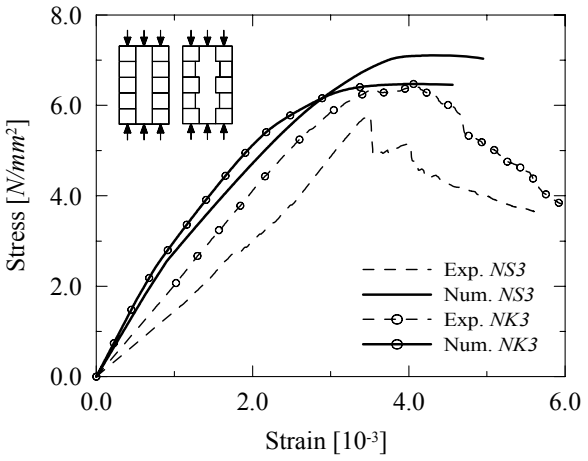

Figure 5.45 – Compression stress-strain diagrams obtained on wallets with straight collar joints (*NS3*) and keyed collar joints (*NK3*).

Another point is that the numerical strength of the wallet with keyed connections is lower than the strength of the wallet with straight connections, as predicted also by the simple expressions discussed in Section 5.2. Such behaviour is explained by the smaller cross-sectional area of the outer-leaves in the case of the wallets with keyed collar joints, for which a reduced thickness of 130 *mm* was adopted for the courses without shear keys. On the contrary, the outer-leaves of wallets with straight collar joints have a constant

thickness of 170 *mm*. Concerning the failure patterns, it is stressed that, of course, continuum finite element models can not realistically reproduce the propagation of cracks typical of compressive failure. The numerical failure patterns obtained are just phenomenological and consist of localization of deformation in a single finite element, as typical of strain softening or non-associated plasticity models.

5.4 Summary

The present study addresses load-transfer and compressive failure in composite masonry walls, which seems to be not a sufficiently debated issue in literature. From the experimental tests, the following conclusions can be drawn:

a) Shear strength values found for straight collar joints are between 0.09-0.17 N/mm^2, whereas for keyed joints the values are in the 0.58-0.81 N/mm^2 range.
b) In wallets with straight collar joints, shear failure occurs due to vertical cracks that arise in the connections while in wallets with keyed collar joints, failure is mainly due to the development of inclined cracks in the inner-leaf.

Numerical assessment of the experimental data was also addressed using a plasticity based finite-element model, in which units and mortar were smeared out in a continuum. The influence of the boundary conditions on the response was investigated and good agreement with the experimental results has been found.

Simplified calculations for predicting the compressive strength of composite walls have also shown good agreement with experimental results and with advanced numerical methods. Thus, simplified expressions may be used as a first estimate of the wallets strength. It is stressed that width/length ratio and height/width ratio of the tested wallets have an influence on the confinement of the inner-leaf and in the compressive instability of the leaves at failure. Thus, extrapolation to real-case walls must be very careful.

Suggestions for future work include further compression testing on composite wallets, considering also specimens with different ratios between inner and outer-leaves thicknesses.

6 Conclusions

The present study addresses the compressive behaviour of unreinforced masonry structures, with an emphasis on historical structures. The ability to numerically predict the compressive strength of masonry under short-term static loading has been investigated using simplified analytical methods, continuum non-linear numerical simulations and a phenomenological particle model developed in a discrete framework. Long-term effects have been also investigated by standard compressive tests, short-term creep tests and long-term creep tests carried out on ancient masonry prisms. Finally, load-transfer and compressive failure mechanisms in multiple-leaf walls were analysed in an integrated experimental-numerical investigation. The conclusions that can be derived from this study are presented next for each subject addressed.

Strength prediction using analytical and continuum non-linear models

The ability of analytical methods and continuum models based on plasticity and cracking to reproduce the experimental compressive behaviour of masonry has been addressed. The comparison between obtained numerical results and experimental results available in literature from compression tests on masonry prisms allow to conclude that: (a) continuum finite element modelling largely overestimates the strength and peak strain of the prisms; (b) plane-stress, plane-strain and "enhanced-plane-strain" lead to different strengths and different failure mechanisms, which is physically non-realistic but numerically correct. The usage of 3D models or enhanced-plane-strain models is therefore recommended; (c) simplified methods to predict the strength based on elastic considerations provide results different from advanced numerical analyses and experimental values. This last conclusion has also been confirmed by Brencich and Gambarotta (2005), indicating that experimental testing or rather conservative empirical formulae are the only possible solution at the present state of knowledge.

In addition, a comparison between the numerical results obtained for running-bond prisms and simulations on stack-bond specimens was presented. A higher strength was found for the stack-bond configuration, which still requires experimental validation. Moreover, a larger difference was observed in prisms built with weaker mortars.

Strength prediction using a discrete particle model

A particle model consisting in a phenomenological discontinuum approach has been proposed to represent the microstructure of masonry components, attempting to adequately reproduce the experimental behaviour of masonry under compression. The model is discussed in detail, including proposals for selection of numerical data, sensitivity studies, fracture processes and failure mechanisms, and size effect studies. Finally, the particle model is compared with experimental results on masonry wallets under uniaxial compression and with numerical simulations using a continuum finite element model.

It is possible to conclude that: (a) discontinuum models show clear advantages when compared to continuum models, based in plasticity and cracking, in predicting the compressive strength and peak strain of masonry prisms; (b) compressive and tensile strength values provided by the particle model can be considered as particle size and particle distortion independent for practical purposes; (c) relations between structural and particle sizes lower than seven to ten should be avoided in simulations; (d) size dependent responses have been obtained with the proposed model; and (e) shear parameters rather than tensile parameters play a major role at the micro-level and greatly influence the overall response of compressed masonry, as also confirmed by Vonk (1993).

Creep behaviour under high sustained stresses

The creep behaviour under high stresses of three different types of ancient masonry specimens has been analysed. Short-term creep tests have been conducted on regular and rubble masonry prisms recovered from the ruins of the collapsed Pavia Civic Tower and, also, on rubble prisms collected in the crypt of the Monza Cathedral. In addition, long-term creep tests were also carried out on regular prisms coming from the Pavia Civic Tower.

From experimental practice, it is possible to conclude that creep tests on ancient masonry prisms should be carried out by applying the load in successive steps, at a given time interval, starting from a low stress level. In this way, a throughout description of the viscous behaviour of the material can be obtained. Creep tests in which the load is applied in a single step are unwieldy in the case of ancient masonry due to the high scatter in the mechanical properties and to the small number of specimens usually available.

The time period between successive load steps should be sufficiently long to extinguish primary creep. In fact, the evolution for different stress levels of the strain rate associated to secondary creep can only in such way be evaluated. From the results obtained on the regular masonry prisms tested, a minimum time period under sustained loading of 70 to 80 days should be adopted. For this reason, remarkable differences were observed between secondary creep rates calculated from short-term or long-term creep tests. Short-term creep results should, therefore, be interpreted carefully.

Finally, it should be stressed that secondary creep was found to initiate at 60 to 70% of the compressive strength. A hyperbolic fit to describe the evolution of secondary creep rate with the applied stress-level has been suggested in the present study.

Shear and compressive behaviour of multiple-leaf walls

Load-transfer and compressive failure mechanisms in composite masonry walls have been addressed. From the experimental tests, the following conclusions can be drawn:

a) Shear strength values found for straight collar joints are between 0.09-0.17 N/mm^2, whereas for keyed joints the values are in the 0.58-0.81 N/mm^2 range.
b) In wallets with straight collar joints, shear failure occurs due to vertical cracks that arise in the connections, while in wallets with keyed collar joints, failure is mainly due to the development of inclined cracks in the inner-leaf.

Numerical assessment of the experimental data was also addressed using a plasticity based finite-element model, in which units and mortar were smeared out in a continuum. The influence of the boundary conditions on the response was investigated and good agreement with the experimental results has been found.

Simplified calculations for predicting the compressive strength of composite walls have also shown good agreement with experimental results and with advanced numerical methods. Thus, simplified expressions may be used as a first estimate of the wallets strength. It is stressed that width/length ratio and height/width ratio of the tested wallets have an influence on the confinement of the inner-leaf and in the compressive instability of the leaves at failure. Thus, extrapolation to real-case walls must be very careful.

6.1 Suggestions for future work

For a reliable prediction of masonry compressive strength from the properties of masonry constituents, an investigation on models that are able to consider the discrete nature of the masonry components is suggested. Detailed modelling approaches are, however, hindered by the lack of knowledge on the mechanical characteristics of mortar inside masonry composites, which are influenced by mortar laying and curing. Thus, an advanced experimental program to characterize mortar inside masonry would be of great interest to masonry research.

For masonry creep behaviour under high sustained stresses, further creep tests should be conducted for an adequate characterization of the material, given the wide scatter associated to ancient masonry. Regarding the masonry constituents, experimental results on the non-linear creep behaviour of units and mortar are virtually absent in literature, meaning that further investigation is required. In terms of numerical modelling, the development of suitable 3D models for viscous inelastic behaviour is still needed.

Regarding multiple-leaf walls, further compression testing is suggested, considering specimens with different ratios between inner and outer-leaves thicknesses. Moreover, experiments are suggested that consider more complex test setups able to analyse the behaviour of multiple-leaf walls when an equal stress, rather than an equal deformation, is applied on the wallets leaves.

References

ACI (2004). Commentary on specification for masonry structures. ACI 530.1-02, *Manual of Concrete Practice*, Detroit, USA.

Ameny P, Loov RE and Shrive NG (1984). Models for long-term deformation of brick work. *Masonry Int.*, **1**, 27-36.

Anzani A, Binda L and Melchiorri G (1995). Time-dependent damage of rubble masonry walls. *Proc. 4th Int. Masonry Conf.*, London, UK, **2,** 341-351.

Anzani A, Binda L and Mirabella Roberti G (2000). The effect of heavy persistent actions into the behaviour of ancient masonry. *Materials and Structures*, RILEM, **33(228)**, 251-261.

ASTM (2004). Test method for compressive strength of cylindrical concrete specimens. ASTM 04.02-C39, *Annual book of ASTM standards*, Philadelphia, USA.

Atkinson R, Noland J and Abrams D (1985). A deformation failure theory for stack-bond brick masonry prisms in compression. *Proc. 7th Int. Brick and Block Masonry Conf.*, Melbourne, Australia, 577-592.

Bazant ZP (1988). Material models for structural creep analysis. *Mathematical modelling of creep and shrinkage of concrete*, ed. ZP Bazant, John Wiley & Sons, New York, USA, 99-215.

Bazant ZP (1993). Current status and advances in the theory of creep and interaction with fracture. *Proc. 5th Int. RILEM Symp. on Creep and Shrinkage of Concrete*, Barcelona, Spain, 291-307.

Bazant ZP and Planas J (1998). *Fracture and size effect in concrete and other quasi-brittle materials*. CRC Press, Boca Raton, USA.

Berto L, Saetta A, Scotta R and Vitaliani R (2005). Failure mechanism of masonry prism loaded in axial compression: computational aspects. *Materials and Structures*, RILEM, **38(276)**, 249-256.

Binda L, Fontana A and Frigerio G (1988). Mechanical behaviour of brick masonries derived from unit and mortar characteristics. *Proc. 8th Int. Brick and Block Masonry Conf.*, Dublin, Ireland, **1**, 205-216.

Binda L, Fontana A and Anti L (1991). Load transfer in multiple-leaf masonry walls. *Proc. 9th Int. Brick and Block Masonry Conf.*, Berlin, Germany, 1488-1497.

Binda L, Gatti G, Mangano G, Poggi C and Landriani GS (1992). The collapse of the Civic Tower of Pavia: a survey of the materials and structure. *Masonry Int.*, **6(1)**, 11-20.

Binda L, Fontana A and Mirabella Roberti G (1993). Modelling of the mechanical behaviour of multiple-leaf stone walls. *Proc. Int. Symp. on Computer Methods in Structural Masonry*, Swansea, UK, 229-241.

Binda L, Fontana A and Mirabella Roberti G (1994). Mechanical behaviour and stress distribution in multiple-leaf walls. *Proc. 10th Int Brick and Block Masonry Conf.*, Calgary, Canada, 51-59.

Binda L, Palma M and Penazzi D (1999). Cautious repair of stone-masonry structures in seismic areas. *Proc. Int. Conf. of the SFB315 Research Centre of Karlsruhe University*, Karlsruhe, Germany, 99-108.

Binda L, Saisi A, Messina S and Tringali S (2001). Mechanical damage due to long-term behaviour of multiple-leaf pillars in Sicilian churches. *Proc. 3rd Int. Sem. on Historical Constructions*, Guimarães, Portugal, 707-718.

Binda L, Saisi A, Benedictis R De and Tringali S (2003a). Experimental study on the damaged pillars of the Noto Cathedral. *Proc. 8th Int. Conf. on Structural Studies, Repairs and Maintenance of Heritage Architecture*, Halkidiki, Greece, 89-98.

Binda L, Saisi A, Tiraboschi C, Valle S, Colla C and Forde M (2003b). Application of sonic and radar tests on the piers and walls of the Cathedral of Noto. *Construction and Building Materials*, **17**, 613-627.

Bolander JE, Hong GS and Yoshitake K (2000). Structural concrete analysis using rigid-body-spring networks. *Computer-Aided Civil and Infrastructure Engineering*, **15**, 120-133.

Brencich A and Gambarotta L (2005). Mechanical response of solid clay brickwork under eccentric loading. Part I: unreinforced masonry. *Materials and Structures*, RILEM, **38(276)**, 257-266.

Brooks JJ (1990). Composite modelling of masonry deformation. *Materials and Structures*, RILEM, **23**, 241-251.

Carol I, López CM and Roa O (2001). Micromechanical analysis of quasi-brittle materials using fracture-based interface elements. *Int. J. Numerical Methods in Engineering*, **52**, 193-215.

CEB-FIP (1993). *Model Code 1990*. Bulletin D'Information No. 213/214, Comite Euro-International du Beton, T Telford, London, UK.

CEN (1998a). *Methods of test for masonry: Determination of compressive strength*. EN 1052-1:1998, CEN, Brussels, Belgium.

CEN (1998b). *Methods of test for masonry units: Determination of real and bulk density and of total and open porosity for natural stone masonry units*. EN 772-4:1998, CEN, Brussels, Belgium.

CEN (1999). *Methods of test for mortar for masonry: Determination of flexural and compressive strength of hardened mortar*. EN 1015-11:1999, CEN, Brussels, Belgium.

CEN (2000). *Methods of test for masonry units: Determination of compressive strength*. EN 772-1:2000, CEN, Brussels, Belgium.

CEN (2002). *Methods of test for masonry: Determination of initial shear strength*. EN 1052-3:2002, CEN, Brussels, Belgium.

CEN (2003). *Eurocode 6: Design of masonry structures*. prEN 1996-1-1:2002, CEN, Brussels, Belgium.

Cundall PA (1971). A computer model for simulating progressive, large scale movements in blocky rock systems. *Proc. Symp. Int. Society Rock Mechanics*, Nancy, France, **1(II-8)**, 129-136.

Cusatis G, Bazant ZP and Cedolin L (2003). Confinement-shear lattice model for concrete damage in tension and compression. *J. Engineering Mechanics*, ASCE, **129(12)**, 1439-1458.

DIANA (1999). *Diana Finite Element Code, version 7.2*. TNO Building and Construction Research, Delft, The Netherlands.

DIANA (2003). *DIANA Finite Element Code, version 8.1*. TNO Building and Construction Research, Delft, The Netherlands.

Drei A and Fontana A (2001). Influence of geometrical and material properties on multiple-leaf walls behaviour. *Proc. 7th Int. Conf. on Structural Studies, Repairs and Maintenance of Heritage Architecture*, Bologna, Italy, 681-691.

Egermann R and Newald-Burg C (1994). Assessment of the load bearing capacity of historic multiple-leaf masonry walls. *Proc. 10th Int. Brick and Block Masonry Conf.*, Calgary, Canada, 1603-1612.

Feenstra P (1993). *Computational aspects of biaxial stress in plain and reinforced concrete*. Dissertation, Delft University of Technology, Delft, The Netherlands.

Francis A, Horman C and Jerrems L (1971). The effect of joint thickness and other factors on the compressive strength of brickwork. *Proc. 2nd Int. Brick and Block Masonry Conf.*, Stoke-on-Trent, UK, 31-37.

Frigerio G and Frigerio P (1985). *Influence of the components and surrounding environment in the mechanical behaviour of brick masonry* (in Italian). Graduation thesis, Politecnico di Milano, Milan, Italy.

Gens A, Carol I and Alonso E (1988). An interface element formulation for the analysis of soil-reinforcement interaction. *Computers and Geotechnics*, **7**, 133-151.

Haseltine B (1987). International rules for masonry and their effect on the UK. *Masonry Int.*, **1(2)**, 41-43.

Hendry A (1990). *Structural masonry*. McMillan Education, London, UK.

Hilsdorf H (1969). An investigation into the failure mechanism of brick masonry loaded in uniaxial compression. *Designing, Engineering and Construction with Masonry Products*, FH Johnson, Houston, USA.

Ingraffea AR and Saouma VE (1985). Numerical modelling of discrete crack propagation in reinforced and plain concrete. *Fracture mechanics of concrete*, eds. G Sih and A Di Tomasso, Martinus Nijhoff Publishers, Dordrecht, The Netherlands, 171-225.

Jing L (2003). A review of techniques, advances and outstanding issues in numerical modelling for rock mechanics and rock engineering. *Int. J. Rock Mechanics and Mining Sciences*, **40**, 283-353.

Khoo C and Hendry A (1973). A failure criterion for brickwork in axial compression. *Proc. 3rd Int. Brick and Block Masonry Conf.*, Essen, Germany, 139-145.

Kim JK and Yi ST (2002). Application of size effect to compressive strength of concrete members. *Sadhana*, **27(4)**, 467-484.

Kirtschigg K (1985). On the failure mechanism of masonry subject of compression. *Proc. 7th Int. Brick and Block Masonry Conf.*, Melbourne, Australia, 625-629.

Lemos JV (2001). Modelling the behaviour of a stone masonry arch structure under cyclic loads. *Proc. 5th Int. Symp. on Computer Methods in Structural Masonry*, Rome, Italy, 101-108.

Lemos JV, Azevedo F, Oliveira C and Sincraian G (1998). Three-dimensional analysis of a block masonry pillar using discrete elements. *Proc. Monument 98 - Workshop on Seismic Performance of Monuments*, LNEC, Lisbon, Portugal, 117-126.

Lenczner D (1986). Creep and prestress losses in brick masonry. *The Structural Engineer*, **64B(3)**, 57-62.

Lofti HR and Shing PB (1994). Interface model applied to fracture of masonry structures. *J. Structural Engineering*, ASCE, **120(1)**, 63-80.

Lorig LJ and Cundall PA (1987). Modelling of reinforced concrete using the distinct element method. *Proc. SEM/RILEM Int. Conf. on Fracture of Concrete and Rock*, Houston, USA, 459-471.

Lourenço PB (1996a). *Computational strategies for masonry structures*. Dissertation, Delft University of Technology, Delft, The Netherlands. Available from www.civil.uminho.pt/masonry.

Lourenço PB (1996b). *A user/programmer guide for the micro-modelling of masonry structures*. Report 03.21.1.31.35, Delft University of Technology, Delft, The Netherlands. Available from http://www.civil.uminho.pt/masonry.

Lourenço PB (1997). *An anisotropic macro-model for masonry plates and shells: implementation and validation*. Report 03.21.1.31.07, Delft University of Technology, Delft, The Netherlands. Available from http://www.civil.uminho.pt/masonry.

Lourenço PB, Rots JG and Feenstra P (1995). A tensile "Rankine" type orthotropic model for masonry. *Proc. 3rd Int. Symp. on Computer Methods in Structural Masonry*, Lisbon, Portugal, 167-176.

Lourenço PB and Rots JG (1997). A multi-surface interface model for the analysis of masonry structures. *J. Engineering Mechanics*, ASCE, **123(7)**, 660-668.

Lourenço PB, Barros JO and Oliveira JT (2004). Shear testing of stack bonded masonry. *Construction and Building Materials*, **18(2)**, 125-132.

Mann W and Betzler M (1994). Investigations on the effect of different forms of test samples to test the compressive strength of masonry. *Proc. 10th Int. Brick and Block Masonry Conf.*, Calgary, Canada, 1305-1313.

Mazzotti C and Savoia M (2002). Nonlinear creep, Poisson's ratio, and creep-damage interaction of concrete in compression. *ACI Materials J.*, ACI, **99(5)**, 450-457.

Mazzotti C and Savoia M (2003). Nonlinear creep damage model for concrete under uniaxial compression. *J. Engineering Mechanics*, ASCE, **129(9)**, 1065-1075.

McCann D and Forde M (2001). Review of NDT methods in the assessment of concrete and masonry structures. *NDT&E Int.*, **34**, 71-84.

Mier JGM van (1997). *Fracture processes of concrete*. CRC Press, Boca Raton, USA.

Mier JGM van, Schlangen E and Vervuurt A (1995). Lattice type fracture models for concrete. *Continuum models for materials with microstructure*, ed. H Mühlhaus, John Wiley & Sons, New York, USA, 341-377.

Mirabella Roberti G, Binda L and Cardani G (1998). Numerical modelling of shear bond tests on small brick-masonry. *Proc. 4th Int. Symp. on Computer Methods in Structural Masonry*, Florence, Italy, 144-152.

Modena C, Valluzzi MR, Tongini Folli R and Binda L (2002). Design choices and intervention techniques for repairing and strengthening of the Monza cathedral bell-tower. *Construction and Building Materials*, **16**, 385-395.

Neville AM (1997). *Properties of concrete*. John Wiley & Sons, New York, USA.

Ohler A (1986). Calculation of masonry compressive strength considering the multi-axle states of stress in units and mortar (in German). *Bautechnik*, **5**.

Papa E, Taliercio A and Gobbi E (1998). Triaxial creep behaviour of plain concrete at high stresses: a survey of theoretical models. *Materials and Structures*, RILEM, **31**, 487-493.

Pickett G (1942). The effect of change in moisture content on the creep of concrete under a sustained load. *ACI J.*, ACI, **38**, 333-355.

Pluijm R van der (1999). *Out-of-plane bending of masonry: behaviour and strength*. Dissertation, Eindhoven University of Technology, Eindhoven, The Netherlands.

QHULL (2001). *QHULL, version 3.1*. CB Barber and H Huhdanpaa, University of Minnesota, Minneapolis, USA.

RILEM (1994). Tension by splitting of concrete specimens. CPC6, *Compendium of RILEM Technical Recommendations*, E&FN Spon, London, UK.

Roman HR and Gomes IR (2004). Numerical modelling of blockwork prisms tested in compression using the finite element method with interface behaviour. *Proc. 13th Int. Brick and Block Masonry Conf.*, Amsterdam, The Netherlands, **2**, 421-429.

Rostampour M (1973). *Aspects of the design of multi-storey buildings in light-weight concrete blockwork*. Dissertation, University of Edinburgh, Edinburgh, UK.

Rots JG (1988). *Computational modelling of concrete fracture*. Dissertation, Delft University of Technology, Delft, The Netherlands.

Rots JG and Schellekens JCJ (1990). Interface elements in concrete mechanics. *Computer aided analysis and design of concrete structures*, eds. N Bicanic and H Mang, Pineridge Press, Swansea, UK, 909-918.

Schellekens JC (1992). *Computational Strategies for Composite Structures*. Dissertation, Delft University of Technology, Delft, The Netherlands.

Schlangen E (1993). Experimental and numerical analysis of fracture processes in concrete. *Heron*, **38(2)**, 1-117.

Schubert P (1988). The influence of mortar on the strength of masonry. *Proc. 8th Int. Brick and Block Masonry Conf.*, London, UK, 162-174.

Shi GH (1988). *Discontinuous deformation analysis: a new numerical model for the statics and dynamics of block systems*. Dissertation, University of California, Berkeley, USA.

Toumbakari EE (2002). *Lime-pozzolan-cement grouts and their structural effects on composite masonry walls*. Dissertation, Leuven Catholic University, Leuven, Belgium.

Valluzzi MR, Porto F Da and Modena C (2004). Behaviour and modelling of strengthened three-leaf stone masonry walls. *Materials and Structures*, RILEM, **37(267)**, 184-192.

Van der Pluijm R - see Pluijm R van der

Van Mier JGM - see Mier JGM van

Van Vliet M - see Vliet M van

Van Zijl GP - see Zijl GP van

Vermeer PA and de Borst R (1984). Non-associated plasticity for soils, concrete and rock. *Heron*, **29(3)**, 1-64.

Vermeltfoort A (1994). Compression properties of masonry and its components. *Proc. 10th Int. Brick and Block Masonry Conf.*, Calgary, Canada, 1433-1442.

Vintzileou E and Tassios TP (1995). Three-leaf stone masonry strengthened by injecting cement grouts. *J. Structural Engineering*, ASCE, **121(5)**, 848-856.

Vliet M van (2000). *Size Effect in Tensile Fracture of Concrete and Rock*. Dissertation, Delft University of Technology, Delft, The Netherlands.

Vonk R (1993). A micromechanical investigation of softening of concrete loaded in compression. *Heron*, **38(3)**, 1-94.

Zijl GP van (2000). *Computational modelling of masonry creep and shrinkage*. Dissertation, Technical University of Delft, Delft, The Netherlands.

ANNEX A: ADDITIONAL RESULTS OF CREEP TESTS ON ANCIENT MASONRY SPECIMENS

A.1 SHORT-TERM CREEP TESTS ON *MRU* SPECIMENS

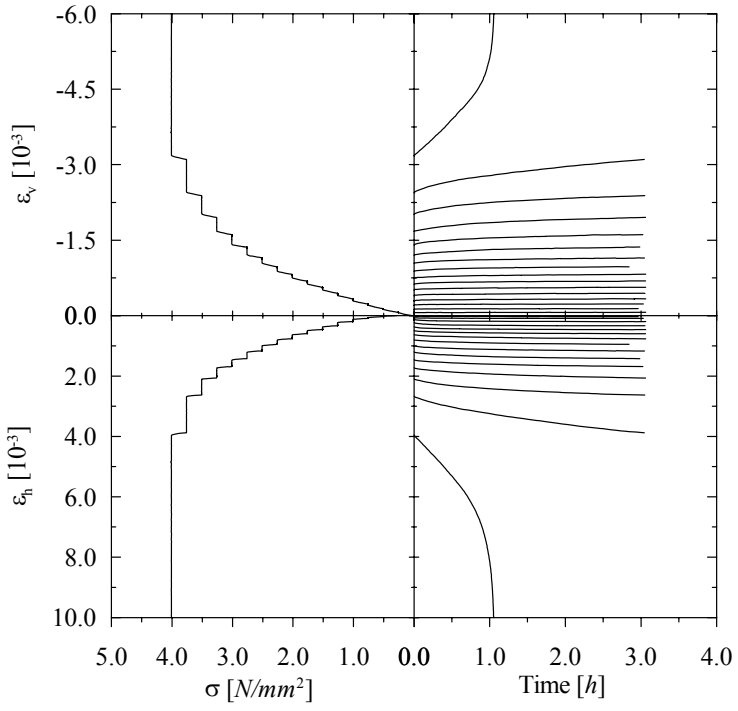

(a)

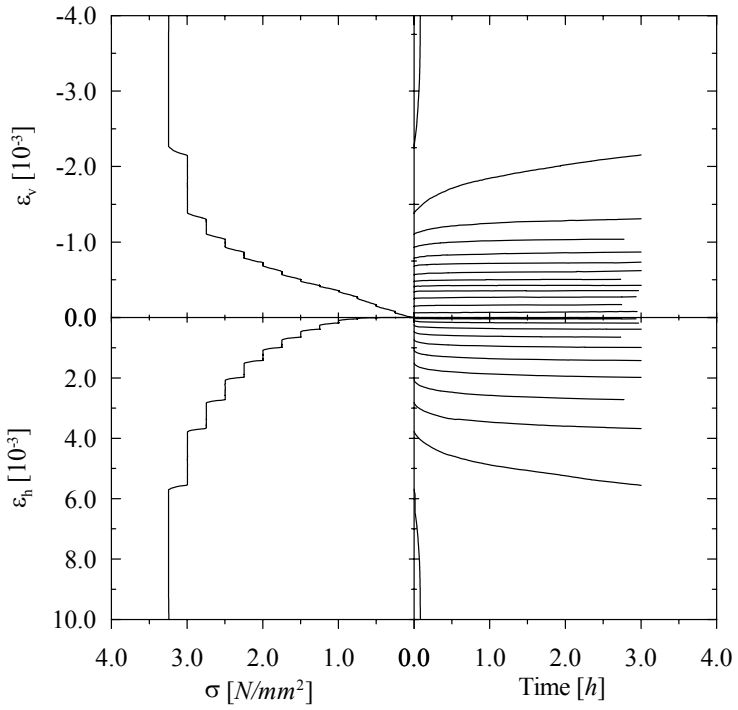

(b)

Figure A.1 – Time-stress-strain diagrams for *MRu* specimens: (a) *MRu_1* and (b) *MRu_2*.

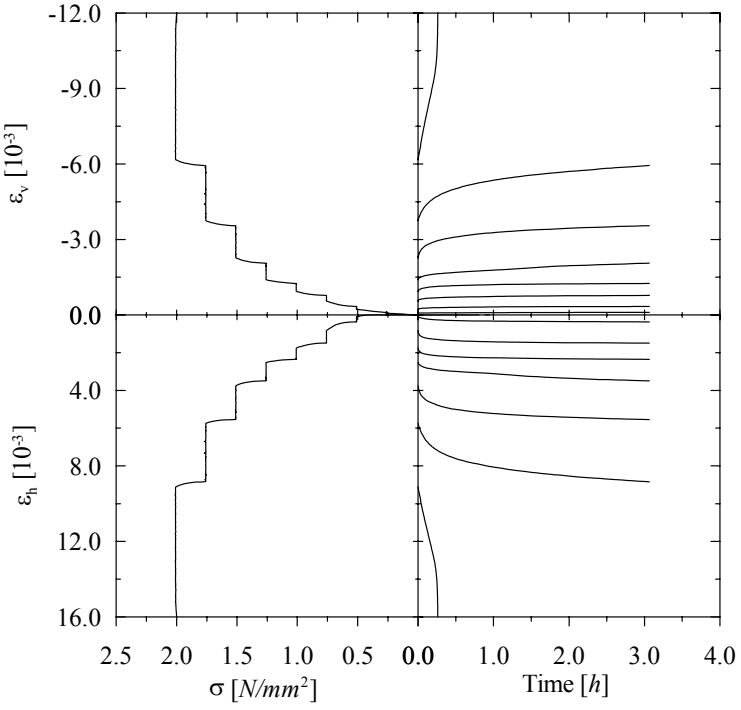

(a)

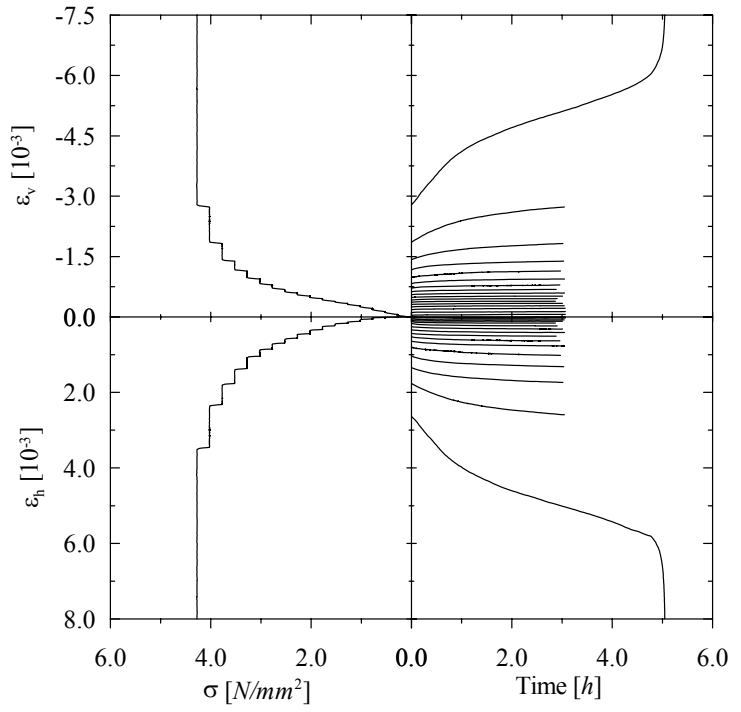

(b)

Figure A.2 – Time-stress-strain diagrams for *MRu* specimens: (a) *MRu_3* and (b) *MRu_4*.

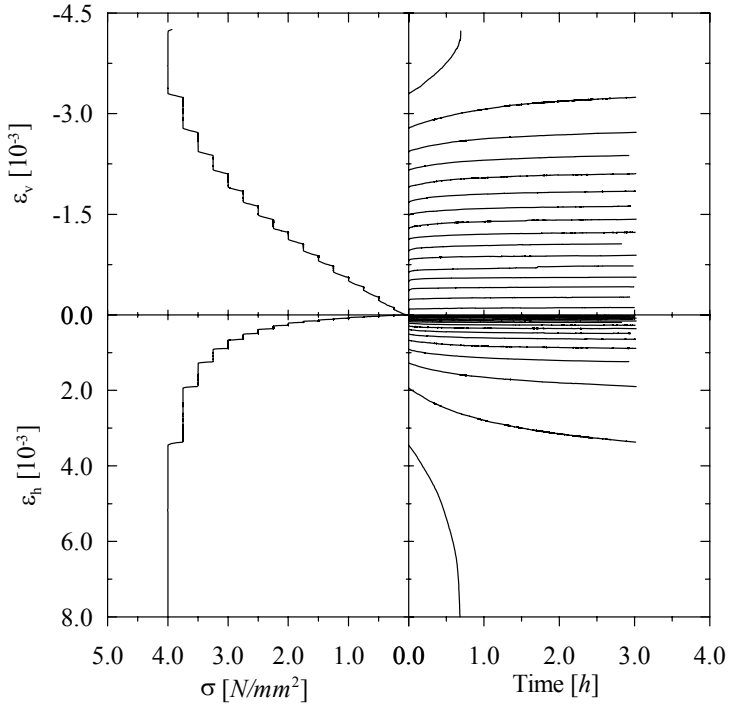

(a)

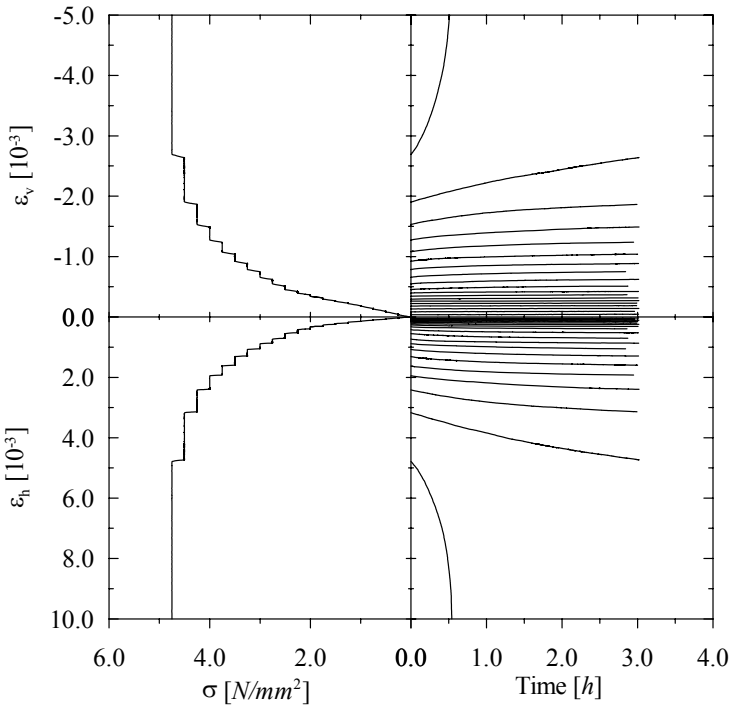

(b)

Figure A.3 – Time-stress-strain diagrams for *MRu* specimens: (a) *MRu_5* and (b) *MRu_6*.

A.2 SHORT-TERM CREEP TESTS ON *PRU* SPECIMENS

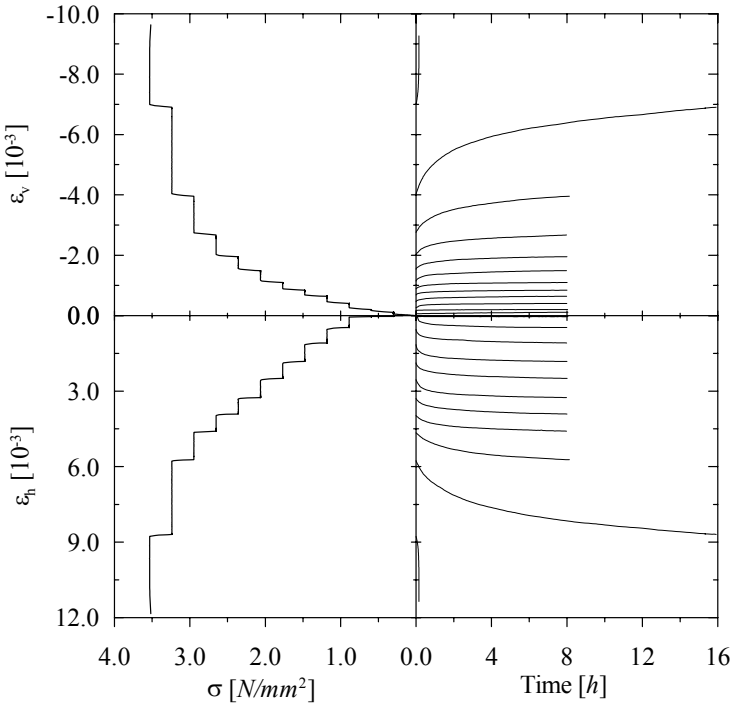

(a)

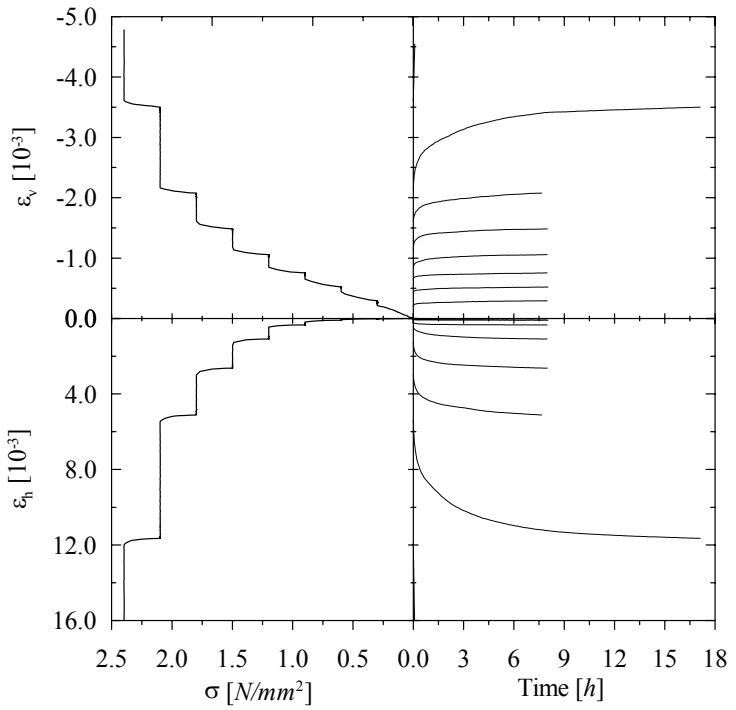

(b)

Figure A.4 – Time-stress-strain diagrams for *PRu* specimens: (a) *PRu_2* and (b) *PRu_3*.

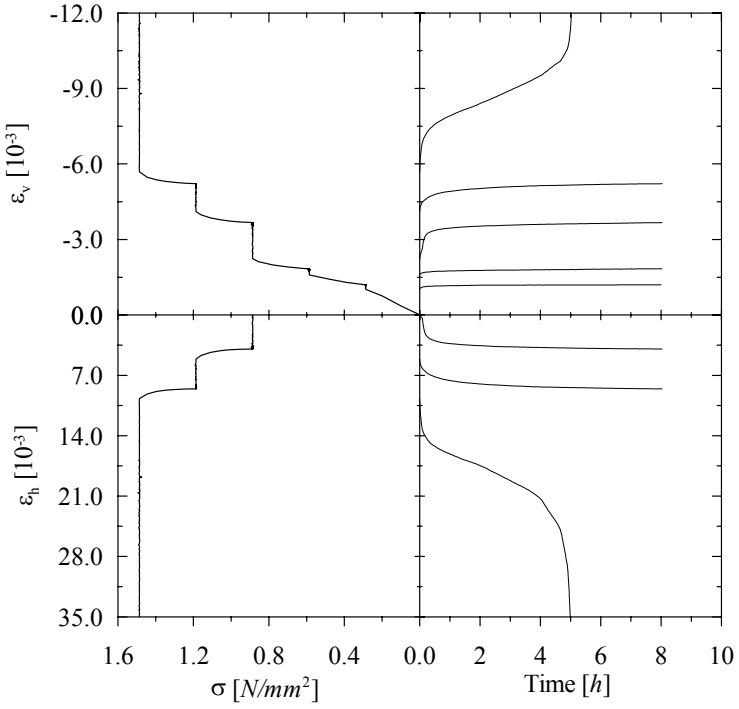

(a)

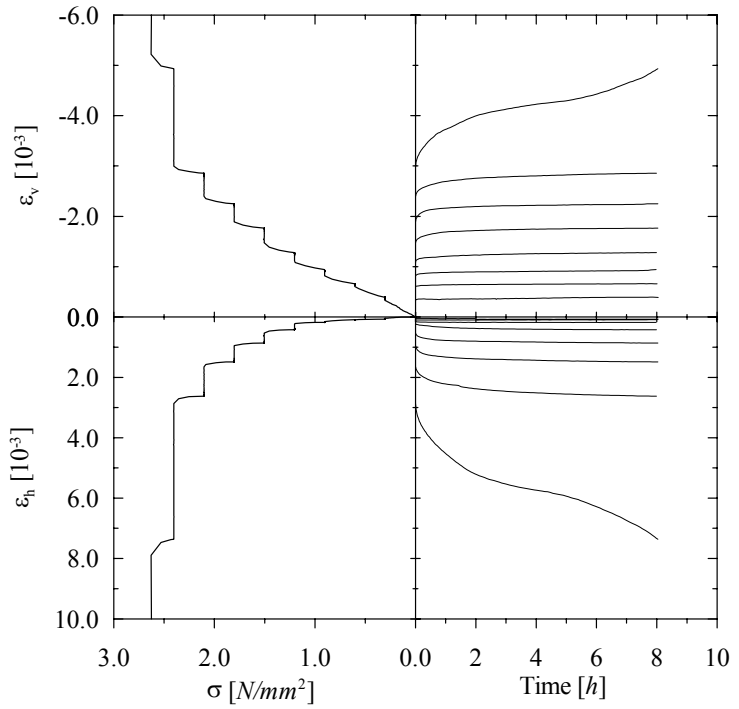

(b)

Figure A.5 – Time-stress-strain diagrams for *PRu* specimens: (a) *PRu_4* and (b) *PRu_5*.

A.3 SHORT-TERM CREEP TESTS ON *PRE* SPECIMENS

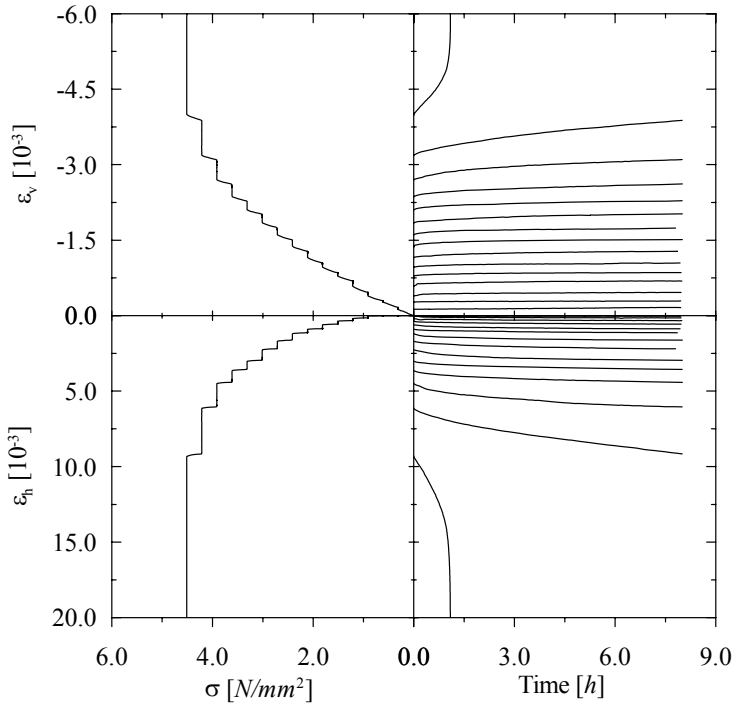

(a)

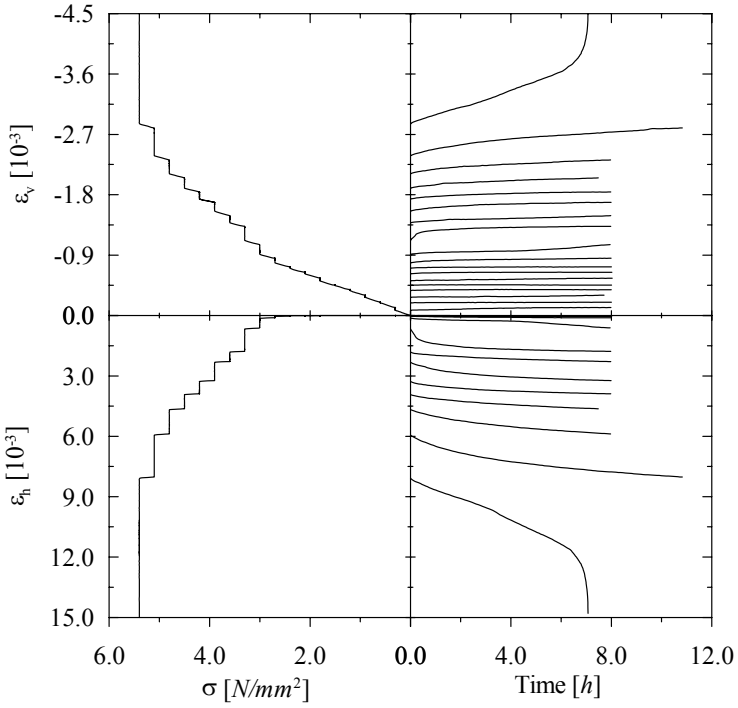

(b)

Figure A.6 – Time-stress-strain diagrams for *PRe* specimens: (a) *PRe_5* and (b) *PRe_6*.

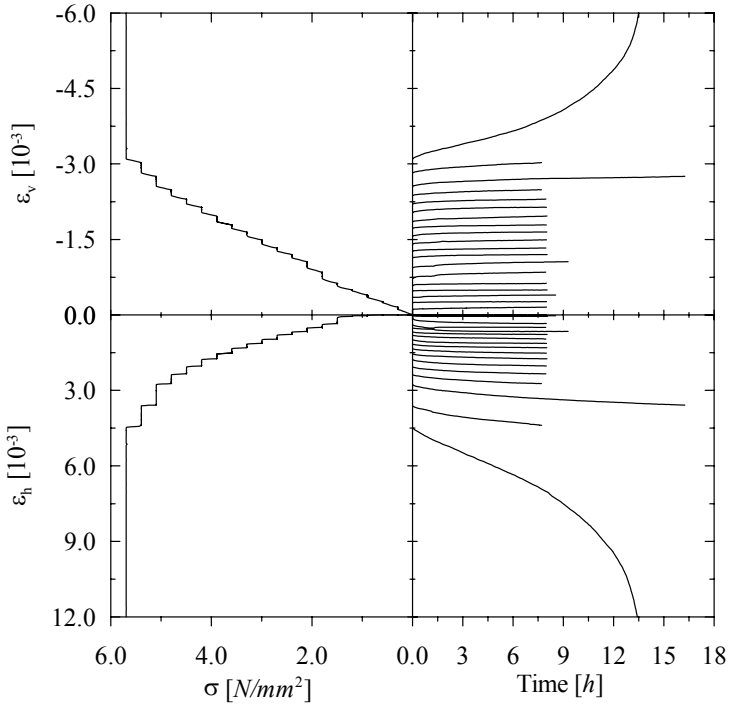

(a)

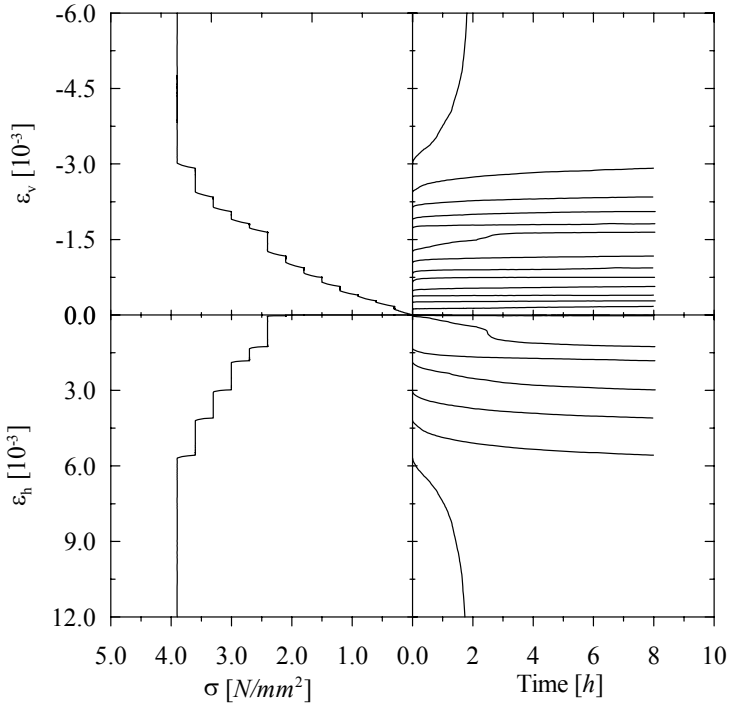

(b)

Figure A.7 – Time-stress-strain diagrams for *PRe* specimens: (a) *PRe_7* and (b) *PRe_8*.

A.4 LONG-TERM CREEP TESTS ON *PRE* SPECIMENS (TIME-STEPS OF 3 MONTHS)

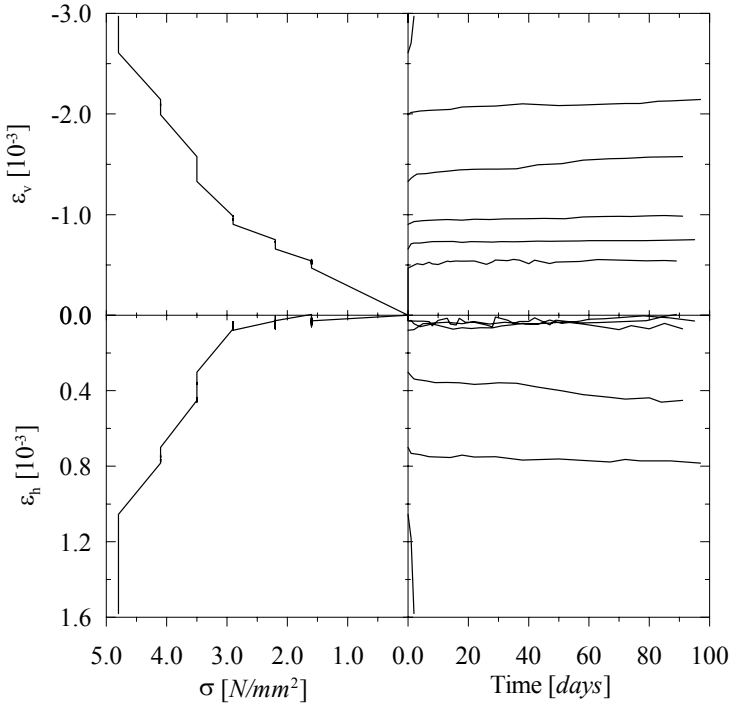

(a)

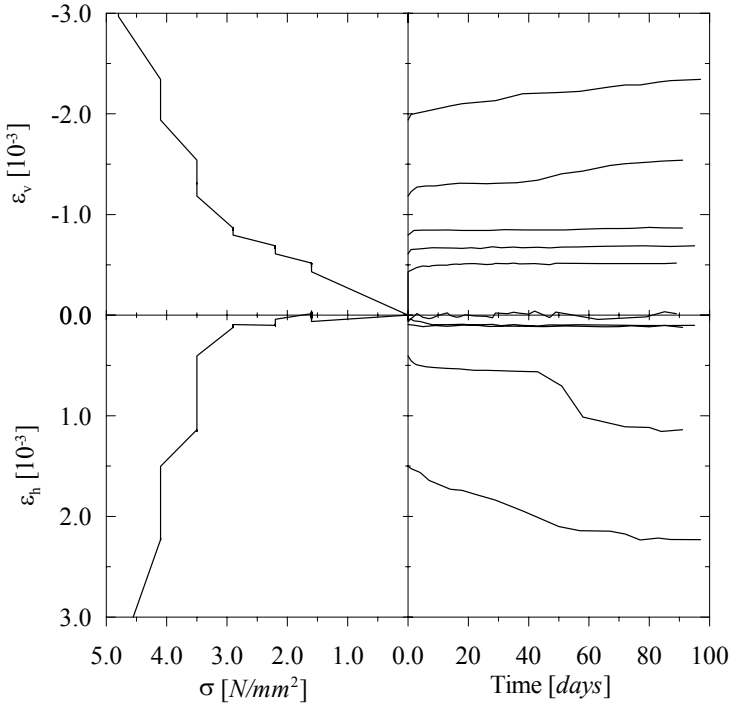

(b)

Figure A.8 – Time-stress-strain diagrams for *PRe* specimens (time-steps of 3 months): (a) *PRe_9* and (b) *PRe_10*.

A.5 LONG-TERM CREEP TESTS ON *PRE* SPECIMENS (TIME-STEPS OF 6 MONTHS)

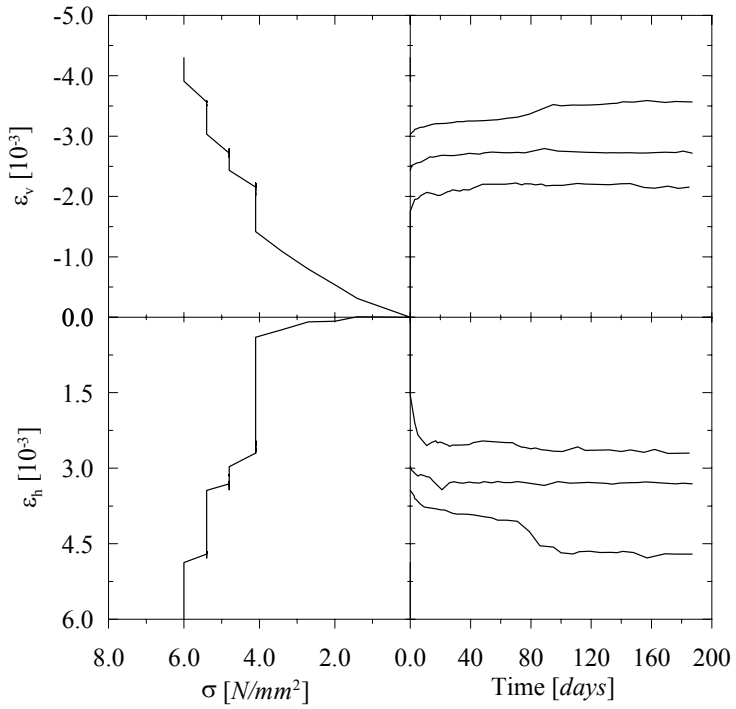

(a)

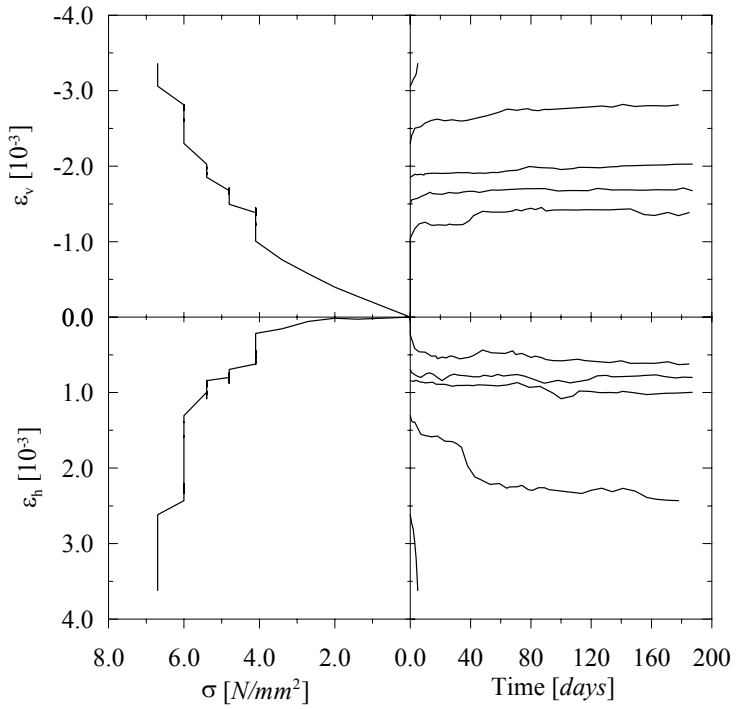

(b)

Figure A.9 – Time-stress-strain diagrams for *PRe* specimens (time-steps of 6 months): (a) *PRe_11* and (b) *PRe_12*.

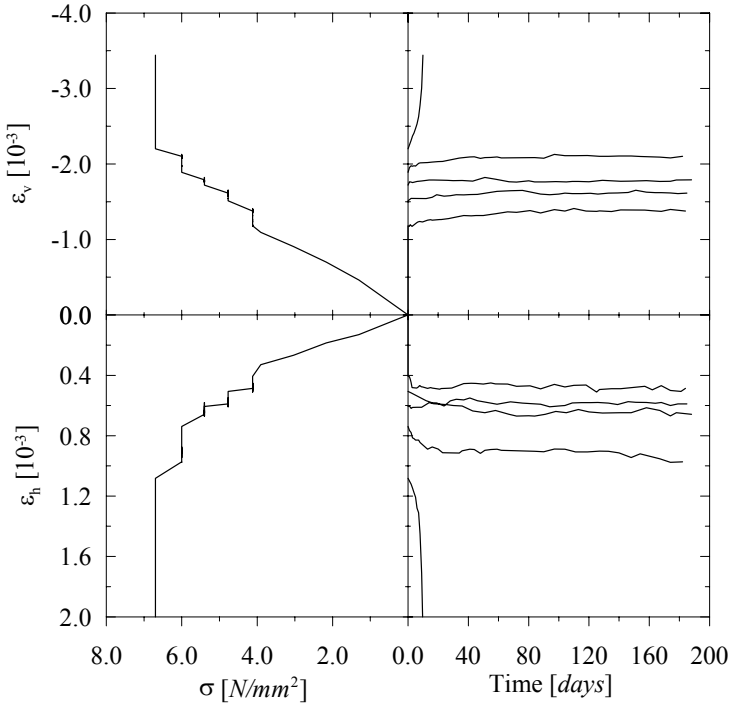

(a)

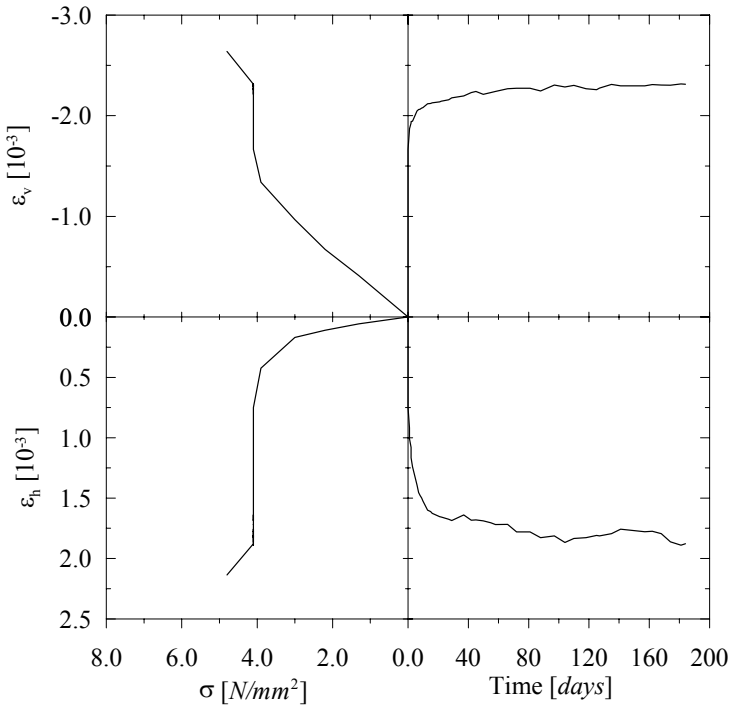

(b)

Figure A.10 – Time-stress-strain diagrams for *PRe* specimens (time-steps of 6 months): (a) *PRe_13* and (b) *PRe_14*.

ANNEX B: ADDITIONAL RESULTS OF TESTS ON MULTIPLE-LEAF WALLETS

B.1 COMPRESSIVE AND TENSILE TESTS ON STONE SPECIMENS

Table B.1 – Results of the compression tests on *Noto* stone specimens.

Specimen	Orientation (1)	f_c N/mm^2	ε_p 10^{-3}	E N/mm^2	ν -
1A	*A*	22.0	2.8	8870	0.11
2A	*A*	19.3	2.2	9910	0.09
3A	*A*	20.4	2.3	9650	0.10
4B	*B*	13.2	2.0	7375	0.07
5B	*B*	20.4	2.5	9390	0.11
6B	*B*	19.2	2.5	8815	0.10

(1) *A* stands for coring of the specimens along the *loading direction* of the units in the wallets and *B* for the *bedding direction*.

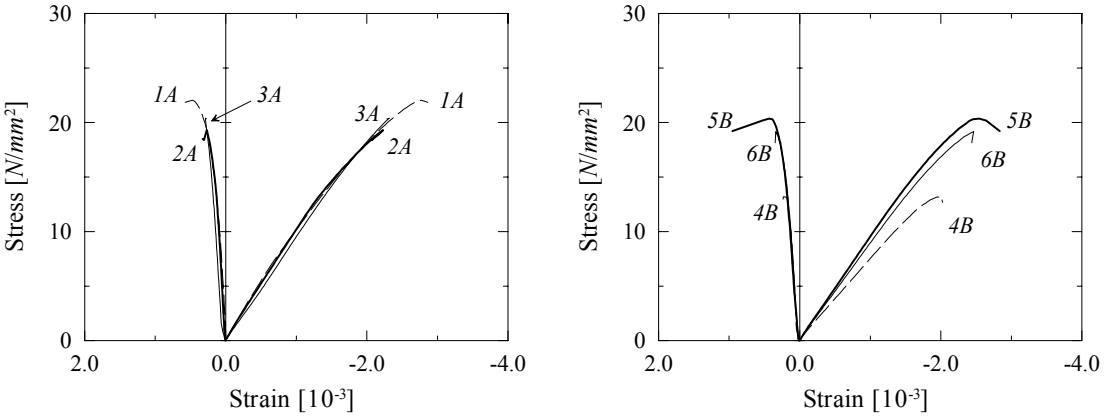

Figure B.1 – *Noto* stone compression diagrams obtained with transducers attached to the specimens: (a) *1A*, *2A*, *3A* and (b) *4B*, *5B 6B*. Transversal strains are given on the left side of the graphics and vertical strains on the right side.

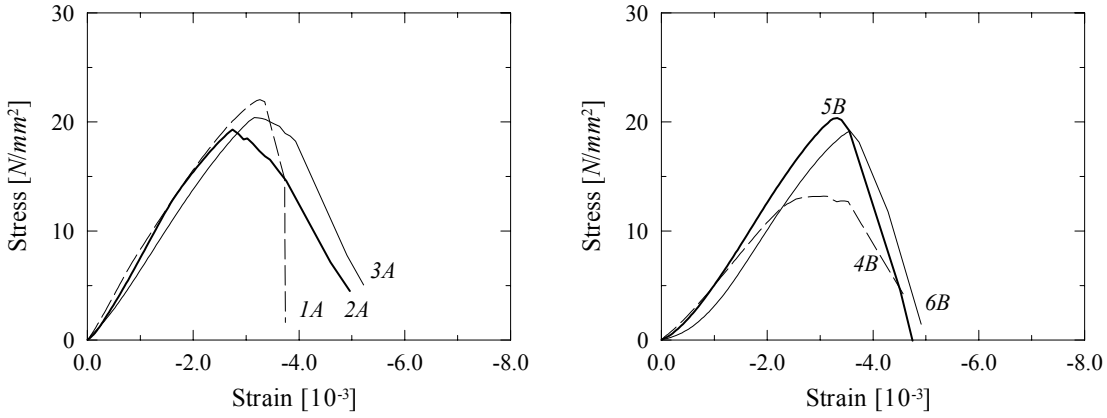

Figure B.2 – *Noto* stone compression diagrams given by the transducers positioned between plates for samples: (a) *1A*, *2A* and *3A*, (b) *4B*, *5B* and *6B*.

Table B.2 – Results of the compression tests on *Serena* stone specimens.

Specimen	Orientation (1)	f_c N/mm^2	E N/mm^2	ν -
1A	*A*	104.3	18045	0.21
2A	*A*	105.3	18840	0.19
3A	*A*	102.9	17765	0.18
4B	*B*	98.3	24650	0.23
5B	*B*	94.3	22940	0.24
6B	*B*	74.2	22285	0.18

(1) *A* stands for coring of the specimens along the *loading direction* of the units in the wallets and *B* for the *bedding direction*.

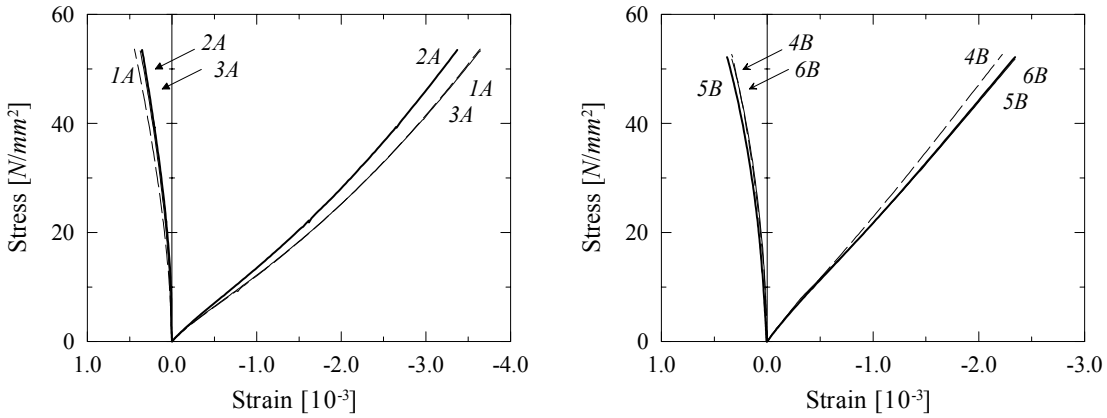

Figure B.3 – *Serena* stone compression diagrams up to 53 N/mm^2 (about 50% of of f_c) for specimens: (a) *1A*, *2A*, *3A* and (b) *4B*, *5B*, *6B*. Transversal strains are illustrated on the left side of the graphics and vertical strains on the right side.

Table B.3 – Results of tension tests for both *Noto* and *Serena* stone specimens. All tested specimens were cored along the bedding direction *B* of the units in the wallets.

Noto samples			*Serena* samples		
Specimen	Peak load *kN*	$f_{t,s}$ *N/mm²*	Specimen	Peak load *kN*	$f_{t,s}$ *N/mm²*
7B1	18.2	1.80	*7B1*	72.4	7.20
7B2	20.8	2.05	*7B2*	61.6	6.05
8B1	22.9	2.30	*8B1*	59.4	5.90
8B2	20.9	2.05	*8B2*	62.5	6.15
9B1	17.2	1.70	*9B1*	51.4	5.05
9B2	23.9	2.40	*9B2*	58.2	5.70

B.2 FLEXURAL AND COMPRESSIVE TESTS ON MORTAR SPECIMENS

Table B.4 – Results of the flexural and compressive tests on mortar specimens.

Prism	Curing time *days*	Batch	Flexion		Compression 1		Compression 2	
			Peak load *N*	f_f *N/mm²*	Peak load *N*	f_c *N/mm²*	Peak load *N*	f_c *N/mm²*
P1	28	first	637.7	1.60	11968.2	7.50	11772.0	7.35
P2	28	first	598.4	1.50	12360.6	7.75	11772.0	7.35
P3	28	first	608.2	1.50	12164.4	7.60	12654.9	7.90
P4	28	second	539.6	1.35	11673.9	7.30	11870.1	7.40
P5	28	second	588.6	1.45	11379.6	7.10	11477.7	7.15
P6	28	second	627.8	1.55	11575.8	7.25	11379.6	7.10
P7	75	first	843.7	2.10	15597.9	9.75	15205.5	9.50
P8	75	first	922.1	2.30	15401.7	9.65	15794.1	9.85
P9	75	first	765.2	1.90	15303.6	9.55	15303.6	9.55
P10	75	second	637.7	1.60	14028.3	8.75	14126.4	8.85
P11	75	second	775.0	1.95	13832.1	8.65	13832.1	8.65
P12	75	second	696.5	1.75	13930.2	8.70	13635.9	8.50
P13	90	first	1069.3	2.65	17167.5	10.75	17069.4	10.65
P14	90	first	892.7	2.25	15401.7	9.65	15794.1	9.85
P15	90	first	1000.6	2.50	16284.6	10.20	15892.2	9.95
P16	90	second	951.6	2.40	15009.3	9.40	15303.6	9.55
P17	90	second	804.4	2.00	14911.2	9.30	13537.8	8.45
P18	90	second	902.5	2.25	14028.3	8.75	15009.3	9.40
P19	172	first	775.0	1.95	17952.3	11.20	17167.5	10.75
P20	172	first	1010.4	2.55	18540.9	11.60	18442.8	11.55
P21	172	first	902.5	2.25	19031.4	11.90	18933.3	11.85
P22	172	second	863.3	2.15	15990.3	10.00	16971.3	10.60
P23	172	second	853.5	2.15	17363.7	10.85	17952.3	11.20
P24	172	second	941.8	2.35	17854.2	11.15	18050.4	11.30

B.3 SHEAR TESTS: LOAD-DISPLACEMENT DIAGRAMS

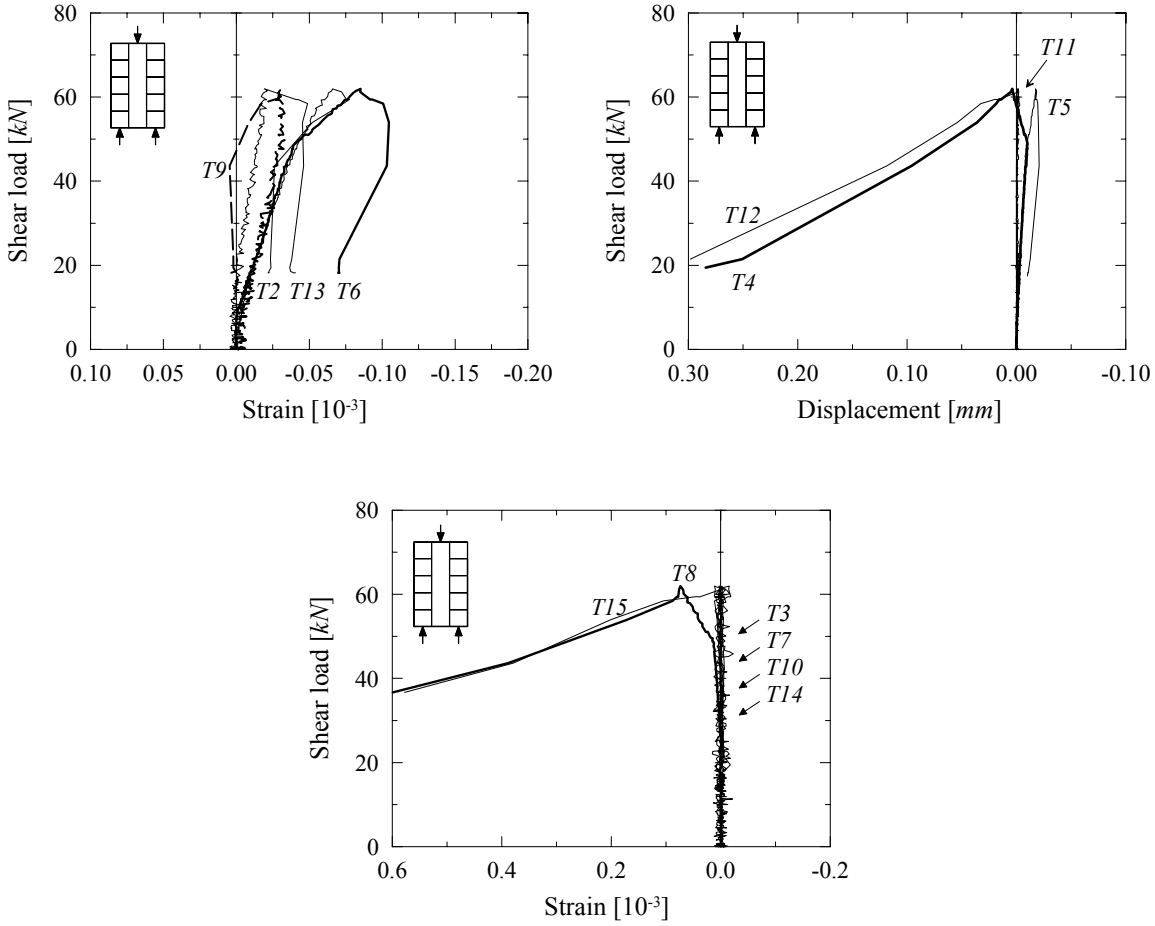

Figure B.4 – Load-displacement diagrams for wallet *NS1*. Positive sign is adopted for elongation and negative for contraction.

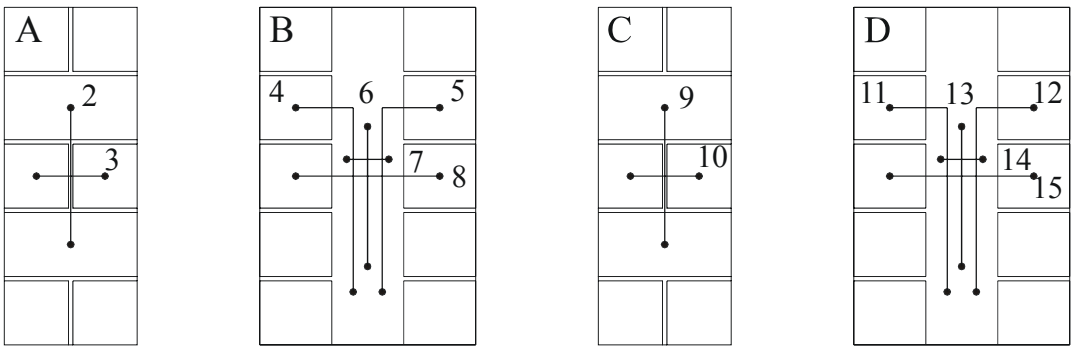

Figure B.5 – Position of the transducers for wallet *NS1*.

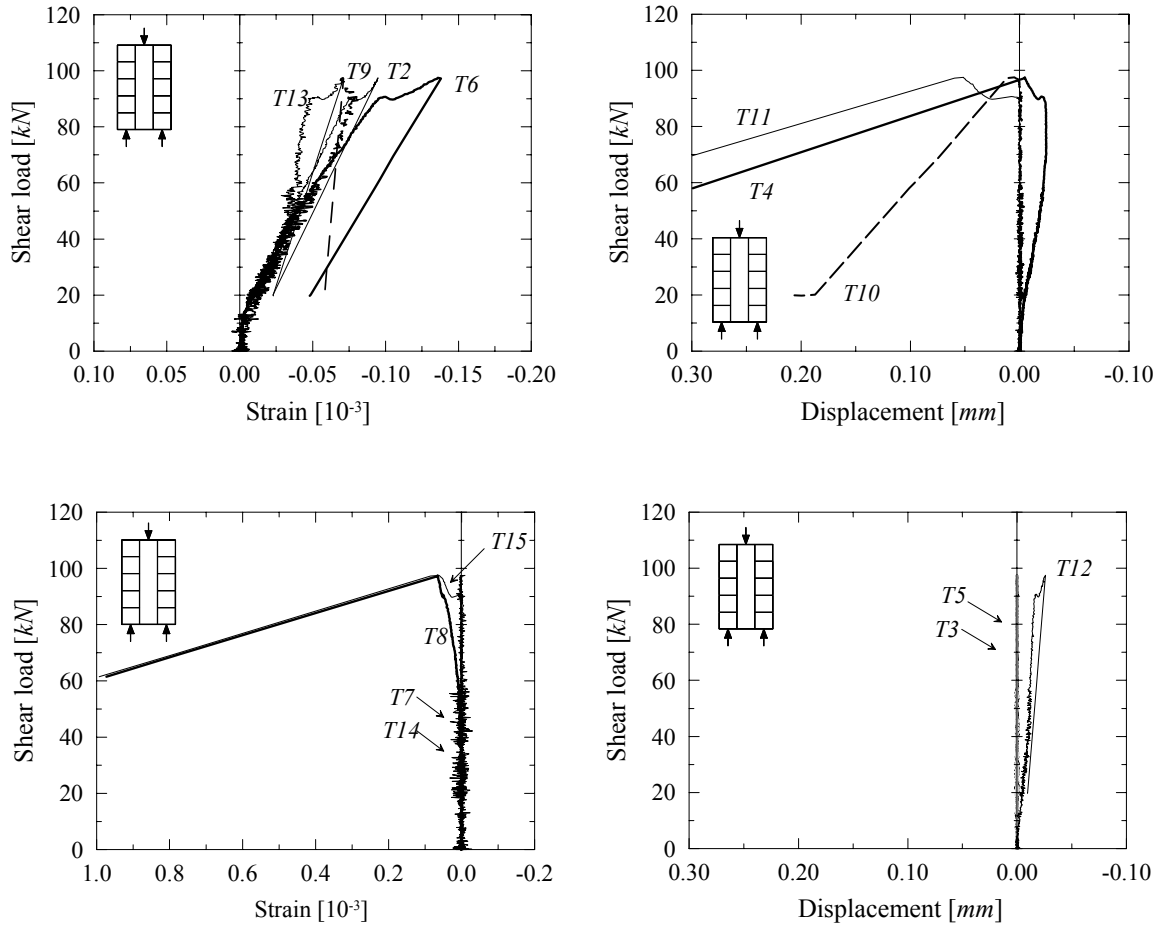

Figure B.6 – Load-displacement diagrams for wallet *NS2*. Positive sign is adopted for elongation and negative for contraction.

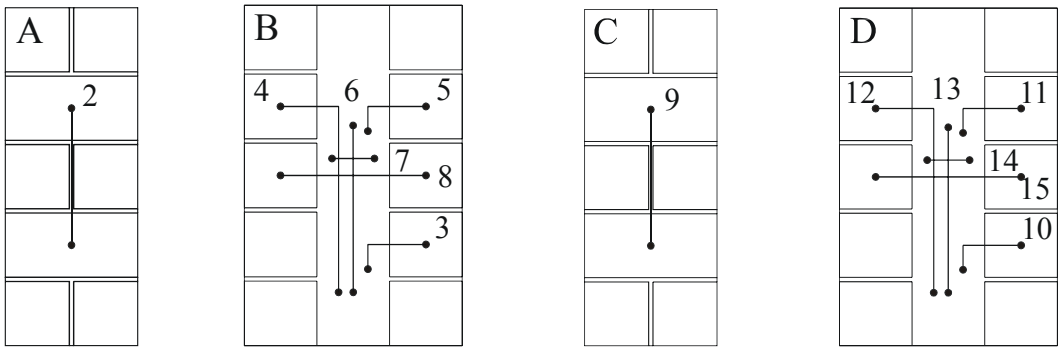

Figure B.7 – Position of the transducers for wallet *NS2*.

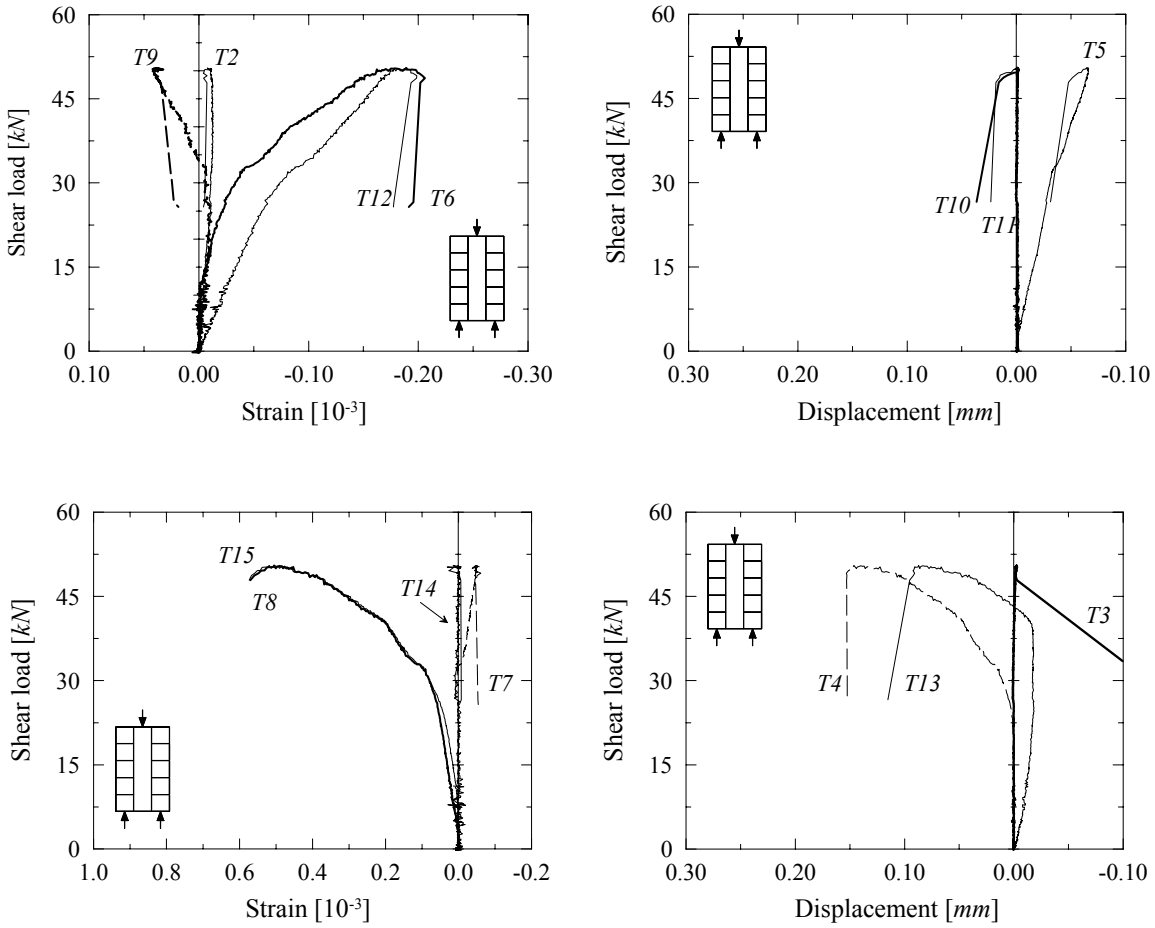

Figure B.8 – Load-displacement diagrams for wallet *SS1*. Positive sign is adopted for elongation and negative for contraction.

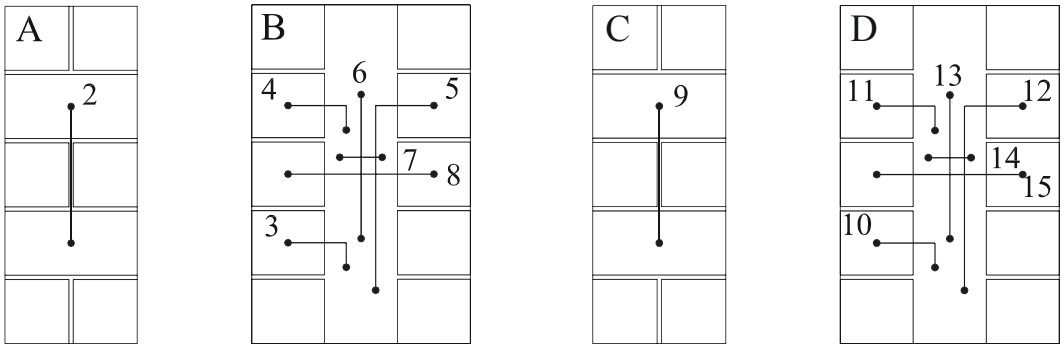

Figure B.9 – Position of the transducers for wallet *SS1*.

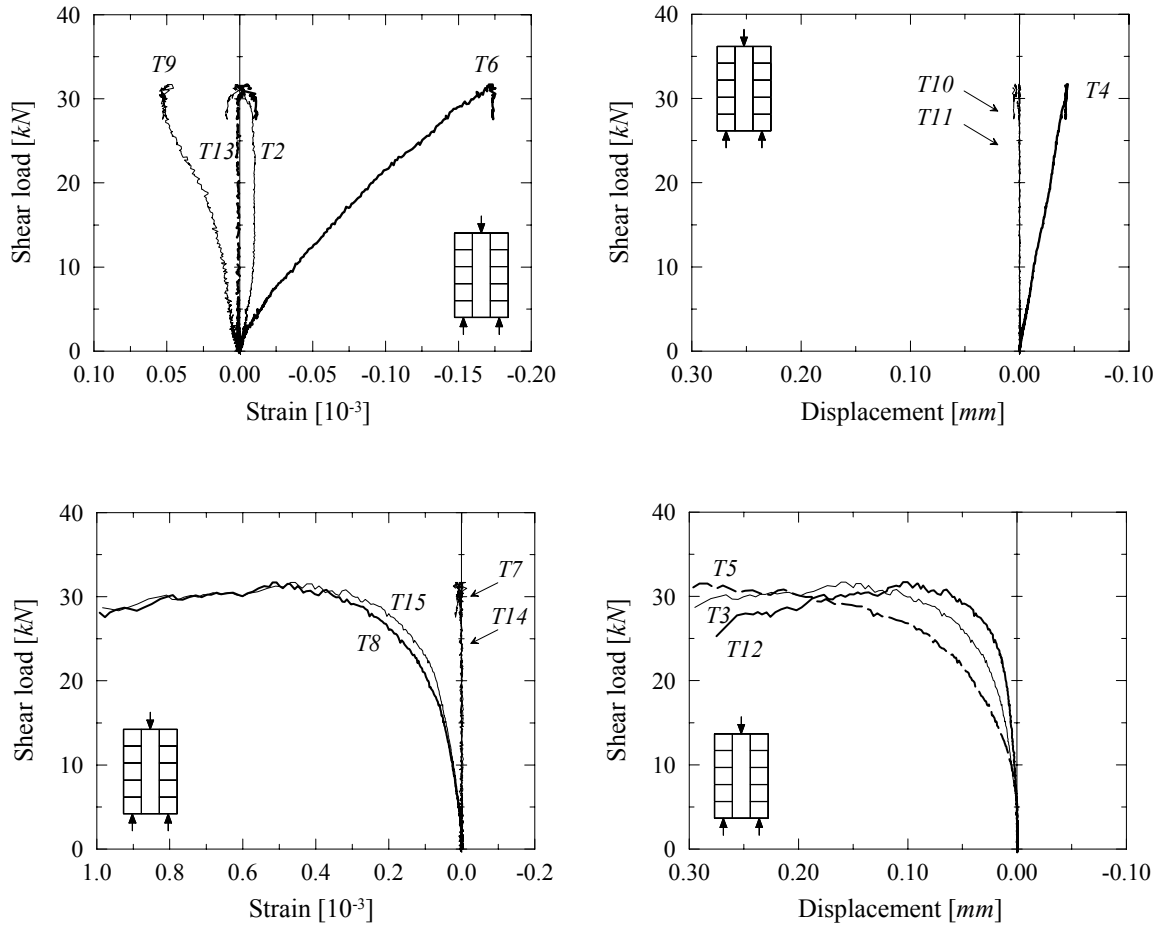

Figure B.10 – Load-displacement diagrams for wallet *SS2*. Positive sign is adopted for elongation and negative for contraction.

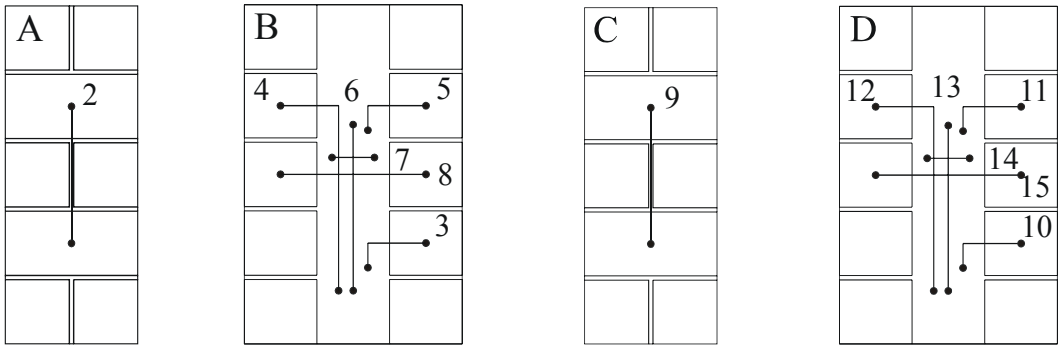

Figure B.11 – Position of the transducers for wallet *SS2*.

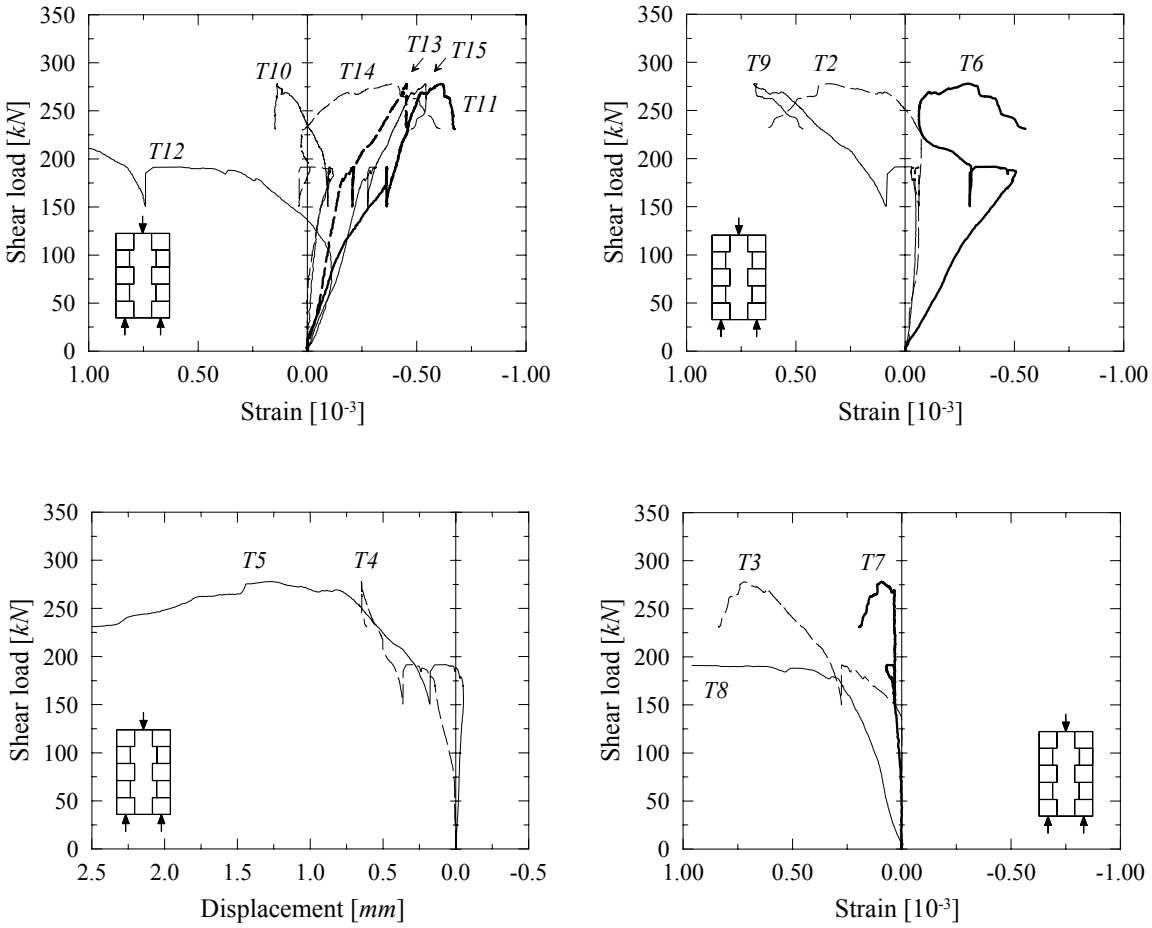

Figure B.12 – Load-displacement diagrams for wallet *NK1*. Positive sign is adopted for elongation and negative for contraction.

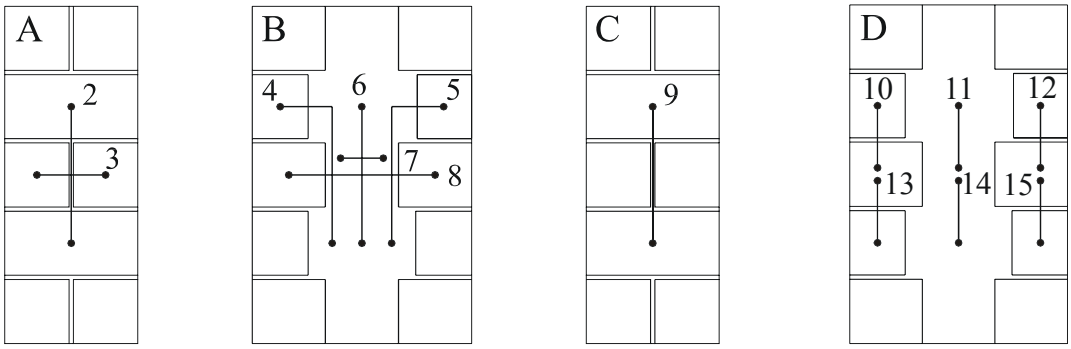

Figure B.13 – Position of the transducers for wallet *NK1*.

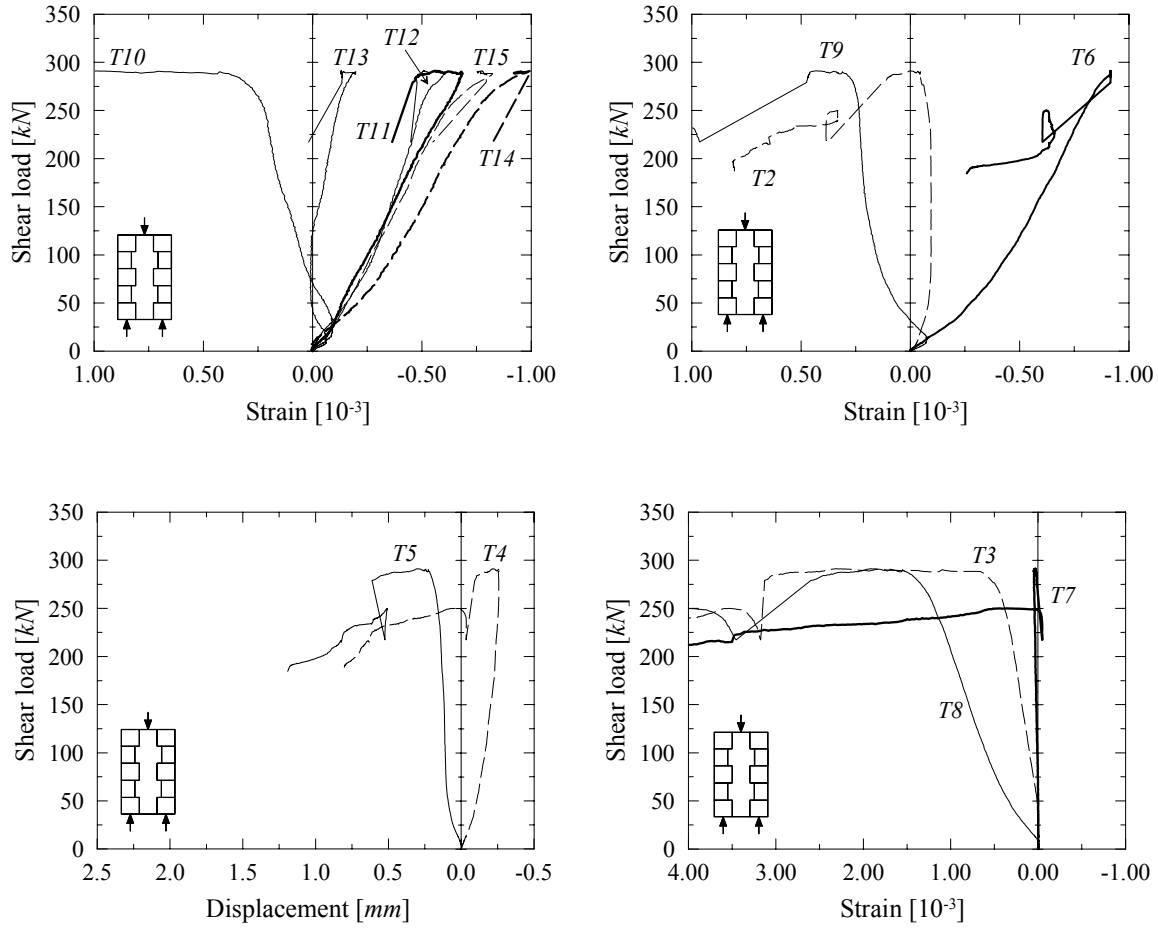

Figure B.14 – Load-displacement diagrams for wallet *NK2*. Positive sign is adopted for elongation and negative for contraction.

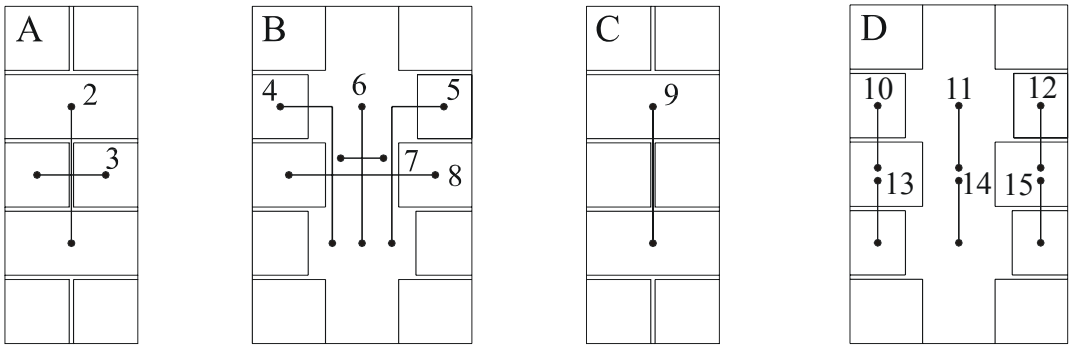

Figure B.15 – Position of the transducers for wallet *NK2*.

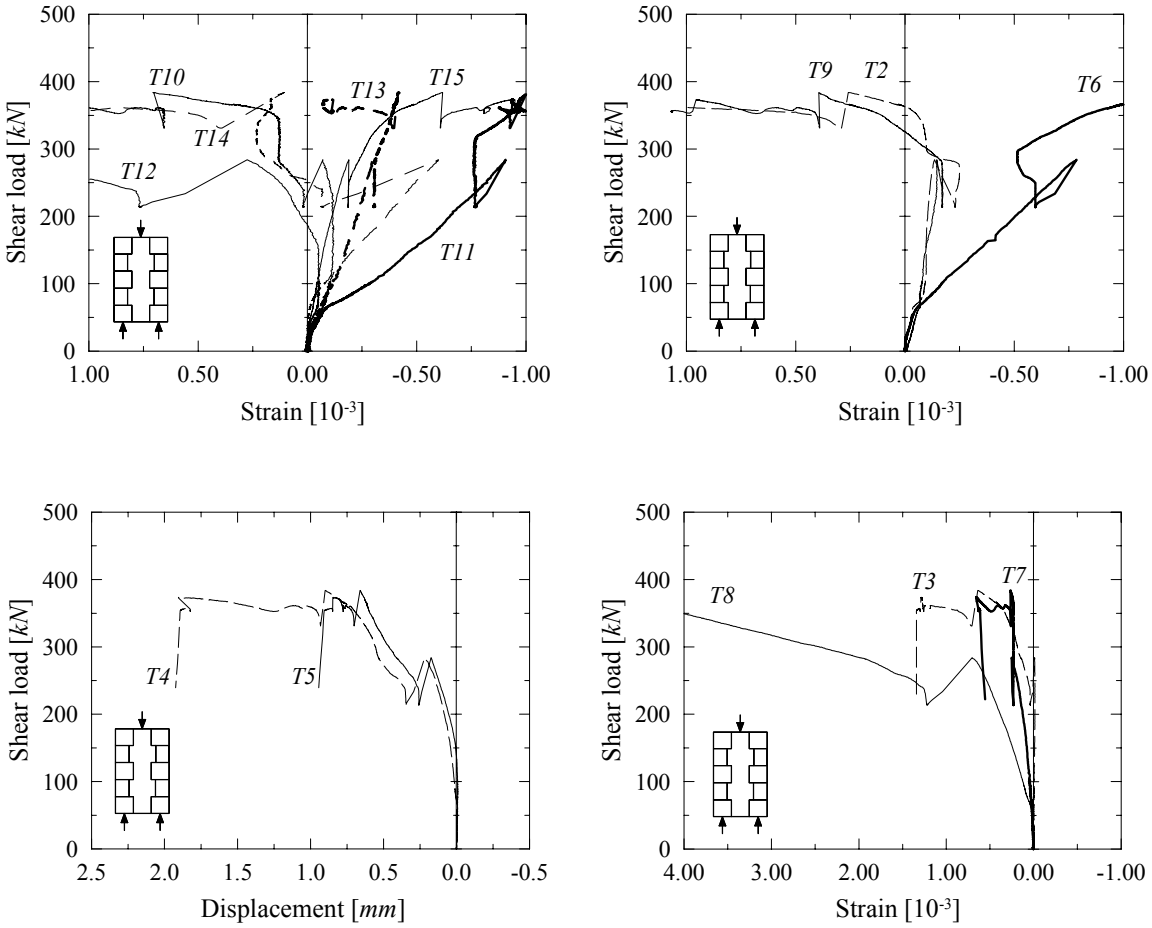

Figure B.16 – Load-displacement diagrams for wallet *SK1*. Positive sign is adopted for elongation and negative for contraction.

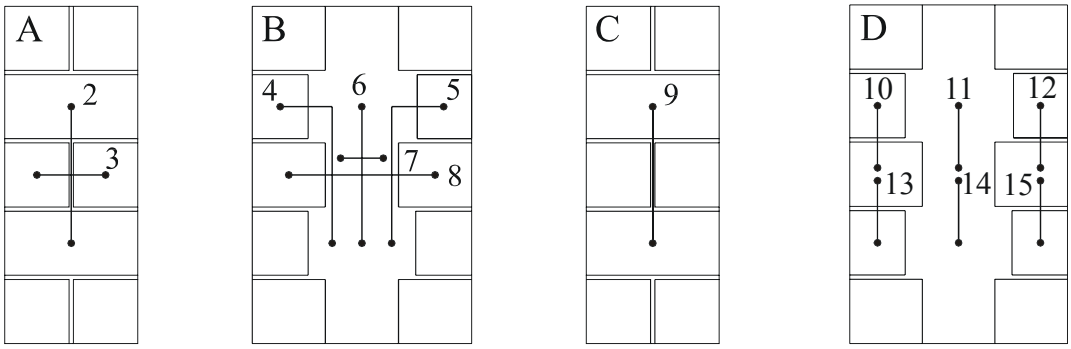

Figure B.17 – Position of the transducers for wallet *SK1*.

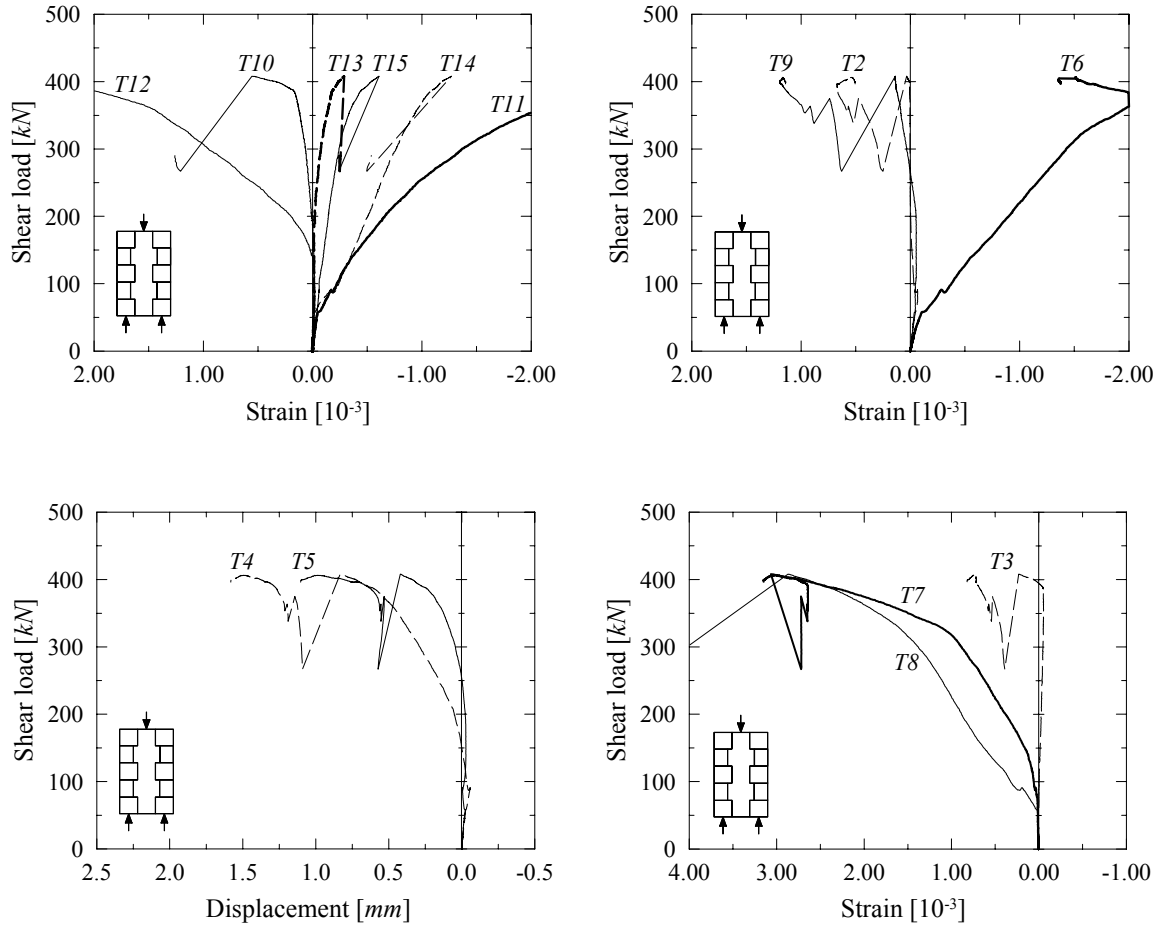

Figure B.18 – Load-displacement diagrams for wallet *SK2*. Positive sign is adopted for elongation and negative for contraction.

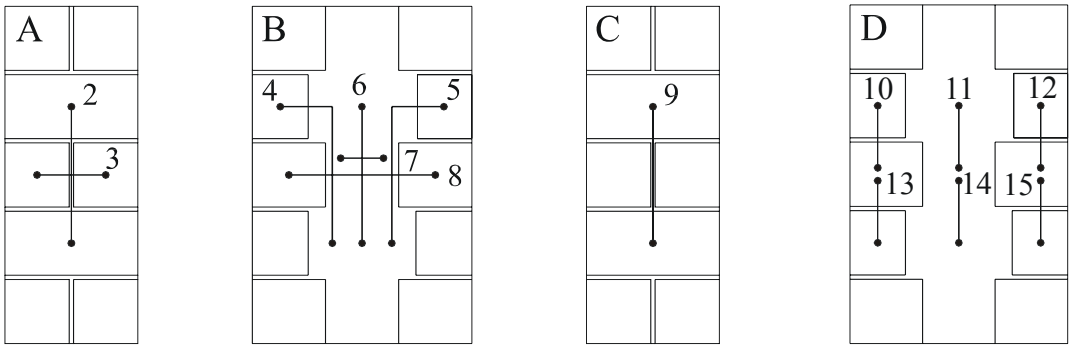

Figure B.19 – Position of the transducers for wallet *SK2*.

B.4 SHEAR TESTS: CRACK PATTERNS

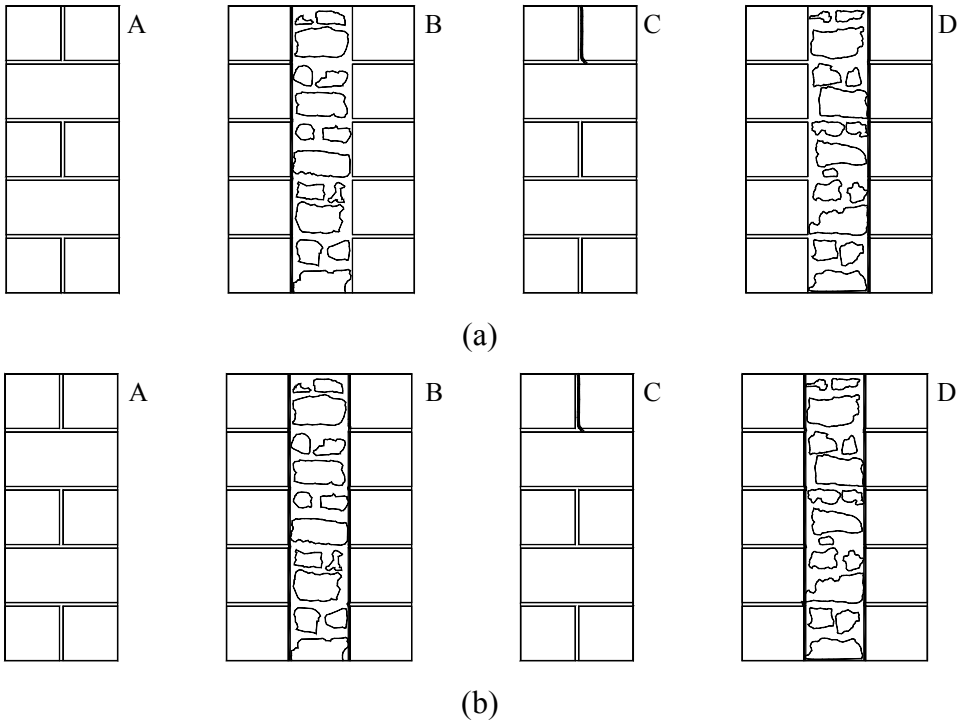

Figure B.20 – Crack pattern for *NS1* at: (a) 62 *kN* (failure of the first connection) and (b) 43 *kN* (failure of the second connection).

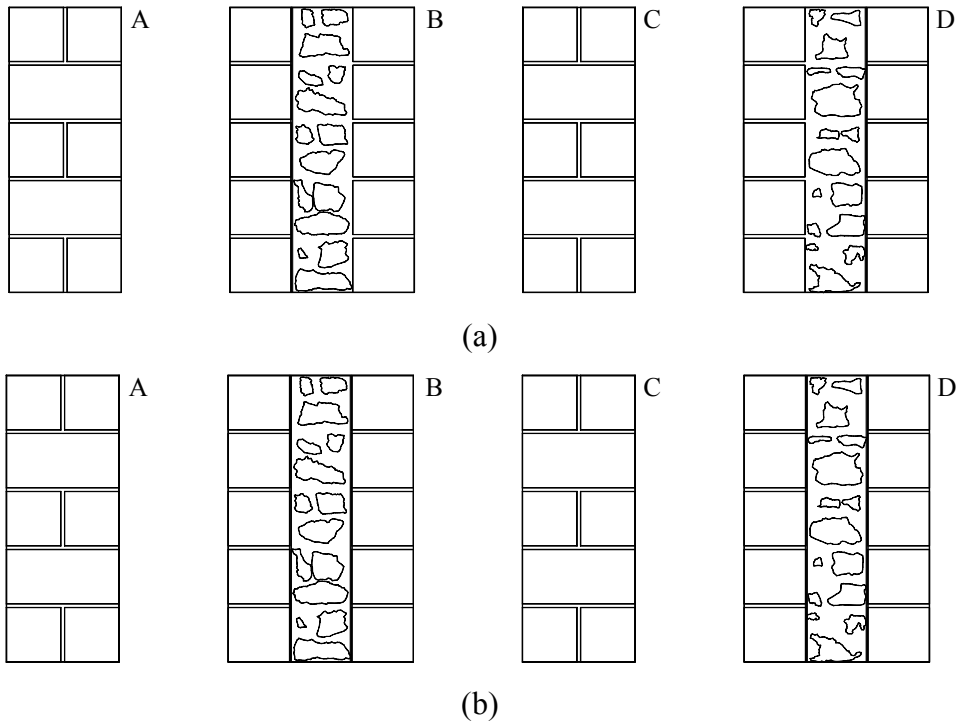

Figure B.21 – Crack pattern for *NS2* at: (a) 97 *kN* (failure of the first connection), (b) 60 *kN* (failure of the second connection).

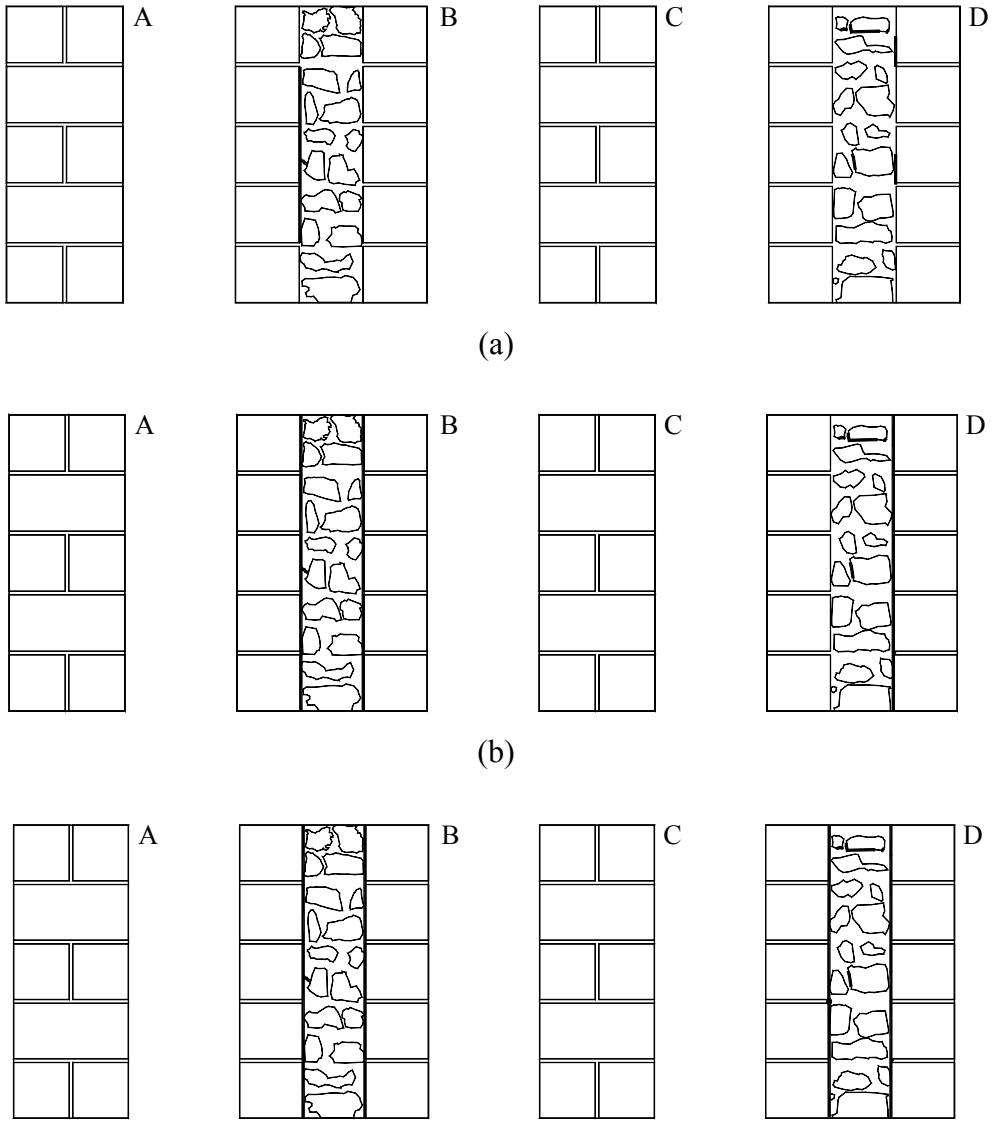

Figure B.22 – Crack pattern for *SS1* at: (a) 29 *kN* (51% of of f_c), (b) 50 *kN* (peak load - failure of the first connection) and (c) 29 *kN* (failure of the second connection).

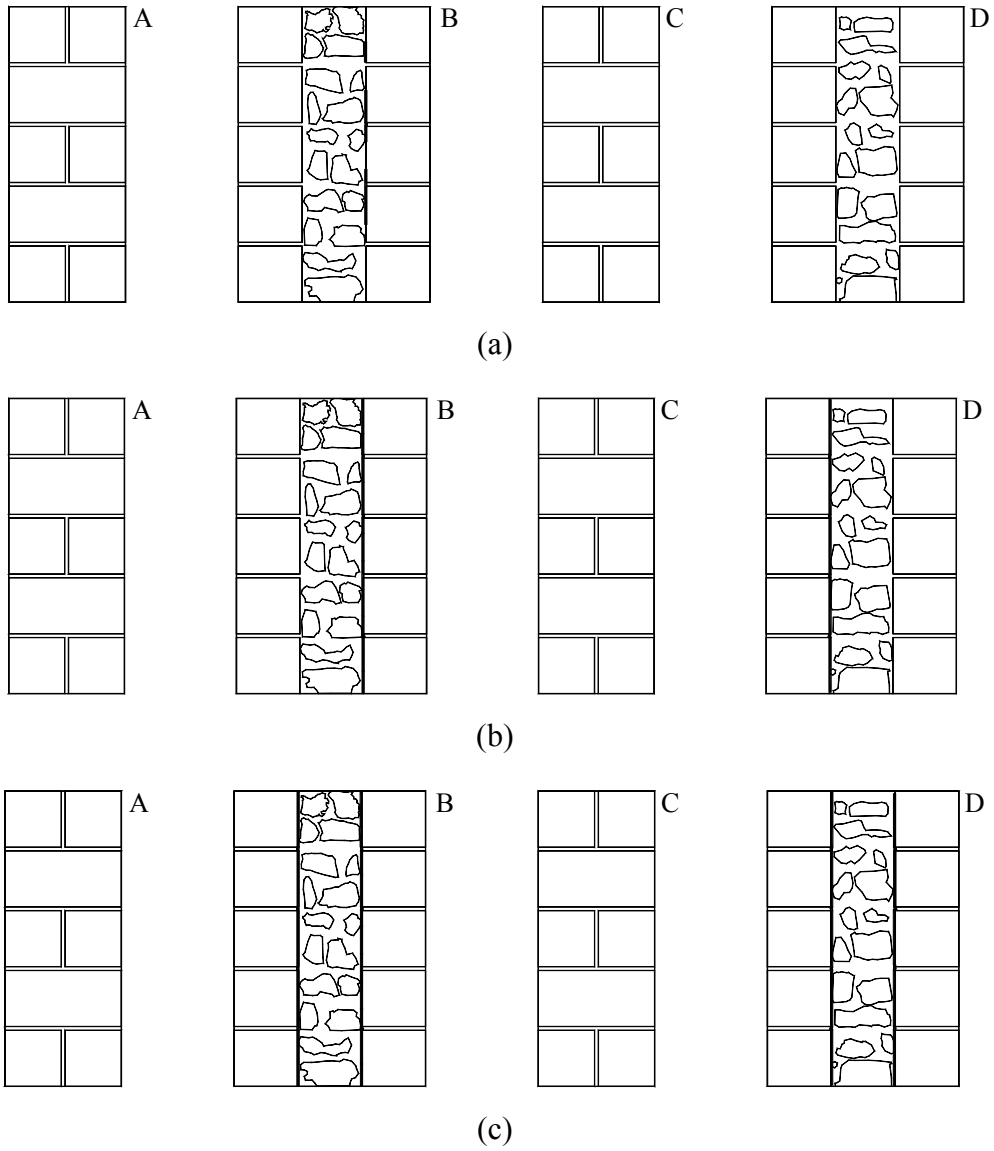

Figure B.23 – Crack pattern for *SS2* at: (a) 25 *kN* (78% of f_c), (b) 32 *kN* (peak load - failure of the first connection) and (c) 25 *kN* (failure of the second connection).

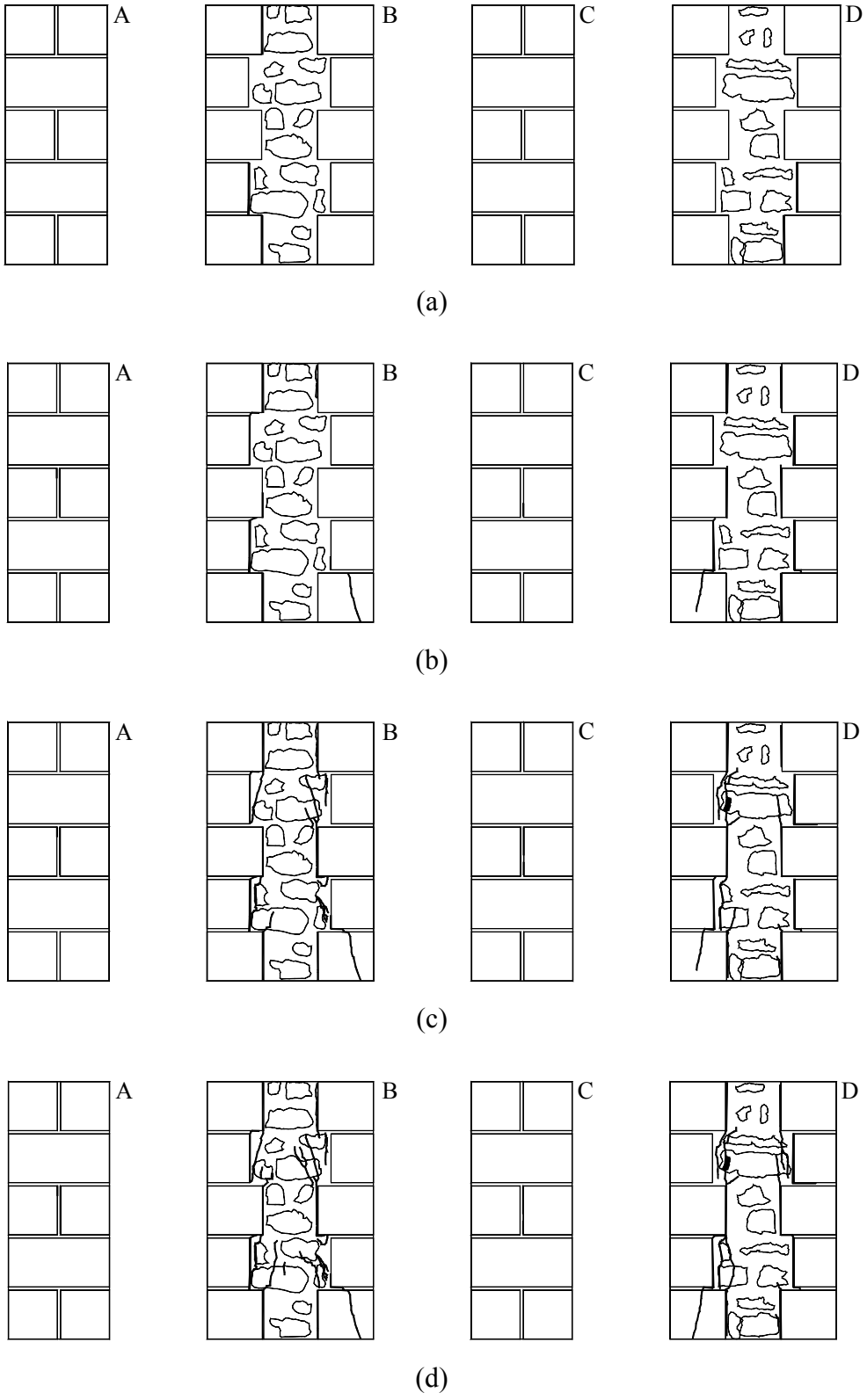

Figure B.24 – Crack pattern for *NK1*: (a) prior to test, (b) at 137 *kN* (50% of f_c), (c) at 278 *kN* (peak load) and (d) at 179 *kN* (64% of f_c, post-peak regime).

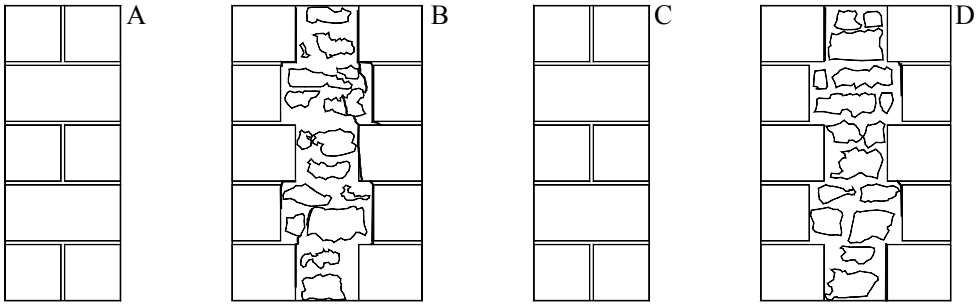

(a)

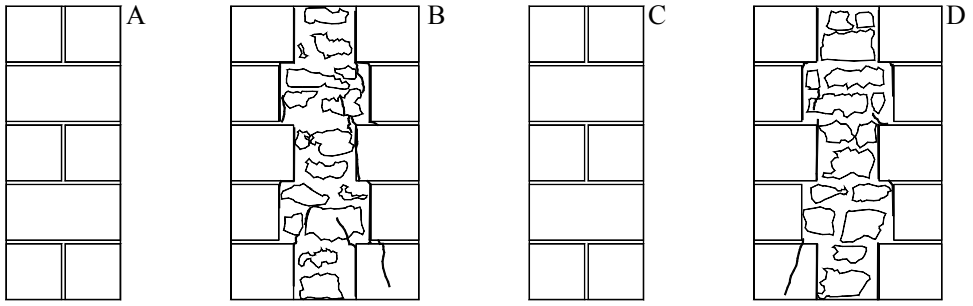

(b)

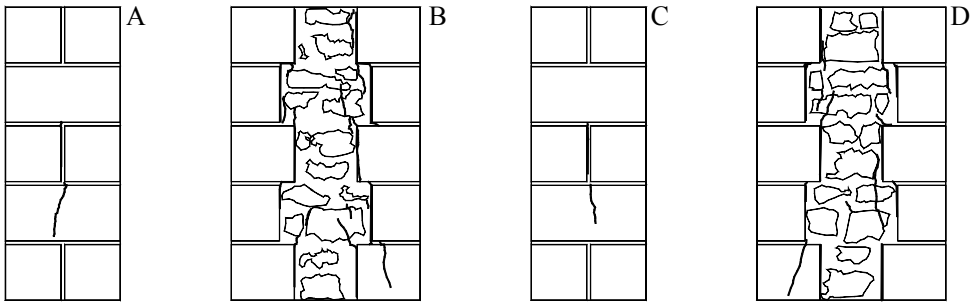

(c)

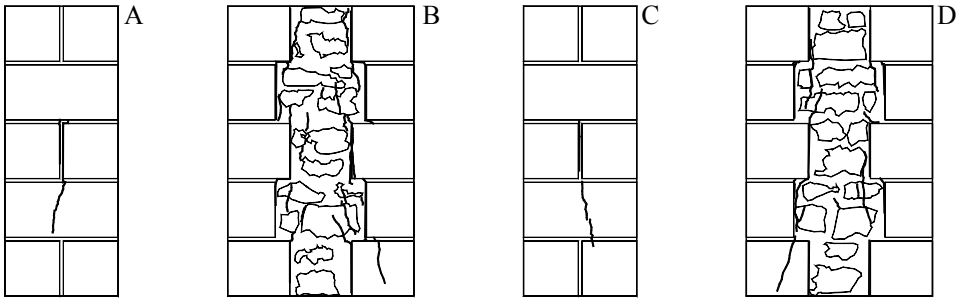

(d)

Figure B.25 – Crack pattern for *NK2*: (a) prior to test, (b) at 162 *kN* (55% of f_c), (c) at 291 *kN* (peak load) and (d) at 188 *kN* (65% of f_c, post-peak regime).

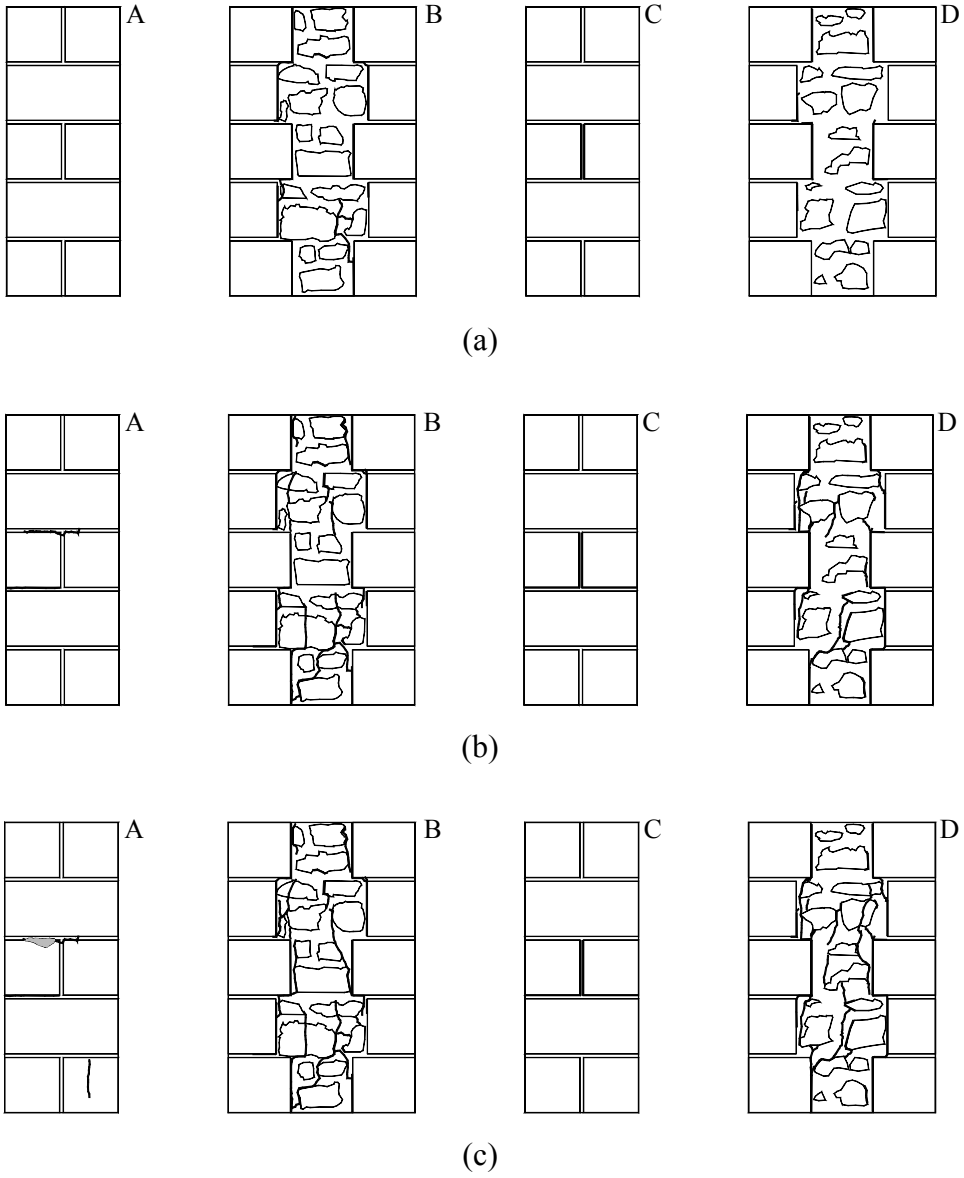

Figure B.26 – Crack pattern for *SK1* at: (a) 235 *kN* (61% of f_c), (b) 383 *kN* (peak load) and (c) 350 *kN* (91% of f_c, post-peak regime).

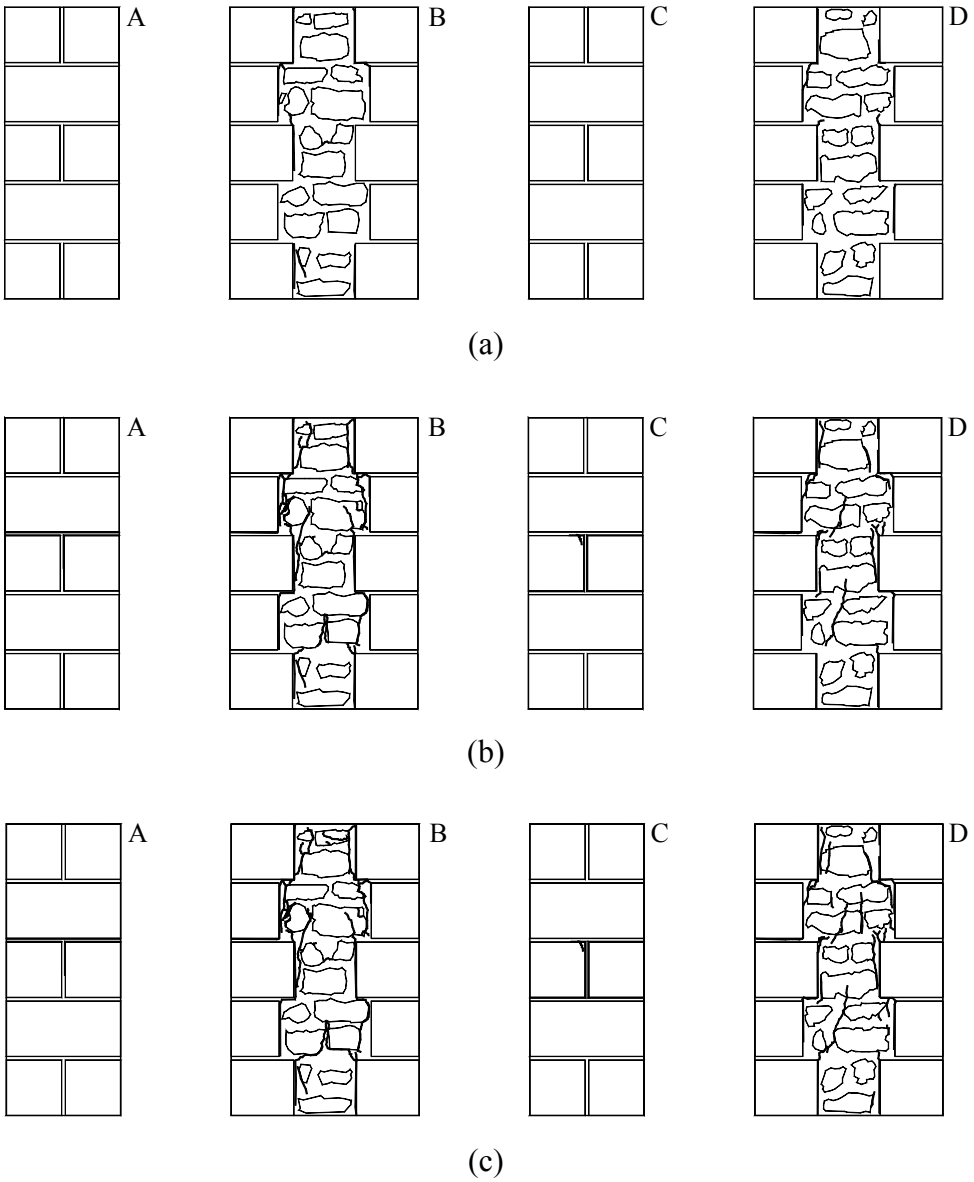

Figure B.27 – Crack pattern for *SK2* at: (a) 240 *kN* (59% of f_c), (b) 408 *kN* (peak load) and (c) 395 *kN* (97% of f_c, post-peak regime).

B.5 COMPRESSION TESTS ON SINGLE LEAVES: STRESS-STRAIN DIAGRAMS

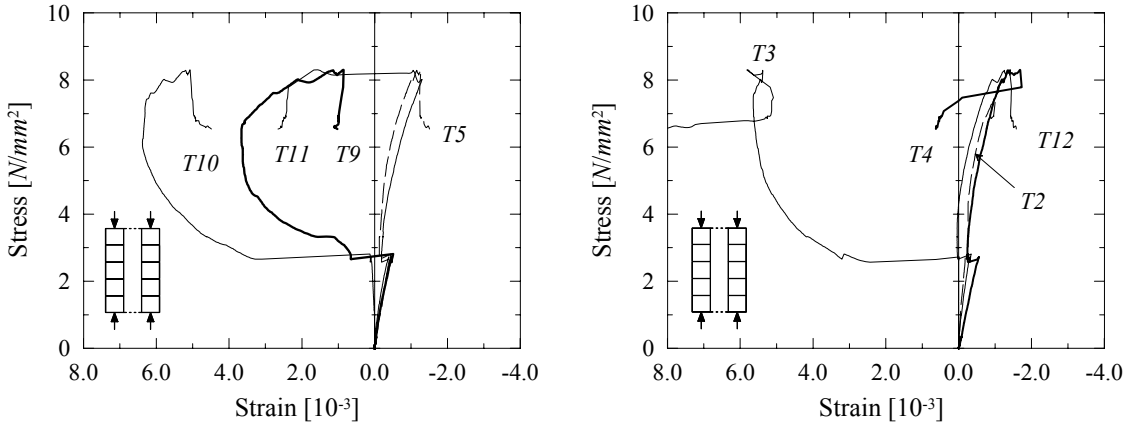

Figure B.28 – Load-deformation diagrams for leaves *NS2_E*. Positive sign is adopted for elongation and negative for contraction.

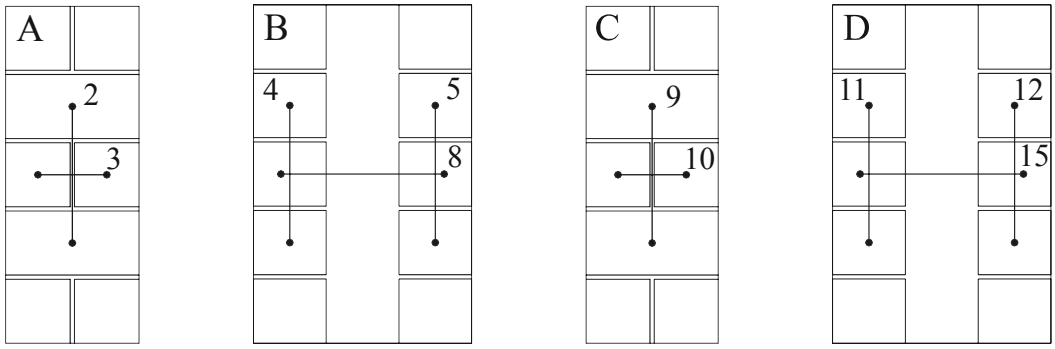

Figure B.29 – Position of the transducers for leaves *NS2_E*.

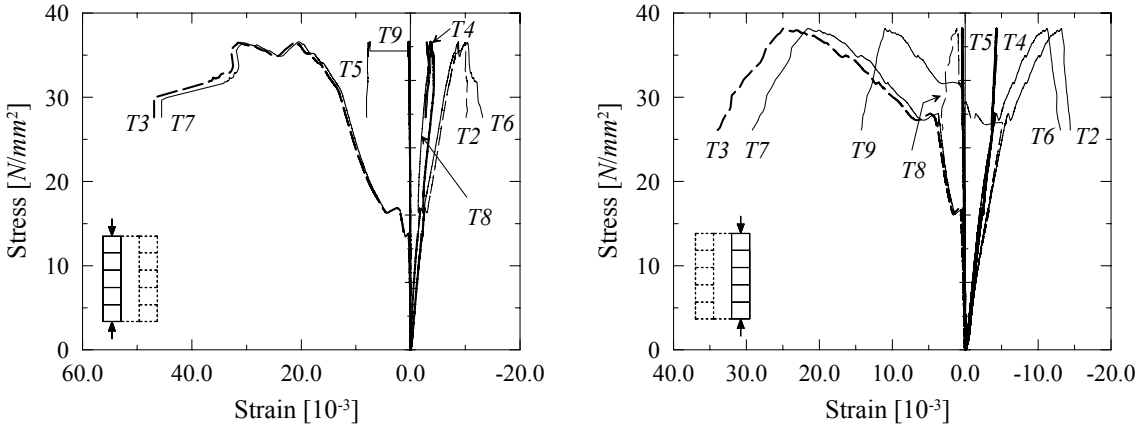

(a) (b)

Figure B.30 – Load-deformation diagrams for leaves (a) *SS1_E1* and (b) *SS1_E2*. Positive sign is adopted for elongation and negative for contraction.

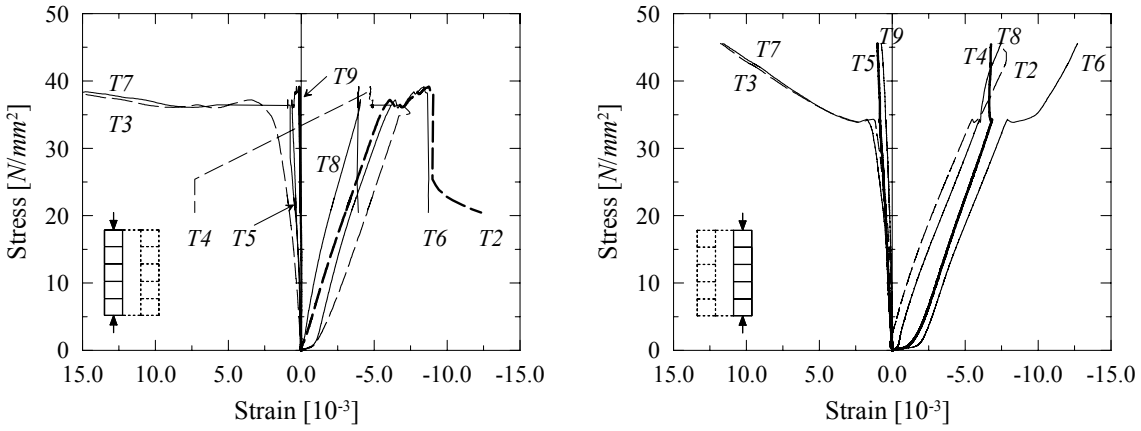

(a) (b)

Figure B.31 – Load-deformation diagrams for wallets (a) *SS2_E1* and (b) *SS2_E2*. Positive sign is adopted for elongation and negative for contraction.

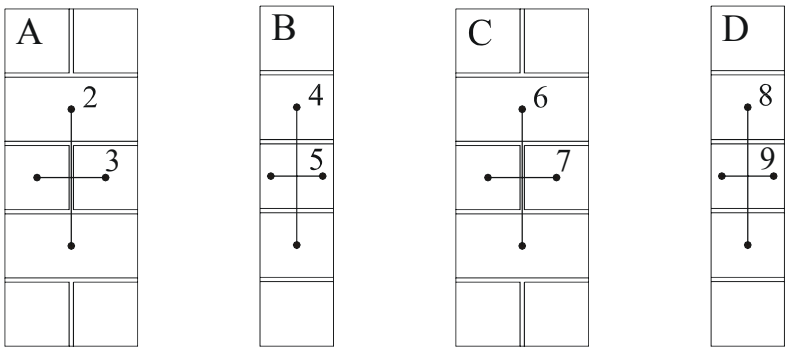

Figure B.32 – Position of the transducers for leaves *SS1_E1*, *SS1_E2*, *SS2_E1* and *SS2_E2*.

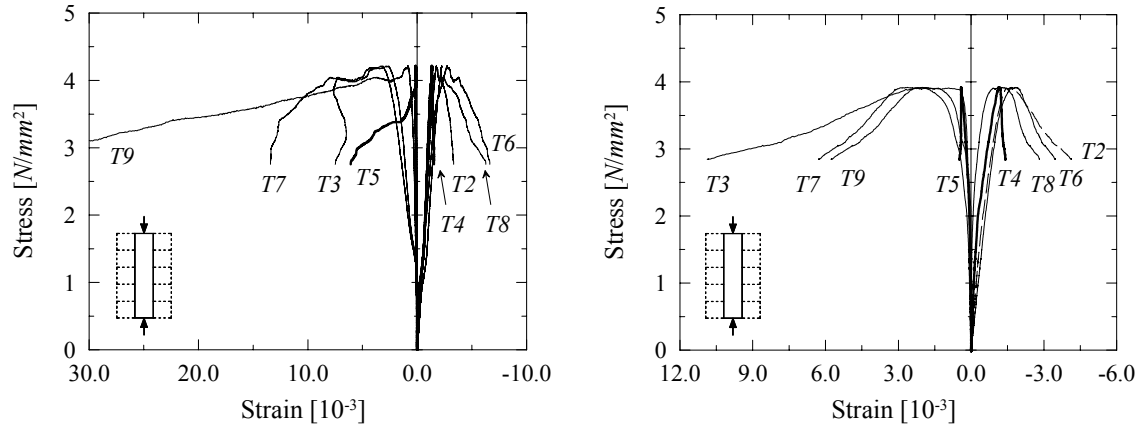

(a) (b)

Figure B.33 – Load-deformation diagrams for leaves *NS1_I*. and *NS2_I*. Positive sign is adopted for elongation and negative for contraction.

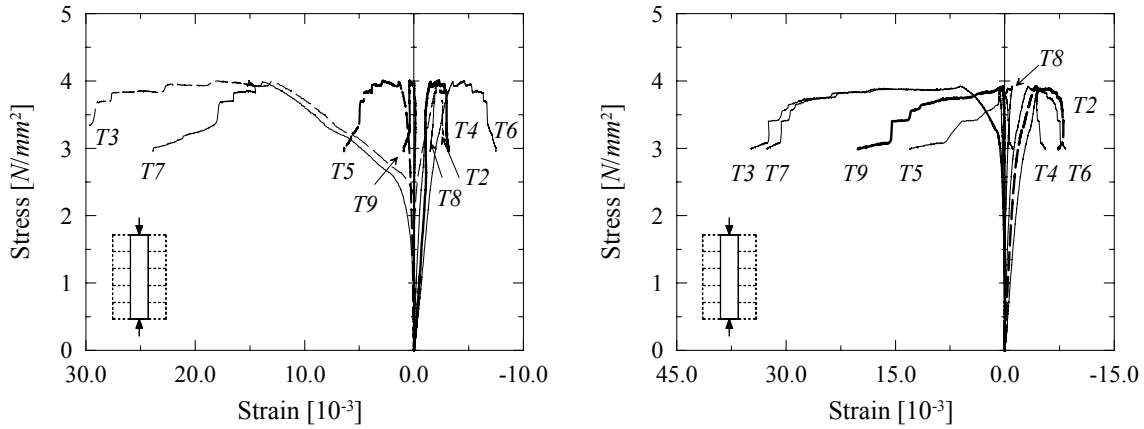

(a) (b)

Figure B.34 – Load-deformation diagrams for leaves *SS1_I* and *SS2_I*. Positive sign is adopted for elongation and negative for contraction.

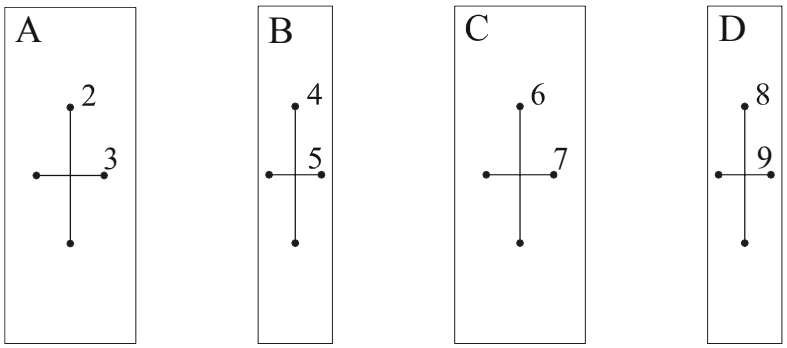

Figure B.35 – Position of the transducers for leaves *NS1_I*, *NS2_I*, *SS1_I* and *SS2_I*.

B.6 COMPRESSION TESTS ON SINGLE LEAVES: CRACK PATTERNS

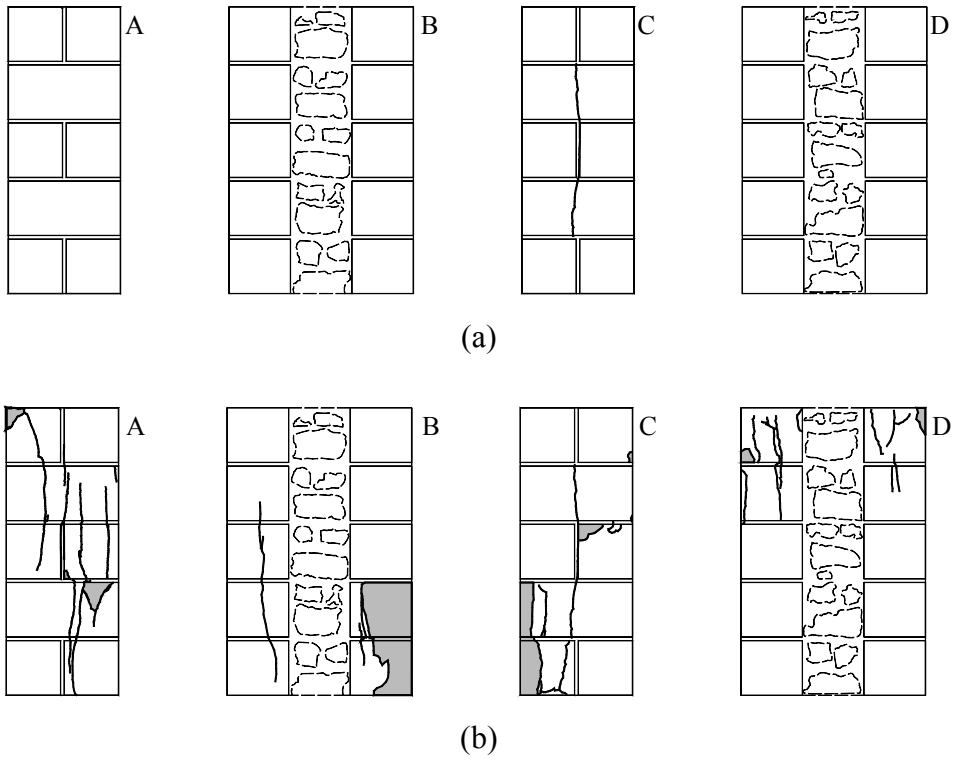

Figure B.36 – Crack pattern for *NS1_E*: (a) 588 *kN* (60% of f_c) and (b) 951 *kN* (peak load). Due to a problem in the data acquisition system, the specimen had to be unloaded immediately after reaching the peak load.

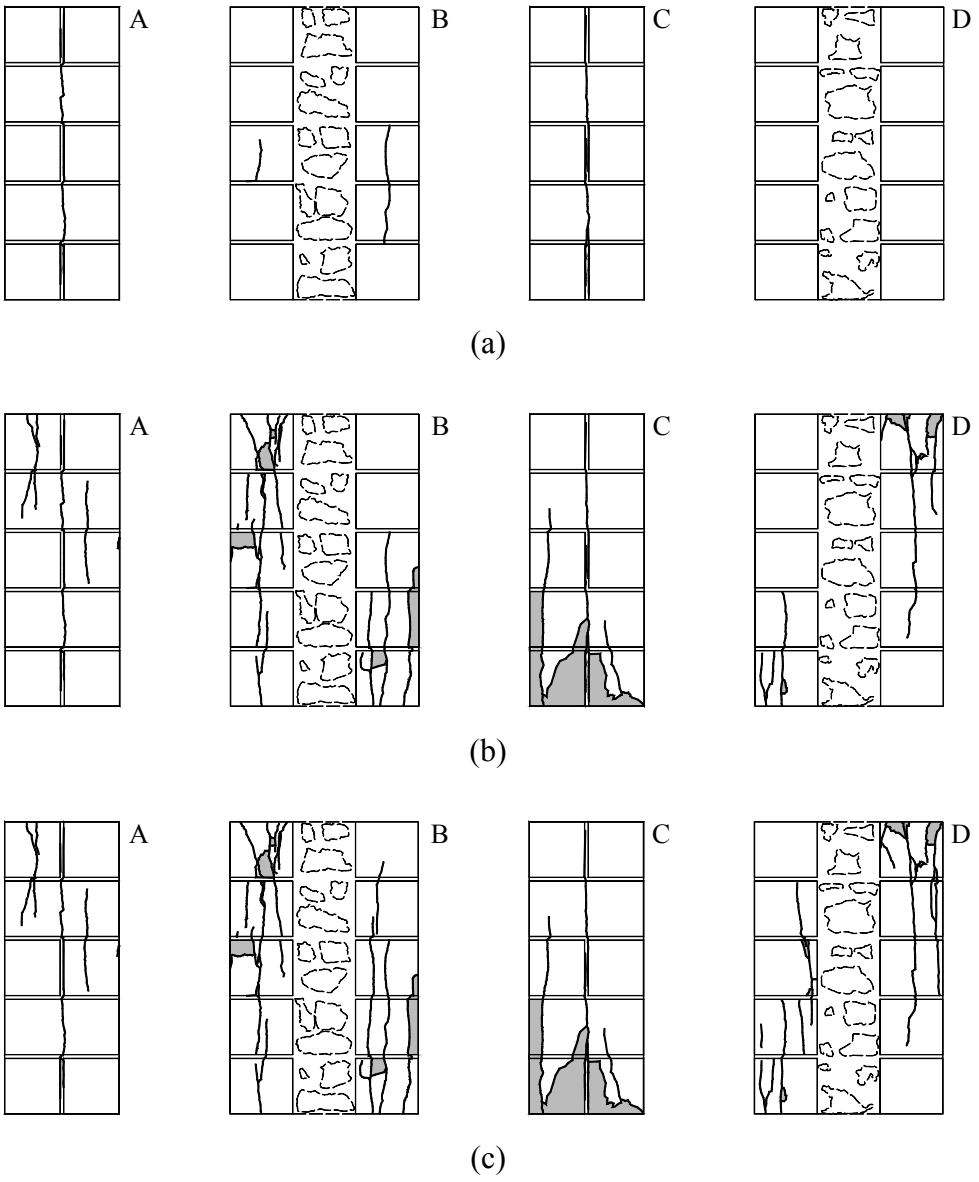

Figure B.37 – Crack pattern for *NS2_E* at: (a) 421 *kN* (48% of f_c), (b) 874 *kN* (peak load) and (c) 296 *kN* (34% of f_c, post-peak regime).

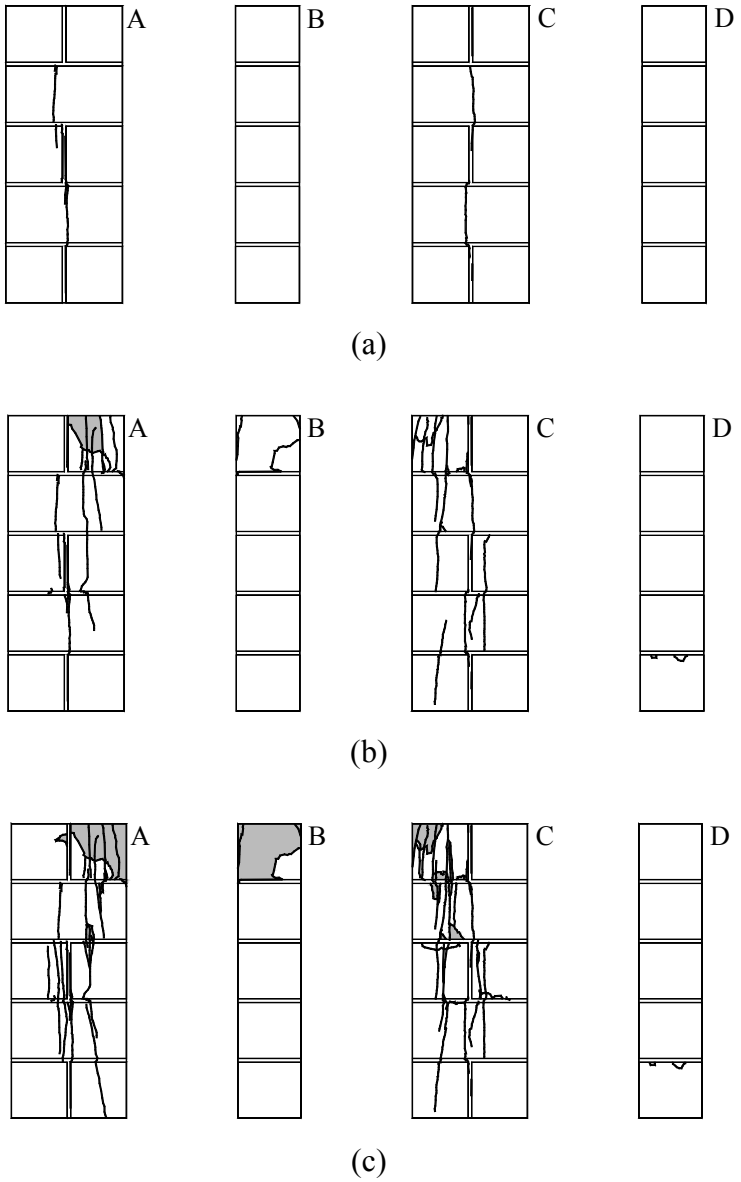

Figure B.38 – Crack pattern for *SS1_E1* at: (a) 882 *kN* (46% of f_c), (b) 1926 *kN* (peak load) and (c) 1417 *kN* (74% of f_c, post-peak regime).

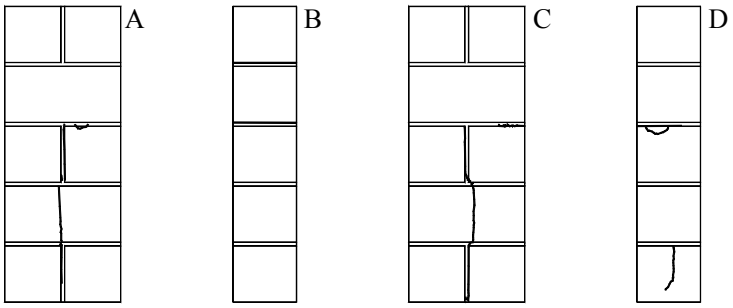

(a)

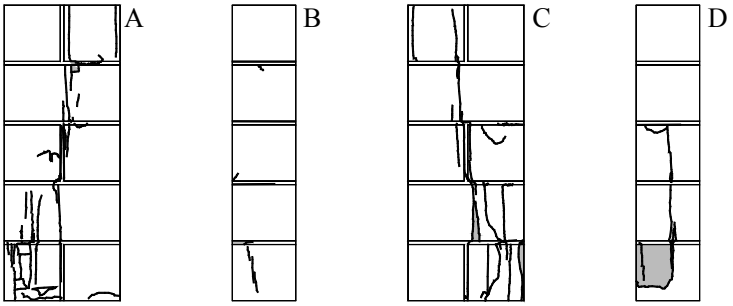

(b)

Figure B.39 – Crack pattern for *SS1_E2* at: (a) 1275 *kN* (63% of f_c) and (b) 2011 *kN* (peak load).

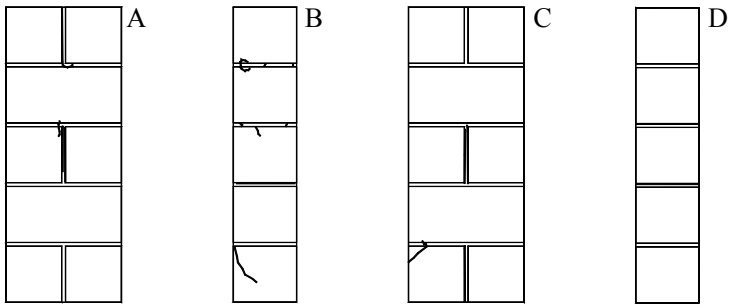

(a)

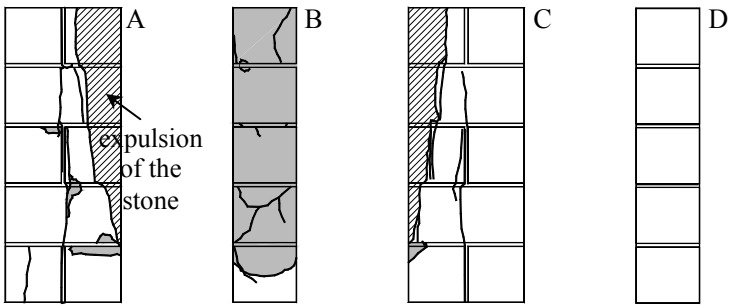

(b)

Figure B.40 – Crack pattern for *SS2_E1* at: (a) 1833 *kN* (89% of f_c) and (b) 2061 *kN* (peak load).

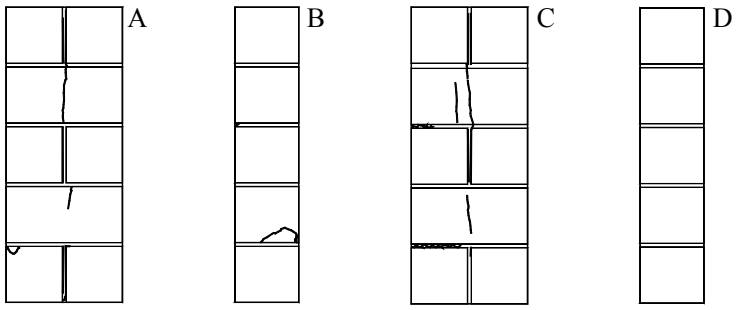

(a)

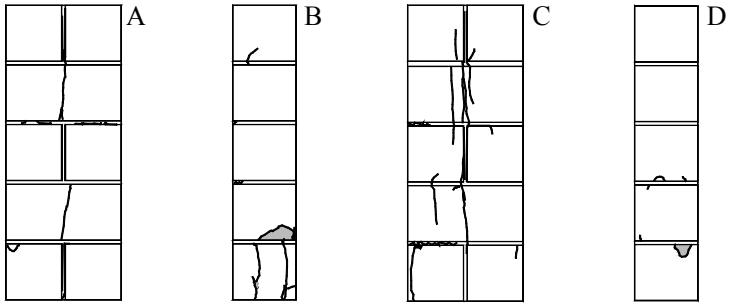

(b)

Figure B.41 – Crack pattern for *SS2_E2* at: (a) 1800 *kN* (76% of of the maximum load reached) and (b) 2380 *kN* (maximum load reached).

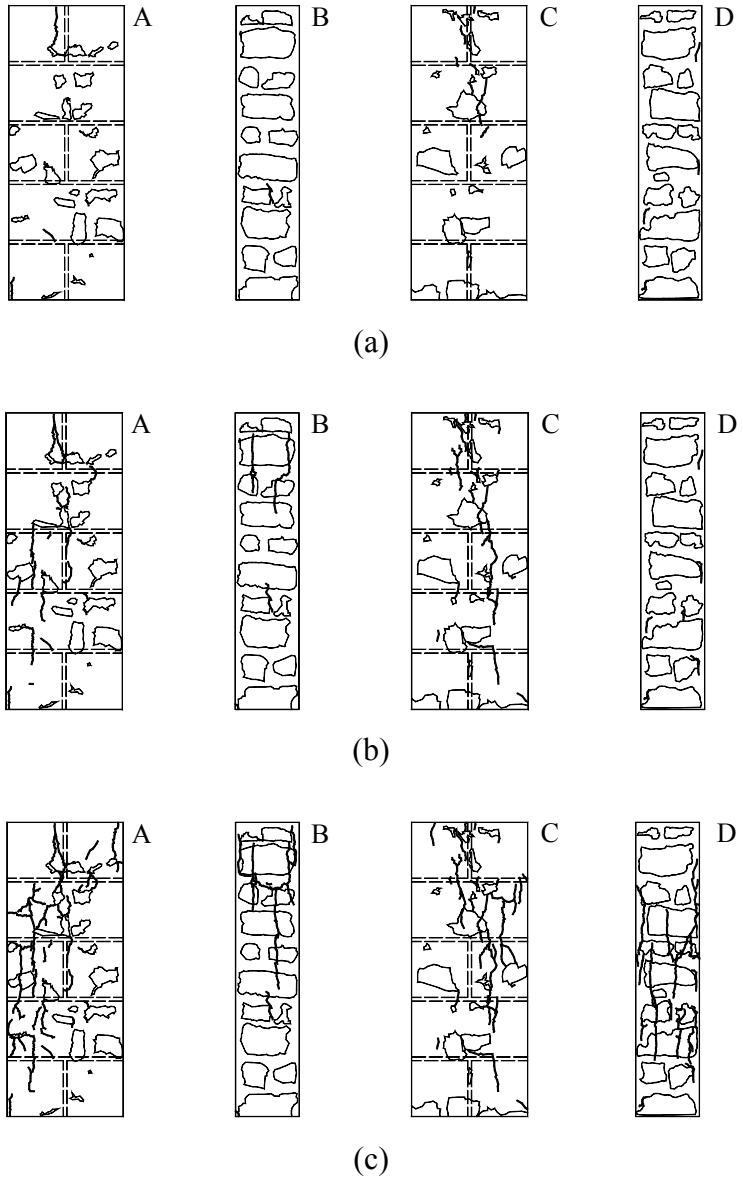

Figure B.42 – Crack pattern for *NS1_I* at: (a) 139 *kN* (63% of f_c), (b) 222 *kN* (peak load) and (c) 146 *kN* (66% of f_c, post-peak regime).

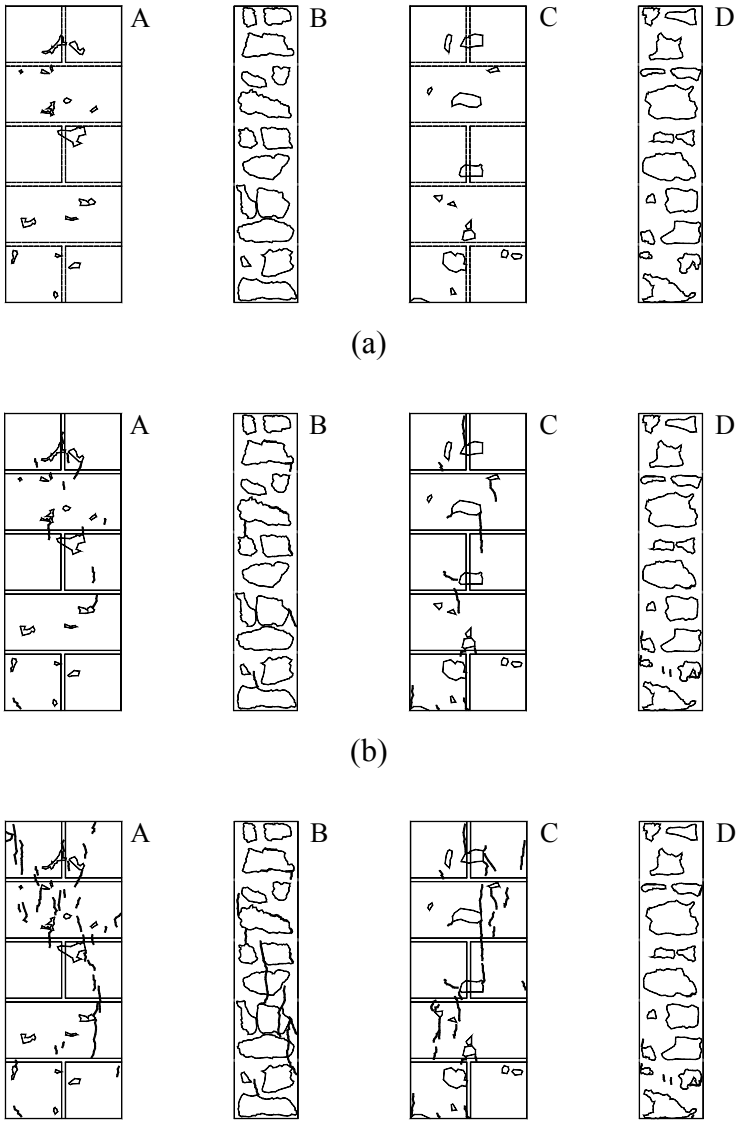

Figure B.43 – Crack pattern for *NS2_I* at: (a) 124 *kN* (60% of f_c), (b) 206 *kN* (peak load) and (c) 148 *kN* (72% of f_c, post-peak regime).

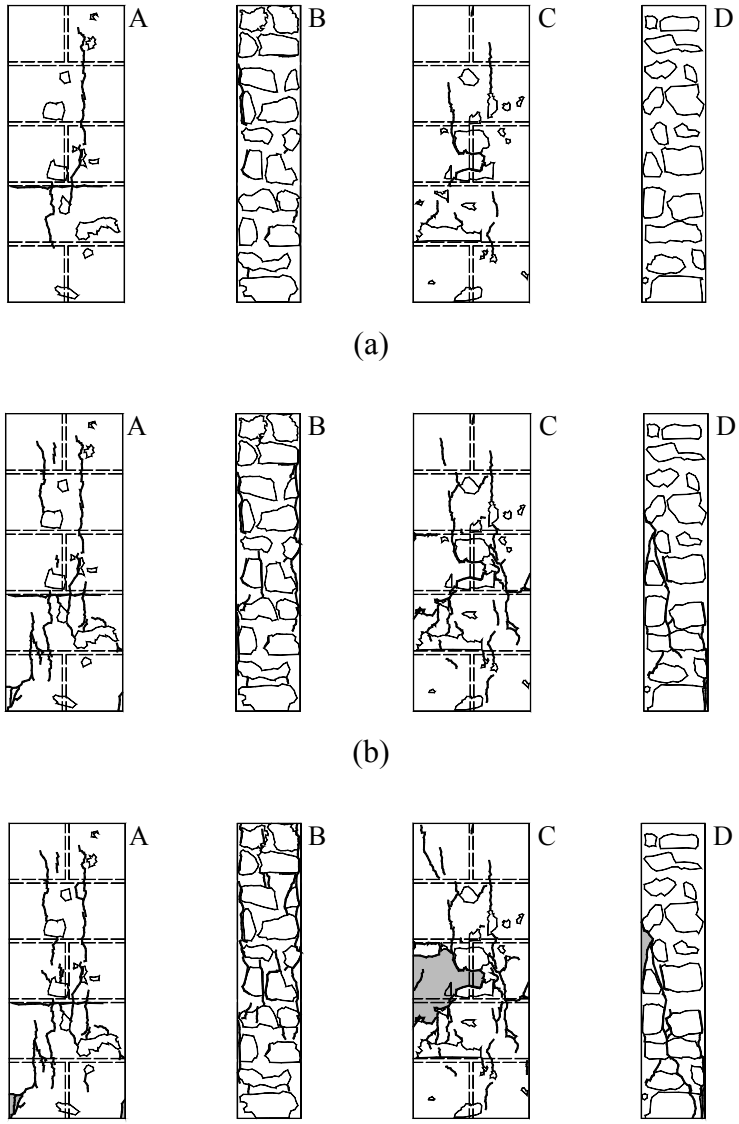

Figure B.44 – Crack pattern for *SS1_I* at: (a) 147 *kN* (70% of f_c), (b) 211 *kN* (peak load) and (c) 156 *kN* (74% of f_c, post-peak regime).

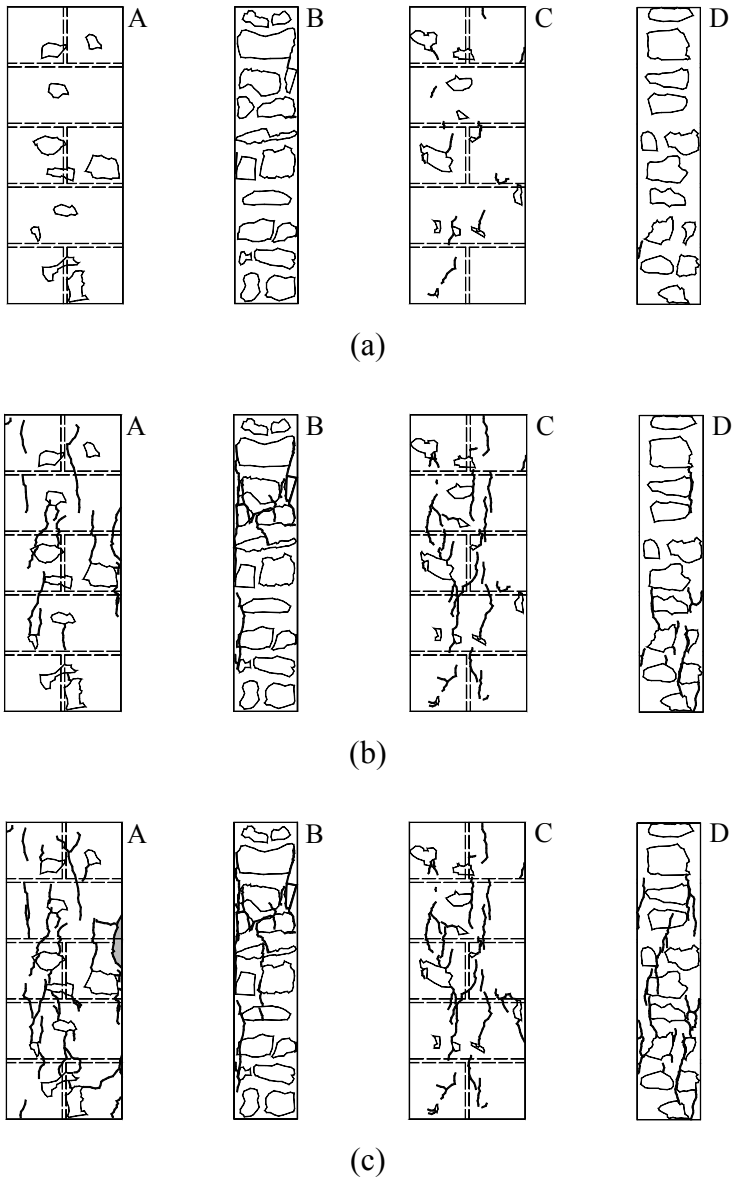

Figure B.45 – Crack pattern for *SS2_I* at: (a) 113 *kN* (55% of f_c), (b) 207 *kN* (peak load) and (c) 156 *kN* (75% of f_c, post-peak regime).

B.7 COMPRESSION TESTS ON FULL WALLETS: CRACK PATTERNS

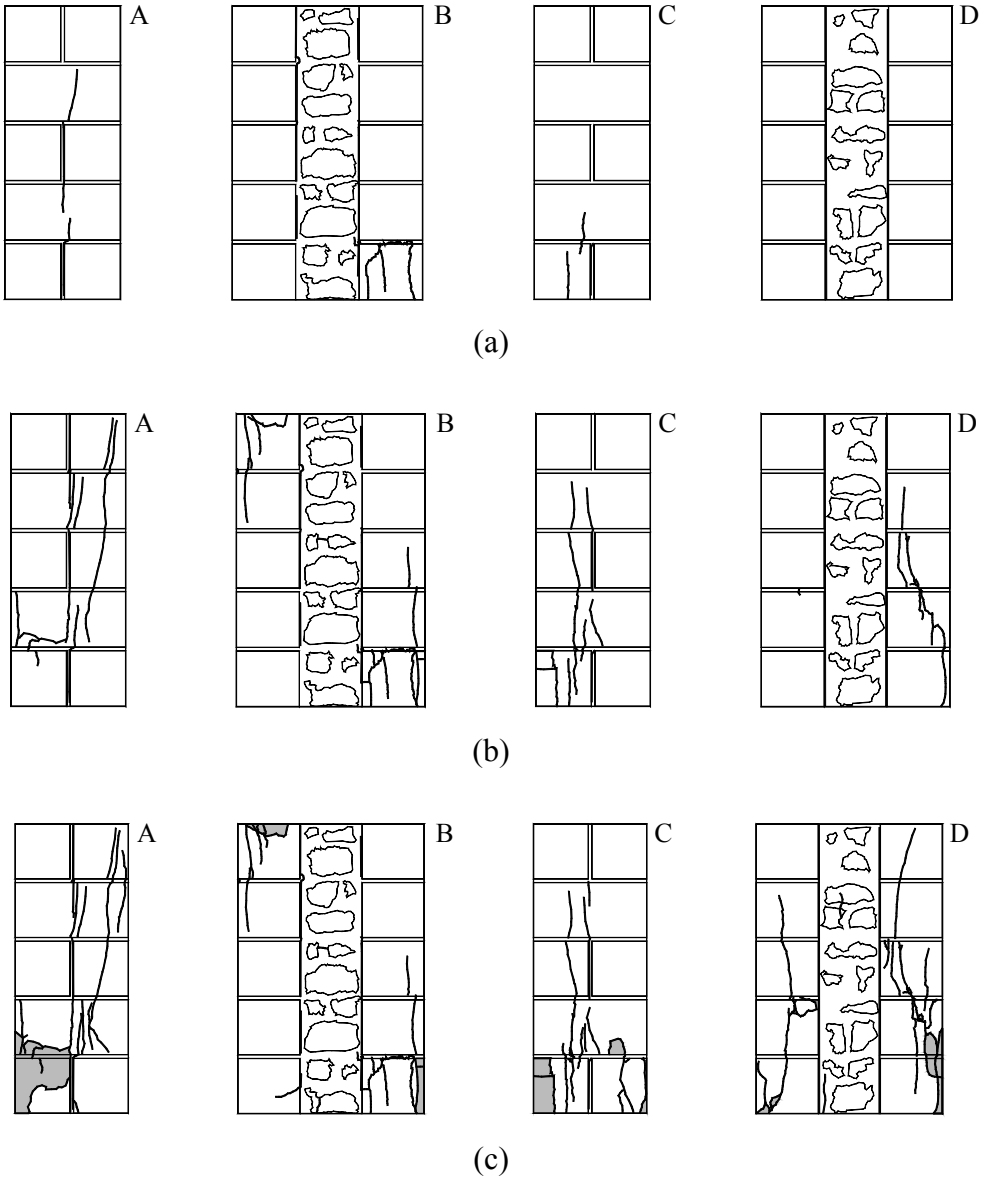

Figure B.46 – Crack pattern for *NS3* at: (a) 539 *kN* (59% of f_c), (b) 913 *kN* (peak load) and (c) 569 *kN* (62% of f_c, post-peak regime).

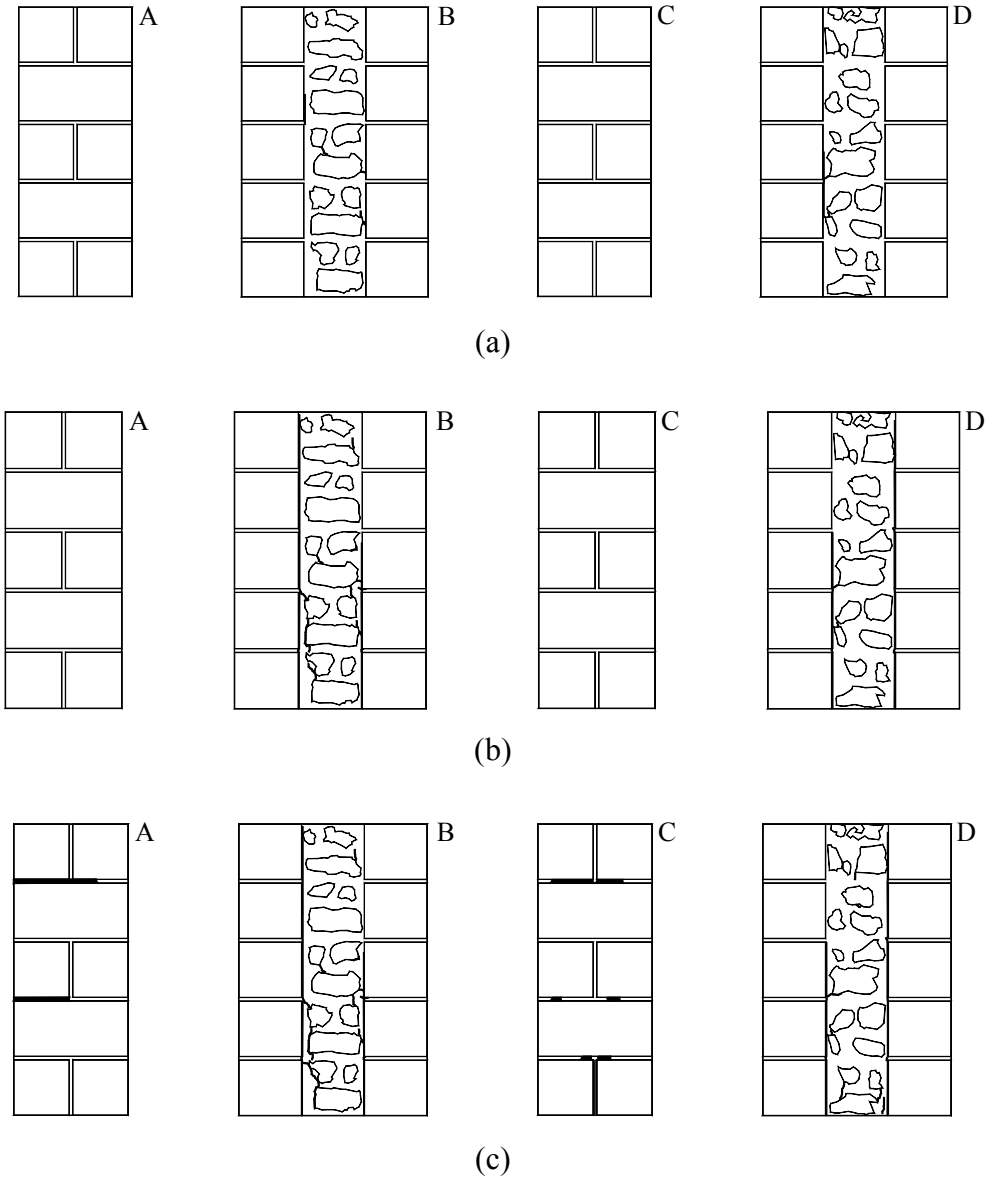

Figure B.47 – Crack pattern for *SS3*: (a) prior to test, (b) at 441 *kN* and (c) at 2380 *kN* (maximum load reached).

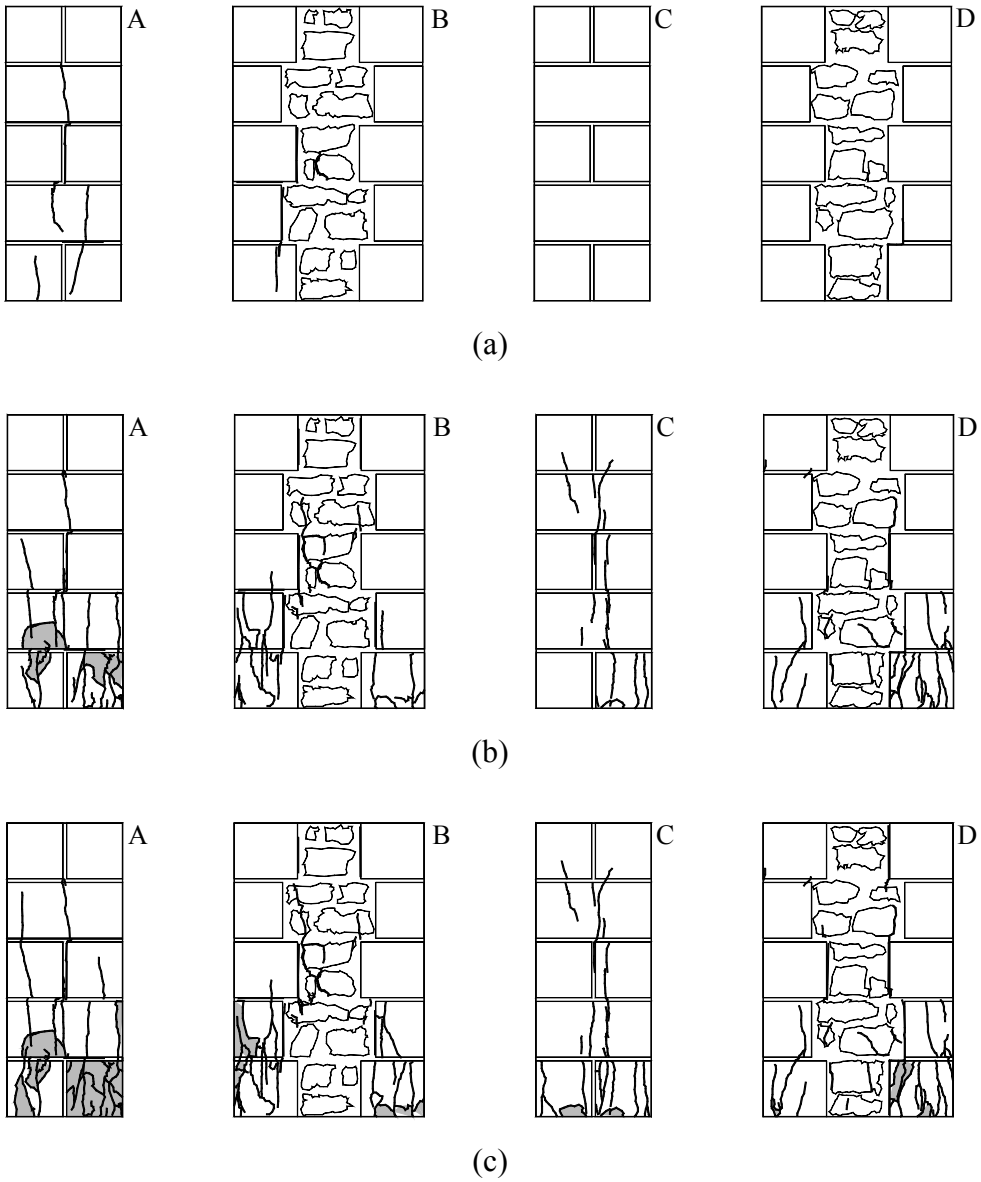

Figure B.48 – Crack pattern for *NK3* at: (a) 515 *kN* (51% of f_c), (b) at 1013 *kN* (peak load) and (c) 588 *kN* (58% of f_c, post-peak regime).

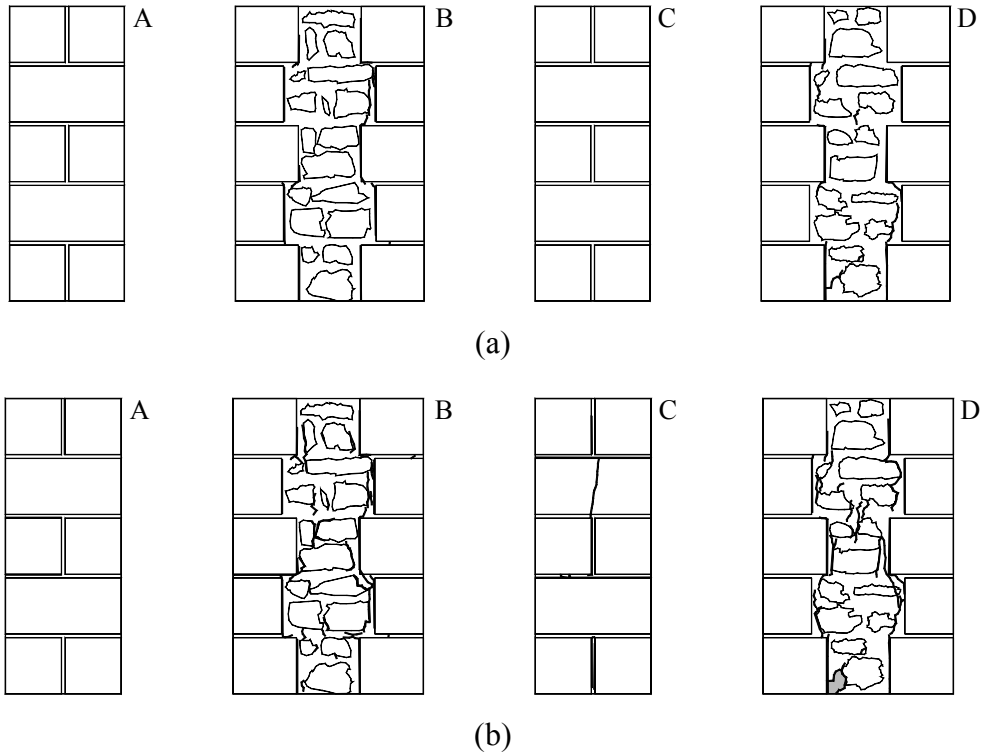

Figure B.49 – Crack pattern for *SK3* at: (a) 1289 *kN* and (b) 2380 *kN* (maximum load reached).

B.8 DISPLACEMENT TRANSDUCERS LENGTH

Table B.5 – Length of the transducers employed in the shear tests (in *mm*).

Transducer	*NS1*	*NS2*	*SS1*	*SS2*	*NK1*	*NK2*	*SK1*	*SK2*
2	326	324	319	322	325	320	318	318
3	143	60	58	63	160	160	161	164
4	448	463	56	447	340	350	311	343
5	448	51	437	61	340	340	317	338
6	342	433	343	450	345	345	318	342
7	81	99	99	98	95	85	100	100
8	325	342	341	343	340	345	344	340
9	325	324	325	318	325	320	322	324
10	143	60	58	48	150	150	151	151
11	443	60	60	29	150	150	162	151
12	450	470	338	448	150	150	150	150
13	339	431	436	421	150	150	146	151
14	84	90	99	102	150	153	159	149
15	325	335	340	343	150	150	148	146

Table B.6 – Length of the transducers employed in the compression tests on single leaves (in *mm*).

Trans-ducer	*NS1_E*	*NS2_E*	*SS1_E1*	*SS1_E2*	*SS2_E1*	*SS2_E2*	*NS1_I*	*NS2_I*	*SS1_I*	*SS2_I*
2	326	324	320	320	321	322	364	320	341	326
3	143	158	164	156	160	158	188	250	160	157
4	327	321	321	322	318	328	345	322	342	364
5	327	321	121	118	120	117	100	99	100	98
6	-	-	327	320	318	325	319	325	343	320
7	-	-	167	162	161	160	165	255	156	155
8	385	361	322	322	316	320	341	329	339	321
9	325	324	117	119	118	118	96	90	99	102
10	143	160	-	-	-	-	-	-	-	-
11	325	321	-	-	-	-	-	-	-	-
12	325	319	-	-	-	-	-	-	-	-
13	-	-	-	-	-	-	-	-	-	-
14	-	-	-	-	-	-	-	-	-	-
15	385	355	-	-	-	-	-	-	-	-

Table B.7 – Length of the transducers employed in the compression tests on full wallets (in *mm*).

Transducer	*NS3*	*SS3*	*NK3*	*SK3*
2	317	323	317	317
3	316	320	319	320
4	326	332	318	322
5	100	99	321	319
6	121	119	121	122
7	120	120	123	119
8	338	340	332	345
9	321	322	98	99
10	321	322	320	312
11	322	320	319	320
12	99	98	319	317
13	121	117	324	329
14	120	119	183	103
15	342	344	380	373